

---

# Synthesis and optical spectroscopy of (hetero)-nanocrystals: *An exciting interplay between chemistry and physics*

—

*Synthese en optische spectroscopie van (hetero)nanokristallen:  
een boeiend samenspel van natuur-en scheikunde (met een samenvatting  
in het Nederlands)*

PROEFSCHRIFT

ter verkrijging van de graad van doctor aan de Universiteit Utrecht op  
gezag van de rector magnificus, prof.dr. G.J. van der Zwaan, ingevolge  
het besluit van het college voor promoties in het openbaar te verdedigen  
op woensdag 17 oktober 2012 des middags te 2.30 uur

door ESTHER GROENEVELD  
geboren op 2 februari 1985, te Breda

Promotor: Prof.dr. A. Meijerink  
Co-promotor: Dr. C. de Mello Donegá

**Table of Contents**

Chapter 1:	<b>Warming up, A Brief Introduction to Colloidal (Hetero) Nanocrystals</b>	5
Chapter 2:	<b>Chemistry for Physicists, Synthesis of Colloidal (Hetero) Nanocrystals</b>	13
Chapter 3:	<b>Physics for Chemists, Size effects on the Electronic Structure and Optical Properties of Semiconductor (Hetero)Nanocrystals</b>	39
Chapter 4:	<b>Growth and Stability of ZnTe Magic-Size Nanocrystals, The start of something small</b>	61
Chapter 5:	<b>Highly Luminescent (Zn,Cd)Te-CdSe Colloidal Heteronanowires with Tunable Electron-Hole Overlap, From Small to Nano: Magic Clusters for Bright and Blinking Colloidal Nanowires</b>	87
Chapter 6:	<b>Enhanced Exciton-Phonon Coupling in Colloidal Type-II CdTe-CdSe Heteronanocrystals, Shaking up the excitons</b>	119
Chapter 7:	<b>Size dependence of the Exciton Transitions in Colloidal CdTe Quantum Dots, Absorption, Analysis and Agreement: experimental versus calculations</b>	155
Chapter 8:	<b>Formation of ZnSe/CdSe heteronanocrystals and alloy nanocrystals via cation-exchange, Living on the edge: cation exchange</b>	177
Chapter 9:	<b>Ligand Mediated Surface Reconstruction and Relaxation of Colloidal CdTe QDs, Shining Light on Photobrightening</b>	197
Chapter 10:	<b>Samenvatting in het Nederlands, 'Voetballen is heel simpel, maar het moeilijkste wat er is, is simpel voetballen.' Johan Crujff</b>	219
	<b>List of publications</b>	244
	<b>Dankwoord</b>	248
	<b>Curriculum vitae</b>	252



# Chapter 1

## **Warming up**

—

*A Brief Introduction to Colloidal  
(Hetero)Nanocrystals*

## 1.1 – Semiconductor (Hetero)Nanocrystals: Small things that make a big difference

In our daily lives we experience the properties of materials as being completely independent from the dimensions of the objects they make. For example, the colour of a sheet of paper does not change if we cut it into increasingly smaller pieces and a grain of sugar melts at the same temperature as a large sugar candy crystal. However, when the dimensions of materials reach the nanoscale regime (smaller than 100 nm), their properties can become size-dependent and strikingly different from those of their macroscopic (bulk) counterparts. Semiconductor nanocrystals (NCs), also known as quantum dots, have dimensions in the nanoscale regime (1-100 nm). They have remarkable properties, which can be tailored by controlling their size and shape. The origin of this size dependence can be traced to two fundamental nanoscale effects:<sup>[1,2]</sup> (a) the fraction of surface atoms (*i.e.*, the surface/volume ratio) increases with decreasing size and becomes significantly large in NCs; and (b) the limited dimensions of the NC lead to spatial confinement effects that may restrict the electronic motion and the propagation of vibrational waves in the nanocrystal.

The first effect (a) increases the free energy of NCs and makes them more reactive and dynamic than their larger counterparts and thereby modifying a number of material properties (*e.g.*, reactivity, solubility, melting and evaporation temperatures, plasticity etc.). It also makes NCs easily dispersible in solvents and very open to surface modification and functionalization. This is one of the most attractive features of colloidal NCs, since it opens up the possibility of fabricating optoelectronic devices by using solution processing techniques and of targeting NCs for specific biomedical applications (*e.g.*, labelling).<sup>[3-6]</sup> Colloidal NCs consist of an inorganic core coated by a layer of organic molecules, as depicted in figure 1.1. Not only the size but also the combination of a organic and inorganic part, makes NCs a versatile system of which the properties (luminescence, colloidal stability, and functionality) can be easily manipulated.<sup>[1]</sup> Moreover, as will be discussed later in this thesis (chapter 2), the interplay between the inorganic and the organic components and the large surface to volume ratio of colloidal NCs has a significant impact on their synthesis, being one of the driving forces behind the remarkable control achieved in recent years over the size and shape of colloidal NCs (figure 1.2).

The second effect (b) affects a number of properties (*viz.*, conductivity, magnetic properties, etc), but its most evident demonstration is in the

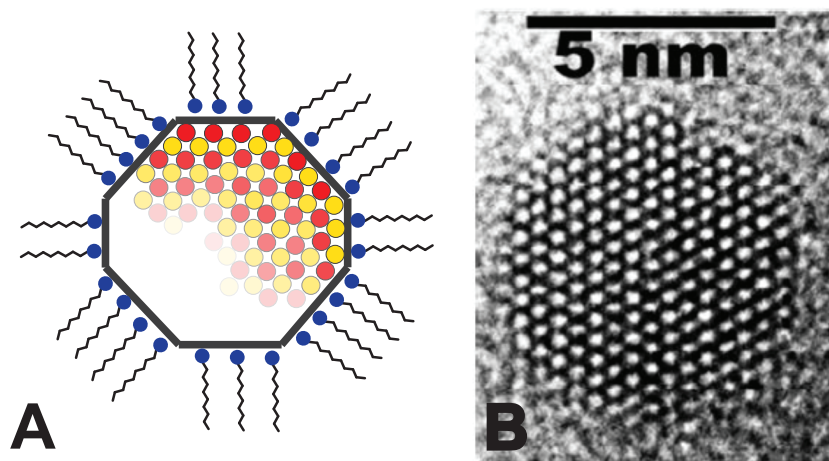


**Figure 1.1** – (a) Schematic illustration of a colloidal NC consisting of an inorganic crystal coated with an organic ligand layer. (b) High-resolution transmission electron microscope (TEM) image of a CdSe NC.

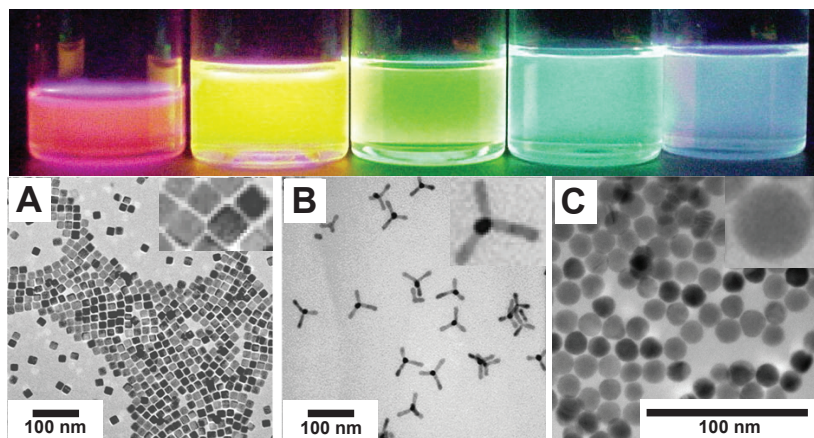


**Figure 1.2** – (Top panel) Colloidal suspensions of CdSe nanocrystals of decreasing size (from left to right) under ultraviolet excitation, showing size dependent photoluminescence colours. (Bottom panel) Transmission Electron Microscopy images of colloidal NCs of various compositions and shapes: PbSe cubes<sup>[7]</sup>, CdTe tetrapods<sup>[7]</sup> and CdTe spheres.

size- and shape-dependent optoelectronic properties of semiconductor NCs. This effect is better known as the quantum confinement effect, and takes place when the dimensions of the semiconductor NC becomes comparable to or smaller than the spatial extension of excitons (*i.e.*, electron-hole pairs) in the material. In this regime, the reduction of the NC size leads to an increase of the band gap (or HOMO-LUMO gap in a more chemical language), resulting in size- and shape-dependent optical properties, as clearly illustrated in figure 1.2. The fundamental principles behind the quantum confinement effect will be addressed in Chapter 3.

The development of semiconductor heteronanocrystals (HNCs) has opened up more exciting possibilities regarding property control and applications.<sup>[1]</sup> HNCs consist of two (or more) materials that are joined by one or more heterointerfaces, and can be made in different (complex) morphologies, as depicted in figure 1.3. The main advantage of semiconductor HNCs is that the spatial localization of the electron and hole can be controlled by a thoughtful choice of the composition, size and shape of the components of the HNC. In this way, quantum confinement effects can be used to tune the offsets between the energy levels across the heterointerface.

The first reports on the size dependence of the properties of semiconductor colloidal NCs were published in the beginning of the eighties.<sup>[9,10]</sup> Since then an increasingly large number of scientists has

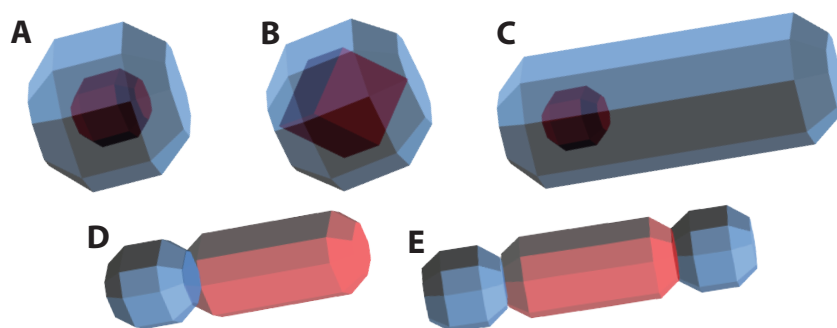


**Figure 1.3** – Schematic illustration of commonly used heteronanocrystal structures. (a) Concentric core/shell with spherical core (e.g. ZnSe/CdS), (b) concentric core/shell with cubic core (e.g. PbSe/CdSe), (c) dot core/rod shell (e.g. CdSe/CdS), (d) matchstick (e.g. CdSe/Au), (e) dumbbell (e.g. CdSe/PbSe, CdSe/Au).<sup>[1,8]</sup>



been attracted by the properties of semiconductor NCs and HNCs.<sup>[1,2,11-16]</sup> The NC research field is thus a young and flourishing multidisciplinary area in science which makes use of fundamentals from physics, chemistry, biology and materials science. It focuses on the NC synthesis, the fundamental understanding of size and dimensionality dependent properties in NCs, and the implementation of NCs in technological applications.

## 1.2 – Outline of this thesis

This thesis describes the synthesis as well as study of the optical properties of various colloidal (hetero)nanocrystals ((H)NCs). Both type of experiments involve chemistry and physics, leading to the bilateral character of this thesis. Before experimental results are discussed in detail, the essential theoretical background on the chemical and physical aspects of this work is provided in chapter 2 and 3, respectively. In **chapter 2** the concept of a nanocrystal as a dynamic hybrid particle consisting of an inorganic crystal core and organic surfactant shell is introduced. Furthermore, the synthesis of colloidal (H)NCs is discussed as well as the most important mechanisms on nucleation and growth of (H)NCs. **Chapter 3** describes the effect of spatial confinement on the electronic structure of (H)NCs taking the properties of bulk semiconductors as a starting point. The formation of ZnTe magic sized nanocrystals is discussed in **chapter 4**. The experimental results indicate that not only the reaction temperature, and concentration of precursors but also type of ligands play a crucial role in the formation of magic size NCs during NC syntheses. These ZnTe magic size clusters form the starting point of **chapter 5**, in which the synthesis and optical properties of highly luminescent (Zn,Cd)Te-CdSe heteronanowires is presented. The use of ZnTe MSC as seeds is found to be essential for the formation of the heteronanowires. The nanowires were formed via a growth mechanism in which the magic size clusters first undergo a fast  $\text{Zn}^{2+}$  by  $\text{Cd}^{2+}$  exchange resulting in (Zn,Cd)Te magic size clusters. The resulting (Zn,Cd)Te magic size clusters form nanowires via oriented attachment in which CdSe is incorporated. The optical properties of the heteronanowires imply the formation of a spatially indirect exciton after photoexcitation. The degree of electron-hole overlap of the spatial indirect exciton can be tuned by the amount of CdSe incorporated in the heteronanowires. **Chapter 6** discusses the coupling of excitons with longitudinal optical phonons in Type-II heteronanocrystals at 4.2 K. The results clearly show that this coupling is larger for Type-II HNCs than for other type of (H)NCs. This increase is explained by the decreased electron-hole wavefunction

overlap in Type-II HNCs which leads to larger exciton polarizabilities that enhance the exciton-phonon coupling via Fröhlich interactions. A distinct demonstration of the size dependence of the exciton levels in CdTe QDs is given in **chapter 7**. Analysis of the size dependent CdTe QD absorption spectra allowed a comparison with calculated absorption spectra. Best agreement for the energy position of the exciton transitions was found for tight binding calculations in which electron-hole configuration interactions were included, which shows the importance of the configuration interaction between electron and hole states in CdTe QDs. **Chapter 8** deals with the formation and optical properties of concentric core/shell ZnSe/CdSe heteronanocrystals synthesized via a cation exchange reaction. The optical properties of the core/shell HNCs suggest that the HNCs are type-I<sup>1/2</sup>. Furthermore, the influence of the reaction temperature on the cation exchange reaction and the final HNC elemental distribution profile is investigated. Exchange reaction at 220°C resulted in a gradient alloy NC whereas at 150°C core/shell HNC were obtained. This result implies that there is an energy barrier for the formation of a (Cd,Zn)Se alloy from a ZnSe/CdSe core/shell HNCs. In **chapter 9** a study of the photoluminescence (PL) enhancement of suspensions of colloidal CdTe QDs as a function of the equilibration time after dilution is presented. Two different alkylamines (*viz.*, dodecylamine, DDA, and octadecylamine, ODA) were used as capping ligands. The temporal evolution of the PL quantum yields (QYs) was followed both under periodic illumination and in the dark, for up to 25 h. Based on our results we propose a ligand mediated surface reconstruction and surface relaxation model. This model emphasizes the importance of the ligand-ligand and ligand-NC surface interactions which determine the evolution of the PL-enhancement of the colloidal CdTe QDs.

## REFERENCES

1. C. de Mello Donegá, *Chem. Soc. Rev.* 2011, 40, 1512–1546.
2. A. P. Alivisatos, *J. Phys. Chem.*, 1996, 100, 13226-13239.
3. D. V. Talapin, J. Lee, M. V. Kovalenko, E. V. Shevchenko, *Chem. Rev.* 2010, 110, 389.
4. R. C. Somers, M. G. Bawendi, D. G. Nocera, *Chem. Soc. Rev.* 2007, 36, 579.
5. N. A. Frey, S. Peng, K. Cheng, S. Sun, *Chem. Soc. Rev.*, 2009, 38, 2532.
6. P. V. Kamat, *J. Phys. Chem. C*, 2008, 112, 18737.
7. D. V. Talapin, J.-S. Lee, M. V. Kovalenko, E. V. Shevchenko, *Chem. Rev.* 2010, 110, 389-458.
8. L. Carbone, P. D. Cozzoli, *Nano Today*, 2010, 5, 449-493.
9. R. Rosetti, J. L. Ellison, J. M. Gibson, L. E. Brus, *J. Chem. Phys.* 1984, 80, 4464.
10. A. I. Ekimov, A. A. Onoshchenko, *Fizika I Tekhnika Poluprovodnikov* 1982, 16, 1215.
11. C. B. Murray, C. R. Kagan, M. G. Bawendi, *Annu. Rev. Mater. Sci.* 2000, 30, 545–610.
12. V. I. Klimov, *Annu. Rev. Phys. Chem.* 2007, 58, 635–673.
13. C.L. Choi, A. P. Alivisatos, *Annu. Rev. Phys. Chem.* 2010, 61, 369–389.
14. D. Vanmaekelbergh and P. Liljeroth, *Chem. Soc. Rev.* 2005, 34, 299-312.
15. A. Meijerink, 'Exciton dynamics and energy transfer processes in semiconductor nanocrystals', A. L. Rogach (Ed.) 'Synthesis, Assembly, Spectroscopy and Applications', Austria: Springer-Verlag/Wien, 2008.
16. W. G. J. H. M. v. Sark, K. W. J. Barnham, L. H. Slooff, A. J. Chatten, A. Büchtemann, A. Meyer, S. J. McCormack, R. Koole, D. J. Farrell, R. Bose, E. E. Bende, A. R. Burgers, T. Budel, J. Quilitz, M. Kennedy, T. Meyer, C. D. M. Donegá, A. Meijerink, D. Vanmaekelbergh, *Opt. Express* 2008, 16, 21773-21792.



# Chapter 2

# **Chemistry for Physicists**

—

## *Synthesis of Colloidal (Hetero) Nanocrystals*

## Abstract

*Colloidal (hetero)nanocrystals ((H)NCs) can be regarded as inorganic-organic hybrid nanomaterials consisting of a multi faceted crystal inorganic core and a dynamic organic surfactant layer. This chapter discusses the essential concepts involved in the wet chemical (H)NC synthesis and the impact of the inorganic and organic (H)NC components on the growth of the colloidal (H) NCs.*

## 2.1 – Introduction

High-quality colloidal (hetero)nanocrystals [(H)NCs] are required for the fundamental study of their properties and for their implementation in technological applications. High-quality implies that the (H)NCs have a small dispersion in size and shape, high (colloidal) stability, and low concentration of defects leading to high photoluminescence quantum yields. The demand for high quality colloidal (H)NCs has turned the research on new synthesis methods into a very active and booming field. As a result a remarkable degree of control over the size, shape, composition, and surface of NCs and HNCs has been achieved during the last decade.<sup>[1-6]</sup> Wet chemical colloidal synthesis route yields (H)NCs that are readily dispersible into a variety of polar or apolar solvents due to a stabilizing organic coating layer. In this chapter the basic principles of colloidal (H) NC synthesis via wet chemical methods are described. First, the colloidal NC and its organic capping layer will be addressed, followed by a basic description of colloidal (H)NC synthesis. Finally, a general description of the fundamentals of nucleation and growth of (H)NCs is given, which is insightful for researchers (chemists and physicists) working in the field of colloidal NCs.

## 2.2 – Colloidal (hetero)nanocrystals: organic and inorganic components

Colloidal NCs consist of a multifaceted inorganic nanocrystal that is coated with a monolayer of amphiphilic organic ligands (figure 2.1), and can thus be described as a two component system: an inorganic core and an organic ligand shell. The properties of colloidal NCs are thus not only determined by the inorganic nanocrystal core, but rather by the combination of the inorganic core and the organic shell. To achieve a strict control over the characteristics of colloidal NCs one must acquire a comprehensive understanding of all the relevant interactions taking place within the system, such as interactions of atoms within the NCs, interactions between surface atoms and the polar head of the organic surfactant molecules, and

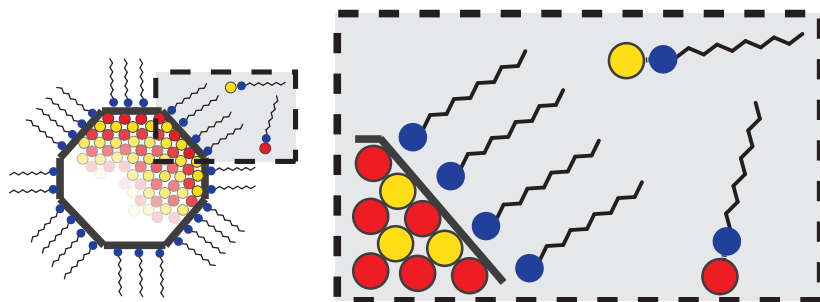


**Figure 2.1** – Schematic representation of a colloidal NC showing the crystalline and multifaceted nature of the inorganic core and the monolayer of amphiphilic organic molecules (the ligand shell) bound to the surface. The right panel emphasizes the essential interactions taking place between the atoms within the NC, at the surface and in the growth medium.

intermolecular interactions between the surfactant molecules themselves both at the surface and in solution.

### 2.2.1 – The inorganic core

The inorganic NC core can have different shapes (*e.g.*, spherical, rod shaped, pyramidal) and various compositions, such as single materials (metals, semiconductors, insulators), alloys, or a combination of two or more materials joined by one or more heterointerface (*i.e.*, a heteronanocrystal). In this thesis only II-VI semiconductor (H)NCs (*e.g.*, ZnTe, CdTe, CdSe, ZnSe-CdSe) are investigated. These materials can crystallize in the zinc blende phase or the wurtzite phase. Bulk crystals crystallize in the thermodynamically stable phase, whereas NCs may also crystallize in metastable phases. As mentioned in Chapter 1, NCs have a large surface to volume ratio and therefore the overall surface free energy may be such that crystalline phases that are metastable for bulk crystals become energetically favourable for NCs.<sup>[2,7,8]</sup> The crystal structure of the NC is important since it not only determines the electronic structure but it also defines which facets will be exposed on the surface. The crystallographic nature of the facets can have a large impact on the NC growth, as will be discussed later in this chapter.

### 2.2.2 – The organic surfactant shell

The surfactant molecules on the surface of the NC are amphiphilic organic molecules that consist of a polar head and a non-polar hydrocarbon tail. In colloidal semiconductor NC synthesis the polar head can coordinate to the metal or chalcogenide atoms in solution and at the NC surface, while the hydrocarbon tail determines the interactions of the surfactant layer with the surrounding medium. Surfactants are due to their coordinating character usually referred to as ligands or coordinating solvents. Ligands are an important aspect of the colloidal NC,<sup>[7]</sup> since they not only control the NC growth during the synthesis, but also its colloidal stability in solution and optical properties.<sup>[9]</sup> Moreover, the interactions with the ligands can be utilized to assemble molecules with new functionalities around the NCs (*e.g.* for biomedical imaging).<sup>[10]</sup>

Ligands provide the NCs with **colloidal stability**, preventing aggregation of the NCs by means of repulsive Van der Waals or electrostatic interactions (steric stabilization and charge stabilization, respectively).<sup>[11]</sup> The type of interaction depends on the nature of the ligand bound to the NC surface. The NC colloidal stability is very useful and can for example be used to narrow the size distribution in a NC dispersion. Larger NCs have larger attractive forces towards each other. Therefore, upon addition of a non-solvent to a NC dispersion larger NCs destabilize earlier than smaller ones, thereby allowing separation of the different NC sizes.

Typical ligands used in II-VI semiconductor synthesis are alkylamines ( $R-NH_2$ ), fatty acids ( $R-COOH$ ), alkylphosphine oxides ( $R_3PO$ ), phosphonic acids ( $R-PO(OH)_2$ ), alkylthiols ( $R-SH$ ), and alkylphosphines ( $R_3P$ ). The latter ligands are one of the few available ligands that bind primarily to the non-metal component of the NC (chalcogenides, *e.g.* Te, Se). Examples of commonly used ligands are given in figure 2.2. **The metal-ligand binding strength<sup>[12]</sup>** is determined by the Lewis acidity of the metal (electron acceptor, *e.g.*  $Zn^{2+}$ ) and the Lewis basicity of the head group of the ligand (electron donor, *e.g.*  $O^{2-}$ ). **The chalcogenide-ligand bond<sup>[12]</sup>** is formed via a different interaction, namely via  $\pi$ -backbonding from the chalcogenide to the ligand head atom (phosphorus for alkylphosphine ligands). The metal-ligand bonding strength is also influenced by the length of the hydrocarbon tail, for example shorter alkyl chains result in a weaker bond. The strength of the chalcogenide-ligand bond displays an opposite chain length dependence, since the bond strength increases with increasing chain length. The metal/chalcogenide-ligand bonding strength has a large influence on the NC



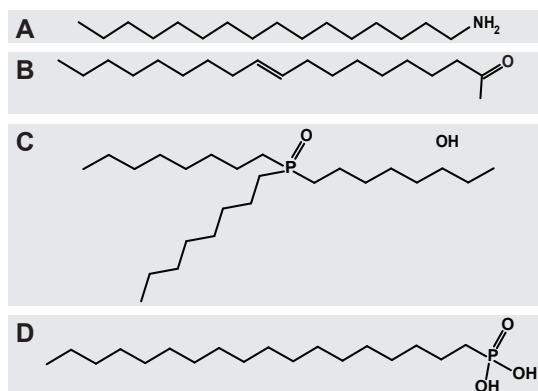


**Figure 2.2** – Examples of ligands commonly used in colloidal NC synthesis. (a) hexadecylamine (HDA), (b) oleic acid (OA), (c) trioctylphosphine oxide (TOPO), (d) octadecylphosphonic acid (ODPA).

growth and its stability. It not only determines the reactivity of the **metal/chalcogenide-ligand complex** (monomer) but it also influences the **binding strength to the NC surface**. Strong metal/chalcogenide-ligand bonds give NC a high colloidal stability but can result in (too) slow growth during synthesis, whereas weak bonds can result in fast (uncontrolled) growth and low (insufficient) colloidal stability. Depending on the desired NC size and shape a reasonable choice of ligands for NC synthesis can be made based on their binding nature and chain length. The different NC surface-ligand interactions of the various ligands can be used to change the NC solubility in solution.<sup>[3,25]</sup> The exchange of a weakly binding ligand (*e.g.*, nonpolar) by a strongly binding ligand (*e.g.*, polar) can change the NC solubility and make it soluble polar solvents.

The **optical properties** of NCs depend strongly on the nature of the ligands on the surface.<sup>[7]</sup> Photoluminescence (PL) is quenched by non-radiative decay of the exciton in defect and surface states (this will be explained in more detail in chapter 3). Dangling orbitals at the NC surface form energy states that are located in the HOMO-LUMO gap, and therefore trap the exciton and favour its recombination via non-radiative pathways. PL can be influenced by the ligands via different mechanisms, namely surface passivation, surface relaxation and reconstruction, and carrier trapping. In **surface passivation** the bond formed between the donor atom of the ligand and the dangling orbitals at the NC surface shifts the energy of the surface states away from the HOMO-LUMO gap, thereby preventing nonradiative

relaxation via these states. Another way to shift the surface states away from the HOMO-LUMO gap is via **surface relaxation or reconstruction**. Ligands have the ability to modify the surface free energy and thereby hinder or facilitate the reorganisation of the surface atoms leading to relaxation or reconstruction of the NC surface. Radiative exciton recombination can be prohibited when ligands act as **carrier traps** scavenging the photogenerated electrons or holes from the NCs.<sup>[3, 12]</sup>

### 2.3 – Colloidal (hetero)nanocrystal synthesis

Colloidal NCs can be fabricated via wet chemical synthesis methods in which ligands are used. In this method, NCs are grown via the addition and consecutive reaction of metal and chalcogenide ligand complexes in a (hot) solution, leading to the precipitation of an insoluble metal chalcogenide compound, as schematically shown in figure 2.3a. A HNC synthesis is different because the metal- and chalcogenide-ligand complexes are added to a (hot) solution already containing single component NCs, as illustrated in figure 2.3b.

For the growth of **colloidal nanocrystals** it is important that the conditions are such that NC growth is controlled and arrested when the desired dimensions are reached.<sup>[13]</sup> This is achieved by using precursors, that contain metals and chalcogenides (*e.g.* organometallic compounds or inorganic salts), at sufficiently high temperatures and/or concentrations in the presence of coordinating ligands. The (thermal) decomposition of the precursors results in a high concentration of metal and chalcogenide ions (atoms) over a short time period, which leads to a **nucleation** event followed by a period of **growth** of the formed nuclei. There are two approaches to achieve a short nucleation followed by slow growth, namely the “**hot injection**” method<sup>[15,16]</sup> and the “**heating-up**” method.<sup>[16]</sup> In the “hot-injection” method, as is illustrated in figure 2.3a, one (or both) precursor is quickly injected in a hot (~100°C~300°C) high boiling point apolar solvent containing the other precursor leading to a quick increase in the total precursor concentration. In the “heating-up” method a rapid increase in the decomposition rate is obtained by quickly increasing the reaction temperature.

**Colloidal heteronanocrystals** are made by growing a second material over a pre-existing NC. The HNC synthesis is usually performed at lower temperatures than used for the growth of the NC seed. There are mainly two strategies for synthesis, namely the single stage and the multistage seeded growth approach.<sup>[7]</sup> In the **single stage approach** the heteronanocrystals

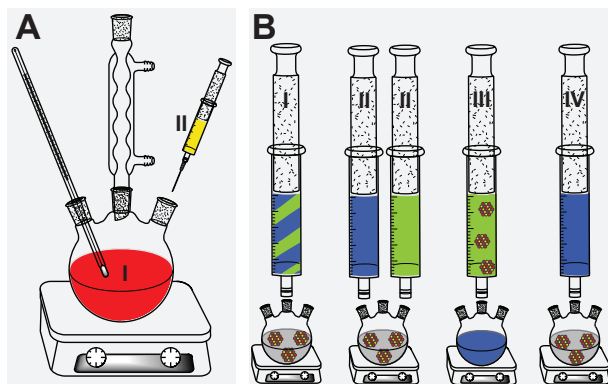


**Figure 2.3** – (a) Schematic representation of a typical colloidal nanocrystal synthesis by the Hot injection method: one of the two precursors (I) is in the reaction flask at high temperatures while the other precursor (II), which is at room temperature, is swiftly injected into the reaction flask. (b) Schematic overviews of several strategies to synthesize colloidal heteronanocrystals I) dropwise addition of mixed precursor, II) alternate addition (dropwise/injection) of precursors, III) seeded injection, IV) cation exchange.

are grown directly after the growth of the NC seeds via the addition of the precursors of the second material. It is a quick and simple approach, but because the growth of the NC seed and the HNC is done in the same reaction mixture there is a high risk of forming a (partially) alloyed NC instead of a HNC. In the **multistage approach** (which is used in this thesis) NC seeds are first separated from their reaction mixture by precipitation, purified and subsequently added to a ‘fresh’ solution to which precursors of the second component of the HNC are added. This approach has many advantages over the single stage approach. It effectively separates nucleation and growth, allows for different reaction conditions to be used for each HNC segment, and prevents (minimizes) interfacial alloying by the use of a ‘fresh’ coordinating solvent mixture that is free from precursors from the seed NC. Moreover, the NC seed can be subjected to post-synthetic processing (purification, size-selection, ligand exchange or annealing) which is a large advantage since the properties of the seed have an important influence on the final shape of the HNC. Finally, there is also a high flexibility on the choice of synthesis techniques. There are, for example, various manners to add the NC seed and the precursor of the second material, as illustrated

in figure 2.3b. The precursors can be mixed before addition (I) or added subsequently (II). In a seeded injection (III) addition, NC seeds are injected together with one of the precursors. Addition of only one of the precursors (IV) can be used to make HNCs via a method referred to as cation exchange.

[17,18,19]

**Ligands** serve an essential role in (H)NC synthesis since they control both the nucleation and growth rates. The binding strength of ligand-metal/chalcogenide determines the decomposition rate of the precursor and the binding dynamics of the ligand to the NC surface. Ligands can be introduced as the (coordinating) organic solvent (optionally diluted by a non-coordinating solvent, *e.g.* octadecene) of the reaction mixture, but can be also part of the precursor compound (*e.g.* Cd-oleate).

## 2.4 – Formation of colloidal nanocrystals

The colloidal (H)NC synthesis research area has developed into a rather mature field over the last decades. Despite the large amount of publications on this topic, the underlying mechanisms leading to nucleation and growth are still not fully understood. Consequently, a general theoretical model that accurately describes the formation of colloidal NCs has not yet been developed. So far researchers design their NC synthesis methods based on previous experience and they are guided by a number of fundamental principles that evolved from a few classical models<sup>[20,21]</sup> for nucleation and growth and a large body of empirical data accumulated over the last two decades. Different stages of **colloidal nanocrystal growth**, consisting of elementary kinetic steps<sup>[7,22-24]</sup>, can be recognized (as illustrated in figure 2.4):

**I. Induction or pre-nucleation period:** This period starts with the addition of the precursors and ends when stable crystal nuclei are formed. Monomers are formed from precursors at an average rate  $K_1$ . For NCs of binary ME semiconductors (*e.g.*, CdSe) the monomer units are thought to consist of at least one [ME] unit, possibly stabilized by a number of ligand molecules. When the concentration of monomers increases, small and unstable clusters (*i.e.*, sub-critical nuclei or crystal embryos) start to form at an average rate  $K_2$ .

**II. Nucleation stage:** Nucleation marks the end of the induction period and is defined as a single step process through which the crystal nuclei (embryos) reach a sufficiently large size to become viable, *i.e.*, capable of

growing rather than redissolving. The crystal nucleus radius at which the probabilities of growth and dissolution become equal is referred to as critical radius ( $r_c$ ). The nucleation stage is thus the time period in which single step nucleation events occur. In this stage nuclei with radius  $r$  equal to or larger than  $r_c$  are formed with a rate  $K_{rc}$ , either by the addition of one more monomer unit to the largest possible subcritical nucleus forming a critical nucleus, or by the coalescence of two (or more) smaller subcritical nuclei into a nucleus with  $r \geq r_c$  (*i.e.*, critical or super-critical nuclei). Critical (and super-critical) nuclei are only formed at monomer supersaturations higher than a critical value ( $S_{crit}$ ), as is depicted in figure 2.4a. A **supersaturated** solution is a thermodynamically unstable system in which the solute concentration becomes higher than its solubility limit. The degree of supersaturation  $S$  is thus the ratio between the actual (transient) solute activities in the reaction medium and the solute solubility under the reaction conditions (temperature, solvent composition, etc.). In the present case, supersaturation can thus be obtained by a sudden increase in the monomer concentration (*e.g.*, by injection of precursors or by raising the temperature), or by a sudden decrease in the solubility of the solute (*e.g.*, by a drop in temperature). Monomers are still being formed during nucleation but when the monomer consumption rate exceeds the monomer production rate  $S$  starts to decline to a level that eventually becomes too low to sustain nucleation. The time period of the nucleation stage is thus determined by the balance between the monomer production and consumption rates.

**III. Growth stage:** Growth of the critical (and supercritical) crystal nuclei proceeds, at an average rate  $K_g$ , via the sequential addition of monomer units to the growing NCs or by coalescence of smaller NCs, or by a combination of both processes. If allowed, growth proceeds until the monomer concentration is as low as the solubility equilibrium level. Usually, growth is arrested before the equilibrium level is reached to prevent Ostwald ripening. Ostwald ripening is the growth of larger NCs at the expenses of smaller NCs, and consequently leads to a broadening of the size distribution.

Sufficient separation between the nucleation and growth stages is needed to synthesize (H)NCs with a **narrow size distribution**.<sup>[7, 15, 22, 23, 25]</sup> This can be achieved by using the above mentioned ‘hot injection’ and ‘heating up’ methods. For the design of a (H)NC synthesis it is essential to realize that all three stages are coupled, since both nucleation and growth rely on the limited supply of monomers that are formed in stage I. Therefore, the monomers available during the growth stage are either those that were not

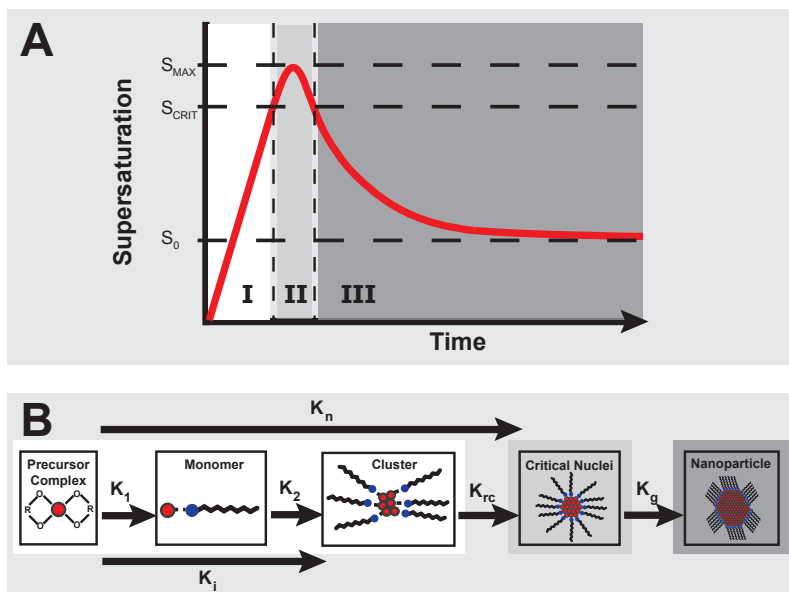


**Figure 2.4** – (a) Temporal evolution of the supersaturation degree  $S$  during the three stages in NC synthesis (I: induction; II: nucleation; III: growth).  $S_0$  is equal to the solubility limit of the solute material. (b) Graphic illustration of the different steps in NC synthesis and corresponding reaction rates.  $K_1$  is the rate of formation of monomers from precursors.  $K_2$  is the formation rate of subcritical nuclei. The length of the induction period is inversely proportional to  $K_1$ .  $K_{rc}$  is the nucleation rate (formation of critical nuclei).  $K_n$  is the effective nucleation rate.  $K_g$  is the average growth rate of NCs from critical nuclei.

consumed in the nucleation stage or are being produced from monomers at a rate that is too low to sustain nucleation. A well considered kinetic balance between the nucleation and growth rates is thus necessary to have good control over the size and shape of the NCs.

The elementary kinetic stages during the synthesis of **colloidal heteronanocrystals** are similar to those observed during the formation of single composition colloidal nanocrystals, except for the nucleation stage. This stage is fundamentally different for heteronanocrystals since in this case the second material is grown over pre-existing nanocrystals of a different material. Therefore, homogeneous nucleation (*i.e.*, the formation of critical nuclei of the second material directly in the growth solution) is no longer desired, but instead nucleation directly over the seed NC (*i.e.*,

heterogeneous nucleation) is preferred. These two types of nucleation will be discussed in more detail below (2.4.1). In some cases (for example, to synthesize concentric core/shell heteronanocrystals) it is necessary to prevent both homogeneous and heterogeneous nucleation, in order to allow the reaction to start directly in the growth stage, which will then take place via heteroepitaxy. The growth mechanisms will be discussed in more detail in section 2.4.2.

### 2.4.1 – Nucleation

Nucleation can be homogeneous or heterogeneous, as depicted in figure 2.5.<sup>[4, 7, 15, 22, 23]</sup>

**Homogeneous nucleation** requires spontaneous density fluctuations of the medium which initiates the self-assembly of atoms into a crystal nucleus that is sufficiently large to be stable. As mentioned above, the minimum stable nuclei size is defined by the critical radius ( $r_c$ ). Nuclei with radius smaller than  $r_c$  will redissolve, while nuclei with radius larger than  $r_c$  undergo further growth. There are various models to describe nanoparticle (NP) formation, but the basics of homogeneous nucleation are probably explained best with the simplest, and possibly the most inaccurate, model: **Classical Nucleation Theory (CNT)**.<sup>[4,15,22]</sup> CNT can be used to qualitatively discuss the principles involved in the nucleation of colloidal NCs. The driving force for nucleation is the difference in free energy between the crystal components (monomers) in the crystal and in solution. The total change in free energy for the formation of a spherical crystal nucleus is given by:

$$\Delta G_{TOT} = \Delta G_V + \Delta G_S = \left(\frac{4}{3}\right)\pi r^3 \rho \Delta\mu + 4\pi r^2 \gamma \quad (2.1)$$

in which  $r$  is the crystal nucleus radius,  $\rho$  is the density of the crystalline phase,  $\gamma$  is the interfacial tension between the developing crystal and the supersaturated solution, and  $\Delta\mu$  represents the chemical potential difference between the nucleus and the monomers in solution.  $\Delta G_V$  is the **volume excess free energy** and will be negative due to energy freed when chemical bonds are formed in the crystal nucleus.  $\Delta G_S$  is the **surface excess free energy** and will be positive due to the fact that the NC surface atoms have unsaturated bonds. Because  $\Delta G_V$  and  $\Delta G_S$  have opposite signs and different size dependences,  $\Delta G_{TOT}$  will reach a maximum for nuclei with the critical radius. Above the critical radius  $\Delta G_{TOT}$  will decrease with increasing radius, as is depicted in figure 2.6.

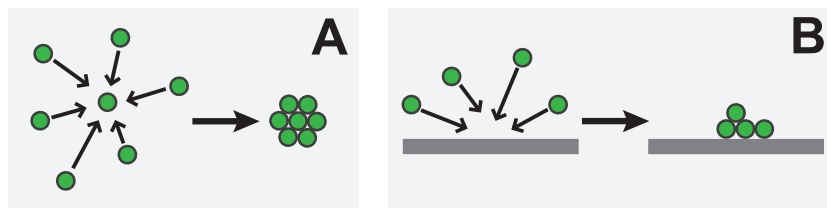


**Figure 2.5** – Schematic illustration of (a) homogeneous nucleation. (b) heterogeneous nucleation.

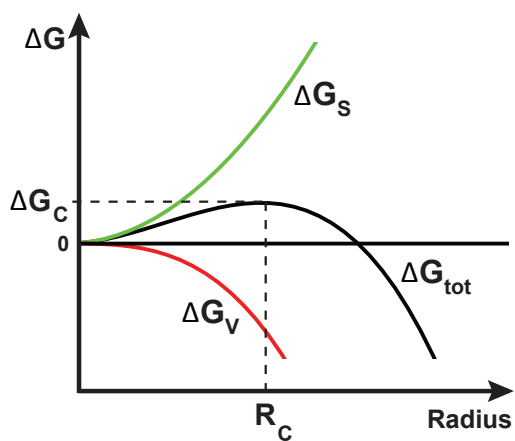


**Figure 2.6** – Change in free energy during the formation of a spherical crystal nucleus.  $\Delta G_v$  gives the volume excess free energy,  $\Delta G_s$  the surface excess free energy, and  $\Delta G_{tot}$  is the free energy change.  $\Delta G_c$  indicates the activation energy for nucleation.



There is thus an energy barrier for nucleation,  $\Delta G_c$ . This barrier imposes that a crystal nuclei smaller than the critical radius will redissolve to monomers, while crystal nuclei larger than the critical size are able to grow further and become mature NCs. The critical radius is given by:

$$r_c = -\frac{2\gamma}{\rho k_b T \ln S} \quad (2.2)$$

in which  $k_b$  is the Boltzmann constant and  $T$  is the reaction temperature. Equation 2.2 demonstrates that a higher synthesis temperature or a higher degree of supersaturation leads to a smaller critical radius. The nucleation rate increases with increasing temperature and degree of supersaturation, and decreasing interfacial tension. Larger nucleation rates lead to a larger concentration of smaller NCs, while slower nucleation results in a smaller concentration of larger NCs. The principles outlined above can explain the success of the hot-injection technique. The injection leads to a large degree of supersaturation at a high temperature, which results in a quick nucleation burst forming many small nuclei that rapidly lower the monomer concentration. The injection of the cold precursor also leads to fast cooling. The combination of lower  $S$  and lower  $T$  drops the nucleation rates to negligible values and only further growth of the formed nuclei can occur. This technique effectively separates the nucleation and growth stages, leading to a small size distribution.

**Ligands** play an essential role in the nucleation stage, since they may lower or increase the nucleation rates by **changing the reactivity of the precursor**. The ligand may enhance the decomposition rate of the precursor, thereby enhancing the monomer formation rate and consequently the nucleation rates. The strength of the **metal/chalcogenide-ligand bond** has also to be considered. A higher stability of the monomer in solution leads to a lower  $\Delta\mu$  and consequently a larger  $\Delta G_c$ . Furthermore, a higher monomer stability in solution is equivalent to increasing the solubility of the crystallizing material, which lowers  $S$  and thereby increases  $r_c$  and decreases the nucleation rate. For these reasons, the **ligand concentration** is also important parameter, since it may boost or suppress the ligand influence on the nucleation rates.

**Heterogeneous nucleation** involves nucleation on a pre-existing surface. This surface provides a low-energy interface with the newly formed crystal phase and thereby lowers the activation energy for nucleation ( $\Delta G_c$ ),<sup>[7,23,27]</sup> as illustrated in figure 2.7a Heterogeneous nucleation will therefore take

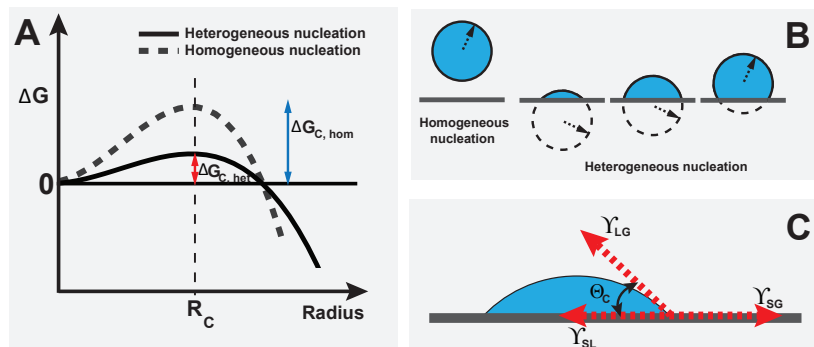


**Figure 2.7** – (a) Change in free energy during the formation of a spherical crystal nucleus for heterogeneous and homogeneous nucleation.  $\Delta G_c$  indicates the activation energy for nucleation.  $R_c$  indicates the critical radius, which is the same for homogeneous and heterogeneous nucleation under identical conditions (i.e., temperature, degree of supersaturation and interfacial tension between nucleating crystal and solution, see eq. 2.2). (b) The volume of material required to form a critical nucleus of radius  $r_c$  is much larger for homogenous nucleation, and decreases further for heterogeneous nucleation as the wetting angle  $\vartheta_c$  decreases. (c) Illustration of the wetting angle  $\vartheta_c$  between the nucleating material and the substrate, and the three different interfacial energies involved in the heterogeneous nucleation process ( $\gamma_{NS}$ ,  $\gamma_{NL}$ , and  $\gamma_{SL}$ , which represent the solution-nucleus, the nucleus-substrate, and the substrate-solution interfacial tensions, respectively, see eq. 2.4).

place at lower temperatures and/or supersaturations than homogeneous nucleation, allowing reaction conditions to be used that suppress homogeneous nucleation.  $\Delta G_c$  for heterogeneous nucleation is given by:

$$\Delta G_c(het) = \Delta G_c(hom) \times f(\theta) \quad (2.3)$$

in which  $f(\theta)$  is a parameter that depends on the contact angle  $\theta$  between the nucleating crystal and the substrate surface (figure 2.7c).

The ability of the growing material to wet the substrate surface, which is reflected in the contact angle, increases with decreasing interfacial tension. A better wettability results in lower contact angles and minimizes  $f(\theta)$ , which in turn reduce the nucleation barrier and thereby increase the heterogeneous nucleation rates. It is important to consider that heterogeneous nucleation

involves the interplay between three different interfaces: solution-nucleus, nucleus-substrate, and substrate-solution. The interplay between the three interfacial energies and the wetting angle  $\theta$  can be described as follows:

$$\gamma_{NS} + \gamma_{NL} \cos\theta = \gamma_{SL} \quad (2.4)$$

in which  $\gamma_{NS}$ ,  $\gamma_{NL}$ , and  $\gamma_{SL}$  are the interfacial tensions of the solution-nucleus, nucleus-substrate, and substrate-solution, respectively. The interfacial tension in the nucleus-substrate interface ( $\gamma_{NS}$ ) is mainly related to the lattice mismatch between the two materials. Heterogeneous nucleation is thus facilitated if the lattice mismatch between the substrate and the growing crystal is small.

The influence of **ligands** on the heterogeneous nucleation is even larger than for homogeneous nucleation, since they do not only determine the chemical potential of the monomer in solution, but also the free energy and accessibility of the substrate. In the case of the synthesis of heteronanocrystals, ligands bound to different facets of the seed NC will **change the free energies** of these facets. The higher the free energy of a facet, the higher the heterogeneous nucleation rates at that specific facet will be. Furthermore, the bulkiness of a ligand can sterically hinder incoming monomers and therefore limit or even **block the access to certain facets** or surface sites. Ligands (of different nature or in different concentrations) can thus be utilized to control the availability of facets for nucleation and thereby accelerate, slow down, or prevent heterogeneous nucleation on selected facets of the seed NCs.

#### 2.4.2 – Growth

NCs can grow either via addition of a monomer unit or by coalescence of smaller NCs into larger ones (figure 2.8).<sup>[7,21,28]</sup> In the NC growth via **monomer addition**, the crystallographic orientation of the growing monolayer is dictated by the substrate facet. This type of growth is referred to as epitaxial growth. Homoepitaxial growth involves growth over a pre-existing nuclei consisting of the same material, whereas in heteroepitaxial growth different materials form a shared interface. An overview of the essential concepts involved in the growth of NCs via monomer addition is given in the left panel of figure 2.9. Two sequential steps can be distinguished in the NC growth: monomer diffusion to the NC surface, and incorporation of the monomer into the NC.<sup>[26]</sup> The driving force for diffusion is the gradient between the monomer concentration on the NC surface and the monomer



**Figure 2.8.** Growth mechanisms of NCs: (a) growth by monomer addition, (b) growth by coalescence of smaller NCs.

concentration in the bulk solution. Diffusion rates can be increased by increasing the temperature and the monomer activities. If the monomer diffusion is the rate limiting step then the NC growth is said to be in the **diffusion controlled regime**. The incorporation of the monomer into the NC involves a reaction between the monomer and the NC surface, and the release of one or more ligand molecules (from the NC surface and/or from the monomer). The rate of this process is determined by the reaction rates between the monomers and the NC surface site. The reaction rates are also influenced by the crystallographic orientation of the facet, and the specific position of the site on the facet (*e.g.*, centre, corner, etc.). The NC growth is said to be in the **reaction controlled regime** when the incorporation of the monomers into the NCs is the rate limiting step. During the initial NC growth it is expected that the reaction controlled regime dominates because the diffusion process can be neglected due to the fast diffusion rates as a result of the high monomer concentration. As the NC growth proceeds, the monomer activity drops due to the monomer consumption and monomer diffusion is expected to become the rate limiting step.

The **growth rate** can be expressed, by making use of the Gibbs-Thomson relation, in terms of  $r_c$ :<sup>[22, 26, 29, 30]</sup>

$$\frac{dr}{dt} = \frac{2\gamma D a_0 V_m^2}{k_b T r} \left( \frac{1}{2r_c} - \frac{1}{2r} \right) \quad (2.5)$$

where  $V_m$  is the molar volume of the solid, and  $a_0$  gives the monomer activity in equilibrium with the bulk crystal material. The **monomer activity** is introduced here because the monomer concentration does not include information on the reactivity of the monomer and the interactions with the ligands and the solvent. Equation 2.5 clearly demonstrates that NCs with a radius smaller than  $r_c$  will have a negative growth rate, whereas

NCs with a radius larger than  $r_c$  will have a positive growth rate. This size dependence of the growth rate is illustrated in the right panel of figure 2.9. The size distribution of the ensemble of NCs is determined by the monomer activity at the start of the reaction.<sup>[7,26,22]</sup> At high monomer activities (dashed curve in the right panel of figure 2.9) the critical radius  $r_c$  is very small and therefore an ensemble of NC nuclei with an initially broad size distribution can undergo **size distribution focusing**. In the size focusing regime, all NCs in the ensemble grow, since they are all larger than  $r_c$ . However, smaller NCs grow faster than larger NCs and therefore the overall size distribution narrows while the average size increases. At low monomer activities (solid curve in the right panel of figure 2.9) the critical radius  $r_c$  is large and therefore size broadening occurs, since only NCs larger than  $r_c$  will grow while smaller NCs will have a negative growth rate (*i.e.*, will redissolve). The right panel of figure 2.9 clearly shows that a small size distribution is obtained by keeping the monomer activities sufficiently high to keep the NCs in the focussing regime during growth. High monomer activities are maintained either by repeated injections of fresh precursors<sup>[27]</sup> or by using an excess of one of the precursors. In all cases the NC synthesis must be terminated quickly (*e.g.* via quick cooling) while the monomer activity is still in the focussing regime.

**Ligands** affect the NC growth in two ways, namely via binding to the NC surface and by being part of the monomers in solution. Both the reaction and the diffusion rates can be changed by the choice of ligands. The ligand layer at the NC surface decreases the reaction rates by limiting access to the NC surface (steric hindrance) and by competing with the monomers for the reaction sites. The interactions between the ligands will also impact the growth rates, because these interactions define the ligand dynamics in the reaction medium and at the NC surface. Faster dynamics result in faster growth because short ligand residence times on the NC surface make the surface more accessible to monomers. As mentioned above, the monomer reactivity is determined by the strength of the metal/chalcogenide-ligand bond. Strong bonds result in stable monomer complexes and therefore slow growth rates (low reaction rates). The length of the alkyl chain also influences the growth kinetics by changing the metal/chalcogenide-ligand binding strengths and the diffusion rates. Shorter ligands experience weaker inter-ligand interactions (weaker van der Waals interactions) and lead to higher diffusion rates and more dynamic interactions with the NC surface.

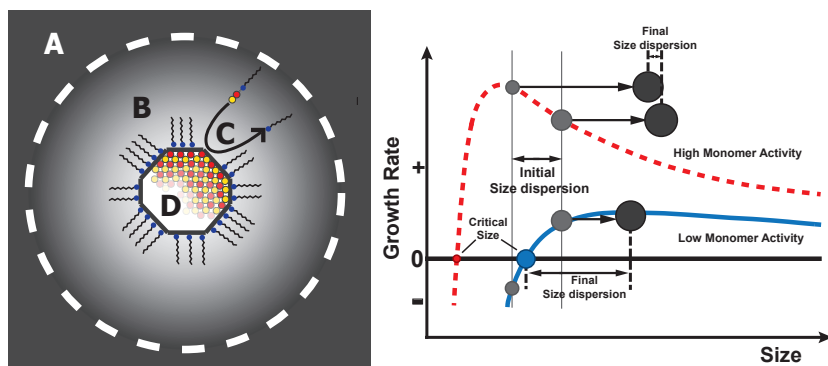


**Figure 2.9 – (Left panel)** Schematic representation of growth via monomer addition in which the dashed white circle indicates the diffusion sphere for the monomers. The region A is the bulk of the solution, where the monomer concentration is independent of the distance from the NC surface. B marks the diffusion sphere, where a monomer concentration gradient occurs due to the consumption of monomers at the NC surface. The arrow C indicates the monomer diffusion to the NC surface, followed by monomer incorporation into the NC, and diffusion of the released ligand away from the NC. The crystalline and faceted nature of the nanocrystal is highlighted in D. **(Right panel)** Size dependence of the NC growth rates for reaction mixtures in two representative monomer activity limits: low (solid curve) and high (dashed curve). The high activity limit allows for size focusing to occur, while in the low activity limit size defocusing occurs, through which the size dispersion broadens.

## 2.5 – Growth and shape control

The control over the shape of colloidal (H)NCs has increased dramatically in recent years and has led to the availability of 0-dimensional (*e.g.*, cubes, stars, pyramids), 1-dimensional (*e.g.*, wires), 2-dimensional (*e.g.*, platelets), and even more complex nanostructures (*e.g.*, multipods, matchsticks, and dumbbells).<sup>[1,2,4,26,27]</sup> Colloidal NCs are very often referred to as spherical, although they are never truly so. Because NCs are always highly faceted, they are therefore better described as nearly spherical (isotropic). To understand the mechanisms behind the shape control of colloidal NCs it is best to divide the shape of NCs only in two categories: isotropic (*i.e.*, low aspect ratio) or anisotropic (*i.e.*, high aspect ratio). Growth mechanisms on shape control will be briefly discussed below for single composition NCs (2.5.1) and heteronanocrystals (2.5.2).

### 2.5.1 – Homoepitaxial growth and shape control

**Equilibrium shape control:** <sup>[7,12,22]</sup> The equilibrium shape of a NC is the one that minimizes the overall surface free energy, and is usually isotropic. NCs are multifaceted and different crystallographic facets have different free energies. As stated by Wulff's theorem, the equilibrium shape of a crystal will be dictated by the relative surface energies of the various facets that can be exposed. In the case of a colloidal NC, the free energies of the facets may be modified by ligands bound to the NC surface. This further extends the number of possible equilibrium shapes for colloidal NCs. In order to allow equilibrium to be achieved, slow growth rates are needed which implies that the growth must be under **thermodynamic control** (low monomer activities and slow growth rates). This model assumes that the binding between the ligands and the NC surface is sufficiently strong to thermodynamically drive the system toward a particular average size under a given set of conditions.

**Kinetic shape control:** <sup>[7,12,26,27]</sup> The shape of colloidal NCs is frequently not the equilibrium one because the growth is usually quenched while the growth rates are still significant. In this manner metastable anisotropic structures are obtained. In the **kinetic growth control model**, growth occurs under conditions far from equilibrium (high monomer activities and fast growth). The size and shape of the NCs are then determined by the kinetic balance between several competing processes. The growth rate of a crystal facet depends exponentially on the surface free energy<sup>[26]</sup>, therefore at high growth rates, high-energy facets will grow faster than low-energy facets, typically yielding high aspect ratio shapes.

**Monomer fluxes and shape:** <sup>[7,12,22,23,31]</sup> The monomer flux is defined by the monomer diffusion rate, which increases with the temperature and the monomer activity in the reaction medium. High monomer fluxes favour kinetic control and anisotropic growth (1D growth), while low fluxes favour thermodynamic control and lead to isotropic growth (3D growth), as depicted in figure 2.10. Monomer fluxes that are too low to sustain growth, but are still sufficiently high to prevent NC dissolution, lead to a process called internal ripening. Material is then transported from high-energy facets to low-energy facets, causing the NC aspect ratio to slowly decrease towards a roughly isotropic shape. Even lower monomer fluxes will lead to Ostwald ripening, as discussed in section 2.4.2 above.

**Monomer incorporation rates and shape:** <sup>[3,7,27]</sup> Under kinetic control the growth rates are usually determined by the reaction rates between the

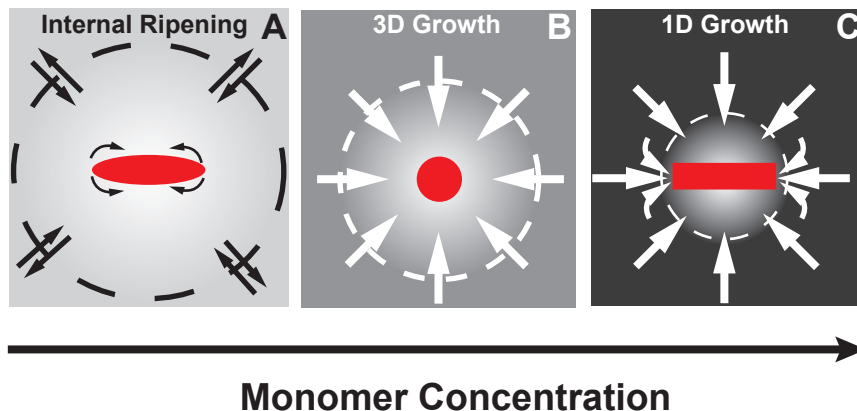


**Figure 2.10** – Schematic illustration of the influence of the monomer fluxes on the shape of a colloidal NC. (a) very low monomer flux, (b) low monomer flux, (c) high monomer flux.

incoming monomers and the surface sites. Therefore, differences between the free energy of the various crystallographic facets of the NC become relevant. High energy facets can incorporate monomers at faster rates and therefore lead to anisotropic growth. This process becomes important for growth at relatively low temperatures (where reaction rates become slower than diffusion rates) or at high monomer concentrations (where monomer diffusion rates are so high that the reaction rates become discriminatory).

**Surfactants and shape:** <sup>[3,7,4,22,27]</sup> Some ligands may bind more strongly to certain facets, thereby limiting access of the monomers to the NC surface and increasing the activation energy for monomer addition to those specific facets. When different facets have different ligand-facet bonding strengths, their relative growth rates will vary and this may lead to anisotropic shapes as depicted in figure 2.11.

**Crystal structure and shape:** <sup>[2,3,7,22]</sup> The crystalline phase of the NC seed also influences the final shape of the NC, since this will expose different crystallographic facets to the growth medium. Non-centrosymmetric crystal structures, such as wurtzite, are inherently polar and tend to grow anisotropically, easily yielding rods and multipods under kinetically controlled growth conditions. In contrast, centrosymmetric crystal structures, such as zinc blende, tend to grow isotropically.



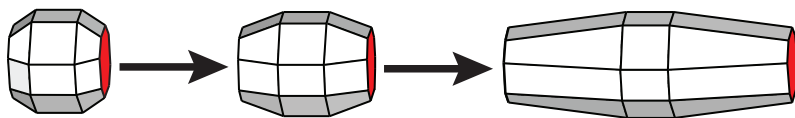


**Figure 2.11** – Schematic illustration of the impact of the selective adhesion of ligands on the final shape of a colloidal nanocrystal. Red facets are coated by weakly bound ligands, while white facets are covered by strongly bound ligands. As a result of the difference in binding strength, anisotropic growth occurs.

### 2.5.2 – Heteroepitaxial growth and shape control

Shape control has been extended to colloidal HNCs and has yielded a wide variety of sophisticated heteronanostructures, in which the composition and structure can be varied (*viz.*, concentric core/multishell HNCs, heterodimers, nanodumbbells, heteronanorods and multipods figure 2.12).<sup>[3,23]</sup> HNCs are grown with the use of hetero-epitaxial growth. The principles described above for the shape control by homoepitaxial growth also apply to heteroepitaxial growth. However, HNC growth is more challenging because the lattice mismatch at the heterointerface imposes large constraints on the growth rates of different crystallographic facets and thereby on the possible HNCs architecture. The shape of the HNC is sensitive to the characteristics of the seed (crystal structure, size, shape and faceting, surface defects, etc.) and the nature of the growing material. The choice of possible compositions is large but not unrestricted. The overgrowing material must be chemically and structurally compatible with the NC seed surface and the desired HNC type (*e.g.* type I, type II) imposes also strict constraints on the possible material combinations. Therefore, for a given combination of materials there are only a limited number of HNC morphologies that can be obtained under a given set of reaction conditions. Nevertheless, certain limitations can be bypassed by using different synthetic strategies, as will be discussed in chapter 8.

**Concentric core/shell HNCs:**<sup>[12]</sup> The lattice mismatch between the core and the shell materials constrains the formation of a concentric isotropic shell. Too large lattice mismatches will prevent isotropic growth. Smaller mismatches can lead to isotropic growth in which the shell thickness is limited by the degree of lattice mismatch. Nevertheless, due to their small size and highly faceted nature, colloidal HNCs are able to accommodate

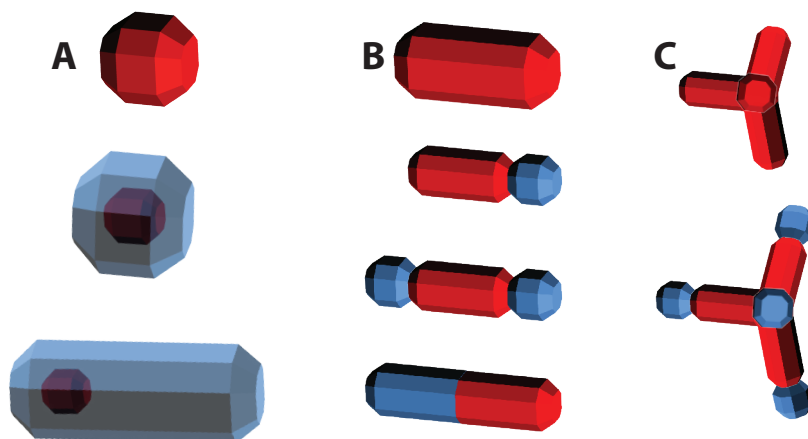


*Figure 2.12 – Schematic illustration of various HNC shapes obtained by using different seeds and different growth conditions.<sup>[3,23]</sup> HNCs obtained from (a) isotropic shaped seeds, (b) rod shaped seeds, (c) tetrapod shaped seeds.*

larger interfacial strains than their bulk counterparts grown by Vapour-phase epitaxy.<sup>[3]</sup> Moreover, the strain in the shell can be minimized by the formation of partially strained chemical bonds. Important for concentric core/shell growth are the growth rates. Under fast growth conditions it is impossible to grow concentric core/shell HNCs. Fast growth conditions results in shapes that minimize the overall free and strain energy, and those are often not isotropic. Concentric shells can thus only be obtained by **slow heteroepitaxial growth** of materials with a small lattice mismatch with respect to the seed.

**Anisotropic HNCs:** It has been experimentally demonstrated that anisotropic HNCs, such as heterorods, can accommodate much larger mismatches than concentric structures.<sup>[32]</sup> Therefore, the number of material combinations that yield anisotropic heteronanocrystals is much larger. Usually fast growth conditions favour the growth of anisotropic HNCs.

**Influence of NC seed and growth conditions on shape:** The nature of the NC seed and the growth conditions have a decisive influence on the HNC morphology and various architectures can be obtained (figure 2.12). Under slow heteroepitaxial growth conditions, in combination with small lattice

mismatches, an isotropic seed can be over-coated with a concentric shell. Under fast heteroepitaxial growth conditions, in combination with ligands that selectively bind to specific facets, the HNC shape will be determined by the crystalline phase of the NC seeds. Wurtzite NC seeds will result in heteronanorods<sup>[7,8,33]</sup> whereas zinc blende NC seeds can yield either tetrapods or octapods<sup>[1,4,8]</sup>. Not only isotropically shaped NC seeds can be used in HNC synthesis, but nanorods and tetrapods NCs are also widely employed as seeds. The tips of nanorods and pods with a wurtzite structure typically consist of the polar facets, which are more reactive than other facets. Heteroepitaxial growth will thus be faster at these facets, leading to the growth of complex structures. Under slow growth conditions, isotropic growth leads to dumbbell- and matchstick-shaped HNCs, whereas fast growth conditions promote one-dimensional growth leading to heterorods and heterotetrapods.

The shape of a colloidal (H)NC is thus a result of the balance between the growth rates and the relative stabilities of all possible crystallographic facets of the growing HNC. These facets are also competing with each other for the limited monomer supply in the growth solution. To make the picture even more complex, the fate of NC growth and shape is determined by the initial conditions present at the end of the nucleation stage and onset of the growth stage. The conditions involve temperature, composition of the reaction medium, concentration, size, shape and structure of the NC seeds, and remaining concentration of monomers and precursors. This complexity is also one of the strengths of colloidal NC synthesis approaches since it offers plenty of room for the design of creative strategies to make numerous novel and complex nanomaterials.

## REFERENCES

1. L. Carbone, P. D. Cozzoli, *Nano Today* 2010, 5, 449-493.
2. Y.-W. Jun, J.-S. Choi, J. Cheon, *Angew. Chem. Int. Ed.* 2006, 45, 3414 – 3439.
3. C. de Mello Donegá, *Chem. Soc. Rev.* 2011, 40, 1512–1546.
4. S. Kumar, T. Nann, *Small* 2006, 2, 316 – 329.
5. P. D. Cozzoli, T. Pellegrino, L. Manna, *Chem. Soc. Rev.* 2006, 35, 1195–1208.
6. C.L. Choi, A. P. Alivisatos, *Annu. Rev. Phys. Chem.* 2010, 61, 369–389.
7. A. P. Alivisatos, *J. Phys. Chem.* 1996, 100, 13226.
8. D. V. Talapin, J. H. Nelson, E. V. Shevchenko, S. Aloni, B. Sadtler, A. P. Alivisatos, *Nano Lett.* 2007, 7, 2951.
9. S. F. Wuister, C. de Mello Donegá, A. Meijerink, *J. Am. Chem. Soc.* 2004, 126, 10397.
10. W. J. M. Mulder, R. Koole, R. J. Brandwijk, G. Storm, P. Chin, G. J. Strijkers, C. de Mello Donegá, K. Nicolay, A. W. Griffioen, *Nano Lett.* 2006, 6, 1.
11. P. W. Atkins, 'Physical Chemistry', Fifth edition, Oxford: Oxford University Press, 1995.
12. E. Groeneveld, C. de Mello Donegá, 'The challenge of colloidal nanoparticle synthesis' in 'Nanoparticles: Workhorses of Nanoscience. Fundamentals, Preparation and Applications', C. de Mello Donegá (Ed.), Berlin: Springer-Verlag, (to be published in 2013).
13. C. Burda, X. Chen, R. Narayanan, M. A. El-Sayed, *Chem. Rev.* 2005, 105, 1025-1102.
14. C. B. Murray, D. J. Norris, M. G. Bawendi *J. Am. Chem. Soc.* 1993, 115, 19, 8706–8715.
15. C. de Mello Donegá, P. Liljeroth, D. Vanmaekelbergh, *Small*, 2005, 1, 1152-1162.
16. S. F. Wuister, F. Van Driel, A. Meijerink, *Phys. Chem. Chem. Phys.* 2003, 5, 1253–1258.
17. J. M. Pietryga, D. J. Werder, D. J. Williams, J. L. Casson, R. D. Schaller, V. I. Klimov, J. A. Hollingsworth, *J. Am. Chem. Soc.* 2008, 130, 4879.
18. K. Miszta, D. Dorfs, A. Genovese, M. R. Kim, L. Manna, *ASC Nano* 2011, 5, 7176-7183.
19. M. Casavola, M. A. Van Huis, S. Bals, K. Lambert, Z. Hens, D. Vanmaekelbergh, *Chem. Mater.* 2012, 24, 294–302.
20. H. Reiss, *J. Chem. Phys.* 1951, 19, 482-487.
21. T. Sugimoto, *J. Colloid Interf. Sci.* 1992, 150, 208-225.
22. L. Manna, S. Kudera, 'Advanced Wet-Chemical Synthetic Approaches to Inorganic Nanostructures', Ch. 1, P. D. Cozzoli (Ed.), Kerala: Transworld Research Network, 2008.
23. G. Caputo, R. Buonsanti, M. Casavola, P. D. Cozzoli, 'Advanced Wet-Chemical

- Synthetic Approaches to Inorganic Nanostructures', Ch. 14, P. D. Cozzoli (Ed.), Kerala: Transworld Research Network, 2008.
24. J. Park, J. Joo, S. G. Kwon, Y. Jang, T. Hyeon, *Angew. Chem. Int. Ed.* 2007, 46, 4630-4660.
  25. D. V. Talapin, J.-S. Lee, M. V. Kovalenko, E. V. Shevchenko, *Chem. Rev.* 2010, 110, 389-458.
  26. Y. Yin, A. P. Alivisatos, *Nature* 2005, 437, 664.
  27. M. Casavola, R. Buonsanti, G. Caputo, P. D. Cozzoli, *Eur. J. Inorg. Chem.* 2008, 6, 837-854.
  28. C. Besson, E. E. Finney, R. G. Finke, *J. Am. Chem. Soc.* 2005, 127, 8179-8184.
  29. A.L. Rogach, D.V. Talapin, E.V. Shevchenko, A. Kornowski, M. Haase, H. Weller, *Adv. Funct. Mater.* 2002, 12, 653-664.
  30. S.G. Kwon, T. Hyeon, *Small* 2011, 7, 2685-2702.
  31. Z. A. Peng, X. Peng, *J. Am. Chem. Soc.* 2001, 123, 1389-1395.
  32. D. J. Milliron, S. M. Hughes, Y. Cui, L. Manna, J. Li, L.-W. Wang, A. Paul Alivisatos, *Nature* 2004, 430, 190-195.
  33. L. Carbone, C. Nobile, M. De Giorgi, F. D. Sala, G. Morello, P. Pompa, M. Hytch, E. Snoeck, A. Fiore, I. R. Franchini, M. Nadasan, A. F. Silvestre, L. Chiodo, S. Kudera, R. Cingolani, R. Krahne, L. Manna, *Nano Lett.* 2007, 7, 2942-2950.



# Chapter 3

## **Physics for Chemists**

—

*Size effects on the Electronic  
Structure and Optical Properties  
of Semiconductor (Hetero)  
Nanocrystals*

## Abstract

*The electronic structure of semiconductor (hetero)nanocrystals ((H)NCs) become size dependent due to quantum confinement effects. This chapter addresses the electronic structure and electronic transitions of bulk semiconductor, and semiconductor (H)NCs.*

### 3.1 – Introduction

Quantum confinement influences the electronic structure of semiconductor nanocrystals (NCs) and heteronanocrystals (HNCs).<sup>[1,2]</sup> Understanding the origin of quantum confinement and how it influences the electronic structure of a semiconductor NC is essential for researchers (e.g., chemists and physicists) working in the field of NCs. In this chapter, a general introduction to the physics behind NCs is given. We start with the description of the electronic structure and electronic transitions of bulk semiconductors. Subsequently we address the impact of reducing the size of the semiconductor crystal to the nanoscale on its electronic structure. This is followed by a brief description of the electronic transitions and optical properties of semiconductor NCs. In the final section we discuss the essential characteristics of semiconductor HNCs.

### 3.2 – Electronic structure of bulk semiconductors<sup>[3,4]</sup>

The electronic structure of a bulk semiconductor can be understood by considering that electrons in a semiconductor experience a periodic potential due to interactions with the atoms in the crystal lattice. To simplify the problem we will start with a description of a one dimensional (1-D) crystal and later we will extend the treatment to the three dimensional (3-D) case.

The energy levels of an electron in a **one dimensional crystal** are given by the following Hamiltonian:<sup>[3,4]</sup>

$$\hat{H}\Psi(x) = (H^0 + U(x))\Psi(x) = \frac{-\hbar^2}{2m} \frac{\delta^2}{\delta x^2} \Psi(x) + U(x)\Psi(x) = E\Psi(x) \quad (3.1)$$

where  $H^0$  is the kinetic energy operator, and  $U(x)$  is the periodic potential coinciding with the periodic crystal lattice. When the lattice is periodic over distance  $a$ , the periodic potential satisfies the conditions  $U(x) = U(x + a)$ . The influence of the periodic potential on  $\Psi(x)$  is investigated by applying a translation of  $a$  over  $x$  ( $x \rightarrow x+a$ ). This translation changes equation 3.1 as follows:



$$\frac{-\hbar^2}{2m} \frac{\delta^2}{\delta x^2} \Psi(x+a) + U(x)\Psi(x+a) = E\Psi(x+a) \quad (3.2)$$

Since the difference between  $\Psi(x)$  and  $\Psi(x+a)$  is only a translation over  $x$  of the same wavefunction, both functions have necessarily the same eigenvalues and satisfy the same second-order differential equation ( $\delta^2/\delta x^2$ ). These conditions indicate that  $\Psi(x)$  and  $\Psi(x+a)$  are periodic functions which only differ by a phase factor given by:

$$\Psi(x+a) = e^{ika} * \Psi(x) \quad (3.3)$$

A solution for a wavefunction obeying the above stated conditions is given by the *Floquet* theorem as follows:<sup>[3]</sup>

$$\Psi_k(x) = e^{ikx} U_k(x) \quad (3.4)$$

where  $k$  is the wavevector ( $k=2\pi/\lambda$ ) and  $U_k(x)$  is a function that is periodic with the crystal lattice. In the three dimensional form this function is referred to as a Bloch function.<sup>[3]</sup> The solution of the wavefunction (Equation 3.4) contains two terms, a plane wavefunction ( $e^{ikx}$ ) and a periodic potential ( $U_k(x)$ ) that modulates the amplitude of  $e^{ikx}$ . When translation of the wavefunction over the distance  $a$  is considered equation (3.4) becomes:

$$\Psi_k(x+a) = e^{ik(x+a)} U_k(x+a) = e^{ika} e^{ikx} U_k(x) = e^{ika} \Psi_k(x) \quad (3.5)$$

which is analogous to equation 3.3. This implies that equation 3.4 is the description of the wavefunction of an electron travelling in the periodic potential of a crystal lattice. This electron can be seen as a perturbed free electron. Before examining the energy levels of this perturbed electron we first consider the **energy levels of a free (unperturbed) electron** in vacuum. The energy levels of the latter can be calculated via the Schrödinger equation for a free electron and the resulting eigenvalues are given by a so called dispersion relation:<sup>[3,4]</sup>

$$E_{k=} = \frac{\hbar^2 k^2}{2m_0} \quad (3.6)$$

where  $m_0$  is the free electron mass. There is thus a quadratic relation between energy  $E$  and the wavevector  $k$ , which gives rise to a continuum of energy levels (figure 3.1a). The **dispersion relation of an electron travelling in a periodic potential** will be different from equation 3.6 due

to the perturbation by the crystal lattice. When the wavelength of the electron is much larger than the periodicity of the crystal lattice, namely at small  $k$ -values, the electron is not perturbed and behaves as a free electron. Therefore, at small  $k$ -values equation 3.6 remains valid. When the wavelength of the electron is about 2 times the crystal lattice constant (*i.e.*,  $k=\pi/a$ ) the electron waves will experience Bragg reflections due to the periodic potential of the crystal lattice. The result of these Bragg reflections is that the electron wave function at that particular  $k$ -value diverges into 2 standing plane waves that are identical, except for a displacement along  $x$  by  $a/2$ . One standing wave concentrates the electronic charge at the positively charged nuclei of the crystal lattice, thereby lowering the potential energy, whereas the other concentrates the charge in the region between nuclei and therefore increases the potential energy. Hence, due to the difference in electronic charge distribution, the two standing waves have a different energy at the same  $k$ -value, leading to an energy gap in the dispersion relation at that specific  $k$ -value. The periodicity of the lattice causes Bragg reflections to occur at multiple  $k$ -values:

$$k = n \frac{\pi}{a}; \quad n = \pm 1, \pm 2, \pm 3, \dots \quad (3.7)$$

This leads to a dispersion relation containing multiple energy gaps, which are often referred to as **band gaps**, as shown in figure 3.1b.

The dispersion curve of an electron in a periodic potential thus consists of multiple continuous parts (**Brillouin Zones**). The first Brillouin zone is

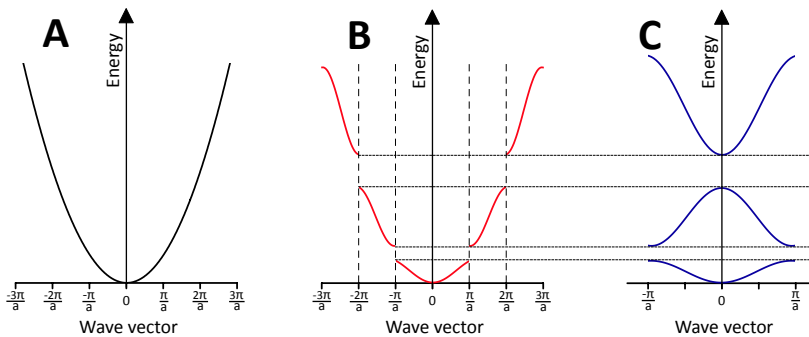


**Figure. 3.1** – (a) Dispersion relation of a free electron in vacuum. (b) Dispersion relation of an electron in a one dimensional crystal with lattice constant  $a$ . (c) Reduced zone scheme for dispersion relation given in (b).

located at  $-\pi/a < k < \pi/a$ , and the second zone at  $-2\pi/a < k < -\pi/a$  and  $\pi/a < k < 2\pi/a$ . A consequence of the periodicity of the potential ( $U_k(x) = U_k(x+a)$ ) and the periodicity of the phase coefficient ( $e^{ikx} = e^{i(k+(2\pi/x))x}$ ) in the Bloch wavefunction is that  $k$  values differing by an integer number of  $2\pi/a$  are equivalent:

$$\Psi_k(x) = e^{ika} U_k(x) = e^{i(k+\frac{n2\pi}{a})a} U_k(x) = e^{ika} e^{in2\pi} U_k(x) = e^{ika} U_k(x) \quad (3.8)$$

Because of this equivalence, values of the dispersion curve can be moved by  $2\pi/a$ . By moving the higher lying  $k$  values to the restricted region of  $-\pi/a < k < \pi/a$ , a reduced Brillouin zone scheme is obtained as depicted in figure 3.1c. This reduced zone scheme is referred to as the band structure, in which the band gaps are located at  $k = \pi/a$  and  $k = 0$ .

The electronic structure of a **3-D semiconductor crystal** can be explained along the same lines as the 1-D case. However, Bragg reflections in a 3-D crystal lattice are more complex because the periodicity is not the same in different directions. In a 3-D crystal lattice the electron will experience different Bragg reflections when travelling in different directions, leading to band gaps at several  $k$ -values in the Brillouin zone and thus to a more complex band structure. The band structure of a 3-D crystal is presented in a so called band diagram. The energy bands will be filled with electrons and the degree of occupation determines the electronic properties of the solid. The highest occupied energy band is called the valence band (VB) and the lowest unoccupied energy band is referred to as conduction band (CB). The energy difference between the VB and CB is referred to as the band gap energy. For a semiconductor this energy gap is smaller than 4 eV, which allows electrons to be thermally excited from the VB to the CB at sufficiently high temperatures. The top of the VB and the bottom of the CB for the smallest energy gap can be located at the same  $k$ -value, yielding a direct band-gap semiconductor (e.g., CdSe), or at different  $k$ -values, in which case the material is referred to as an indirect band gap semiconductor (e.g., silicon).<sup>[3]</sup>

### 3.3 – Electronic transitions in bulk semiconductors<sup>[3]</sup>

The VB of a semiconductor is completely filled with electrons, while the CB is unoccupied. An electron can be promoted from the VB to the CB as result of an external perturbation, e.g., the absorption of a photon with energy equal to or higher than the band gap. The promotion of an electron from the VB to the CB can be described as a system in which the CB contains

one particle whereas the VB, consisting of many particles, lacks a particle. This situation is a many-body system. A standard approach to simplify a many-body system is by describing a large number of interacting particles by as little as possible non-interacting particles called ‘**quasiparticles**’. A first step is the introduction of a quasi-particle in the VB, namely ‘**hole**’, which is correlated to the ensemble of electrons in the VB from which the electron is removed. The electron in the CB is described by charge ( $e^-$ ), spin ( $S = 1/2$ ), and effective mass ( $m_e^*$ ), whereas the hole in VB is characterized by a positive charge ( $e^+$ ), spin ( $S = 1/2$ ), and effective mass ( $m_h^*$ ). Due to their charge, electrons and holes are generally referred to as charge carriers. The concept of **effective mass** is introduced to incorporate the interaction of the particle with the periodic crystal lattice. The effective mass thus reflects the mobility of a charge carrier (electron or hole) in the lattice. An effective mass that is ‘heavier’ than the free electron mass corresponds to an interaction with the crystal lattice which slows down the charge carrier, whereas a higher mobility is reflected by a lighter effective mass. Since electrons and holes have opposite charges they interact via a Coulomb potential, forming an electron-hole pair that can be described as a quasiparticle (the ‘**exciton**’). The formation of an exciton requires a minimum amount of energy given by:<sup>[4,5]</sup>

$$E = \hbar\omega = E_g + E_{e,kin} + E_{h,kin} \quad (3.9)$$

in which  $E_{e,kin}$  and  $E_{h,kin}$  are the kinetic energies of the electron and hole, respectively, and  $E_g$  is the semiconductor bandgap. Further, **momentum conservation** requires that:

$$\hbar k_{cb} = \hbar k_{vb} + \hbar k_{photon} \quad (3.10)$$

where  $k_{cb}$  and  $k_{vb}$  are the wavevectors of the promoted electron in the CB and the hole in the VB, respectively. Because photons have negligible momentum,  $k_{cb} = k_{vb}$  must be met. Therefore, without other external perturbations, only transitions within the same  $k$ -values (*i.e.*, vertical or direct transitions) can occur, as shown in figure 3.2.<sup>[3,5]</sup>

The **energy of an exciton** can be expressed by the following dispersion relation:

$$E_n = E_g - \frac{Ry^*}{n^2} + \frac{\hbar^2 K^2}{2(m_e^* + m_h^*)} \quad (3.11)$$

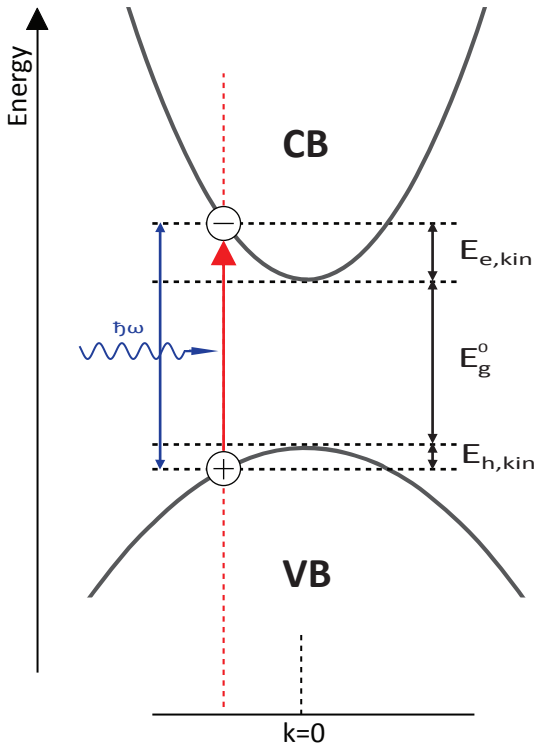


**Figure 3.2** – Schematic representation of the promotion of an electron from the valence band to the conduction band in a direct band gap semiconductor as result of the absorption of a photon. The diagram shows that energy and momentum conservation laws must be obeyed.

where the second term contains hydrogen-like set of energy levels in which  $Ry^*$  is the exciton Rydberg energy (corresponds to the ionization energy of the lowest hydrogen state).<sup>[3]</sup> The third term in equation 3.11 accounts for the kinetic energy of the exciton center of mass motion in which  $K$  is the exciton wave vector. The kinetic energy term resembles the dispersion curve of a free electron, but with the difference that it is corrected for the effective mass of the exciton. The third term originates from the fact that the interacting holes and electrons can be described as two particles interacting via a coulomb potential. A Hamiltonian analogous to the hydrogen atom Hamiltonian is used to calculate the energy of the exciton, in which the exciton effective mass replaces the free electron mass ( $m_0$ ). By analogy to the hydrogen atom the most probable distance between the electron and hole in an exciton is given by a Bohr radius ( $a_B$ ) which is referred to as the exciton Bohr radius ( $a_B^*$ ).<sup>[3]</sup>

$$a_b^* = 4\pi\epsilon_0 \frac{\epsilon\hbar^2}{\mu_{eh}e^2} = \epsilon \frac{\mu_H}{\mu_{eh}} \times 0.053 \text{ nm} = \epsilon \frac{m_0}{\mu_{eh}} \times 0.053 \text{ nm} \quad (3.12)$$

where  $\mu_{eh}$  is the electron and hole reduced mass,  $\mu_H$  and  $m_0$  are the hydrogen and electron reduced masses, respectively. Further,  $e$  is the electron charge, and  $\epsilon_0$  and  $\epsilon$  are the dielectric constant of vacuum and of the semiconductor, respectively. The most common semiconductors have exciton bohr radii in the range of 1-10 nm,<sup>[3]</sup> which are much larger than the Hydrogen Bohr radius. This large difference is caused by the large dielectric constant of semiconductors and the smaller effective masses of charge carriers in semiconductors.

### 3.4 – Electronic structure of semiconductor nanocrystals

The electronic structure of a semiconductor nanocrystal changes and becomes size (and shape) dependent when its dimensions are decreased to the nanoscale. This effect, known as **quantum confinement**, can be understood via two different approaches. In the first approach, the nanocrystal is treated as a small piece of semiconductor material in which the exciton is spatially confined. The second method involves a quantum chemical (molecular) approach, in which the nanocrystal is build up atom by atom and is treated as an increasingly larger molecular cluster that eventually evolves into a bulk semiconductor crystal.

#### 3.4.1 – Nanocrystal as a small crystal: Confining the exciton

When the size of a semiconductor nanocrystal becomes comparable to the exciton Bohr radius of the bulk material, the exciton energy levels begin to change due to the spatial confinement of the exciton wavefunction. This means that the onset of quantum confinement effects will occur at different nanocrystal dimensions for different semiconductors, since the exciton Bohr radius  $a_0$  varies widely within the semiconductor materials (*e.g.*, 1.9 nm for ZnO, 4.9 nm for CdSe, and 46 nm for PbSe). In the discussion below we will consider a spherical nanocrystal, which implies that the exciton will be spatially confined in three dimensions. This situation is usually referred to as a quantum dot (QD), since the exciton is then effectively confined in a zero-dimensional potential well.<sup>[4]</sup> Nevertheless, as discussed in Chapter 2, nanocrystals can have a wide variety of shapes. It is thus possible to have non-spherical QDs (*e.g.*, cubes or pyramids),<sup>[6]</sup> provided all dimensions are small enough with respect to  $a_0$ . If only the diameter of the nanocrystal is small enough to induce quantum confinement effects, the exciton will experience a 2-dimensional confinement and the nanocrystal will be then

referred to as a quantum wire or quantum rod, depending on its relative aspect ratio (wires are significantly longer than  $a_0$ , while rods have lengths of the order of a few  $a_0$ ). If the exciton is confined only in the thickness direction a quantum well is formed (1-D confinement). Until recently quantum wells were only obtained by thin film deposition on substrates, but ultrathin colloidal nanoplatelets of a number of II-VI semiconductors (*e.g.*, CdSe, CdTe) have been prepared over the few years.<sup>[7,8]</sup>

The changes in the exciton energy levels can be described by using the effective mass approximation and a ‘particle-in-a-box’ approach. To describe the effect of quantum confinement it is easier to consider only the band diagram for  $k$ -values near the band gap. This part of the band diagram can be described via the effective mass approximation. In this method the bands are assumed to have a parabolic form near the extremes in the band diagram. In a two band model the position of the VB and CB of a direct semiconductor can be approximated as follows:

$$E_k^{vb} = \frac{\hbar^2 k^2}{2m_{eff}^{vb}} \quad (3.13)$$

where  $m_{eff}^{cb}$  and  $m_{eff}^{vb}$  are the effective masses of charge carriers in the CB and VB, respectively. These equations are nearly identical to the dispersion relation of a free electron, except that the free electron mass is replaced by the effective masses, and will be used in the following subsections. Quantum confinement can be divided in a weak (nanocrystal radius  $a$  is larger than  $a_b$ ) and a strong ( $a < a_b^*$ ) confinement regime. The impact of quantum confinement is usually no longer observable for sizes larger than 2-3 times the exciton Bohr radius.

In the **weak confinement regime**<sup>[3,4]</sup> the increase in exciton energy is due to quantization of the exciton center-of-mass motion. The exciton in the nanocrystal is described as a particle in a spherical potential. The wavefunction of a particle in a spherical potential is given by:

$$\Psi_{spherical\ potential}(\theta\phi r) = Y_{lm}(\theta\phi)R(r) \quad (3.14)$$

where  $Y_{lm}$  are the spherical Bessel functions and  $R(r)$  is the radial Bessel function. Eigenvalues of the wavefunction, when inserted in the Schrödinger equation that contains a spherical potential ( $u = 0$  for  $r < a$ ,  $u = \infty$  for  $r > a/2$ ), are given by:

$$E_{nl} = \frac{\hbar^2 \chi_{nl}^2}{2m^* a^2} \quad (3.15)$$

in which  $m^*$  is the effective mass of the particle and  $\chi_{nl}$  are roots of the Bessel function with  $n$  the number of the root and  $l$  the order of the function. Due to this spherical Bessel function the energy states are classified by the principal quantum number  $n$  ( $n = 1, 2, 3, \dots$ ) and by the orbital quantum number  $l$  ( $l = 0, 1, 2, 3, \dots$  also referred to as S, P, D, F, respectively). The lowest energy state ( $E_{10}$ ) is characterized by  $n = 1$  and  $l = 0$  and its corresponding wavefunction has an s orbital symmetry. In contrast to atoms, there are no restrictions of orbital number  $l$  in NCs because the potential in a NC is a square well (nanocrystal is the well and the surrounding is finite potential), while in atoms a coulombic potential is used.<sup>[2]</sup> The second energy level ( $E_{11}$ ,  $n = 1$  and  $l = 1$ ) is thus a 1p orbital, instead of the 2s orbitals present in atoms. The third energy level ( $E_{12}$ ,  $n = 1$  and  $l = 2$ ) is a 1d orbital. The energy of the exciton is obtained by replacing the kinetic energy term of the center of mass motion in the exciton dispersion relation (equation 3.11) by the energy of a particle in a spherical potential. When this “particle-in-a-spherical-potential” energy term is inserted into the dispersion relation of the exciton (equation 3.11), the following expression is obtained:<sup>[3,4]</sup>

$$E_{nml} = E_g - \frac{Ry^*}{n^2} + \frac{\hbar^2 \chi_{ml}^2}{2(m_e^* + m_h^*) a^2} \quad (3.16)$$

in which the third term corrects the exciton kinetic energy for the finite size of the NC. The quantum number  $n$  describes the energy states arising from the coulomb interaction between the electron and hole in the exciton. Quantum numbers  $m$  and  $l$  label the energy states connected to the center of mass motion in the presence of a potential barrier.

In the **strong confinement regime**<sup>[3,4]</sup> the electron and the hole no longer form a bound state that resembles a hydrogen-like exciton, since the confinement potential becomes larger than the Coulomb interaction. Therefore, the electron and hole energy states are no longer correlated and are treated independently. In a first approximation only the change in kinetic energy of the electron and hole are considered, whereas the Coulomb interaction is ignored. Intuitively one realizes that the Coulomb interaction does not vanish when two charged particles are brought in such a near distance. Actually, it becomes much larger than in a bulk crystal. However, the kinetic energy term in equation (3.16) is still much larger than the Coulombic term when  $a < a_b^*$  and therefore, Coulomb interactions can



be neglected in first approximation and added later as first order energy corrections. When the energy of the VB top is considered as the offset of the energy scale the **energy levels of the electron and hole** can be displayed as:<sup>[3,4]</sup>

$$E_{nl}^e = E_g + \frac{\hbar^2 \chi_{nl}^2}{2m_e^* a^2} ; \quad E_{nl}^h = -\frac{\hbar^2 \chi_{nl}^2}{2m_h^* a^2} \quad (3.17)$$

Both equations contain the roots of the spherical Bessel function and thus both the electron and the hole energy levels are discrete, and are labeled as the levels of a particle in a spherical potential (*i.e.*, 1S, 1P, 1D, ...). To distinguish between electron and hole energy levels the subscripts “e” and “h” are added. A schematic energy level diagram for electrons and holes in nanocrystals (quantum dots) is given in figure 3.3. The bandgap energy of semiconductor nanocrystals can now be described, neglecting Coulomb interactions, as:

$$E_g^{NC} = E_g^0 + E_{1s}^e + E_{1s}^h = E_g^0 + \frac{\hbar^2 \chi_{10}^2}{2m_e^* a^2} + \frac{\hbar^2 \chi_{10}^2}{2m_h^* a^2} \quad (3.18)$$

from which one can see that the band gap of the quantum dot is constructed from the bulk bandgap ( $E_g^0$ ) and the confinement energy ( $E_{1s}^e + E_{1s}^h$ ) as result of the finite nanocrystal size. The size dependence of the quantum confinement effect is clearly visible in the energy confinement part of equation 3.18. As the size of the nanocrystal quantum dot ( $a$ ) decreases, the confinement energy terms become larger. Therefore, the energy differences between the electron and hole levels increase, leading to wider band gaps and more widely spaced energy levels. The increase in the bandgap will not necessarily be symmetric with respect to the edges of the VB and CB, since the effective masses of the electron and the hole may be different (as is the case for all the II-VI semiconductors, where the hole is heavier than the electron).

### 3.4.2 – Nanocrystal as a large molecule: building up atom by atom<sup>[1,9,10]</sup>

A more chemical approach to describe a semiconductor NC is to consider it as a large molecule (or cluster). In analogy with molecules, the electronic structure can then be described by the molecular orbital theory. The simplest example of a multiple electron molecule is that of diatomic hydrogen ( $H_2$ ). In this molecule, two atomic orbitals (AOs) combine to form two molecular orbitals (MOs) that spread out over both H atoms, namely a bonding and an anti-bonding MO. The bonding MO is lower in energy compared to the

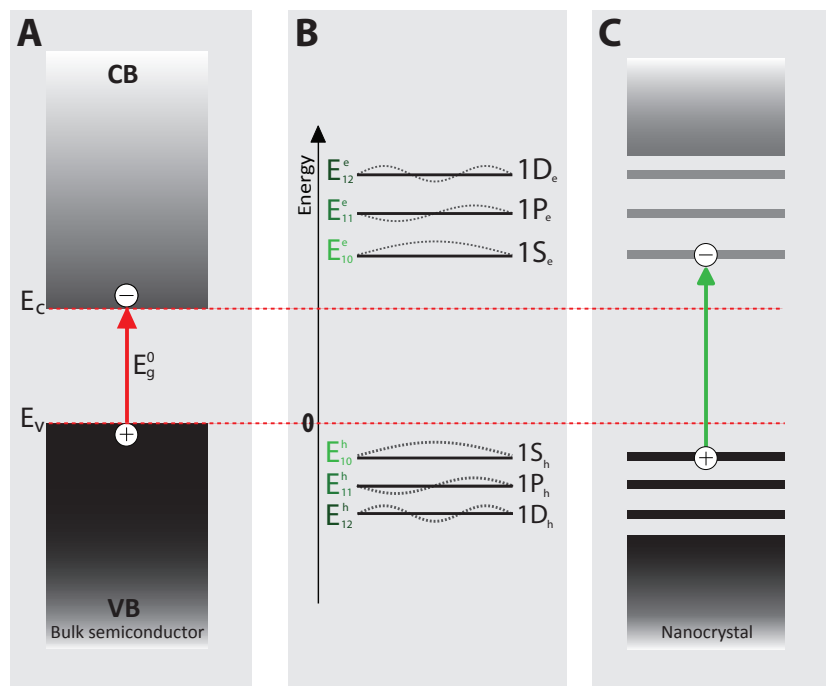


**Figure 3.3** – Schematic representation of the effect of quantum confinement on the electronic structure of a semiconductor. (a) Bulk semiconductor. (b) Electron and hole energy levels (c) Nanocrystal Quantum Dot.

individual AOs, whereas the anti-bonding MO is higher in energy than the individual AOs.

The MOs will be occupied by electrons in such manner that the potential energy of the molecule is minimized. In the  $H_2$  molecule the 2 electrons originally in the 1 s AOs of the individual H atoms will be accommodated in the bonding MO, thereby leaving the anti-bonding MO unoccupied. The **highest occupied molecular orbital** is referred to as **HOMO** and the **lowest unoccupied molecular orbital** is called **LUMO**. The same approach can be extended to larger molecules, clusters and even bulk materials. As the molecule (or cluster) becomes larger, the number of AOs that are combined to form MOs (bonding and anti-bonding) increases, leading to an increasingly larger number of energy levels and decreasing the HOMO-LUMO energy gap (figure 3.4). Each MO combination has a well defined energy value, but MOs with intermediate energy values are more common than those with energies

near the minimum or maximum values (*i.e.*, fully bonding or fully antibonding). For a sufficiently large number of combining atoms (*i.e.*, when the bulk limit is reached) the energy levels become so close and so numerous that a quasi-continuum or an energy band is formed, analogous to the conduction and valence bands described above. The HOMO level is the top of the VB, whereas the LUMO is the bottom of the CB. The number of atoms in a semiconductor nanocrystal (50-10000 atoms) is intermediate between that of molecules and bulk solids. Therefore, its electronic structure will be characterized by energy bands with a large density of levels at intermediate energy values and discrete energy levels near the band edges, where the density of MOs is small. The HOMO-LUMO gap will be larger than for bulk and size-dependent, decreasing with increasing number of atoms in the nanocrystal (figure 3.4).

The molecular orbital approach described above (figure 3.4) provides a simple and general description of the electronic structure of a 1-D NC, and clearly illustrates the size dependence of the HOMO-LUMO gap. However, figure 3.4 presents the evolution of the MOs that would be obtained from combining an increasingly larger number of identical AOs (*i.e.*, with the same energy and symmetry). The situation for compound semiconductors (*e.g.*, CdSe, CdTe, PbSe, InP) is more complicated since elements with

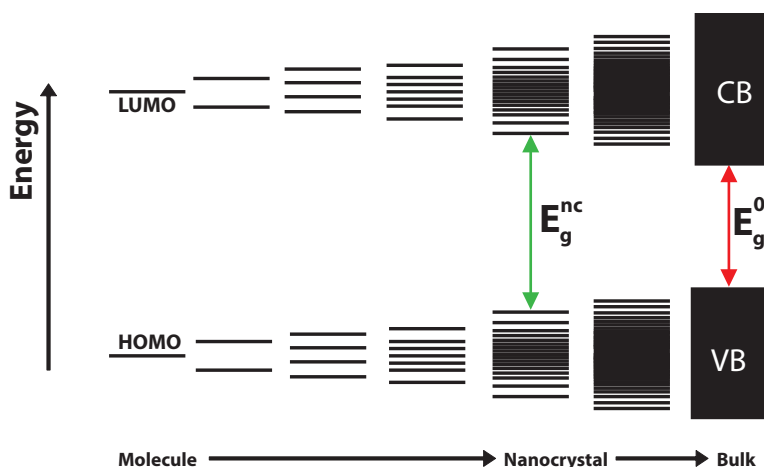


**Figure 3.4** – Evolution of molecular orbital levels as the number of atoms in the structure increases from a few atoms (molecule) to a few hundred to thousand of atoms (nanocrystal) to bulk semiconductors.

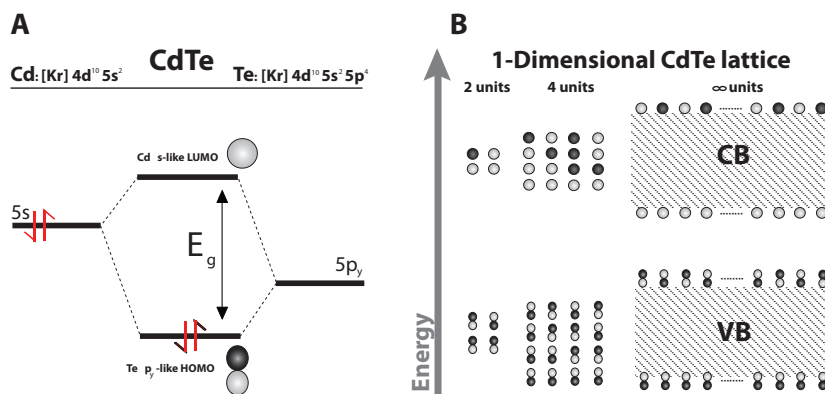


**Figure 3.5** – (a) LCAO diagram of a hypothetical CdTe unit. (b) LCAO representation of  $n$ -units of CdTe. Dark gray and light gray are used to indicate different phases of the MO's.

different electron negativities and different types of AOs are combined. A general qualitative understanding of the electronic structure of compound semiconductors is important, and is of particular interest in this thesis. We will use CdTe as a representative example of a II-VI semiconductor, and employ a simplified 1-D crystal to illustrate the effect of a more complex composition on the the VB and CB of a semiconductor NC.<sup>[10]</sup> In a hypothetical 1-D CdTe crystal (constructed along the  $y$ -axis) the atomic structure of Cd and Te are  $[\text{Kr}]4d^{10}5s^2$  and  $[\text{Kr}]4d^{10}5s^25p^4$ , respectively. For a single unit of CdTe the highest filled AOs of Cd ( $5s^2$ ) and empty AOs of Te ( $5p_x$ ) combine to form  $s$ -like and  $p_y$ -like MO's. The VB of a larger 1D crystal is thus constructed from  $p_y$ -like MO's whereas the CB is constructed from  $s$ -like MO's (figure 3.5). Filled  $p_y$ -like anti-bonding MO's will form the top of the VB, whereas empty  $s$ -like bonding MO's will form the bottom of the CB (figure 3.5). This 1D example is a oversimplification of the NC electronic structure,<sup>[1]</sup> but it is still helpful to understand the NC optical properties, since it shows that the nature of the orbitals constituting the VB and the CB in II-VI semiconductors is different.

### 3.5 – Electronic Transitions in semiconductor nanocrystal quantum dots

The effect of quantum confinement is clearly demonstrated by the **optical properties of nanocrystal quantum dots (QDs)**.<sup>[1]</sup> The absorption spectra of colloidal CdTe QDs of different sizes are given in figure 3.6. As expected from

the discussion above, the absorption transitions shift to higher energies as the NC becomes smaller. The photograph of colloidal CdTe QD suspensions in figure 3.6b shows that quantum confinement effects are also clearly manifested in the photoluminescence (PL) colors. The QD absorption spectra presented in figure 3.6 show multiple peaks corresponding to optical transitions between the electronic levels of the QD. These spectra clearly illustrate the principles described in the sections above, since the transitions shift to higher energies as the size of the QD decreases. Furthermore, the energy separation between the peaks decreases with increasing nanocrystal size. As discussed in the sections above, the discrete energy levels of electrons and holes in semiconductor QDs are sequentially labeled as S, P, D, and so forth (figure 3.7). The optical transitions observed in the absorption spectra of QDs can thus be assigned to  $1S_h - 1S_e$ ,  $1P_h - 1P_e$ ,  $1D_h - 1D_e$ , (and so forth, the subscripts h and e indicate hole and electron levels, respectively) electronic transitions. It should be noted that these transitions are fully parity-allowed, despite the fact that the symmetry labels of both the initial and the final levels are the same. This apparent contradiction is explained by taking into account the different origin of the hole and electron energy levels (for a detailed analysis the reader is referred to ref<sup>[11]</sup>). As illustrated above for the specific case of CdTe, the VB (*i.e.*, the hole energy levels) originates from the p orbitals of Te, while the CB (*i.e.*, the electron energy levels) is constructed from the s orbitals of Cd. Therefore, any transition between hole and electron levels of the same symmetry (*e.g.*,  $S_e - S_h$ ) will be characterized by a large electric dipole moment, while transitions between levels of different symmetry (*e.g.*,  $S_e - P_h$ ) will be in fact parity-forbidden.

### 3.5.1 – Exciton recombination

The exciton can recombine via **radiative** and **non-radiative** pathways, as depicted in figure 3.8. Exciton relaxation via radiative recombination results in the emission of a photon (photoluminescence, PL). In the emission spectra the direct recombination of the exciton is observed as a well-defined peak with energy close to the lowest energy absorption transition. The PL peak position presents thus the same size dependence as the absorption transitions. The PL peak width is determined by the size and shape dispersion of the measured NC ensemble (inhomogeneous line broadening). Radiative recombination can also occur after one (or both) charge carriers is trapped in a defect or surface state. The resulting emission is known as defect PL or trap PL, and is characterized by a very broad emission band at lower energies than the band gap.<sup>[12]</sup> Trapping of the

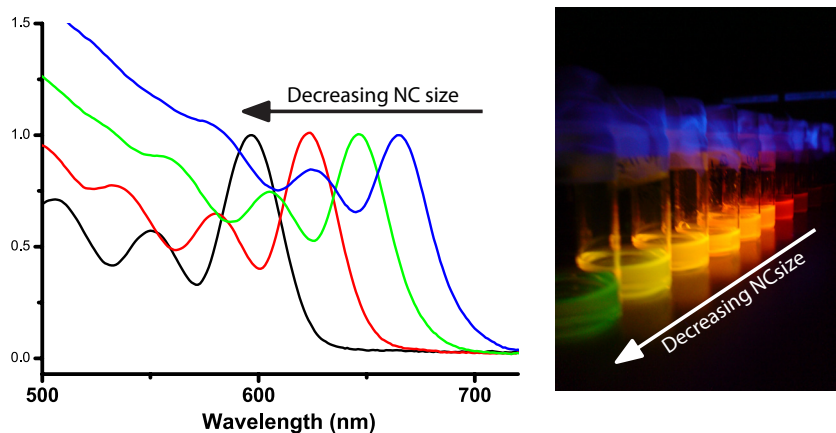


**Figure 3.6 – (a)** Absorption spectra of colloidal suspensions of CdTe nanocrystal quantum dots of different sizes. As the size of the nanocrystal increases all transitions shift to longer wavelengths (lower energies). **(b)** Photograph of vials containing colloidal suspensions of CdTe nanocrystals of different sizes under UV excitation.

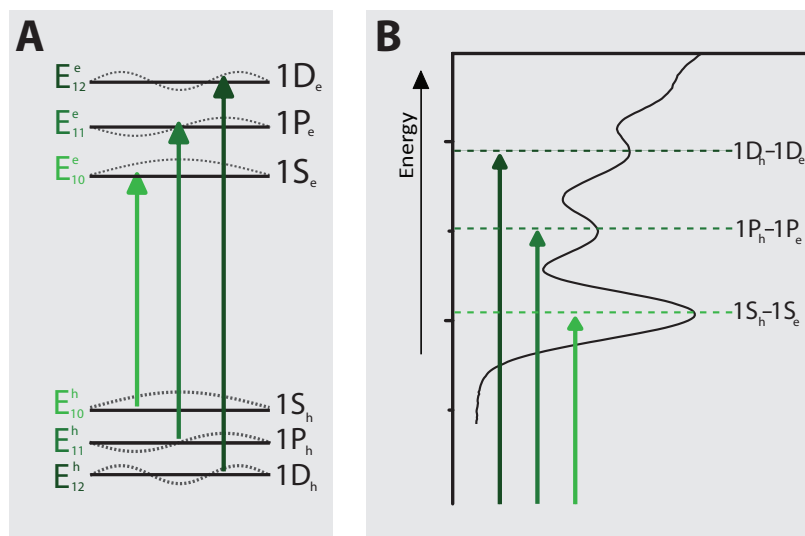


**Figure 3.7 – (a)** Schematic illustration of the electron and hole energy levels in a semiconductor quantum dot. Allowed optical transitions are given by the green arrows. **(b)** Assignment of the different optical transitions in a CdTe nanocrystal QD absorption spectrum.

charge carriers in defect or surface states can also result in non-radiative recombination, through which the exciton energy is fully dissipated as heat in the crystal lattice.

An additional non-radiative relaxation pathway for semiconductor nanocrystals is **energy transfer (ET)**, which becomes relevant when the distance between the NCs is sufficiently small to allow strong dipolar interactions. In this situation ET can occur from a donor NC to an acceptor NC, provided the resonance condition is fulfilled (*i.e.*, the donor level and the acceptor level have the same energy). The ET rate is determined by the strength of the donor-acceptor (D-A) interaction, which strongly increases with decreasing D-A distances (the rates are inversely proportional to  $d^6$ , where  $d$ = D-A distance).<sup>[12]</sup>

The lifetime of an exciton in a semiconductor NC can thus be determined by measuring the PL decay times  $t$ , and can be described as

$$\tau = \frac{1}{W_{TOT}} = \frac{1}{W_{Rad}} + \frac{1}{W_{NonRad}} + \frac{1}{W_{ET}} \quad (3.19)$$

where  $W_{Tot}$  is the total decay rate,  $W_{Rad}$  is the radiative decay rate,  $W_{NonRad}$  the non-radiative decay rate, and  $W_{ET}$  the energy transfer decay rate. The latter can be neglected for a sufficiently diluted ensemble of NCs. If the excitons in a system decay only radiatively, the PL decay will follow a single exponential behaviour:

$$N(t) = N_0 e^{-t/\tau} \quad (3.20)$$

where  $t$  is the elapsed time after the excitation,  $\tau$  is the exciton radiative lifetime and  $N_0$  is the population of the emitting state at  $t = 0$ , which will determine the PL intensity at  $t = 0$ . When also nonradiative recombination and energy transfer contribute to the exciton relaxation, the PL decay will no longer follow equation 3.20. The total decay rate will then contain different contributions and therefore the PL decay curves will deviate from the single-exponential behaviour. The balance between the radiative and nonradiative decay rates will be reflected in the PL quantum efficiency (or quantum yield QY), which is the ratio between the number of photons emitted ( $n_{Emit}$ ) and absorbed ( $n_{abs}$ ), as given by:

$$QY = \frac{n_{Emit}}{n_{Abs}} = \frac{W_{Rad}}{W_{Tot}} \quad (3.21)$$

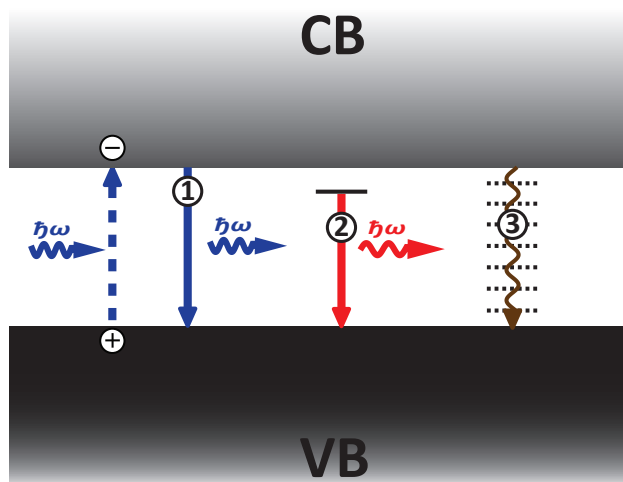


**Figure 3.8** – Schematic illustration of exciton recombination pathways in semiconductors. (1) radiative recombination. (2) defect assisted radiative recombination. (3) non-radiative recombination.

### 3.6 – Electronic structure and optical transitions in semiconductor heteronanocrystals<sup>[2]</sup>

Heteronanocrystals are multicomponent NCs which comprise two (or more) different materials joined by one or more heterointerfaces. Semiconductor HNCs give even more possibilities regarding property control than single composition NCs, because the localization of the photoexcited charge carriers in HNCs can be tuned by controlling the energy offsets between the HOMO and LUMO levels of the materials that are combined at the heterointerface. This can be achieved by individually tailoring the properties of the different HNC components by varying their size, shape and composition. Semiconductor heteronanostructures can be divided into three different classes regarding the charge carrier localization after photoexcitation, namely **type-I**, **type-I<sup>1/2</sup>** (also referred to as quasi type-II)<sup>[13]</sup> and **type-II** (figure 3.9).

In the **type-I** regime the band alignment is such that the bandgap of one material lies entirely within the bandgap of the other material (**enclosed alignment**). After photoexcitation both charge carriers will localize in the material with the smaller bandgap, resulting in the formation of a direct exciton. The band alignment in the **type-II** regime is such that the top of the VB and the bottom of the CB of one material are at higher potential



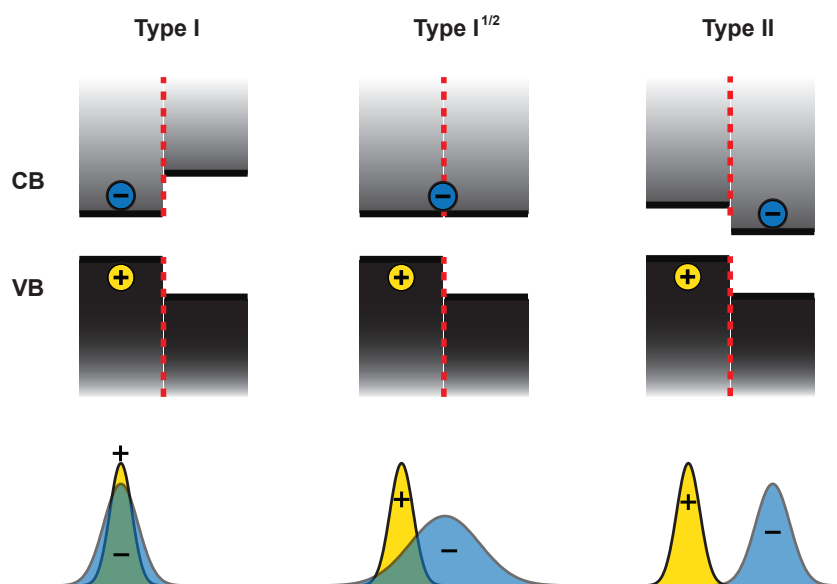


**Figure 3.9** – Schematic representation of the three charge carrier localization regimes in semiconductor heteronanostructures. The minus and plus signs represent the electron and hole, respectively. The ground state electron and hole wavefunctions (indicated by + and -, respectively) are schematically depicted in the lower panel.

energy than the top of the VB and the bottom of the CB of the other material (**staggered alignment**). As a result of this alignment the photoexcited electron and hole will localize in different materials, and therefore on different sides of the heterojunction, forming a spatially indirect exciton. The **type-I<sup>1/2</sup>** regime is an intermediate regime between type-I and type-II. In this case, the offset is restricted to only one of the bands (either the VB or CB). As a result, one of the photoexcited charge carriers (either the electron or the hole) will be localized in one material, whereas the other charge carrier is delocalized over the whole heteronanostructure. The **different charge carrier localization** regimes result in specific properties that are advantageous for certain applications. For example, colloidal **type-I** core/shell HNCs (quantum dots or quantum rods) are ideally suited for applications requiring high PL QYs and excitons that do not interact with the environment, such as labels for biomedical imaging<sup>[11]</sup> or lasers. In these HNCs the exciton is confined to the core and therefore does not interact with the surface (dangling orbitals) and the environment of the HNC. Therefore, the PL QY and photostability of type-I concentric core/shell HNCs are usually

higher than those of the single composition NCs used as seeds.<sup>[2]</sup> Since the exciton is confined to the core material, the properties of the direct exciton are primarily dictated by the narrow gap material. Therefore, the radiative exciton lifetime, and the absorption and PL spectra of type-I core/shell HNCs will be very similar to those of the core NCs. Nevertheless, a small shift to lower energies is observed because the confinement potentials are finite and therefore the exciton wavefunction partially extends into the shell ('exciton leakage'). The energy difference between the lowest energy absorption band and the maxima of the emission band (Stokes shift) remains negligible.

In **Type-I<sup>1/2</sup>** HNCs a larger redshift in absorption and emission is observed upon shell growth. This shift to lower energies is due to the loss of confinement of the charge carrier that is delocalized over the whole structure. This delocalization also increases the exciton radiative lifetimes as a result of a reduced electron-hole wavefunction overlap. Similarly to Type-I HNCs, Type I<sup>1/2</sup> HNCs are also characterized by a negligible Stokes shift and discrete transitions in the absorption and emission spectra. The PL QY of Type-I<sup>1/2</sup> HNCs can be as high as those observed for type-I HNCs (up to 80%).<sup>[2]</sup>

By using suitable combinations of materials the HNC properties can be tailored from the type-I to the **type-II** regime. The formation of the spatially indirect exciton gives rise to large changes in the optical properties.<sup>[2,14]</sup> The absorption spectrum shifts to lower energies and a featureless absorption tail appears at energies below the band edge absorption of both components of the HNC. Furthermore, the PL peak also appears at lower energies than the band edges of both HNC materials and is significantly broader than the PL peaks observed for type-I and type-I<sup>1/2</sup> HNCs. The Stokes shift increases and this leads to reduced PL reabsorption. The exciton radiative lifetime in type-II HNCs is longer than in type-I and type-I<sup>1/2</sup> HNCs because the electron and hole wavefunction overlap is reduced. Complete spatial charge separation will not be obtained in quantum confined HNCs, since the energy offsets are finite. Therefore, a non-zero electron-hole wavefunction overlap is obtained even when the electron and hole are primarily localized in different materials. Despite the longer exciton radiative lifetimes, the PL QYs of Type-II HNCs can be as high as those observed for type-I and type-I<sup>1/2</sup> HNCs.<sup>[2]</sup> Type-II HNCs are promising candidates for various applications. For example, they are interesting materials for photovoltaic applications, since the long exciton lifetime and spatial charge separation allows for the extraction of the charge carriers. Further, the reduced PL reabsorption is beneficial for LED applications and luminescent solar concentrators.

## REFERENCES

1. A. P. Alivisatos, *J. Phys. Chem.* 1996, 100, 13226-13239.
2. C. de Mello Donegá, *Chem. Soc. Rev.* 2011, 40, 1512-1546.
3. S. V. Gaponenko, 'Introduction to Nanophotonics', S. V. Gaponenko (Ed.), Cambridge: Cambridge University press, 2010.
4. C. R. Ronda, T. Jüstel, 'Luminescence: From Theory to Applications'. C. R. Ronda (Ed.), Chapter 2. Weinheim: Wiley-VCH Verlag GmbH & Co. KGaA, 2008.
5. B. Henderson, G. F. Imbusch, 'Optical spectroscopy of Inorganic Solids', G. F. Imbusch (Ed.), Oxford: Clarendon Press, 1989.
6. Y.-W. Jun, J.-S. Choi, J. Cheon, *Angew. Chem. Int. Ed.* 2006, 45, 3414 - 3439.
7. S. Ithurria, M. D. Tessier, B. Mahler, R. P. S. M. Lobo, B. Dubertret, A. L. Efron, *Nat. Mater.* 2011, 10, 936-941.
8. C. Schliehe, B. H. Juarez, M. Pelletier, S. Jander, D. Greshnykh, M. Nagel, A. Meyer, S. Foerster, A. Kornowski, C. Klinke, H. Weller, *Science*, 2010, 329, 550-553.
9. M. G. Bawendi, M.L. Steigerwald, L. E. Brus, *Annu. Rev. Phys. Chem.* 1990, 41, 477-496.
10. P. W. Atkins, 'Physical Chemistry', Fifth edition, Oxford: Oxford University Press, 1995.
11. R. Koole, 'Fundamentals and applications of semiconductor nanocrystals', (Ph.D. Thesis), Utrecht University, Utrecht, 2008
12. A. Meijerink, 'Semiconductor Nanocrystal Quantum Dots', A. L. Rogach (Ed.), 'Chapter: Exciton dynamics and energy transfer processes in semiconductor nanocrystals', Austria: SpringerWienNewYork, 2008.
13. S. A. Ivanov, A. Piryatinski, J. Nanda, S. Tretiak, K. R. Zavadil, W. O. Wallace, D. Werder, V. I. Klimov, *J. Am. Chem. Soc.* 2007, 129, 11708-11719.
14. C. de Mello Donegá, *Phys. Rev. B* 2010, 81, 165303.



## Chapter 4

# **Growth and Stability of ZnTe Magic-Size Nanocrystals**

—

*The start of something small*

## Abstract

*A synthesis method for ZnTe magic-sized clusters (MSCs) is reported, and the stability and growth kinetics of these clusters are investigated. Four distinct MSC families, with lowest energy absorption peaks at 330, 354, 378, and 392 nm, are observed. The stability and growth kinetics of the MSCs are strongly influenced by the reaction temperature, precursor concentration, and nature of the ligands used as coordinating solvent. High precursor concentrations result in faster growth and MSC formation at lower temperatures. Higher temperatures accelerate the growth kinetics and lead to a gradual shift from the stepwise MSC growth regime to a continuous growth regime. For temperatures above 260°C, only continuous growth of nanocrystals is observed. The nature of the ligands also influences the stability and growth of ZnTe MSCs, which are formed with primary alkylamines as ligands, but not when trioctylphosphine, trioctylphosphine oxide, or trioctylamine are used as the sole ligands. This demonstrates the crucial role of ligands in the formation of stable ZnTe MSCs using colloidal synthesis methods. Under optimum synthesis conditions (viz., 200°C, hexadecylamine as ligand, and suitable precursor concentrations), the method presented here allows the synthesis and isolation of a single MSC family (absorbing at 330 nm).*

## 4.1 – Introduction

Colloidal semiconductor nanocrystals (NCs) or quantum dots (QDs) have opened up exciting new possibilities in the field of materials science. Control over the size and shape of the NCs makes it possible to tune the optoelectronic properties of a material without changing its composition.<sup>[1]</sup> The tunability of the emission color, associated with large absorption cross sections over a wide spectral range, makes colloidal QDs attractive materials for a number of applications, such as LEDs, solar concentrators, solar cells, and biolabels.<sup>[1]</sup> The size dependence of the electronic structure of semiconductor NCs can also be exploited to follow their growth during colloidal synthesis by absorption spectroscopy. As the NCs grow, the lowest energy absorption peak shifts continuously towards lower energies. Under some circumstances sharp and narrow peaks have been observed in the early stages of the NC growth, which has been ascribed to the presence of well-defined clusters in the reaction mixture. These clusters, often referred to as “magic size clusters” (MSCs), contain only tens of atoms and form a transition between molecules and NCs.

MSCs contain a well-defined number of atoms, and are characterized by a much higher stability than slightly larger or smaller clusters. As a result,

only specific cluster configurations can be formed, and, therefore, growth in the magic size regime will proceed in a stepwise fashion, from one magic-size to the next (*e.g.*, Au<sub>8</sub>, Au<sub>18</sub>, Au<sub>34</sub>, Au<sub>40</sub>, etc.).<sup>[2]</sup> The stability of MSCs is usually explained by the formation of closed electronic or geometric shells of atoms. This model was originally developed for metal MSCs,<sup>[2]</sup> and it is as yet unclear whether it can satisfactorily explain the nature and stability of semiconductor MSCs as well, given the limited amount of studies on this topic. A better understanding of the formation and stability of semiconductor MSCs in solution would provide valuable insight in the nucleation mechanism of colloidal semiconductor NCs, since the size scales of MSCs and critical (and subcritical) crystal nuclei are the same.<sup>[1]</sup> It has also been suggested that semiconductor MSCs work as monomer reservoirs, thereby modulating the growth kinetics of colloidal NCs.<sup>[3]</sup> Moreover, CdSe MSCs (1.2 nm diameter) have been used as seeds to grow larger MSCs (1.7 nm diameter) and small NCs in the 2.0 to 2.6 nm size range,<sup>[4]</sup> which are difficult to obtain by traditional methods without laborious post-preparative size-selection procedures. Further, the formation of ultra-narrow (2 nm diameter) CdSe nanowires by oriented attachment of MSCs has been recently observed.<sup>[5]</sup>

Most reports on semiconductor MSCs address the model system CdSe,<sup>[3-15]</sup> but MSCs of CdTe,<sup>[8,16,17]</sup> CdS,<sup>[8,15,18-21]</sup> and ZnSe<sup>[8]</sup> have also been synthesized. The formation of ZnTe MSCs has not yet been reported. ZnTe is a II-VI semiconductor with a band gap of 2.26 eV at room temperature<sup>[22]</sup> and band potentials that make it an attractive material for type-II semiconductor heterostructures.<sup>[1]</sup> The band alignment in type-II heterostructures is such that it leads to the formation of a spatially indirect exciton, *i.e.*, the photoexcited electron and hole localize on different sides of the heterojunction, which has important consequences for a number of potential applications.<sup>[1]</sup> For example, recent work has yielded highly luminescent type-II CdTe/CdSe colloidal heteronanocrystals in which the degree of exciton spatial separation can be controlled.<sup>[23]</sup> ZnTe/CdSe is potentially more attractive than CdTe/CdSe because it offers much larger energy offsets between the valence and conduction bands, which should facilitate the formation of an indirect exciton. Moreover, ZnTe also offers the prospect of Cd-free type-II heterostructures, such as ZnTe/ZnSe. ZnTe based heterostructures, such as ZnTe/CdSe and ZnTe/ZnSe, have been grown both by vapor phase epitaxial (VPE) deposition (*e.g.*, molecular beam epitaxy, MBE)<sup>[24]</sup> and colloidal synthesis methods.<sup>[25,26]</sup>

Although colloidal chemistry methods offer a number of advantages over VPE techniques,<sup>[1]</sup> the development of ZnTe based colloidal heteronanocrystals has been hampered by the limited availability of high quality ZnTe NCs. Reports on the synthesis of ZnTe colloidal NCs are scarce,<sup>[26-29]</sup> possibly due to a poor control over the nucleation and/or growth of ZnTe NCs. In this context, the investigation of ZnTe MSCs is highly desirable, as it will provide insight over the nucleation and growth of colloidal ZnTe NCs. Moreover, ZnTe MSCs may be valuable as seeds for the controlled growth of larger ZnTe NCs and as building blocks for type-II colloidal heteronanocrystals. Additionally, ZnTe MSCs may offer an effective route to the fabrication of colloidal NCs doped with magnetic ions, such as Mn<sup>2+</sup>. Diluted magnetic semiconductor QDs are promising materials for applications in spintronics and spin-photonics.<sup>[30-32]</sup> Ideally, each QD should contain only one magnetic ion, since this would allow control over individual spins.<sup>[31]</sup> However, such a level of control over the doping of QDs has proven difficult to achieve, both by VPE and colloidal growth techniques.<sup>[30-32]</sup> MSCs may be ideal for low concentration doping of NCs, since only few (or single) magnetic ions can be incorporated into a MSC. The doped MSCs could subsequently be used as seeds to grow larger NCs in the absence of dopants.

In this chapter we describe the formation, growth and stability of ZnTe MSCs under various synthesis conditions. By varying the reaction temperature and precursor concentration we were able to follow the growth kinetics of four different ZnTe MSC families. Moreover, our results show that the formation and stability of ZnTe MSCs is strongly influenced by the reaction temperature, the precursor concentration, and the nature of the ligands.

## 4.2 – Experimental Methods

**Chemicals:** Trioctylphosphine (TOP, tech. grade 90%), Trioctylphosphineoxide (TOPO, 99%), Hexadecylamine (HDA, 90%), anhydrous Triethylorthoformate (TEOF, 98%), Octadecene (ODE, tech. grade 90%), and anhydrous toluene were purchased from Aldrich. Dodecylamine (DDA, 98%) and Trioctylamine (TOA, 98%) were purchased from Acros Organics. Octadecylamine (ODA, tech. grade  $\geq 90\%$ ) was purchased from Fluka. Diethylzinc (Zn(Et)<sub>2</sub>, 98%) and Tellurium powder (99.999%,  $\leq 250$  micron) were purchased from STREM Chemicals and Chempur, respectively. All reagents were used as received with exception of HDA, DDA, ODA, TOPO, TOA and ODE. Before use, these chemicals were dried and degassed by heating under vacuum (3 h at 200°C, 180°C, 160°C, 150°C, 140°C and 100°C, for TOPO, ODE, DDA, TOA, HDA, and DDA, respectively).



The dried and degassed HDA was subjected to further pre-treatment in order to remove any residual moisture and alcohol impurities. This was done by adding TEOF (5.4 % (m/m)) to the pretreated HDA at 50°C under a N<sub>2</sub> atmosphere (< 5 ppm O<sub>2</sub> and H<sub>2</sub>O). This mixture was heated to 220°C and kept under reflux for ~30 min. Subsequently, the mixture was degassed under vacuum (1 h, ~120°C) to remove residual TEOF and reaction products. The pre-treatment with TEOF was found necessary in order to achieve the high degree of control reported in this chapter for the growth kinetics of the ZnTe MSCs. Similar observations have been reported before for the growth of colloidal CdSe QDs in TOPO:TOP:HDA mixtures.<sup>[33]</sup>

**Synthesis:** ZnTe MSCs were synthesized via a hot injection method, in which a cold solution of Tellurium in TOP was injected into a hot solution containing HDA, ODE, TOP and Zn(Et)<sub>2</sub>. All syntheses were performed in a glove-box under nitrogen (< 5 ppm O<sub>2</sub> and H<sub>2</sub>O). Stock solutions of Zn(Et)<sub>2</sub> and Te in TOP (0.65 M and 0.54 M, respectively) were used to allow the precursor concentrations to be reproducibly controlled. In a standard ZnTe MSC synthesis (precursor concentration C<sub>0</sub>) HDA (2 g) and ODE (2 g) were loaded in a reaction flask and heated to 200°C. At this temperature Zn(Et)<sub>2</sub> stock solution (500 µL) was added. After 5 minutes, Te stock solution (250 µL) was swiftly injected into the reaction mixture under stirring. The reaction temperature was kept constant during 55 minutes and aliquots (~0.5 mL) of the reaction mixture were taken at regular time intervals. Reaction temperatures ranging from 100°C to 280°C were investigated, while keeping all other variables constant. The syntheses were carried out using a custom made aluminum block that allows for the simultaneous heating and stirring of four reaction flasks. This makes it possible to carry out four parallel syntheses at the same reaction temperature, thereby allowing a reliable comparison between different reaction parameters. In this way, the influence of the precursor concentration was investigated by using three different concentrations (C<sub>0</sub> in duplicate, 2C<sub>0</sub>, and 3C<sub>0</sub>). TOP was used to equalize the volume of the four flasks, since the same stock solution was used in all cases. The influence of the ligands (ODA, HDA, DDA, TOP, TOPO, and TOA) was investigated by running four parallel syntheses at a time using the same volumes of ligands and without ODE.

**Characterization:** Absorption spectra were measured on a double beam Perkin-Elmer Lambda 16 UV/Vis spectrometer (scan rate: 1 nm/s). Emission spectra were recorded using the monochromator of a Spex Fluorolog spectrometer (double-grating, 0.22 m, SPEX 1680) and a 450 W Xe lamp as the

excitation source. The luminescence spectra were recorded by a Princeton Instrument CCD-camera and a 0.25 m Acton Research monochromator with a grating of 150 lines/mm blazed at 550 nm. All measurements were performed at room temperature under  $N_2$  atmosphere. Samples for optical measurements were prepared by directly dissolving the crude reaction mixture in anhydrous toluene under nitrogen. In order to avoid deviations from linearity in the absorption spectra, all measurements were carried out on samples with a low optical density ( $\leq 0.2$  at 300 nm). Transmission electron microscopy (TEM) was performed using a Tecnai microscope (FEI TECNAI G2 T20F) operating at 200 kV. The TEM measurements were carried out on ZnTe MSC samples which had been purified in order to remove the excess of organic molecules and unreacted precursors. The purification procedure involved the precipitation of the MSCs from a solution of the crude reaction mixture in toluene (1:1 volume ratio) by adding anhydrous methanol. The precipitate was isolated by centrifugation (3000 rpm, 15 min) and redissolved in anhydrous toluene. Samples for TEM imaging were prepared by dipping a carbon-coated copper (400-mesh) TEM grid into a toluene solution of ZnTe MSCs. The excess liquid was removed by blotting using filter paper. Elemental analysis of purified samples was carried out by Inductively Coupled Plasma Mass Spectrometry (ICP-MS). Mass spectra were taken on an Electrospray Ionisation Time-of-Flight (ESI-ToF) mass spectrometer (LC-T; Micromass, Manchester, U.K.). Mass spectrometry (MS) measurements were performed in both positive and negative ion modes using an Electrospray Ionisation Time-of-Flight (ESI-ToF) mass spectrometer (LC-T; Micromass, Manchester, UK) equipped with a Z-spray nano-electrospray ionisation source. Needles were made from borosilicate glass capillaries (Kwik-Fil, World Precision Instruments, Sarasota, FL) on a P-97 puller (Sutter Instruments, Novato, CA), coated with a thin gold layer by using an Edwards Scancoat (Edwards Laboratories, Milpitas, CA) six Pirani 501 sputter coater. The applied voltage on the needle was 1300 V and the sample cone voltage 50 V. All spectra were mass calibrated by using an aqueous solution of cesium iodide (25 mg/ml). ZnTe MSC samples ( $[ZnTe]=1$  mM) for MS measurements were prepared by directly dissolving the crude reaction mixture in a solution of NaI in diethyl ether and spraying the solutions using dry nitrogen for nebulization.

## 4.3 – Results and discussion

### 4.3.1 – Stepwise growth of ZnTe MSCs

The ZnTe MSC synthesis method developed in this work is based on the injection of a cold solution of Tellurium in trioctylphosphine (TOP) into a

hot (*e.g.*, 200°C) solution containing an alkylamine (*e.g.*, hexadecylamine, HDA), octadecene (ODE), trioctylphosphine (TOP) and diethylzinc ( $\text{Zn}(\text{Et})_2$ ). As a representative example, figure 4.1 shows the absorption spectra of four aliquots taken during a ZnTe MSC synthesis carried out at 187°C and using HDA as ligand. A distinct sharp peak at 330 nm is observed in the absorption spectrum of the sample taken after 10 minutes. After 25 minutes, the 330 nm absorption peak is still present, but a second peak has appeared at 354 nm. The full-width at half-maximum (FWHM) of both peaks is 160 meV, which is narrow compared to the width of absorption peaks usually observed in the initial stages of QD growth (*viz.*, ~300 meV),<sup>[33]</sup> when the inhomogeneous broadening is still large. This narrow width is typical for MSCs and line widths around 150 meV have also been observed for MSCs of CdTe<sup>[16,17]</sup> and CdSe.<sup>[5,6,9]</sup> These narrow widths indicate that MSC families are essentially single sized. CdSe and CdTe MSCs have been shown to be smaller than 2 nm,<sup>[5-7,9,17]</sup> and are therefore in the strong quantum confinement regime.<sup>[34]</sup> In this size regime, small size variations lead to large changes in the energy levels of the QD. For example, based on the known size dependence of the band-gap of CdSe QDs,<sup>[34]</sup> it can be estimated that an ensemble of 2 nm diameter spherical CdSe QDs with 5% size dispersion (*i.e.*,  $\pm 0.1$  nm, which is  $\sim 1/2$  of the ionic radius of  $\text{Se}^{2-}$ ) shows an inhomogeneous line width of 130 meV.

The appearance of a second peak, instead of a continuous shift of the absorption peak towards lower energy, is typical growth behavior for MSCs.<sup>[1,6,8,9,16,17,35]</sup> The growth of MSCs is stepwise because magic size cluster configurations are much more stable than somewhat smaller or larger cluster configurations.<sup>[1,35]</sup> Therefore, a MSC will grow only if enough monomer is incorporated to yield one of the larger MSCs. Intermediate cluster configurations are not sufficiently stable and are therefore not formed. As smaller MSCs evolve into larger ones, their distinct absorption peak at higher energies decreases, while distinct peaks at lower energies appear, corresponding to larger MSCs. The MSC growth can thus be followed in the absorption spectrum via the disappearance and appearance of sharp absorption peaks at fixed energies. The change in the concentration of specific MSC families can be followed via the strength of their characteristic absorption peaks, since the absorbance increases linearly with the concentration of the absorbing species. Accordingly, figure 4.1 shows that the peak positions remain constant throughout the synthesis, while their relative intensities change. This typical change in the relative intensity of characteristic MSC absorption peaks has been observed before

for other systems (*e.g.*, CdSe<sup>[8,9]</sup> and CdTe<sup>[16]</sup> MSCs). To allow the quantitative comparison of samples with different absolute absorption cross sections, the samples were collected quantitatively and diluted in order to achieve comparable optical densities at 330 nm. The measured spectra in figure 4.1 were subsequently corrected for the different dilution factors. It is clear in figure 4.1 that the rise of the peak at 354 nm in the sample taken after 25 min is correlated with a decrease in the absorbance of the peak at 330 nm. This correlation is even more evident in the samples taken after 40 and 55 min of reaction. These observations are consistent with the stepwise growth behavior typically observed for MSCs, and indicate that ZnTe MSCs are formed under the present reaction conditions.

In addition to absorption spectra, luminescence spectra can also provide insight into the properties of QDs and MSCs. The room temperature emission spectra of the various MSC samples were thus measured, but only luminescence from the Zn-HDA complex was observed (*viz.*, broad band with maximum at ~450 nm). Luminescence from MSCs is often quenched due to the presence of surface states. In addition to surface states, the high energy position of the ZnTe band edges (*viz.*, -2.6 eV and -5.0 eV relative to the vacuum level, for the conduction- and valence-band edges,

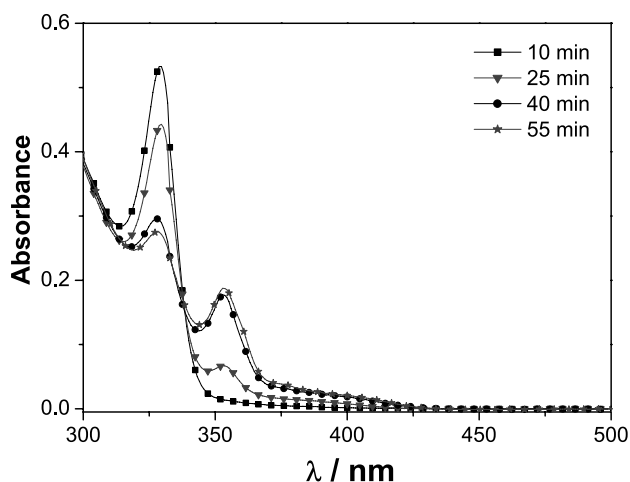


**Figure 4.1** – Absorption spectra of aliquots taken after 10, 25, 40 and 55 min of reaction at 187°C during a ZnTe MSC synthesis in which hexadecylamine was used as ligand (precursor concentration: 3C<sub>0</sub>). The symbols are labels for the curves and are not related to the spectral scan rate (1 nm/s in all cases).

respectively<sup>[1]</sup>) may also play a role in the quenching of the luminescence of ZnTe MSCs. The high energy position of the band edges makes it difficult to efficiently passivate the surface atoms electronically, because most ligands have energy levels below the band edges of (bulk) ZnTe, and may therefore trap photoexcited carriers. This may be the reason for the scarcity of reports on the luminescence of colloidal ZnTe QDs.<sup>[29]</sup> Nevertheless, the high position of the band edges can also be advantageous, since it makes ZnTe nanocrystals ideal components for type-II heteronanostructures, as discussed above.

### 4.3.2 – Temperature dependence of MSC growth

The temperature plays a crucial role in colloidal NC syntheses, since it strongly influences the rates of several processes (*e.g.*, nucleation, monomer diffusion, monomer attachment and detachment rates, etc.).<sup>[1,40]</sup> To investigate the temperature dependence of the growth kinetics and stability of ZnTe MSCs, syntheses were performed at several temperatures ranging from 100°C to 280°C. Growth was observed only at temperatures equal to or higher than 200°C. The absorption spectra of aliquots taken after 10, 25, 40 and 55 min of reaction at two different temperatures (*viz.*, 200°C and 220°C) are presented in figure 4.2. It is clear that only one MSC family, absorbing at 330 nm, is formed at 200°C, whereas at 220°C four different MSC families are observed (families I, II, III and IV, with lowest energy absorption peaks at 330 nm, 354 nm, 378 nm, and 392 nm, respectively). Moreover, a featureless tail starts to develop between 400 and 450 nm after 25 min of reaction at 220°C (figure 4.2). As the reaction proceeds, the intensities of both the absorption tail and the lower energy discrete peaks become more pronounced relative to the 330 nm peak. This shows that during the stepwise growth of the MSCs there are also ZnTe NCs growing continuously towards larger sizes (*i.e.*, stepwise and continuous growth can co-exist). Considering that the featureless tail starts at wavelengths slightly longer than the absorption peak of MSC family IV, one can conclude that at 220°C clusters larger than family IV undergo a transition from the stepwise to the continuous growth regime.

As the reaction temperature increases, the transition from stepwise to continuous growth occurs at increasingly smaller sizes and at increasingly shorter reaction times. This is clearly observed in figure 4.3, which shows the absorption spectra of samples taken after 55 min of reaction at temperatures ranging from 200°C to 280°C. It is evident that while the characteristic absorption peaks of MSC families I to IV are still dominant after 55 min of

reaction at 220°C, they are barely discernable for the sample collected after 55 min at 240°C. Above 260°C ZnTe MSCs are no longer observed, even at reaction times as short as 1 min. The results presented here demonstrate that the temperature has a substantial impact on the stability and growth kinetics of ZnTe MSCs, in agreement with previous studies on different MSC systems (e.g., CdSe,<sup>[4,9,10,35]</sup> CdTe<sup>[16]</sup>). Typically, MSCs are observed only at reaction temperatures well below the usual synthesis temperature of QDs under the same reaction conditions. For example, the hot-injection synthesis of colloidal CdSe NCs from dimethylcadmium and TOP-Se yields CdSe QDs ( $d \geq 2.8$  nm) upon injection at 300°C and growth at 240°C,<sup>[33]</sup> but only CdSe MSCs ( $d = 1.2$  nm) upon injection at 100°C.<sup>[4]</sup> The overall effect of the temperature on the growth kinetics of MSCs is analogous to that observed for regular NCs, and can qualitatively be explained along the same lines.<sup>[1,35]</sup> Higher temperatures lead to faster monomer diffusion towards the growing NC and facilitate monomer attachment to the NC surface sites, thereby increasing the growth rates.<sup>[1]</sup> Considering that the energy barriers for monomer attachment to MSCs are presumably much higher than for regular NCs, the growth kinetics of different families of MSCs should be strongly temperature dependent, in agreement with our observations.

It would be interesting to know the sizes of the ZnTe MSC families observed here. However, it remains a critical experimental challenge to determine the sizes of very small clusters.<sup>[1]</sup> A range of characterization tools is typically used, but the results are often inconclusive due to the intrinsic limitations of the techniques. Although a large number of studies has unambiguously established the presence of semiconductor MSCs in solution based on their characteristic optical signatures (*viz.*, narrow and well defined absorption transitions),<sup>[3-21]</sup> the exact size and composition of MSCs are rarely known. The only examples of well-characterized semiconductor MSCs are the metal chalcogenide solid state clusters, which have been isolated as single crystals suitable for structural determination by X-ray crystallography.<sup>[7,15]</sup> Small-angle and wide-angle X-ray scattering (SAXS and WAXS, respectively) have also been used to estimate the size of CdS and CdSe MSCs isolated from colloidal solutions as powders.<sup>[9,20]</sup> Transmission electron microscopy (TEM) has been successful only in a few cases and for particles with diameters equal to or larger than 2 nm.<sup>[8,9,18]</sup> In the present study, TEM was used as a characterization tool for the ZnTe MSCs, but yielded inconclusive results. This is not unexpected, since size determination by TEM is severely limited for extremely small particles ( $\leq 2$  nm), for which the contrast variation under the electron beam does not sufficiently differ from the normal fluctuations

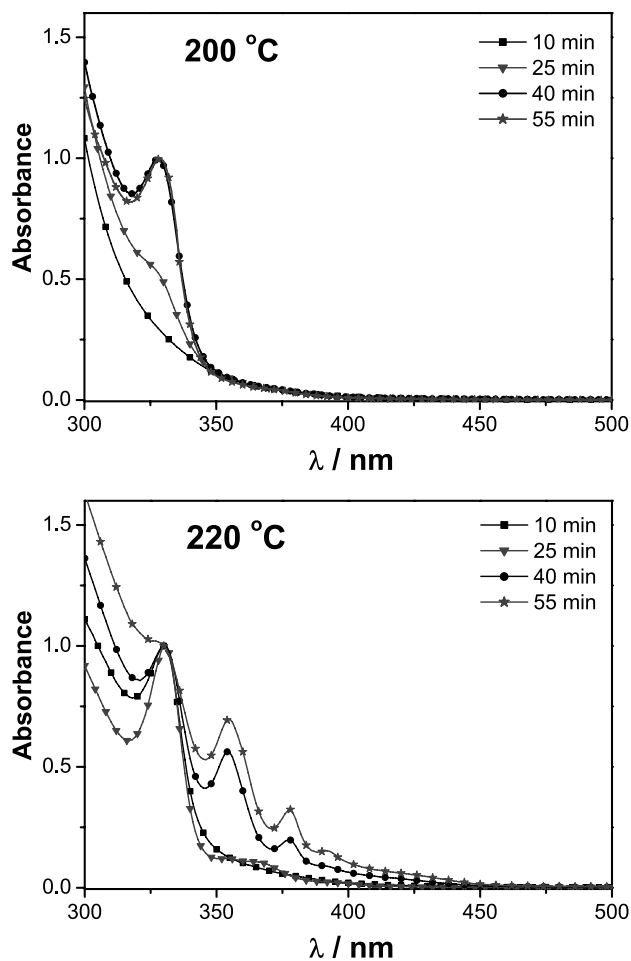


**Figure 4.2** – Absorption spectra of aliquots taken after 10, 25, 40 and 55 min of reaction during ZnTe MSC syntheses using hexadecylamine as ligand and carried out at two different temperatures (200°C and 220°C, precursor concentration: C0 in both cases). The symbols are labels for the curves and are not related to the spectral scan rate (1 nm/s in all cases).

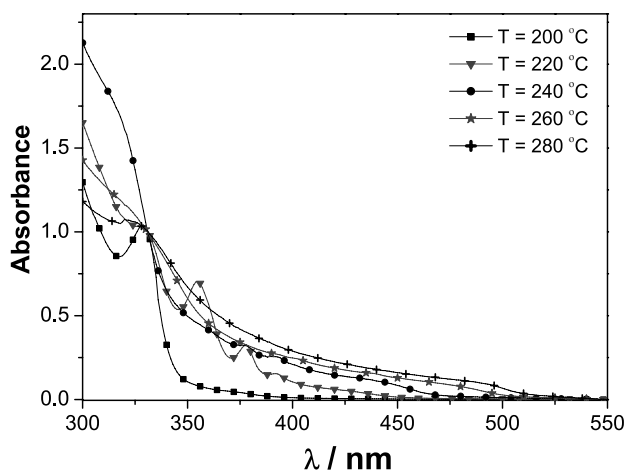


**Figure 4.3** – Absorption spectra of samples taken after 55 min of reaction in ZnTe MSC syntheses performed at various reaction temperatures ranging from 200°C to 280°C (precursor concentration:  $C_0$ ). The symbols are labels for the curves and are not related to the spectral scan rate (1 nm/s in all cases).

of the carbon support film. This limitation is particularly serious for low electron density materials such as ZnTe. Therefore, the TEM results only allow us to establish an upper limit of *ca.* 2 nm for the diameter of the ZnTe MSCs prepared in this work.

Mass spectrometry has also been used to study colloidal MSCs, but was successful as an identification technique in only a few cases.<sup>[6,12]</sup> In many cases, the information obtained was insufficient to infer the size and structure of the clusters in solution, since the same fragmentation pattern was observed, regardless of the initial cluster size.<sup>[9,13]</sup> Mass spectrometric investigations were carried out on ZnTe MSC samples prepared in this work, but only low mass peaks ( $m/z < 1300$ ) were observed in the mass spectra, both in positive and negative ion modes.<sup>[41]</sup> These peaks were identified as charged organic species, formed by ionization of the organic ligands used in the MSC synthesis (*viz.*, hexadecylamine and trioctylphosphine) and in-situ formed oligomers (dimers, trimers and tetramers). The presence of small fragments of ZnTe MSCs, such as  $[Zn_4Te_6]$  (mass: 1027.16) can be unequivocally excluded based on the absence of the expected isotopomere splitting. The absence of peaks due to  $[Zn_xTe_y]$  species implies that the ZnTe MSCs are neutral and failed to ionize under the conditions used in our mass spectrometry experiments.



The size dependence of the band-gap of QDs can be used to estimate the size of semiconductor NCs in the quantum confinement size regime, provided sufficient data is available to allow the construction of an empirical sizing curve correlating the energy of the lowest absorption transition with the QD size.<sup>[34]</sup> Sizing curves are available for a number of QD systems (e.g., CdSe, CdTe, etc.),<sup>[34]</sup> but data on ZnTe QDs are still too limited. The smallest ZnTe NCs reported in the literature are 4.5 nm in diameter and have the lowest energy absorption transition at 440 nm (2.82 eV).<sup>[26]</sup> Clearly, the NCs giving rise to the absorption tail around 420 nm (2.95 eV) are smaller than 4.5 nm. Theoretical calculations of the confinement energy  $\Delta E_g$  in ZnTe QDs predicted a size dependence that can be expressed as  $\Delta E_g = 3d^{-1.43}$  ( $d$  is the QD diameter).<sup>[36]</sup> This theoretical expression can be used to estimate the size of the ZnTe MSCs prepared in this work, given that the scarcity of experimental data on ZnTe QDs precludes the construction of an empirical sizing curve. For the largest ZnTe MSCs (Family IV), absorbing at 392 nm (3.16 eV), the confinement energy is 0.9 eV, suggesting that these clusters are about 2.3 nm in diameter. The confinement energy for MSC family III (absorption at 378 nm) is 1.02 eV, indicating a diameter of about 2.1 nm. For the two smallest ZnTe MSC families (I and II, absorbing at 330 nm and 354 nm, respectively) the confinement energies are 1.5 eV and 1.24 eV, which indicates diameters of 1.6 nm and 1.8 nm, respectively. We note that these estimates are consistent with the upper size limit determined by TEM measurements.

It is insightful to compare the ZnTe MSCs investigated here with those reported for other II-VI semiconductors. The model system CdSe is the most investigated one, and provides the only example where MSCs have not only been identified by optical absorption spectroscopy,<sup>[3-15]</sup> but also investigated by mass spectrometry<sup>[6,12,37]</sup> and isolated as solid state clusters,<sup>[7,15,37]</sup> for which the crystal structure was determined by single crystal X-Ray diffractometry.<sup>[7,15]</sup> These studies established the existence of a homologous series of six different solid state CdSe tetrahedral clusters:  $[\text{Cd}_4(\text{SeR})_6\text{L}_4]^{2-}$  ( $d_{\text{eq}} = 0.4$  nm),  $[\text{Cd}_8\text{Se}(\text{SeR})_{12}\text{L}_4]^{2-}$  ( $d_{\text{eq}} = 0.6$  nm),  $[\text{Cd}_{10}\text{Se}_4(\text{SeR})_{12}\text{L}_4]$  ( $d_{\text{eq}} = 0.7$  nm),  $[\text{Cd}_{17}\text{Se}_4(\text{SeR})_{24}\text{L}_4]^{2+}$  ( $d_{\text{eq}} = 1.0$  nm),  $[\text{Cd}_{32}\text{Se}_{14}(\text{SeR})_{36}\text{L}_4]$  ( $d_{\text{eq}} = 1.5$  nm), and  $[\text{Cd}_{54}\text{Se}_{32}(\text{SeR})_{48}\text{L}_4]^{4-}$  ( $d_{\text{eq}} = 2.0$  nm) ( $d_{\text{eq}} =$  equivalent diameter, which is defined as the tetrahedron height; R= alkyl or aryl groups, L= two electron ligand at the tetrahedral apical sites, typically tertiary phosphines or water).<sup>[7,15]</sup> Examples of these cluster configurations are given in figure 4.4. A series of structurally analogous clusters based on CdS has also been synthesized.<sup>[15,20]</sup> For convenience these clusters are usually referred to by

the number of metal cations (*i.e.*,  $M_n$ ). The smallest homologues ( $M_4$  and  $M_{10}$ ) have also been isolated for ZnS, CdTe,  $(Cd_{1-x}Zn_x)E$  ( $E = S, Se, Te$ ), and  $Cd(E,E')$  ( $E = Te, Se; E' = Te, S, Se$ ).<sup>[15]</sup> The cluster frameworks display a clear structural relationship to the bulk solid materials, being constructed from a combination of adamantane and barrelane cages, which are the building units of, respectively, the zinc-blende (cubic) and the wurtzite (hexagonal) crystal structures of II-VI semiconductor materials.<sup>[15]</sup> The smallest clusters ( $M_4$  and  $M_{10}$ ) consist of adamantane cages only, and are thus best described as tetrahedral fragments of the cubic zinc-blende material. Larger homologues consist of hexagonal barrelane cages fused onto a zinc-blende-type tetrahedral core.<sup>[7,15,20]</sup> The barrelane cages can be distributed in different ways, so that structural isomers containing the same number of metal atoms but slightly different number of ER ligands can also be prepared (*e.g.*,  $[Cd_{32}S_{14}(SeR)_{36}L_4]$  and  $[Cd_{32}S_{14}(SeR)_{38}L_2]^2$ ).<sup>[15]</sup>

Magic size clusters of formula  $(ME)_n$  ( $M = Cd, Zn; E = S, Se, Te; n = 13, 19, 33, 34$ ) have been observed in the gas phase by mass spectrometric analysis of fragments produced by laser ablation of solid targets of II-VI semiconductors (CdSe, CdS, CdTe, ZnS and ZnSe).<sup>[6,12]</sup> Similar  $(ME)_n$  MSCs, with  $n = 13, 19, 33, 34$ , and 48, have also been identified in the mass spectra of organically stabilized  $(CdSe)_n$  clusters prepared in solution by colloidal synthesis methods.<sup>[6,12]</sup> Atomic force microscopy measurements on monolayers of  $(CdSe)_{33,34}$  clusters deposited on graphite indicate a diameter of 1.5 nm.<sup>[6]</sup> It is interesting to note that the II-VI MSCs observed in gas phase are stoichiometric, regardless of whether they were obtained by laser

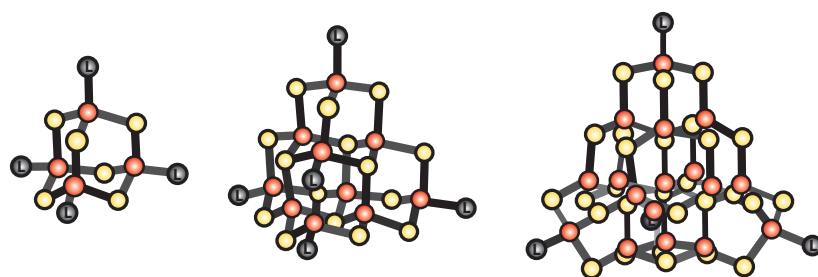


**Figure 4.4** – Examples of observed frameworks<sup>[15]</sup> for colloidal CdSe MSC obtained via solvothermal synthesis with the use of ligands. From left to right:  $[Cd_4(SeR)_6L_4]$ ,  $[Cd_{10}Se_4(SeR)_{12}L_4]$ , and  $[Cd_{17}Se_4(SeR)_{24}L_4]$ . R= alkyl or aryl groups, L= two electron ligand at the tetrahedral apical sites. Carbon chains are omitted for simplicity.

ablation of solids<sup>[6,12]</sup> or from solutions of colloidal MSCs.<sup>[6,9,12,13]</sup> Considering that colloidal II-VI MSCs and QDs are typically non-stoichiometric (cation-rich, with M/E= 1.1-1.5),<sup>[1,9]</sup> this suggests that after the loss of surfactants by vaporization the naked non-stoichiometric MSCs quickly reconstruct into stoichiometric configurations. Nevertheless, the number of metal cations in the stoichiometric clusters (*viz.*, 13, 19, 34, 48) is similar to that observed in the non-stoichiometric solid state clusters (*viz.*, 10, 17, 32, 54), suggesting that the stability of II-VI MSCs is largely determined by the number of cations.

The observations summarized above imply that under similar conditions all II-VI semiconductors will form similar MSC families. This can be understood as a consequence of the fact that the stability of II-VI MSCs stems from their crystal structure,<sup>[6,15]</sup> which is the same for all II-VI semiconductors. Based on this assumption, we can tentatively identify the ZnTe MSCs observed in the present work by analogy with other colloidal II-VI MSCs. A recent study has identified five CdSe MSC families in solution, all of them Cd-rich (Cd/Se= 1.1 – 1.3).<sup>[9]</sup> Wide-angle X-ray diffraction analysis indicated sizes ranging from 1.5 to 2.0 nm for the largest three families.<sup>[9]</sup> Based on these size estimates and on the optical absorption spectra, the five CdSe MSC families observed by Kudera and co-workers<sup>[9]</sup> can be assigned to  $M_n$  clusters with  $n \cong 13, 19, 34, 48,$  and  $54$ . In the present work, four ZnTe MSC families are observed, with lowest energy absorption transitions at 3.76 eV (family I), 3.50 eV (family II), 3.28 eV (family III), and 3.16 eV (family IV). Elemental analysis of samples isolated from the growth solution by precipitation showed that these MSCs are Zn-rich (*viz.*, Zn/Te= 1.4 for a sample consisting primarily of families I and II). The excess Zn is most likely stabilized by ligand molecules, similarly to what has been observed for other non-stoichiometric colloidal nanocrystals.<sup>[1]</sup> As it will be discussed below (section 4.3.4), ZnTe MSCs are only obtained when primary alkylamines are used as ligands, suggesting that under the conditions investigated in this work these ligands are essential components of the clusters. Therefore, the ZnTe MSC families observed here can be assigned to  $[(ZnTe)_n(ZnL_x)_m]$  clusters, with  $(m+n)/n = 1.4$  and  $L = \text{HDA}$  or other primary alkylamines. Considering that spectral features at energies lower than the absorption onset of family IV are already associated with a continuous growth regime (see above), this family is assigned to the largest possible MSC (*i.e.*,  $n \cong 54$ ). The other three ZnTe MSC families can then be tentatively assigned to  $n \cong 19, 34$  and  $48$  (for MSCs I, II, and III, respectively). The diameter of the ZnTe MSCs can be estimated from those reported for the CdSe MSC analogues,

knowing that the bond lengths and lattice parameters of bulk CdSe and ZnTe are very similar (*viz.*, bond lengths: 0.2642 nm and 0.263 nm; lattice constants: 0.6101 nm and 0.605 nm, for bulk zinc-blende ZnTe and CdSe, respectively<sup>[38,39]</sup>). This comparison yields estimated diameters of ~1.3 nm; ~1.5 nm, ~1.8 nm, and ~2.0 nm for the ZnTe MSC families I, II, III, and IV, respectively. We note that these estimates are in good agreement with those presented above on the basis of the theoretically predicted size dependence of the band gap of ZnTe QDs (*viz.*, 1.6 nm, 1.8 nm, 2.1 nm, and 2.3 nm, for MSC families I, II, III, and IV, respectively).

#### 4.3.3 – Effect of precursor concentration

In order to investigate the influence of the precursor concentration on the growth kinetics of the ZnTe MSCs, three syntheses were carried out at 187°C with different precursor concentrations (*viz.*,  $C_0$ ,  $2C_0$  and  $3C_0$ ). The absorption spectra of samples taken after 55 min for all three syntheses are shown in figure 4.5. Since the absorbance is proportional to the cluster concentration, the changes in the concentration of the different MSC families as a function of the precursor concentration can be directly determined from the absorption spectra. The samples were collected quantitatively and the measured spectra were corrected for the different dilution factors as explained above (section 4.3.1). In this way the intensities shown in figure 4.5, albeit rescaled, are directly proportional to the original concentrations in the growth solutions, and therefore reflect the absolute increase in the populations of the different MSC families with increasing precursor concentration. In the  $C_0$  synthesis only MSC family I was observed, while in the  $2C_0$  and  $3C_0$  syntheses cluster families I and II were formed. The dependence of the cluster populations on the precursor concentration is strongly nonlinear for both MSC families. The relative concentration of the MSC family I (determined by taking the 330 nm absorption peak intensity) increases from 1 to 4.7 and to 8.6 as the precursor concentration is raised from  $C_0$  to  $2C_0$  and to  $3C_0$ , respectively, while the relative concentration of the family II peak (at 354 nm) changes from 1.5 to 5.8 when the precursor concentration increases from  $2C_0$  to  $3C_0$ . These results show that the growth of the ZnTe MSCs involves higher order kinetics. This is not unexpected, considering that the stepwise growth of MSCs implies that magic size clusters can only grow if they can in a single step acquire enough atoms to reach the next stable cluster size. Although the growth mechanism of NCs in general is not yet well understood, there is substantial evidence that NCs can grow either by monomer incorporation or particle coalescence.<sup>[1]</sup> For MSCs, particle coalescence is likely the most efficient growth mechanism,

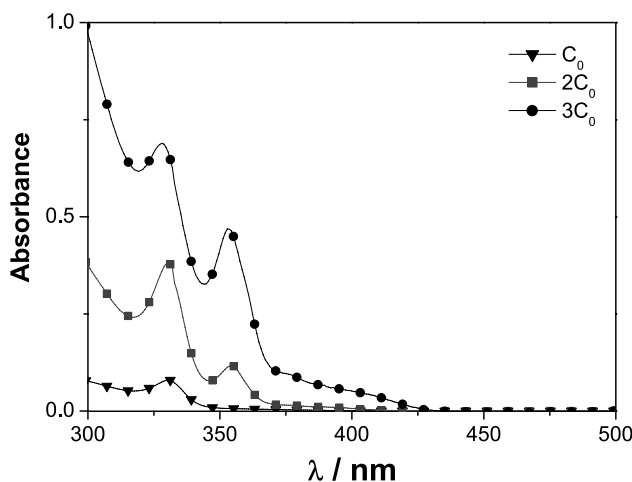


**Figure 4.5** – Absorption spectra of samples taken after 55 min in three ZnTe MSC syntheses at 187°C in which different precursor concentrations (*viz.*,  $C_0$ ,  $2C_0$  and  $3C_0$ ) were used. The absorbance values are proportional to the absolute precursor concentration used in the syntheses. The symbols are labels for the curves and are not related to the spectral scan rate (1 nm/s in all cases).

particularly for larger clusters. This is consistent with our observation that at higher precursor concentrations ( $\geq 2C_0$ ) larger MSCs are observed at lower temperatures (*viz.*, 190°C), whereas at lower precursor concentrations a higher temperature ( $\geq 220^\circ\text{C}$ ) is needed to form MSCs larger than family I. This also provides a qualitative explanation for the less pronounced increase observed from  $2C_0$  to  $3C_0$  in the concentration of cluster family I. In this precursor concentration range family II is also formed, which partially consumes the smaller MSCs from family I. Although the results presented here are as yet insufficient to provide a detailed quantitative description of the growth kinetics of ZnTe MSCs, they clearly show that the growth of ZnTe MSCs and NCs can be controlled by varying the precursor concentration. We expect that also the transition from stepwise to continuous growth, described in section 4.3.2 above, will occur at different temperatures depending on the precursor concentrations. The observation of a featureless absorption tail from 380 nm to *ca.* 420 nm in synthesis  $3C_0$  provides support for this assumption.

#### 4.3.4 – Influence of the ligands

The ligands commonly used in the colloidal synthesis of NCs are amphiphilic molecules, which consist of a polar head group and a non-polar

hydrocarbon tail. The head group possesses donor atoms capable of forming coordinating bonds with the metal atoms at the NC surface and in the growth medium. These characteristics allow ligands to modify the free energies of the NC surface, thereby stabilizing or destabilizing specific facets, and to influence the nucleation and growth kinetics of colloidal NCs.<sup>[1]</sup> Ligands are thus essential to control the size and shape of colloidal NCs. In the case of MSCs, the exact influence of ligands is not yet well understood. For example, CdSe MSCs have been obtained under a variety of conditions, both in the vapor phase (*i.e.*, ligand free),<sup>[12]</sup> and in colloidal suspension using different ligands (*e.g.*, hexadecylamine,<sup>[4,5]</sup> dodecylamine,<sup>[4,9]</sup> nonanoic acid,<sup>[9]</sup> tetradecylphosphonic acid,<sup>[11]</sup> etc.) and at reaction temperatures ranging from 80°C<sup>[9]</sup> to 300°C.<sup>[11]</sup> This suggests that ligands do not modify the intrinsic stability of specific CdSe cluster configurations, but rather decrease or increase the energy barriers for their formation, thereby facilitating or precluding the formation of CdSe MSCs under a given set of conditions.

To investigate the influence of ligands on the formation of ZnTe MSCs, syntheses were performed using a number of different ligands: octadecylamine (ODA), hexadecylamine (HDA), dodecylamine (DDA), trioctylamine (TOA), trioctylphosphineoxide (TOPO) and trioctylphosphine (TOP). The binding strength of these ligands towards Zn decreases from TOPO to TOP (*viz.*, TOPO > R-NH<sub>2</sub> ≥ TOA >> TOP).<sup>[1]</sup> TOP differs from the other ligands in the sense that it binds much more strongly to Te atoms than to Zn.<sup>[1]</sup> Further, due to the three C<sub>8</sub> chains, TOP, TOPO, and TOA are bulkier and occupy a larger surface area when bound to metal atoms than the primary alkylamines. Amines are very dynamic ligands, binding and unbinding to metal atoms on a ~10 ms timescale.<sup>[1]</sup> The dynamic character of the N-metal bond and the ligand diffusion rates increase with decreasing chain length of the alkyl group, leading to faster growth rates for shorter chain amines.<sup>[1]</sup>

The absorption spectra of samples collected after 20 min of reaction for syntheses using DDA, TOP, TOPO and TOA as ligands are shown in figure 4.6. The temperature was 180°C in all cases. No MSCs were observed in the syntheses using TOP, TOPO, and TOA, which resulted only in the continuous growth of NCs. In striking contrast, the syntheses using primary alkylamines as ligands invariably yielded MSCs family I, regardless of the alkyl chain length. This interesting observation implies that the binding strength of the head group and the chain length of the ligand are not

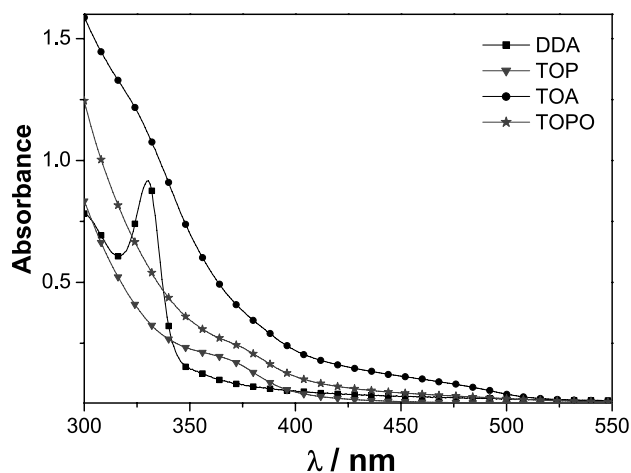


**Figure 4.6** – Absorption spectra of samples collected after 20 min of reaction in ZnTe nanocrystal syntheses in which DDA, TOP, TOPO and TOA were used as ligands. The precursor concentration was  $C_0$  and the reaction temperature was  $180^\circ\text{C}$ . The symbols are labels for the curves and are not related to the spectral scan rate ( $1\text{ nm/s}$  in all cases).

relevant for the formation of ZnTe MSCs, which appears to be essentially determined by steric factors, since ZnTe MSCs are formed with linear chain ligands but not with bulky ligands. It is probable that the configuration of the ZnTe atoms provides additional stability to clusters of specific sizes and/or geometries, but the present results clearly demonstrate that ligands are crucial in the formation of MSCs. As long as the understanding of the nature of semiconductor MSCs is limited, it is difficult to explain the exact role of ligands in the MSC formation process. Nevertheless, the present observations can be qualitatively rationalized by considering the impact of ligands on the kinetic steps involved in the formation of colloidal MSCs, as will be shown in the next section.

#### 4.5 – Qualitative model for the formation of colloidal MSCs

Three consecutive elementary stages can be distinguished in the formation of colloidal NCs:<sup>[44]</sup> (a) monomer formation from precursors; (b) monomer assembly into crystal nuclei (*i.e.*, nucleation); and (c) growth of the nuclei into larger NCs. These three stages can also be recognized in the formation of colloidal MSCs, although important differences are observed in the growth stage. As discussed above, the growth of MSCs is stepwise, while NCs grow in a continuous way, *i.e.*, there are no constraints regarding the

number of monomer units that a NC can incorporate in a single growth step. The nucleation of MSCs also appears to be different from that of regular NCs, as will be discussed below. The first stage is not relevant in the present discussion, since the high reactivity of the precursors used (*viz.*, diethylzinc and TOP-Te) makes the monomer formation much faster than the nucleation and growth steps.

Several models have been used in the literature to describe the nucleation of colloidal NCs.<sup>[1]</sup> The classical nucleation theory (CNT) is the most widely used model, probably due to its simplicity. CNT has several shortcomings, but is useful to qualitatively describe the fundamental principles involved in the nucleation of NCs. The driving force for nucleation is the difference in free energy between the crystal constituents (monomers) in the crystal and in solution. Within the CNT framework the total change in free energy,  $\Delta G_{\text{TOT}}$ , for the formation of a spherical crystal nucleus is given by two contributions: the volume excess free energy  $\Delta G_v$  and the surface (interface) excess free energy  $\Delta G_s$ . The volume contribution is negative due to the energy freed by the chemical bonds formed in the crystal nucleus, which compensates the energy spent to break the bonds between the monomers and the solvent (or ligand) molecules. In contrast, the surface contribution is positive due to the fact that monomers at the surface (interface) have unsaturated bonds. Because  $\Delta G_v$  and  $\Delta G_s$  have opposite signs and different size dependences ( $r^3$  and  $r^2$ , where  $r$  is nucleus radius),  $\Delta G_{\text{TOT}}$  will reach a maximum for nuclei with critical radius  $r_c$  and then decrease with increasing radius. This imposes an energy barrier for nucleation, as it implies that crystal nuclei with  $r < r_c$  (subcritical nuclei) will redissolve to monomers, while those with  $r > r_c$  (supercritical nuclei) will grow out to mature NCs.<sup>[1]</sup> This simple picture is qualitatively consistent with the nucleation and growth of regular colloidal NCs,<sup>[1]</sup> but is unable to explain the formation of colloidal MSCs. MSCs are relatively stable towards both dissolution and growth, and therefore can neither be seen as subcritical nuclei nor as supercritical nuclei.

The inability of CNT to explain the formation of MSCs highlights its greatest shortcoming: crystal nuclei are treated as bulk material having macroscopic properties.<sup>[1]</sup> The key assumptions in CNT are: (a) nuclei are spherical particles with uniform and size-independent density; (b) the nucleus/solvent interface is sharp and the interfacial tension is size independent; (c) interactions with surfactants and solvents are negligible. These assumptions become unreasonable when considering a nucleus of only several tens of atoms.<sup>[1]</sup> Most likely, both  $\Delta G_v$  and the interfacial tension vary considerably with the size and inherent structure of the growing



nuclei, as well as with the particular arrangement of the surface atoms and the surfactant molecules.<sup>[1]</sup> This may lead to modulations in both  $\Delta G_v$  and  $\Delta G_s$ , inducing local minima in the  $\Delta G_{TOT}$  curve. As proposed by Manna and Kudera, these minima would correspond to MSC families.<sup>[35]</sup> The cluster families can grow from one MSC to the next by overcoming energy barriers.

The picture sketched above is in agreement with the results reported here. Multiple families of ZnTe MSCs ( $d \leq 2$  nm) were synthesized at 180-220°C using amine ligands. The temperature plays a crucial role, and by raising the reaction temperature a transition from stepwise to continuous growth was induced. This change in growth mechanism is consistent with the proposed model: higher temperatures make it easier for the MSCs to overcome the energy barriers and induce a transition to a faster and continuous growth regime. Probably, at very short reaction times, MSCs can also be found at higher temperatures.

Our results also clearly demonstrate that the formation of MSCs is strongly influenced by the nature of the ligands. Interestingly, the binding strength of the head group and the chain length of the ligand are not relevant for the formation of ZnTe MSCs, which appears to be essentially determined by steric factors. The results presented above strongly suggest that linear chain ligands, such as the primary alkylamines used in the present study, are required to form ZnTe MSCs. This can be qualitatively understood through the influence of ligands on the depth and position of the local minima in the  $\Delta G_{TOT}$  curve. Nevertheless, a complete understanding of the formation of ZnTe MSCs (and of semiconductor MSCs in general) will require further experimental and theoretical work, in which not only the interactions between the atoms in the cluster are considered, but also the ligand-MSC and ligand-ligand interactions.

#### 4.4 – Conclusions

We developed a synthesis method for colloidal ZnTe magic sized clusters (MSCs). Four distinct ZnTe MSC families, with lowest energy absorption peaks at 330 nm, 354 nm, 378 nm, and 392 nm, are observed. The typical stepwise growth regime and the fixed spectral position of the absorption peaks provide clear signatures of the formation of MSCs. The growth kinetics and stability of the ZnTe MSCs are strongly temperature dependent. By increasing the reaction temperature, the MSC growth rates increase and a gradual shift from stepwise to continuous growth occurs. At temperatures above 260°C only continuous growth of QDs takes place. For

higher precursor concentrations MSCs are formed at lower temperatures, and grow faster to larger MSCs. The populations of the different MSC families increase supra-linearly with the precursor concentration. The choice of ligands is crucial for the MSC formation. Magic size clusters are only formed when straight chain alkylamines (HDA, DDA, and ODA) are used as ligands. The use of TOP, TOPO, and TOA as ligands precludes the formation of MSCs and results in continuous growth of ZnTe QDs. A model, based on the presence of local minima in the size-dependent free energy curve of colloidal NCs, is used to explain our observations. Under optimum synthesis conditions (200°C, HDA as ligand, and suitable precursor concentrations), the presently reported method allows the synthesis and isolation of a single MSC family, absorbing at 330 nm. These ZnTe MSCs are attractive as seeds for the growth of larger ZnTe NCs and as building blocks for Type-II semiconductor heteronanostructures. This possibility is demonstrated in Chapter 5 of this thesis<sup>[42]</sup>, where we report on the use of ZnTe MSCs as seeds for the growth of ultranarrow (Zn,Cd)Te-CdSe colloidal heteronanowires. Further, the method reported here is potentially useful to achieve low concentration doping of NCs with magnetic ions (*e.g.*, Mn<sup>2+</sup>). In MSCs only a few, or even single, magnetic ions can be incorporated. Doped MSCs may be subsequently used as seeds for further growth of NCs in the absence of dopants, thus yielding NCs with a low concentration of magnetic centers, which are of interest in the field of spintronics. Work in this direction has been started in our group and has recently led to the successful preparation of Mn<sup>2+</sup> doped ZnTe MSCs.<sup>[43]</sup>

## REFERENCES

1. C. de Mello Donegá, *Chem. Soc. Rev.* 2011, 40, 1512.
2. T. P. Martin, *Phys. Reports* 1996, 273, 199.
3. Z. Jiang, D. F. Kelley, *ACS Nano* 2010, 4, 1561.
4. C. de Mello Donegá, M. Bode, A. Meijerink, *Phys. Rev. B* 2006, 74, 085320.
5. F. S. Riehle, R. Bienert, R. Thomann, G. A. Urban, M. Krüger, *Nano Lett.* 2009, 9, 514.
6. A. Kasuya, R. Sivamohan, Y. A. Barnakov, I. M. Dmitruk, T. Nirasawa, V. R. Romanyuk, V. Kumar, S. V. Mamykin, K. Tohji, B. Jeyadevan, K. Shinoda, T. Kudo, O. Terasaki, Z. Liu, R. V. Belosludov, V. Sundararajan, Y. Kawazoe, *Nat. Mater.* 2004, 3, 99.
7. V. N. Soloviev, A. Eichhöfer, D. Fenske, U. Banin, *J. Am. Chem. Soc.* 2001, 123, 2354.
8. M. Zanella, A. Z. Abbasi, A. K. Schaper, W. J. Parak, *J. Phys. Chem. C.* 2010, 114, 6205.
9. S. Kudera, M. Zanella, C. Giannini, A. Rizzo, Y. Li, G. Gigli, R. Cingolani, G. Ciccarella, W. Spahl, W. J. Parak, L. Manna, *Adv. Mater.* 2007, 19, 548.
10. J. Ouyang, M. B. Zaman, F. J. Yan, D. Johnston, G. Li, X. Wu, D. Leek, C. I. Ratcliffe, J. A. Ripmeester, K. Yu, *J. Phys. Chem. C* 2008, 112, 13805.
11. Z. A. Peng, X. Peng, *J. Am. Chem. Soc.* 2002, 124, 3343.
12. V. R. Romanyuk, I. M. Dmitruk, Yu. A. Barnakov, R. V. Belosludov, A. Kasuya, *J. Nanosci. Nanotechnol.* 2009, 9, 2111.
13. E. Kuçur, J. Ziegler, T. Nann, *Small* 2008, 4, 883.
14. A. L. Rogach, A. Kornowski, M. Gao, A. Eychmüller, H. Weller, *J. Phys. Chem. B* 1999, 103, 3065.
15. J. F. Corrigan, O. Fuhr, D. Fenske, *Adv. Mater.* 2009, 21, 1867.
16. S. F. Wuister, F. van Driel, A. Meijerink, *Phys. Chem. Chem. Phys.* 2003, 5, 1253.
17. P. Dagtepe, V. Chikan, *J. Phys. Chem. A* 2008, 112, 9304.
18. T. Vossmeier, G. Reck, B. Schulz, L. Katsikas, H. Weller, *J. Am. Chem. Soc.* 1995, 117, 12881.
19. T. Vossmeier, L. Katsikas, M. Giersig, I. G. Popovic, K. Diesner, A. Chemseddine, A. Eychmüller, H. Weller, *J. Phys. Chem.* 1994, 98, 7665.
20. N. Zheng, X. Bu, H. Lu, Q. Zhang, P. Feng, *J. Am. Chem. Soc.* 2005, 127, 11963.
21. M. Li, J. Ouyang, C. I. Ratcliffe, L. Pietri, X. Wu, D. M. Leek, I. Moudrakovski, Q. Lin, B. Yang, K. Yu, *ACS Nano* 2009, 3, 3832.
22. T. Tanaka, K. Hayashida, S. Wang, Q. Guo, M. Nishio, H. Ogawa, *J. Crystal Growth* 2003, 248, 43.
23. C. de Mello Donegá, *Phys. Rev. B* 2010, 81, 165303.
24. I. R. Sellers, V. R. Whiteside, I. L. Kuskovsky, A. O. Govorov, B. D. McCombe,

- Phys. Rev. Lett. 2008, 100, 136405.
25. J. Bang, J. Park, J. H. Lee, N. Won, J. Nam, J. Lim, B. Y. Chang, H. J. Lee, B. Chon, J. Shin, J. B. Park, J. H. Choi, K. Cho, S. M. Park, T. Joo, S. Kim, *Chem. Mater.* 2009, 22, 233.
  26. R. Xie, X. Zhong, T. Basché, *Adv. Mater.* 2005, 17, 2741.
  27. S. H. Lee, Y. J. Kim, J. Park, *Chem. Mater.* 2007, 19, 4670.
  28. J. Zhang, K. Sun, A. Kumbhar, J. Fang, *J. Phys. Chem. C* 2008, 112, 5454.
  29. F. Jiang, Y. Li, M. Ye, L. Fan, Y. Ding, Y. Li, *Chem. Mater.* 2010, 22, 4632.
  30. M. C. Kuo, J. S. Hsu, J. L. Shen, K. C. Chiu, W. C. Fan, Y. C. Lin, C. H. Chia, W. C. Chou, M. Yasar, R. Mallory, A. Petrou, H. Luo, *Appl. Phys. Lett.* 2006, 89, 263111.
  31. L. Maingault, L. Besombes, Y. Leger, C. Bougerol, H. Mariette, *Appl. Phys. Lett.* 2006, 89, 193109.
  32. R. Beaulac, L. Schneider, P. I. Archer, G. Bacher, D. R. Gamelin, *Science* 2009, 325, 973.
  33. C. de Mello Donegá, S. G. Hickey, S. F. Wuister, D. Vanmaekelbergh, A. Meijerink, *J. Phys. Chem. B* 2003, 107, 489.
  34. C. de Mello Donegá, R. Koole, *J. Phys. Chem. C* 2009, 113, 6511.
  35. L. Manna, S. Kudera, 'Advanced Wet-Chemical Synthetic Approaches to Inorganic Nanostructures', P. D. Cozzoli (Ed.), Ch. 1, Kerala: Transworld Research Network, 2008.
  36. Y. Li, L. Wang, *Phys. Rev. B* 2005, 72, 125325.
  37. A. Eichhöfer, O. Hampe, *Chem. Phys. Lett.* 2005, 407, 186.
  38. M. H. Tsai, F. C. Peiris, S. Lee, J. K. Furdyna, *Phys. Rev. B* 2002, 65, 235202.
  39. S. A. Santangelo, E. A. Hinds, V. A. Vlaskin, P. I. Archer, D. R. Gamelin, *J. Am. Chem. Soc.* 2007, 129, 3973.
  40. E. Groeneveld, 'Synthesis and optical spectroscopy of semiconductor (hetero)nanocrystals: an exciting interplay between chemistry and physics', Ch 3, (Ph.D. Thesis), Utrecht University, Utrecht, 2012.
  41. E. Groeneveld, S. van Berkum, A. Meijerink, C. de Mello Donegá, *Small* 2011, 7, 1247-1256.
  42. E. Groeneveld, S. van Berkum, M. M. van Schooneveld, A. Gloter, J. D. Meeldijk, D. J. van den Heuvel, H. C. Gerritsen, C. de Mello Donegá, *Nano Letters* 2012, 12, 749-757.
  43. J. Eilers, E. Groeneveld, C. de Mello Donegá, A. Meijerink, *The Journal of Physical Chemistry Letters*, 2012, 3, 1663-1667.
  44. E. Groeneveld, 'Synthesis and optical spectroscopy of semiconductor (hetero)nanocrystals: an exciting interplay between chemistry and physics', Ch. 2, (Ph.D. Thesis), Utrecht University, Utrecht, 2012.





---

## Chapter 5

# Highly Luminescent (Zn,Cd)Te-CdSe Colloidal Heteronanowires with Tunable Electron-Hole Overlap

—

*From Small to Nano: Magic  
Clusters for Bright and Blinking  
Colloidal Nanowires*

## Abstract

*We report the synthesis of ultra-narrow (Zn,Cd)Te-CdSe colloidal heteronanowires, using ZnTe magic size clusters (MSCs) as seeds. The wire formation starts with a partial Zn for Cd cation exchange, followed by self-organization into segmented heteronanowires. Further growth occurs by inclusion of CdSe. The heteronanowires emit in the 530 nm to 760 nm range with high quantum yields. The electron-hole overlap decreases with increasing CdSe volume fraction, allowing the optical properties to be controlled by adjusting the heteronanowire composition.*

## 5.1 – Introduction

An essential feature of colloidal semiconductor nanocrystals (NCs) is that nanoscale size effects can be fully exploited to engineer the material properties without changing its composition. Semiconductor NCs comprising two (or more) different materials joined together by heterointerfaces, *i.e.*, heteronanocrystals (HNCs), offer even more exciting possibilities regarding property control.<sup>[1]</sup> The localization regime of photoexcited charge carriers in HNCs (*viz.*, type-I, type-I<sup>1/2</sup>, and type-II) is determined by the offsets between the energy levels of the materials that are combined at the heterointerface.<sup>[1]</sup> In the type-I regime (enclosed alignment) both charge carriers are localized in the same material, whereas in the type-II regime (staggered alignment) the electron and hole are primarily localized in different materials, *i.e.*, in different segments of the HNC. This spatial separation of the electron and hole wave functions leads to the formation of a spatially indirect exciton. In the type-I<sup>1/2</sup> (or *quasi*-type-II) regime the offsets are such that one carrier is localized in one of the HNC components while the other is delocalized over the HNC.<sup>[1]</sup>

Since the energy levels of semiconductor NCs are strongly size- and shape-dependent, the energy offsets in HNCs can be tuned by controlling the composition, size and shape of each component. This allows the electron-hole spatial overlap to be tailored, leading to a remarkable degree of control over the properties of nanoscale excitons in colloidal HNCs.<sup>[1-5]</sup> For example, the rates for Auger recombination,<sup>[6]</sup> hot carrier relaxation,<sup>[4]</sup> and spin relaxation<sup>[5]</sup> have been observed to decrease as a result of the (partial) spatial separation of the photoexcited carriers. Further, control over the electron-hole overlap in type-II (and type-I<sup>1/2</sup>) HNCs has been used to tune the exciton radiative lifetimes,<sup>[3,6-8]</sup> the emission energies,<sup>[1,3,5,7,9]</sup> and the Stokes shifts<sup>[7]</sup> of colloidal semiconductor HNCs. This flexibility in tailoring the properties of HNCs has important consequences for a number of



potential applications (*e.g.*, low-threshold lasers, photovoltaic devices, solar energy conversion, optical switches, LED's, biomedical imaging, etc.),<sup>[1]</sup> and has attracted increasing attention, leading to the investigation of a number of compositions, such as CdTe-CdSe,<sup>[6,7,9-15]</sup> CdSe-ZnTe,<sup>[9,16,17]</sup> ZnTe-ZnSe,<sup>[18]</sup> ZnSe-CdS,<sup>[3,4,19,20]</sup> ZnTe-CdS,<sup>[20]</sup> and CdSe-CdS.<sup>[21,22]</sup>

ZnTe-CdSe is a promising semiconductor combination for type-II HNCs, because the energy offsets between the valence and conduction bands are rather large (*viz.*, 0.68 and 1.24 eV, respectively, for the bulk materials<sup>[23]</sup>). These large energy offsets facilitate the formation of spatially indirect excitons and should result in a wide tunability window for the electron-hole overlap in ZnTe-CdSe HNCs. In addition, the lattice mismatch between these two materials is small (0.8%).<sup>[24,25]</sup> ZnTe-CdSe heteronanostructures have been grown both by vapor phase epitaxial (VPE) deposition<sup>[26]</sup> and colloidal synthetic methods.<sup>[16-18]</sup> Despite the advantages of colloidal chemistry methods,<sup>[1]</sup> the development of ZnTe based colloidal HNCs has been slow, possibly hampered by the limited availability of high quality ZnTe NCs. Tetrapod shaped<sup>[17]</sup> and concentric nearly spherical<sup>[16]</sup> colloidal ZnTe/CdSe core/shell HNCs have been made, but the observed photoluminescence (PL) quantum yields (QYs) were low (<0.1% for heterotetrapods<sup>[17]</sup> and <30% for concentric core/shell HNCs<sup>[16]</sup>). Low PL QYs have been seen as an intrinsic limitation of type-II HNCs,<sup>[5]</sup> since the slower radiative recombination of indirect excitons can result in the dominance of faster non-radiative processes. However, recent work by a number of groups has demonstrated that the PL QYs of Type-II and Type-I<sup>1/2</sup> HNCs can be as high as those observed for Type-I HNCs (*viz.*, 50-80% for CdTe/CdSe and CdS/ZnSe HNCs).<sup>[3,7,14,15]</sup>

This chapter describes the synthesis and optical properties of highly luminescent ultra-narrow (~2 nm diameter) (Zn,Cd)Te-CdSe colloidal heteronanowires is organized as follows. First, the experimental methods are presented. Subsequently, the mechanism behind the formation of the heteronanowires is addressed. We show that the first step consists of a fast cation exchange, through which Zn is partially replaced by Cd. In the second step, the resulting hetero-magic-size-clusters (heter-MSCs) self-organize into segmented heteronanowires. Further growth occurs primarily by inclusion of CdSe into the heterojunctions between adjoining segments. After establishing the composition and structure of the heteronanowires, we turn to their optical properties. The evolution of the optical properties during the formation and growth of the heteronanowires clearly indicates

that the electron-hole overlap decreases with increasing CdSe volume fraction, shifting all exciton transitions to lower energies, and leading to longer exciton lifetimes and smaller spectral overlaps between PL and absorption.

## 5.2 – Experimental Methods

**Chemicals:** Hexadecylamine (HDA, 90%), anhydrous Triethylorthoformate (TEOF, 98%), anhydrous methanol and anhydrous toluene were purchased from Aldrich. Dodecylamine (DDA, 98%) was purchased from Acros Organics. Trioctylphosphine (TOP, tech. grade 90%), was purchased from Alrich (used for ZnTe MSCs) and Fluka (used for (Zn,Cd)Te-CdSe heteronanowires). Diethylzinc ( $\text{Zn}(\text{Et})_2$ , 98%) and Cadmium acetate dihydrate ( $\text{Cd}(\text{Ac})_2 \cdot 2\text{H}_2\text{O}$ , 99.99+%) were purchased from STREM Chemicals. Tellurium powder (99.999%,  $\leq 250$  micron) and Selenium powder (Se, 99.999%) were purchased from Alfa Aesar. All reagents were used as received with the exception of HDA and DDA. Before use, HDA and DDA were dried and degassed by heating under vacuum (3 h at  $100^\circ\text{C}$ ). For the ZnTe MSC synthesis the dried and degassed HDA was subjected to further pre-treatment in order to remove any residual moisture and alcohol impurities. This was done by adding TEOF (5.4 % (m/m)) to the pre-treated HDA at  $50^\circ\text{C}$  under a  $\text{N}_2$  atmosphere ( $< 5$  ppm  $\text{O}_2$  and  $\text{H}_2\text{O}$ ). This mixture was heated to  $220^\circ\text{C}$  and kept under reflux for  $\sim 30$  min. Subsequently, the mixture was degassed under vacuum (1 h,  $\sim 120^\circ\text{C}$ ) to remove residual TEOF and reaction products.

**Synthesis of ZnTe magic size clusters:** ZnTe magic size clusters were made following the method reported in reference [27]. The synthesis was performed in a glove-box under nitrogen ( $< 5$  ppm  $\text{O}_2$  and  $\text{H}_2\text{O}$ ). Stock solutions of  $\text{Zn}(\text{Et})_2$  and Te in TOP (0.54 M and 0.70 M, respectively) were used. HDA (36 g) was loaded in a reaction flask and heated to  $200^\circ\text{C}$ . At this temperature  $\text{Zn}(\text{Et})_2$  stock solution (3325  $\mu\text{L}$ ) was added. After 5 minutes, Te stock solution (1220  $\mu\text{L}$ ) was injected into the reaction mixture under stirring. The reaction temperature was kept constant and after 35 minutes the heating mantle was removed and subsequently 8 mL toluene was added to quench the reaction. When the temperature of the ZnTe reaction mixture dropped to  $80^\circ\text{C}$ , 46 mL of anhydrous toluene was added to the reaction flask. The ZnTe MSCs were precipitated by adding 64 mL of methanol to the resulting solution, isolated by centrifugation, and redispersed in 4.5 mL toluene.

**Synthesis of mixed ZnTe MSCs and small NCs seeds:** The synthesis of the seed mixture containing ZnTe MSCs (1.5 nm and 1.8 nm) and small ZnTe NCs (2 – 3 nm diameter) was carried out following exactly the same procedure described above, with the exception that HDA was used without treatment with TEOF.

**Synthesis of Heteronanowires:** The (Zn,Cd)Te-CdSe heteronanowires were synthesized by alternate addition of Cd and Se precursor solutions to a hot solution containing HDA (dried or degassed without TEOF) and the ZnTe seeds. The growth of the HNCs was followed by taking small aliquots (0.5 mL) from the reaction mixture at different time intervals. The synthesis was performed in a glove-box under nitrogen (< 5 ppm O<sub>2</sub> and H<sub>2</sub>O). A custom made aluminum block that allows for the simultaneous heating and stirring of four reaction flasks (20-40 mL) was used.

**Ultra-narrow (Zn,Cd)Te-CdSe heteronanowire synthesis:** Stock solutions of Cd(Ac)<sub>2</sub>·2H<sub>2</sub>O and Se in TOP (77 mM, and 88 mM, respectively) were used. For the heteronanowire synthesis 1 mL of the washed ZnTe MSC seed solution was added to 1.2 mL TOP and 0.125 g DDA. The concentration of the seed solution was monitored by absorption spectroscopy. The injection seed solution showed an absorbance of 0.25 at 330 nm after dilution by a factor of 500. HDA (5.5 g) was loaded in a reaction flask (20 mL) and heated to 165°C. At this temperature Se stock solution (2000 µL) was added under stirring. When the temperature recovered to 165°C the ZnTe MSC solution was added. The slow addition (during 4 minutes) of Cd stock solution (2000 µL) started 27 minutes after the addition of the seeds. The synthesis was stopped after 42 minutes by removing the heating mantle.

**(Zn,Cd)Te-CdSe heteronanowire synthesis (resulting in differently shaped HNCs):** Stock solutions of Cd(Ac)<sub>2</sub>·2H<sub>2</sub>O and Se in TOP (108 mM, and 129 mM, respectively) were used. For the synthesis, 3.1 g of the crude reaction mixture of the mixed ZnTe seeds were washed using a down-scaled version of the ZnTe MSC washing procedure described above. 2 mL of toluene, 0.25 g DDA, and 1.2 mL TOP were added to the sediment obtained after washing. HDA (5 g) was loaded in a reaction flask (40 mL) and heated to 165°C. At this temperature Se stock solution (1500 µL) was added under stirring. When the temperature recovered to 165°C the ZnTe seed solution was added. The slow addition (during 12 minutes) of Cd stock solution (1250 µL) started 43 minutes after the addition of the seeds. The synthesis was stopped after 78 minutes by removing the heating mantle.

**Separation of differently shaped (Zn,Cd)Te-CdSe heteronanocrystals:** The separation of the differently shaped (Zn,Cd)Te-CdSe heteronanocrystals obtained in the synthesis using mixed ZnTe MSCs and small NCs as seeds was carried out by dissolving the crude reaction mixture in toluene (1:1 volume ratio) and centrifuging the solution at 4000 rpm for 30 min. The sediment was collected and redispersed in THF. The heteronanocrystals in the supernatant were isolated via precipitation with methanol, followed by centrifugation, and redispersion in toluene.

**Optical Spectroscopy:** Absorption spectra were measured on a double beam Perkin-Elmer Lambda 16 UV/Vis spectrometer (scan rate: 1 nm/s). Emission spectra were recorded by using a Princeton Instrument Liquid N<sub>2</sub>-cooled CCD-detector and a 0.25 m Acton Research monochromator (150 lines/mm grating blazed at 550 nm). The excitation wavelength was selected from a 450 W Xe lamp by a double-grating monochromator (0.22 m, SPEX 1680). All measurements were performed at room temperature under N<sub>2</sub> atmosphere. Samples for optical measurements were prepared by directly dissolving the crude reaction mixture in anhydrous toluene under nitrogen. All measurements were carried out on samples with a low optical density ( $\leq 0.2$  at 300 nm).

**PL quantum yields (QY):** QY were determined using rhodamine 101 in 0.01% HCl ethanolic solution as a reference, following the method reported in reference<sup>[28]</sup>. PL decay curves were obtained by time-correlated single-photon counting via time-to-amplitude conversion, as previously described.<sup>[29]</sup> A Pico Quant PDL 800-B laser was used as the excitation source (406 nm, 55 ps pulse width, 0.2–20 MHz repetition rate). Very low excitation fluences were used (0.5 nJ/cm<sup>2</sup>) in order to avoid multiexciton formation, and to keep the ratio of stop to start pulses below 0.04. The raw decay data were fitted to decay functions using a Simplex minimization algorithm implemented in PICOQUANT FLUOFIT 4.4.

**X-Ray Diffraction (XRD):** XRD diagrams were obtained by using a PW 1729 Philips diffractometer, equipped with a Cu K<sub>α</sub> X-ray source ( $\lambda=1.5418 \text{ \AA}$ ). Samples for XRD analysis were prepared by depositing a concentrated solution of purified (Zn,Cd)Te-CdSe heteronanocrystals on a Si wafer substrate under inert atmosphere. The purification procedure consisted of precipitating the heteronanocrystals from a solution of the crude reaction mixture in toluene (1:1 volume ratio) by adding anhydrous methanol. The sediment was isolated by centrifugation (3000 rpm, 15 min), redissolved

in anhydrous toluene, and reprecipitated by adding anhydrous acetone. After centrifugation, the purified heteronanocrystals were suspended in anhydrous toluene.

**Inductively Coupled Plasma Mass Spectrometry (ICP-MS):** Elemental analysis of heteronanocrystal samples was carried out by ICP-MS. Samples for ICP-MS were purified in order to remove excess of organic molecules and unreacted precursors. The purification procedure is similar to that used for the XRD analysis, but included one additional dissolution/precipitation cycle.

**Transmission Electron Microscopy (TEM) and Energy Dispersive X-Ray Spectroscopy (EDS):** TEM and EDS measurements were performed on a Tecnai20F (FEI) microscope equipped with a Field Emission Gun, a Gatan 694 CCD camera and an EDAX spectrometer. The microscope was operated at 200kV. Acquisition time for EDS measurements was 30 s. High-Resolution TEM was performed using an aberration corrected JEOL FE2200 microscope operating at 300 kV. Samples for TEM imaging were prepared by dipping a carbon coated polymer film copper grid (300 mesh) into a toluene solution of purified (Zn,Cd)Te-CdSe heteronanocrystals. The excess liquid was removed by blotting with filter paper. The sample purification procedure was the same used for the XRD measurements (see above).

**Cryo-TEM:** Cryo-TEM images were made by preparing a frozen film of a heteronanocrystal solution on a grid with holey carbon film. The film was prepared by placing a droplet of a solution of purified heteronanocrystals in 75% decaline and 25 % toluene on the grid and using a VITROBOT to automatically blot the grid. Subsequently the film is instantly frozen by plunging the grid into liquid nitrogen. The grid is transferred to a Tecnai12 operated at 120kV using a Gatan 626 cryo-transfer holder.

**Electron Energy-Loss Spectroscopy (EELS):** EELS measurements were carried out on a Scanning Transmission Electron Microscope (VG-HB501) equipped with a tungsten cold field-emission gun. The beam convergence half angle was set to 7.5 mrad. This corresponds to the formation of the smallest possible electron probe (5 Å in diameter) at the sample surface with a current of approximately 0.1 nA. The half angle of collection was limited to 24 mrad. The post-column Gatan 666 parallel spectrometer<sup>[30]</sup> was operated with a dispersion of 0.05 eV per channel. EEL spectra were recorded with a two-dimensional charge-coupled device camera (1,340×100 pixels) optically

coupled to a scintillator in the image plane of the Gatan magnetic sector. The initial energy resolution of the EEL spectra is about 0.3–0.4 eV. Data were acquired in the so-called spectrum imaging mode. The sub-nanometer probe was scanned in 2D over the sample and an electron energy-loss spectrum in the core-loss region of 330–680 eV was acquired at each position of the probe. The dwell time was 500 ms per spectrum and a charge-coupled-device binning of 1x100 was used. The binning conditions were chosen as a compromise between a substantial signal-to-noise ratio and a reasonable acquisition time per spectrum image (with the present conditions, the acquisition time was a few min for 24x24 pixel 2D spectrum images with each pixel being 2x2 nm). Post-acquisition processing of the acquired data was done by using DigitalMicrograph software. Chemical maps were made by integrating electron intensities of ionization edges, while correcting for the material-unspecific inelastic scattering background. A typical energy range ( $\Delta E$ ) of ~70 eV was used from a region between -2 and +68 eV with respect to the determined ionization edges. In the probed core loss region the Cd and Te  $M_{4,5}$  edge start around 405 and 573 eV respectively<sup>[30]</sup>. The Zn and Se  $L_{2,3}$  edges, starting at approximately 1022 and 1434 eV fell outside the current microscope set range, and were not measured as a consequence. Electron energy spectra were obtained by performing a threshold operation on a chemical map and summing over all remaining pixels of the chemical map. Note that the spectral images were not corrected for the edge-specific partial inelastic scattering cross-sections. Although the cross-section for Cd in CdO is approximately an order of magnitude higher than that for metallic Te, estimated using a Hartree-Slater model included in the DigitalMicrograph software<sup>[30]</sup>, the absolute cross-sections for Cd and Te in our nanowires might exhibit variations of the same order of magnitude as a result of the different chemical environments.

**Single heteronanocrystal photoluminescence spectroscopy:** Samples for single particle spectroscopy were prepared by spin-coating diluted solutions of the nanocrystals onto glass slides under a nitrogen atmosphere. After complete solvent evaporation a cover slip was attached to the slides. To obtain the PL spectra of single heteronanocrystals we employed an objective-type TIRF (Total Internal Reflection Fluorescence) system based on an inverted microscope (Nikon, Eclipse TE2000-U) equipped with an oil-immersion objective (Nikon, plan apo 60x, numerical aperture 1.49). Samples were illuminated in TIRF-mode with an Argon laser (Spectra-Physics, model 161C-030). Excitation light was separated from the sample luminescence with a dichroic mirror (Nikon, B-2A), and photons were collected on an

EMCCD camera (Andor, IxonEM+ DU-897e) fitted with a band-pass filter (615-655 nm). Under these conditions, 1 pixel correlated to 182 nm. Cropped images (128x128 pixels) were recorded at 10 ms per frame. A stream of 200 frames is shown in the supporting movie of ref. [52]. Spectral imaging of single nanowires was performed employing a confocal laser scanning microscope (CLSM, Nikon PCM2000). A 473 nm diode laser (Becker&Hickel, BDL-473-SMC, operating in continuous mode) was used for excitation. The detection channels of the microscope were coupled by optical fibers to the detectors. One of the two standard detectors was replaced by a home-built spectrograph.<sup>[53]</sup> In the spectrograph, the light was dispersed by a prism, and detected with a Peltier-cooled, back-illuminated CCD camera (Princeton Instruments, NTE/CCD-1340). The spectral resolution varied between 1 and 7 nm, in the wavelength range from 450 to 750 nm. In the measurements presented in the paper, the emission was collected using a 60 x /1.4 oil immersion objective (NIKON, PlanApo) during a CLSM-scan with a pixel-dwell time of 3ms.

## 5.3 – Results and Discussion

### 5.3.1 – Formation mechanism of heteronanowires

The method reported here yields highly luminescent (PL QY = 20-60%) ultranarrow (~2 nm diameter) (Zn,Cd)Te-CdSe colloidal heteronanowires, with lengths up to ~100 nm (figure 5.1). The PL wavelength can be tuned from 530 to 760 nm by controlling the heteronanowire composition, which also strongly influences the exciton lifetimes and the spectral overlap between the absorption and emission (figure 5.2). The optical properties will be discussed in more detail later. We will first focus on the mechanism behind the formation of the nanowires. As described in the experimental section above the (Zn,Cd)Te-CdSe heteronanowires are prepared by a multistage seeded growth method in which ZnTe magic size clusters (MSCs) are used as seeds. The absorption spectrum of a typical sample of ZnTe MSC seeds is given in figure 5.1a. The narrow peaks (150 meV) observed in the spectrum are characteristic of MSCs,<sup>[27]</sup> and indicate that the sample consists primarily of ZnTe MSCs with a diameter of 1.5 nm (peak at 354 nm), accompanied by smaller populations of 1.3 nm and 1.8 nm diameter ZnTe MSCs (peaks at 330 nm and 378 nm, respectively).<sup>[27]</sup> These MSCs are characterized by the general formula  $[(\text{ZnTe})_n(\text{ZnL}_x)_m]$ , with  $(m+n)/n = 1.4$ ; L= Hexadecylamine,  $n \cong 19, 34$  and 48 for MSCs with 1.3 nm, 1.5 nm, and 1.8 nm diameter, respectively.<sup>[27]</sup> It is worth noting that each MSC family is essentially single-sized, since MSCs contain a well-defined number of atoms arranged in a particularly stable configuration.<sup>[27]</sup> In the second stage of the heteronanowire synthesis,

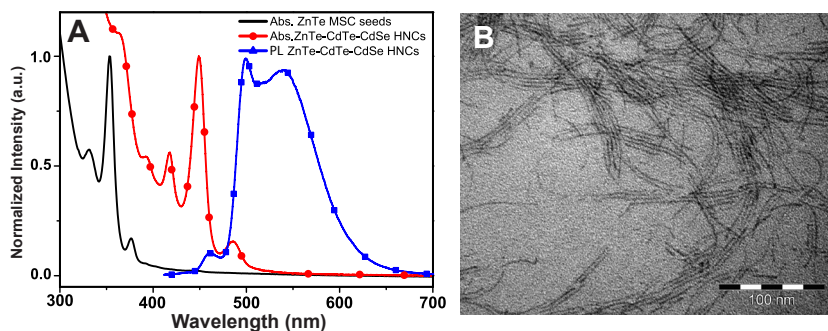


**Figure 5.1** – (a) Absorption (Abs) and photoluminescence (PL, excitation at 400 nm) spectra of (Zn,Cd)Te-CdSe colloidal heteronanowires obtained by using ZnTe magic size clusters (MSCs) as seeds. The absorption spectrum of the ZnTe MSC seeds is also shown. (b) Representative TEM image of the (Zn,Cd)Te-CdSe heteronanowire sample used to obtain the spectra shown in (a).

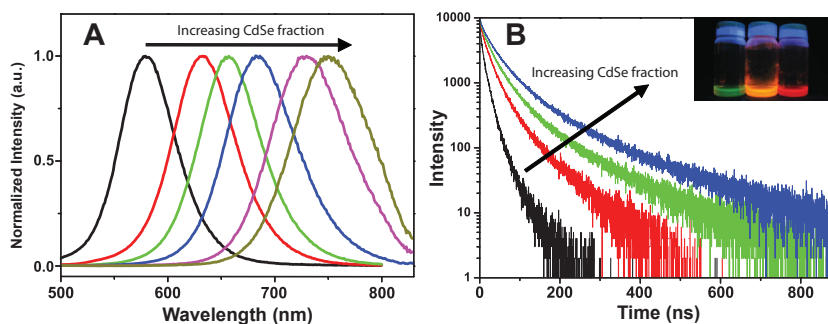


**Figure 5.2** – Photoluminescence (PL) spectra (a) and PL decay curves (b) of a series of (Zn,Cd)Te-CdSe colloidal heteronanowires with increasing CdSe volume fraction. The inset in (b) shows some of the (Zn,Cd)Te-CdSe colloidal heteronanowire samples under UV (365 nm) excitation



purified ZnTe MSC seeds are added to a hot (165°C) coordinating solvent, containing hexadecylamine (HDA), trioctylphosphine (TOP), and the Selenium precursor (Se dissolved in TOP). The final stage consists of the dropwise addition of the Cd precursor (anhydrous cadmium acetate in TOP) to the reaction mixture at 165°C. As an illustrative example, figure 5.1 presents the absorption and PL spectra and a representative TEM image of the final sample after one Cd addition cycle. The sample consists of narrow wires with a diameter of 2 nm and length ranging from ~20 nm to ~100 nm.

To investigate whether ZnTe MSCs are required for the heteronanowire formation, syntheses were performed using a mixture of ZnTe MSCs and small NCs as seeds. The absorption spectra of both the seeds and the final HNC sample for a representative synthesis are shown in figure 5.3. The seeds consist of 1.5 nm ZnTe MSCs (peak at 354 nm) accompanied by a small population of 1.8 nm ZnTe MSCs (peak at 378 nm) and small ZnTe NCs ranging from 2 to 3 nm in diameter (absorption tail from 395 nm to 420 nm). A pronounced shift of the optical transitions to lower energies takes place upon growth of the HNCs, regardless of the seeds used (figures 5.1 and 5.3). The differences between the absorption and PL spectra of the HNC samples shown in figures 5.1 and 5.3 can be ascribed to the larger CdSe volume fraction and larger shape (and size) distribution of the sample in figure 5.3. The relationship between the composition and the optical properties of the HNCs will be discussed in more detail later.

The most striking difference between the syntheses using the two different ZnTe seed populations is observed in the TEM images, which show that HNCs obtained from monodisperse MSC seeds consist of nanowires only (figure 5.1b), while nanowires and irregularly shaped “nearly isotropic” HNCs coexist in samples obtained from mixed seeds (figure 5.3b). Owing to the different solubilities of the two kinds of HNCs, shape selective precipitation was successfully used to separate them. Powder X-Ray diffraction analysis and TEM images of the two HNC fractions (figure 5.4) show that the “nearly isotropic” HNCs possess the zincblende structure and consist of irregularly shaped pyramids (~4 nm equivalent diameter) and short multipods (~5 nm long, ~2-3 nm diameter pods), while the nanowires have the wurtzite structure and are shorter (~50 nm) and slightly thicker (2.5 nm) than those obtained using monodisperse MSCs as seeds. These results show that the characteristics of the ZnTe NC seeds have a decisive role in the shape and crystal structure of the resulting HNCs. The formation of the irregularly shaped nearly isotropic HNCs can be explained

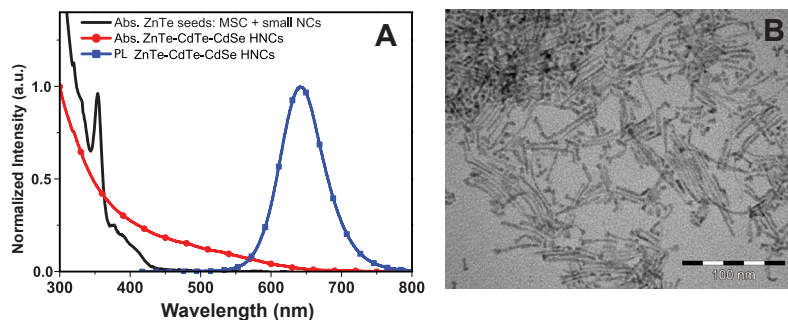


**Figure 5.3** – (a) Absorption (Abs) and photoluminescence (PL) spectra of the (Zn,Cd)Te-CdSe colloidal heteronanocrystal (HNC) sample shown in (b). The absorption spectrum of the ZnTe seeds is also given. (b) Representative TEM image of a (Zn,Cd)Te-CdSe heteronanocrystal sample prepared using mixed ZnTe magic size clusters (MSCs) and small nanocrystals (NCs) as seeds.

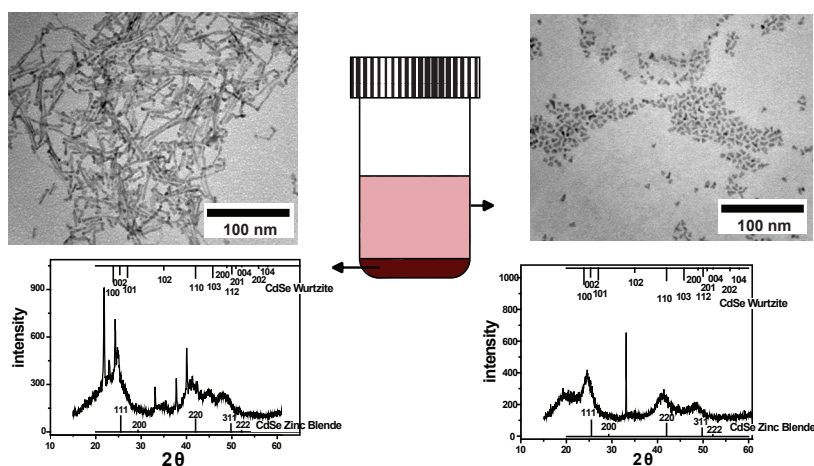


**Figure 5.4** – TEM images (top) and XRD diagrams (bottom) of the sediment (left panel) and the supernatant (right panel) isolated from the final sample of (Zn,Cd)Te-CdSe heteronanocrystals obtained in the synthesis using mixed ZnTe MSCs and small NCs as seeds.

by heteroepitaxial overgrowth on the small NC seeds, while the nanowires clearly require ZnTe MSCs as seeds. This is reflected in the higher quality and longer average length of the nanowires grown from monodisperse ZnTe MSCs as seeds (figure 5.1). A possible mechanism for the formation of (Zn,Cd)Te-CdSe heteronanowires from ZnTe MSCs will be proposed below. High resolution TEM (figure 5.5) confirms the crystallinity of the nanoparticles and shows that many of the heteronanowires grown using mixed ZnTe seeds contain larger segments that resemble the irregularly shaped nearly isotropic HNCs. In several cases the lattice planes in these segments show a different orientation with respect to the adjoining wire segments. Further, the diameter of the nanowires is not constant throughout their length, but oscillates between 1.8 and 2.5 nm, even in the well-formed nanowires obtained from monodisperse ZnTe MSC seeds. It is also clear that the orientation of the fringe patterns varies along the nanowires, sometimes substantially. These observations suggest that the nanowires grow by self-organization of shorter segments into successively longer wires, possibly by oriented attachment. This offers a possible explanation for the imperfections and irregularities in the shape of the nanowires, which are particularly pronounced in the wires grown using the mixture of ZnTe MSCs and small NCs as seeds. Attachment of an irregularly shaped nearly isotropic HNC to a growing nanowire would either disrupt the assembly process, leading to shorter and headed wires, or change the growth direction, leading to malformed wires (L-shaped,  $\Pi$ -shaped, etc.) with thicker segments. Further, imperfect alignment of the nanowire segments during the attachment could account for the changes observed in the orientation of the fringe patterns along the length of the wires.

Self-organization of smaller NCs by oriented attachment has been proposed to explain the formation of nanowires of a number of different materials<sup>[1]</sup> For example, under suitable conditions, colloidal CdTe NCs have been observed to spontaneously assemble into CdTe nanowires.<sup>[31]</sup> Further, the formation of ultra-narrow colloidal nanowires (1.3 – 1.6 nm diameter) from MSCs has been reported for both ZnSe<sup>[32]</sup> and CdSe.<sup>[33,34]</sup> The diameter of the nanowire is determined by the parent NC or MSC, while its length depends on the number of attached units and varies widely.<sup>[1,31-34]</sup> Oriented attachment has also been shown to be involved in the growth of long (>10 nm) CdSe nanorods.<sup>[35]</sup> To exclude the possibility that the presently observed self-organization is due to drying effects, cryo-TEM measurements were performed on samples obtained using monodisperse ZnTe MSCs as seeds. The cryo-TEM images (figure 5.6a) clearly show string-like aggregates of

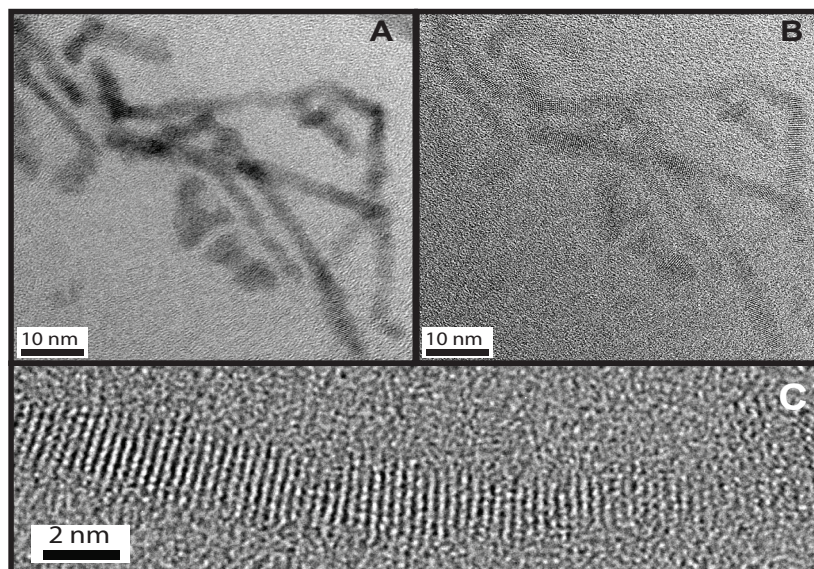


**Figure 5.5** – (a,b) HR-TEM image of (Zn,Cd)Te-CdSe heteronanocrystals prepared using mixed ZnTe magic size clusters and small nanocrystals as seeds. (c) HR-TEM image of part of a (Zn,Cd)Te-CdSe heteronanowire showing that the orientation of the lattice fringes changes along the length of the nanowire.

short wires ( $\sim 20$  nm long) with equal diameter ( $\sim 2$  nm) and variable lengths. The nanowires degrade quickly under electron beam irradiation (figure 5.6b). It is thus possible that the nanowire fragmentation observed in the cryo-TEM images is partially due to the electron beam irradiation.

Key questions that emerge in the present case are whether the parent units involved in the formation of the heteronanowires are already heterostructured, and whether the original ZnTe MSC seeds are preserved in the HNC. To address these questions the composition of the nanowires must be known. Compositional mapping by scanning TEM energy dispersive X-Ray spectroscopy (STEM-EDS) failed to provide information on the elemental profile of individual nanowires, since the wires experienced fast degradation upon exposure to the electron beam. This required the use of low-dose electron beams, which resulted in poor signal to noise ratios at the single nanowire level. Therefore, EDS analyses were performed only on wider areas ( $\sim 10^4 - 10^5$  nm<sup>2</sup>), encompassing  $\sim 100$  to  $\sim 1000$  HNCs (figure 5.7). The composition of the HNCs was also analyzed by inductively coupled plasma

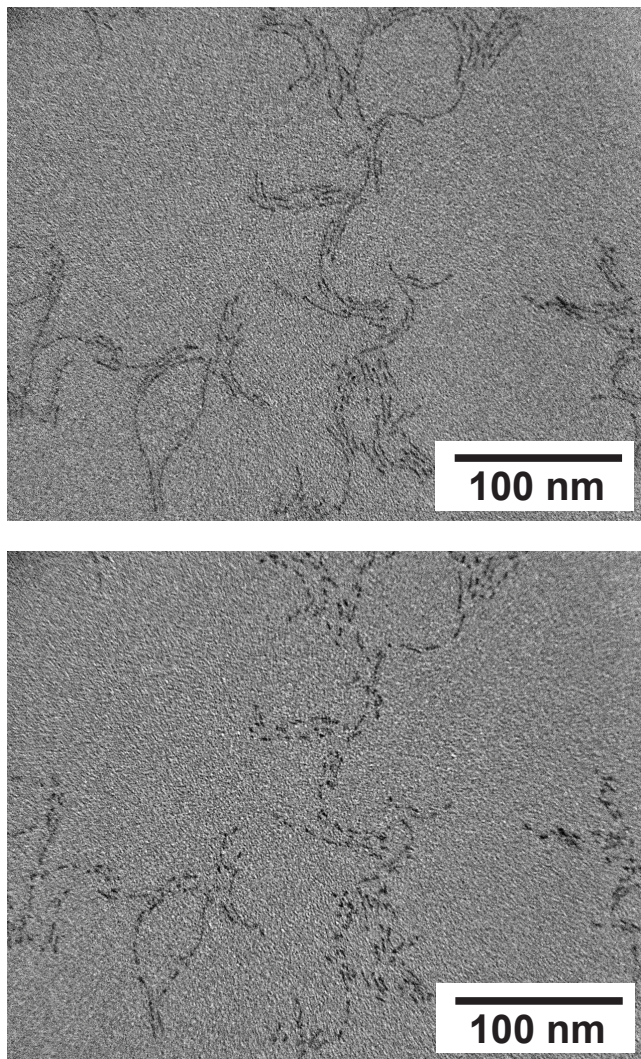


**Figure 5.6** – (a) and (b) are TEM images of the same spot on a Cryo-TEM grid containing the (Zn,Cd)Te-CdSe heteronanocrystals. The image in (b) is taken a few minutes after the image in (a).

mass spectrometry (ICP-MS). A sample of HNCs obtained from mixed ZnTe seeds (similar to that shown in figure 5.3) was also analyzed by scanning TEM electron energy loss spectroscopy (STEM-EELS) (figure 5.8). In order to maximize the resolution, only the Cd and Te edges were analyzed, since inclusion of Zn and Se as well would require probing a wider energy window.

The elemental concentrations (at%) determined by EDS for the HNC sample shown in figure 5.3 are  $(45.1 \pm 4.3)\%$  for Cd,  $(9 \pm 4)\%$  for Zn,  $(15.7 \pm 0.5)\%$  for Te, and  $(30.1 \pm 2.3)\%$  for Se (average over several observation spots). The Zn content is less reliable for two reasons. First, the Zn and Cu EDS peaks partially overlap (see figure 5a), which introduces a larger uncertainty in the estimated Zn intensities. Second, the variation in the Zn content between different observation spots is much larger than that for the other elements, implying the presence of an additional Zn compound in the samples examined by TEM. Most likely, the additional Zn originates from  $\text{Zn}(\text{HDA})_x$  complexes formed in the early steps of the nanowire growth (see below). These complexes can only be removed by repeated washing cycles, which also lead to removal of surfactant molecules, causing aggregation and loss of solubility. Therefore, samples for TEM analysis cannot be extensively washed. The loss of solubility is not a problem for ICP-MS analysis and therefore samples analyzed by this technique could be thoroughly washed, resulting in more reliable elemental concentration values for Zn.

To allow comparison between the compositions determined by EDS and ICP-MS it is convenient to express both as elemental ratios relative to the Te content (the element with the smallest standard deviation in the EDS analysis, *viz.*, 3%). The relative elemental ratios for the HNCs shown in figure 5.3 are then found to be 0.27 for Zn (taking the smallest value determined),  $2.9 \pm 0.3$  for Cd, and  $1.9 \pm 0.2$  for Se by EDS, and 0.2 for Zn, 2.9 for Cd, and 1.8 for Se by ICP-MS (Te content set to 1.0 in both cases). For the heteronanowire sample shown in figure 5.1 the relative elemental ratios are 0.29 for Zn (taking the smallest value determined), 2.3 for Cd, and 1.6 for Se by EDS, and 0.2 for Zn, 2.35 for Cd, and 1.50 for Se by ICP-MS. The agreement between the relative elemental ratios determined by EDS (average over  $10^2 - 10^3$  HNCs) and ICP-MS (average over  $10^{14} - 10^{15}$  HNCs) is very good, implying that the compositional fluctuations within the HNC ensemble are not very large (<15%).

Cation exchange has recently emerged as a versatile and attractive strategy to fabricate shape-controlled HNCs and NCs that are not attainable by

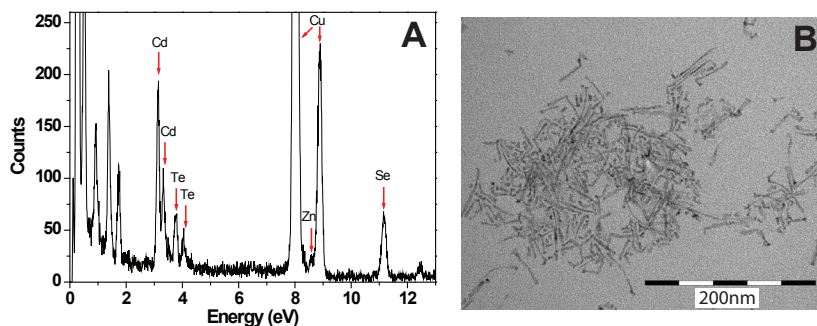


**Figure 5.7** – Energy dispersive X-ray spectrum (a) and TEM image (b) of a group of (Zn,Cd)Te-CdSe heteronanocrystals selected for elemental analysis.

conventional methods,<sup>[1,36-40]</sup> and has successfully yielded a number of novel HNCs (e.g., PbSe/CdSe core/shell QDs,<sup>[37,40]</sup> PbSe/PbS dot core/rod shell heteronanorods,<sup>[38]</sup> CdSe/CdS hetero-octapods<sup>[39]</sup>). The common feature in all these synthetic schemes is the utilization of ion exchange reactions to replace the native cationic sublattice with different ions, while preserving the anionic framework.<sup>[1,36-39]</sup> The cation exchange reactions are driven by the different solubilities of the incoming and outgoing ions, and can thus be tuned by choosing suitable solvents and ligands.<sup>[36,38,41]</sup> The Zn<sup>2+</sup> by Cd<sup>2+</sup> place exchange reaction observed here is probably driven by the higher stability of Zn<sup>2+</sup> complexes with both HDA molecules and acetate anions.<sup>[1]</sup> The cation exchange rates have been observed to strongly depend on the particle size. For example, under the same reaction conditions, the Ag<sup>+</sup> for Cd<sup>2+</sup> exchange has been shown to be virtually absent for micrometer-sized CdSe particles over a period of weeks, but to occur in less than a second for 5 nm diameter CdSe NCs and in ~10 h for 100 nm long CdSe wires.<sup>[36]</sup> The present observation of Zn<sup>2+</sup> for Cd<sup>2+</sup> exchange is thus not surprising considering the extremely small dimensions of the ZnTe MSCs used as seeds (1.3 – 1.8 nm diameter). However, it is quite remarkable that the exchange reaction does not reach completion in the time scale of our experiments (~1 h), but instead leads to (Zn,Cd)Te MSCs containing 20 mol% Zn, which corresponds to only a few ZnTe units per (Zn,Cd)Te MSC (*viz.*, ~ 4, 7, and 10 for the three seed MSC families with 1.3 nm, 1.5 nm and 1.8 nm diameter, respectively). This observation is in line with earlier studies of ion exchange processes in thiophenolate-capped metal chalcogenide clusters (*viz.*, [S<sub>4</sub>M<sub>10</sub>(SPh)<sub>16</sub>]<sup>4-</sup>, [S<sub>4</sub>M<sub>17</sub>(SPh)<sub>28</sub>]<sup>2-</sup>, M= Zn or Cd, Ph= phenyl), which showed that the metal exchange rates decrease for the atoms located toward the center

of the clusters, so that the reaction reaches equilibrium before completion.<sup>[42]</sup> Given that MSCs have very well-defined configurations,<sup>[27]</sup> all MSCs of a given family are expected to show essentially the same stability and reactivity, and thus similar cation exchange rates. However, different MSC families may show different exchange rates. Therefore, the Zn molar ratios reported here should be regarded as a weighted average between the Zn/Te ratios of all the different MSC families present in the reaction mixture.

The relative volume fractions of CdSe and (Zn,Cd)Te in the heteronanowire samples can be estimated from the elemental composition and the densities of the bulk materials, since the amount of Se is proportional to the fraction of CdSe, and the amount of Te reflects the fraction of (Zn,Cd)Te. This analysis shows that the heteronanowire samples contain similar volumes of CdSe and (Zn,Cd)Te (*viz.*, 55% CdSe, 45% (Zn,Cd)Te; and 60% CdSe, 40% (Zn,Cd)Te, for the samples shown in figures 5.1 and 5.3, respectively). This shows that the nanowires cannot consist of a single (Zn,Cd)Te head from which a long CdSe nanowire grows, since this would lead to much larger CdSe volume fractions.

The STEM-EELS measurements (figure 5.8) provide valuable insight in the distribution of CdSe and (Zn,Cd)Te at the single heteronanowire level. These measurements were carried out using an EELS spectrum imaging approach,<sup>[30]</sup> which means that at every pixel of the STEM image (figure 5.8a) a full EELS spectrum was recorded. From this, element-specific chemical maps were constructed for Cd and Te (figure 5.8c and 5.8d, respectively), which clearly show that Cd and Te are distributed throughout the HNCs and are present in all HNCs. Moreover, the Cd/Te elemental ratio map (figure 5.8b) shows that the Cd to Te ratio is not homogeneous throughout the HNCs, but instead exhibit modulations on a length scale of the order of the pixel size ( $\sim 2 \times 2 \text{ nm}^2$ ). These observations rule out that the wires consist of a (Zn,Cd)(Te,Se) homogeneous alloy or that (Zn,Cd)Te-rich and CdSe-rich nanowires co-exist in the same sample. This provides strong evidence that the nanowires are formed by assembly of (Zn,Cd)Te/CdSe segments that are heterostructured on a length scale of the order of 2 – 10 nm. As will be discussed later, this is consistent with the optical properties of the HNCs. However, the dimensions (both diameter and length) of the individual (Zn,Cd)Te and CdSe domains and the way they are organized within the various segments remain to be elucidated. For instance, it is possible that CdSe occurs both as single composition domains collinearly connected to (Zn,Cd)Te domains and as shells (partially) overcoating (Zn,Cd)Te



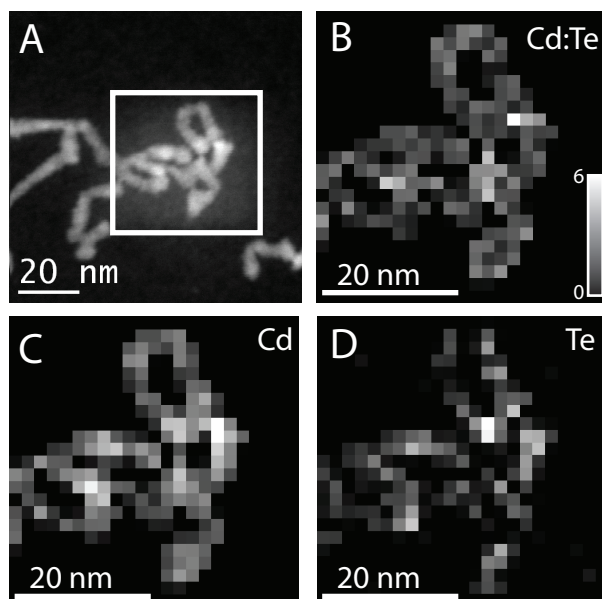


**Figure 5.8** – (a) STEM-HAADF image of (Zn,Cd)Te-CdSe heteronanocrystals. The square indicates the region selected for EELS analysis. The Cd:Te elemental ratio map shown in (b) was constructed from the chemical maps for Cd (c) and Te (d).

sections of the nanowire. Nevertheless, our observations do not allow any quantitative conclusion in this respect. Moreover, the present results are also inconclusive regarding the compositional profile of the (Zn,Cd)Te domains of the hetero-segments, and it is as yet unclear whether they can be regarded as ZnTe/CdTe core/shell HNCs or (Zn,Cd)Te alloy NCs.

It is noteworthy that no spectral changes are observed after mixing the Se precursor and the ZnTe MSC seeds at the reaction conditions. It is only after the addition of the Cd precursor that pronounced spectral changes take place (*viz.*, appearance of PL and shift of the optical transitions to lower energies). To investigate the role of TOP-Se, a synthesis was performed in the absence of Se precursors, while keeping the Cd addition rates and other reaction conditions unchanged. Samples were collected 90 s and 10 min after Cd addition. Despite the absence of the Se precursor, the Cd addition immediately led to the appearance of PL and induced a pronounced shift of the optical transitions to lower energies (figure 5.9). Interestingly, the samples collected also consist of nanowires (figure 5.9b) with dimensions

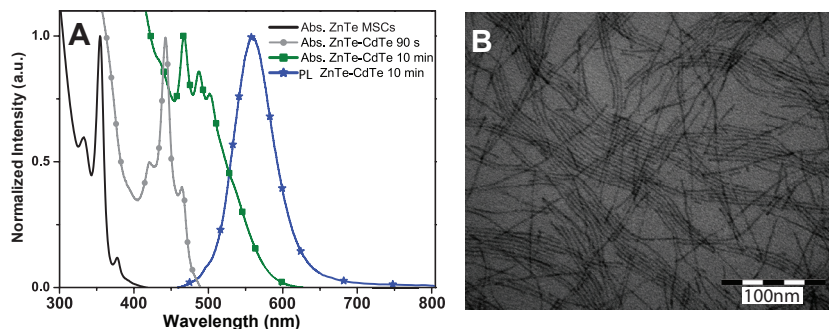


**Figure 5.9** – (a) Absorption (Abs) spectra of (Zn,Cd)Te colloidal heteronanowire samples collected 90 s and 10 min after Cd addition to ZnTe MSC seeds. The absorption spectrum of the ZnTe MSC seeds is also shown. For clarity, only the PL spectrum of the 10 min sample is shown, although the 90 s sample already displayed PL (peak at 500 nm). (b) Representative TEM image of a (Zn,Cd)Te heteronanowire sample collected 10 min after the addition of Cd precursor to ZnTe magic size cluster (MSC) seeds.

similar to those of the (Zn,Cd)Te-CdSe heteronanowires obtained in the presence of Se precursors (see above). The metal to Te ratio was found by ICP-MS to be 0.1 for Zn and 0.9 for Cd for the 90 s sample and 0.1 for Zn and 1.0 for Cd for the 10 min sample. This shows that the  $\text{Zn}^{2+}$  for  $\text{Cd}^{2+}$  place exchange reaction is very fast, reaching equilibrium already before 90 s. Further, as observed for the (Zn,Cd)Te-CdSe heteronanowires, the exchange is not complete, but reaches equilibrium for  $\text{Te}/\text{Zn} = 0.1$ . It is as yet unclear whether the differences between the equilibrium Zn content in the two syntheses reflect a synergistic interaction with the Se precursor or are simply due to experimental uncertainties (*e.g.*, reaction temperature, concentrations, etc.). To check whether Se can be incorporated at later reaction stages, Se precursor was added to the reaction mixture ~10 min after the addition of the Cd precursor. This led to a further shift of all the optical transitions to lower energies. The incorporation of CdSe is clearly evident from the elemental composition of the heteronanowires (*viz.*, Cd: 3.2; Zn: 0.1; Te: 1; Se: 1.85, by ICP-MS). It is interesting to note that the Te/Zn ratio remains constant, showing that Te for Se exchange does not occur.

The results presented above clearly establish that the first step in the formation of the colloidal heteronanowires prepared in this work consists of a fast  $\text{Zn}^{2+}$  for  $\text{Cd}^{2+}$  place exchange that converts the parent ZnTe MSCs

into (Zn,Cd)Te MSCs, while preserving the cluster configuration (figure 5.10). The (Zn,Cd)Te MSCs self-organize into strings, which subsequently undergo fusion forming segmented nanowires. Considering that both (Zn,Cd)Te and (Zn,Cd)Te-CdSe heteronanowires are obtained, it is clear that Se is not required for the nanowire formation. This implies that the ability to self-organize into nanowires is inherent to the (Zn,Cd)Te MSCs. The driving force for this self-organization process remains to be elucidated. It is generally accepted that self-organization by oriented attachment is driven by dipolar interactions between the parent units, even though in most cases the origin of these putative dipole moments remains unclear.<sup>[1]</sup> In the present case, the dipolar interactions could be the result of an asymmetry in the distribution of disparate ligands (long and neutral HDA *vs.* small and charged acetate molecules) among the binding sites in the (Zn,Cd)Te MSCs. It is also possible that the linear HDA molecules have an adjuvant role, facilitating the self-assembly into strings. Further growth of the nanowire occurs by incorporation of CdSe, which can occur both by growth of collinear domains inserted between adjoining segments (since the junctions between segments should be highly dynamic), and by overcoating of sections of the nanowire. This process results into segmented nanowires, in which the segments are heterostructured on short length scales with (Zn,Cd)Te and CdSe domains of the order of 2 - 10 nm.

### 5.3.2 – Evaluation of the optical properties

The heterostructured nature of the colloidal heteronanowires prepared in this work is clearly reflected in their optical properties. The (Zn,Cd)Te-CdSe (figures 5.1-5.3) and (Zn,Cd)Te (figure 5.9) nanowires are both highly luminescent, in striking contrast to the parent ZnTe MSCs. Reports on the luminescence of colloidal ZnTe NCs are scarce, possibly because the high-energy position of the band edges of ZnTe makes it difficult to efficiently passivate the surface atoms, since most ligands have energy levels below the band edges of (bulk) ZnTe.<sup>[27]</sup> This explains why in the present case PL appears immediately after the first Cd addition, reflecting the transformation from a Zn-terminated to a primarily Cd-terminated surface. The PL QYs of the heteronanowires are remarkably high (*viz.*, 20 - 60%), especially considering their large surface to volume ratio and heterostructured nature. Such high PL QYs indicate relatively slow nonradiative recombination rates, implying low defect concentrations and attesting the high-quality of the heteronanowires prepared by the presently reported method.

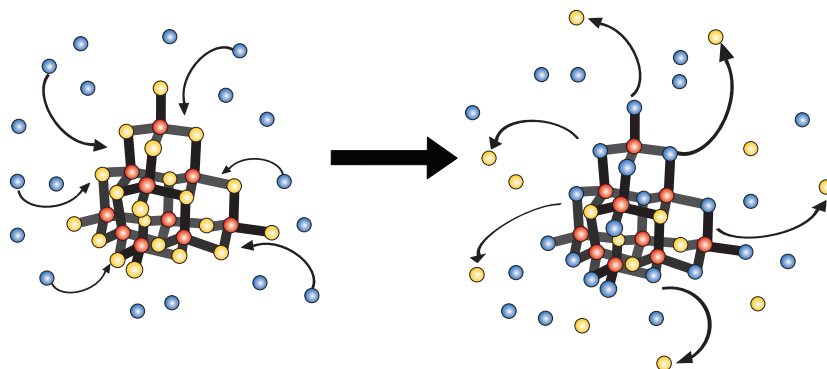


**Figure 5.10** – Schematic illustration of  $\text{Zn}^{2+}$  for  $\text{Cd}^{2+}$  cation exchange that converts the parent  $\text{ZnTe}$  MSCs into  $(\text{Zn,Cd})\text{Te}$  MSCs, while preserving the cluster configuration.

The PL of the  $(\text{Zn,Cd})\text{Te}$ -CdSe heteronanowires can be tuned from 530 nm to 760 nm by increasing the CdSe volume fraction (figures 5.1 and 5.2). The shift of the emission transition to lower energies is accompanied by an increase of the exciton lifetimes (*viz.*, from ~20 ns to 700 ns). The PL decay curves are multiexponential (see, *e.g.*, figure 5.2) and can be adequately described by a three-exponential fit (figure 5.11). The exciton radiative lifetime ( $W_{\text{RAD}}$ ) is taken to be equal to the longest component. The multiexponential character of the PL decay can be ascribed to a combination of factors. First, non-radiative recombination probably contributes to the decay rates at early times, since the PL QYs are non-unity, albeit high. Second, the segmented and heterostructured nature of the nanowires gives rise to an intra-nanowire energy transfer (ET) process, through which the exciton is transferred from segments with larger energy gaps to segments with smaller energy gaps. At earlier times the decay transients are thus dominated by the donor segments of the nanowires, which decay with a faster rate (*viz.*,  $W_{\text{RAD}} + W_{\text{ET}}$ ). At longer times only the acceptor nanowire segments with efficient PL (*i.e.*, negligible  $W_{\text{NRAD}}$ ) are observed.

In this context, it is interesting to note that the PL wavelength and the exciton radiative lifetimes of the differently shaped  $(\text{Zn,Cd})\text{Te}$ -CdSe HNCs obtained in the synthesis using mixed  $\text{ZnTe}$  MSCs and NCs as seeds (*viz.*, heteronanowires and “nearly isotropic” HNCs, see above) are the same, despite the differences in shape and crystal structure. This observation strongly supports the occurrence of intra-nanowire ET processes in

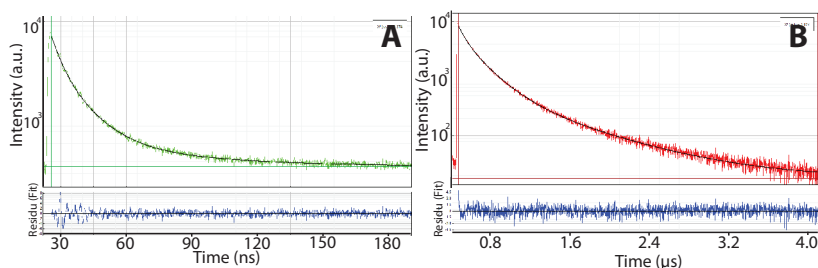


**Figure 5.11** – PL decay curve and three-exponential fit of the (Zn,Cd)Te-CdSe heteronanowires. The lower panel shows the residuals (a) Heteronanowires emitting at 530 nm (figure 5.1.) The three decay constants are: 4.0 ns (Amplitude: 21%); 12.0 ns (Amplitude: 55%); and 46.0 ns (Amplitude: 24%) (b) Heteronanowires emitting at 750 nm (figure 5.2) The three decay constants are: 68.0 ns (Amplitude: 13%); 212.0 ns (Amplitude: 57%); and 730 ns (Amplitude: 30%).

the (Zn,Cd)Te-CdSe heteronanowires investigated here. As discussed above, “nearly isotropic” HNCs are incorporated in the heteronanowires during their assembly process when mixed ZnTe MSCs and NCs are used as seeds. Since the nearly isotropic HNCs are larger than the adjoining heteronanowire segments, they will function as energy acceptor segments after the photoexcitation, thereby dominating the exciton radiative recombination. This intra-nanowire ET process is expected to occur also in regular heteronanowires, such as those shown in figure 5.1, since they consist of random assemblies of heterostructured segments. Segments that are richer in CdSe (for being slightly longer and/or thicker) will have smaller energy gaps (see discussion below), and will thus function as acceptor segments. ET processes have been extensively investigated in QD solids, and are usually assumed to be mediated by dipole-dipole interactions.<sup>[43,44]</sup> ET by exchange interaction is usually neglected for QD solids since it requires very small donor-acceptor distances.<sup>[44]</sup> In the present case, both mechanisms may be active, since the heteronanowire segments are in direct contact.

The evolution of the optical properties of the (Zn,Cd)Te-CdSe heteronanowires as a function of their composition follows the same overall trend previously observed for CdTe-CdSe HNCs.<sup>[7]</sup> The increase in the CdSe volume fraction results in a progressive shift of all optical transitions to lower energies, accompanied by a decrease of the oscillator strengths at emission energies and an increase of the exciton radiative

lifetimes. The radiative exciton lifetimes become longer than those of CdTe or CdSe QDs emitting at similar wavelengths (*viz.*, 15 – 60 ns in the 2.3 – 1.75 eV range<sup>[45]</sup>). For example, the exciton radiative lifetime observed for the (Zn,Cd)Te-CdSe heteronanowire sample shown in figure 5.2 with PL peak at 750 nm is one order of magnitude longer than that of a CdTe QD emitting at similar energies (figure 5.11b). These observations indicate that the overlap between the electron and hole wavefunctions decreases as the CdSe volume fraction in the (Zn,Cd)Te-CdSe heteronanowires increases, as a result of an increasingly larger spatial separation. In the CdTe-CdSe system, it has been demonstrated that the hole localizes in the CdTe part of the HNC already for small CdSe volume fractions, so that the evolution of the optical properties is primarily determined by the localization regime of the electron.<sup>[7]</sup> The electron wavefunction is initially delocalized over the whole HNC and gradually localizes in the CdSe part as its volume fraction increases. In the present system, a similar situation is expected, with the hole localized in the (Zn,Cd)Te domains, since the bulk valence band potentials of ZnTe and CdTe are essentially the same.<sup>[1]</sup> (Zn,Cd)Te homogeneous alloys behave as single composition materials with band potentials intermediate to those of ZnTe and CdTe, while the offset between the conduction bands of bulk ZnTe and CdTe is such that the electron localizes in CdTe.<sup>[1]</sup> Therefore, it can be expected that the electron localization in the CdSe domains of the heteronanowires will be facilitated in the (Zn,Cd)Te-CdSe system, regardless of whether the (Zn,Cd)Te domains behave electronically as ZnTe/CdTe core/shell or (Zn,Cd)Te alloy NCs.

The onset of the type-II localization regime has been shown to be characterized by the loss of structure of the lowest energy absorption band, accompanied by a simultaneous increase in the Stokes shift values and transition linewidths.<sup>[7]</sup> Based on these spectral signatures, we can conclude that in the present system the type-II regime is achieved only for the final samples of the synthesis using mixed ZnTe MSCs and NCs as seeds (see, *e.g.*, figure 5.3). The (Zn,Cd)Te-CdSe heteronanowires obtained by using only ZnTe MSCs as seeds (see, *e.g.*, figure 5.1) are still in the Type-I<sup>1/2</sup> localization regime, as clearly evidenced by the narrow peaks, absence of Stokes shift and reasonably short exciton lifetime (*viz.*, 46 ns, figure 5.11a). The emission spectrum of this sample consists of a combination of narrow peaks and a broad band (figure 5.1). The narrow peaks are resonant with the lowest two peaks in the absorption spectrum and can thus be ascribed to the recombination of a direct exciton (type-I<sup>1/2</sup> regime) in two types of heteronanowires (or segments thereof) that differ slightly in composition

and/or diameter. The excitation spectra of the broad PL band and of the lowest energy narrow PL peak are the same, indicating that the two emitting states share a common excitation channel. This may be attributed to an intra-nanowire energy transfer process involving segments with different degrees of electron-hole overlap, with the broad band originating from the segment with the larger degree of spatial separation.

Interestingly, the absorption spectrum of the heteronanowires obtained by using only ZnTe MSCs as seeds (figure 5.1a) is very similar to that of the parent MSCs, despite a ~750 meV shift to lower energies. As discussed above, this large shift in the transition energies is due to the dramatic change in composition that results from the conversion of ZnTe MSCs to  $(\text{Zn}_{0.2}\text{Cd}_{0.8})\text{Te}/(\text{CdSe})_{1.5}$  heteronanowires. The band width of the absorption peaks is even narrower (95 meV) than that of the parent ZnTe MSCs (150 meV). Considering that the exciton transition energies in quantum confined systems are strongly dependent on the composition and size of the nanostructure,<sup>[1]</sup> the observation of such narrow linewidths for an ensemble of nanowires in the strong quantum confinement regime (exciton Bohr radii are 7.3 nm and 4.9 nm for CdTe and CdSe, respectively<sup>[45]</sup>) implies a narrow distribution in the diameter and composition of the heteronanowire segments. The observation of three narrow peaks is consistent with the fact that the parent ZnTe MSC's consisted of three different families, implying that only three well-defined families of (Zn,Cd)Te MSC's were obtained after the  $\text{Zn}^{2+}$  for  $\text{Cd}^{2+}$  place exchange reaction.

To further investigate the degree of compositional homogeneity within an ensemble of (Zn,Cd)Te-CdSe heteronanowires, the PL spectra of a number of individual nanowires were measured at room temperature. A detailed discussion of the single heteronanowire PL spectra lies beyond the scope of this Chapter and will be presented elsewhere. Here we will focus on the extent to which these measurements provide information over the compositional distribution within the HNC ensemble. The heteronanowires clearly display fluorescence intermittency ("on-off" behavior or blinking) (figure 5.12 and Movie S1 in the supporting info of ref. [52]). Although the fluorescence intermittency mechanism is still not fully understood, it is well established that blinking provides unequivocal evidence that the observed emission originates from a single fluorophore.<sup>[46-48]</sup> The PL spectra of a number of single heteronanowires are shown in figure 5.12. It is clear that the spectral distributions for all the observed heteronanowires are similar. This is remarkable, and can be understood by considering that each

nanowire consists of a large number of (Zn,Cd)Te-CdSe heterostructured segments. Given that the segments are not identical, each nanowire can be seen as a collection of single fluorophores. Because the number of segments per nanowire is large in comparison to the distribution of energy gaps of the available building segments, each heteronanowire will likely contain a sufficiently large diversity of emitting domains to reflect the ensemble distribution. Therefore, the time-integrated PL peak of a single heteronanowire will be close to the ensemble average.

#### 5.4 – Conclusions

In conclusion, we presented a facile synthetic approach to prepare ultra-narrow (Zn,Cd)Te-CdSe and (Zn,Cd)Te colloidal segmented heteronanowires with  $\sim 2$  nm in diameter and up to 100 nm long. The utilization of ZnTe MSCs as seeds is shown to be essential for the heteronanowire formation. The first step in the formation mechanism consists of a fast cation exchange, through which Zn atoms are partially replaced by Cd. In the second step, the resulting (Zn,Cd)Te MSCs self-organize into segmented nanowires. Further growth of the heteronanowire occurs by inclusion and/or deposition of CdSe. The wires are highly luminescent and emit in the 530 nm to 760 nm range. The optical properties can be controlled by adjusting the nanowire composition. The results show that by increasing the CdSe volume fraction of the heteronanowires the electron-hole overlap is reduced, leading to longer exciton lifetimes and smaller spectral overlaps

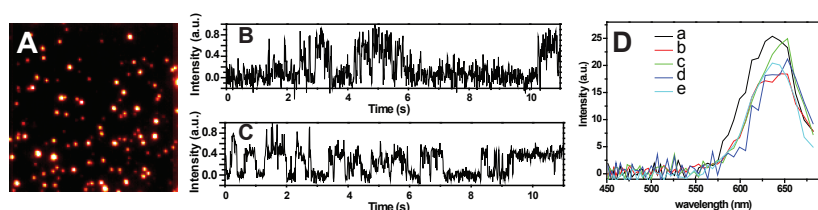


**Figure 5.12** – (a) Photoluminescence (PL) microscopy image of a diluted ensemble of (Zn,Cd)Te-CdSe heteronanocrystals spin-coated on a glass surface (128x128 pixels, 1 pixel =182 nm). The image is an integrated stack of 1000 single frames (10 ms exposure/frame). A stream of 200 frames is shown in the Supporting Information (Movie S1) of ref. [52]. The heteronanocrystals clearly display fluorescence intermittency. Representative PL time traces for selected regions are depicted in (b) and (c). (d) PL spectra of selected regions.



between PL and absorption, and shifting all exciton transitions to lower energies. Semiconductor nanowires hold great promise for applications in photovoltaics, solid-state lighting, solar energy conversion and photonics. <sup>[49-51]</sup> The colloidal heteronanowires reported here are potentially interesting as active elements in light harvesting and photovoltaic devices, since the combination of large surface to volume ratio and partial electron-hole spatial separation may greatly facilitate carrier extraction. In addition, this work raises a number of interesting issues that merit further investigation. First, the exact compositional and structural profiles of the heteronanowires have yet to be unraveled. Further, the extent to which the different nanowire segments are electronically coupled remains to be elucidated. Moreover, the impact of the combined effects of shape anisotropy, wire segmentation, strong quantum confinement, and (partial) carrier separation on a number of properties (*e.g.*, Auger recombination, carrier and spin relaxation rates, emission polarization, etc.) has yet to be evaluated.

## REFERENCES

1. C. de Mello Donegá, *Chem. Soc. Rev.* 2011, 40, 1512-1546.
2. P. Reiss, M. Protière, L Li, *Small* 2009, 5, 154-168.
3. S. A Ivanov, A. Piryatinski, J. Nanda, S. Tretiak, K. R. Zavadil, W. O. Wallace, D. Werder, V. I. Klimov, *J. Am. Chem. Soc.* 2007, 129, 11708-11719.
4. A. Pandey, P. Guyot-Sionnest, *Science* 2008, 322, 929-932.
5. S. S. Lo, T. Mirkovic, C. Chuang, C. Burda, G. D. Scholes, *Adv. Mater.* 2011, 23, 180-197.
6. D. Oron, M. Kazes, U. Banin, *Phys. Rev. B.* 2007, 75, 035330.
7. C. de Mello Donegá, *Phys. Rev. B.* 2010, 81, 165303.
8. S. Brovelli, R. D. Schaller, S. A. Crooker, F. Garcia-Santamaria, Y. Chen, R. Viswanatha, J. A. Hollingsworth, H. Htoon, V. I. Klimov, *Nature Comm.* 2011, 2, 280.
9. S. Kim, B. Fisher, H.-J. Eisler, M. G. Bawendi, *J. Am. Chem. Soc.* 2003, 125, 11466-11467.
10. J. E. Halpert, V. J. Porter, J. P. Zimmer, M. G. Bawendi, *J. Am. Chem. Soc.* 2006, 128, 12590-12591.
11. H. Zhong, G. D. Scholes, *J. Am. Chem. Soc.* 2009, 131, 9170-9171.
12. A. Fiore, R. Mastria, R. M. G. Lupo, G. Lanzani, C. Giannini, E. Carlino, G. Morello, M. De Giorgi, Y. Li, R. Cingolani, L. Manna, *J. Am. Chem. Soc.* 2009, 131, 2274-2282.
13. B. Koo, B. A. Korgel, *Nano Lett.* 2008, 8, 2490-2496.
14. W. Zhang, G. Chen, J. Wang, B.-C. Ye, X. Zhong, *Inorg. Chem.* 2009, 48, 9723-9731.
15. P.T.K. Chin, C. de Mello-Donagá, S. S. van Bavel, S. C. J. Meskers, N. A. J. M. Sommerdijk, R. A. J. Janssen, *J. Am. Chem. Soc.* 2007, 129, 14880-14886.
16. R. Xie, X. Zhong, T. Basché, *Adv. Mater.* 2005, 17, 2741-2745.
17. R. Xie, U. Kolb, T. Basché, *Small* 2006, 2, 1454-1457.
18. J. Bang, J. Park, J. H. Lee, N. Won, J. Nam, J. Lim, B. Y. Chang, H. J. Lee, B. Chon, J. Shin, J. B. Park, J. H. Choi, K. Cho, S. M. Park, T. Joo, S. Kim, *Chem. Mater.* 2010, 22, 233-240.
19. N. N. Hewa-Kasakarage, P. Z. El-Khoury, A. N. Tarnovsky, M. Kirsanova, I. Nemitz, A. Nemchinov, M. Zamkov, *ACS Nano* 2010, 4, 1837-1844.
20. K. P. Acharya, R. S. Khnayzer, T. O'Connor, G. Diederich, M. Kirsanova, A. Klinkova, D. Roth, E. Kinder, M. Imboden, M. Zamkov, *Nano Lett.* 2011, 11, 2919-2926.
21. A. Sitt, A. Salant, G. Menagen, U. Banin, *Nano Lett.* 2011, 11, 2054-2060.
22. C. L. Choi, H. Li, A. C. K. Olson, P. K. Jain, S. Sivasankar, A. P. Alivisatos, *Nano Lett.* 2011, 11, 2358-2362.
23. D. C. G. van de Walle, J. Neugebauer, *Nature* 2003, 423, 626.

24. M. H. Tsai, F. C. Peiris, S. Lee, J. K. Furdyna, *Phys. Rev. B* 2002, 65, 235202.
25. S. A. Santangelo, E. A. Hinds, V. A. Vlaskin, P. I. Archer, D. R. Gamelin, *J. Am. Chem. Soc.* 2007, 129, 3973-3978.
26. I. R. Sellers, V. R. Whiteside, I. L. Kuskovsky, A. O. Govorov, B. D. McCombe, *Phys. Rev. Lett.* 2008, 100, 136405.
27. E. Groeneveld, S. van Berkum, A. Meijerink, C. de Mello-Donegá, *Small* 2011, 7, 1247-1256.
28. C. de Mello Donegá, S. G. Hickey, S. F. Wuister, D. Vanmaekelbergh, A. Meijerink, *J. Phys. Chem. B* 2003, 107, 489-496.
29. C. de Mello Donegá, M. Bode, A. Meijerink, *Phys. Rev. B* 2006, 74, 085320.
30. M. M. van Schooneveld, A. Gloter, O. Stephan, L. F. Zagonel, R. Koole, A. Meijerink, W. J. M. Mulder, F. M. F. de Groot, *Nature Nanotechnol.* 2010, 5, 538 – 544.
31. Z. Tang, N. A. Kotov, M. Giersig, *Science* 2002, 297, 237-240.
32. A. B. Panda, S. Acharya, S. Efrima, *Adv. Mater.* 2005, 17, 2471.
33. S. F. Riehle, R. Bienert, R. Thomann, G. A. Urban, M. Krüger, *Nano Lett.* 2009, 9, 514-518.
34. N. Pradhan, H. Xu, X. Peng, *Nano Lett.* 2006, 6, 720-724.
35. Z. Yu, M. A. Hahn, S. E. Maccagnano-Zacher, J. Calcines, T. D. Krauss, E. S. Alldredge, J. Silcox, *ACS Nano* 2008, 2, 1179-1188.
36. D. H. Son, S. M. Hughes, Y. Yin, A. P. Alivisatos, *Science* 2004, 306, 1009-1012.
37. J. M. Pietryga, D. J. Werder, D. J. Williams, J. L. Casson, R. D. Schaller, V. I. Klimov, J. A. Hollingsworth, *J. Am. Chem. Soc.* 2008, 130, 4879-4885.
38. P. K. Jain, L. Amirav, S. Aloni, A. P. Alivisatos, *J. Am. Chem. Soc.* 2010, 132, 9997-9999.
39. S. Deka, K. Miszta, D. Dorfs, A. Genovese, G. Bertoni, L. Manna, *Nano Lett.* 2010, 10, 3770-3776.
40. D. Grodzinska, F. Pietra, M. A. van Huis, D. Vanmaekelbergh, C. de Mello Donegá, *J. Mater. Chem.* 2011, 21, 11556-11565.
41. J. M. Luther, H. Zheng, B. Sadtler, A. P. Alivisatos, *J. Am. Chem. Soc.* 2009, 131, 16851-16857.
42. T. Lover, W. Henderson, G. A. Bowmaker, J. M. Seakins, R. P. Cooney, *Inorg. Chem.* 1997, 36, 3711-3723.
43. S. F. Wuister, R. Koole, C. de Mello Donegá, A. Meijerink, *J. Phys. Chem. B* 2005, 109, 5504-5508.
44. A. L. Rogach, T. A. Klar, J. M. Lupton, A. Meijerink, J. Feldmann, *Mater. Chem.* 2009, 19, 1208-1221.
45. C. de Mello Donegá, R. Koole, *J. Phys. Chem. C* 2009, 113, 6511-6520.
46. W. G. J. H. M. van Sark, P. L. T. M. Frederix, D. J. van den Heuvel, H. C. Gerritsen, A. A. Bol, J. N. J. van Lingen, C. de Mello Donegá, A. Meijerink, *J.*

- Phys. Chem. B 2001 , 105 , 8281 – 8284.
47. X. Wang, X. Ren, K. Kahen, M. A. Hahn, M. Rajeswaran, S. E. Maccagnano-Zacher, J. Silcox, G. E. Cragg, A. L. Efros, T. D. Krauss, *Nature* 2009, 459, 686-689.
  48. J. Zhao, G. Nair, B. R. Fisher, M. G. Bawendi, *Phys. Rev. Lett.* 2010, 104, 157403.
  49. B. Tian, T. J. Kempa, C. M. Lieber, *Chem. Soc. Rev.* 2009, 38, 16-24.
  50. R. Yan, D. Gargas, P. Yang, *Nature Photon.* 2009, 3, 569-576.
  51. A. I. Hochbaun, P. Yang, *Chem. Rev.* 2010, 110, 527-546.
  52. E. Groeneveld, S. van Berkum, M. M. van Schooneveld, A. Gloter, J. D. Meeldijk, D. J. van den Heuvel, H. C. Gerritsen and C. de Mello Donega, *Nano Letters* 2012, 12, 749-757.





## Chapter 6

# **Enhanced Exciton-Phonon Coupling in Colloidal Type-II CdTe-CdSe Heteronanocrystals**

---

*Shaking up the excitons*

## Abstract

*In this chapter, the observation of LO-phonon progressions in the low temperature (4.2 K) photoluminescence excitation spectra of different types of colloidal NCs is reported. The strength of the exciton-LO-phonon coupling at 4.2 K, as reflected by the Huang-Rhys parameter  $S$ , increases from CdSe QDs ( $S= 0.8-1.0$ ) to Type-I<sub>1/2</sub> CdTe/CdSe HNCs ( $S= 1.5$ ), and from these to Type-II CdTe/CdSe HNCs ( $S= 2.9$ ). This trend is explained by the decrease in the electron-hole wave function overlap that accompanies the gradual increase in the CdSe volume fraction in the HNCs. The decrease in the electron-hole overlap increases the exciton polarization, which in turn enhances the exciton-LO-phonon coupling via the Fröhlich interaction. The results provide novel insights in the nature of spatially indirect exciton transitions and show that compositional control of semiconductor heteronanocrystals can be used as a very effective tool to tailor the exciton-phonon coupling strength of nanoscale excitons.*

## 6.1 –Introduction

Colloidal semiconductor nanocrystals (NCs) have, as a result of quantum confinement effects, size and shape dependent properties.<sup>[1]</sup> Moreover, they offer the prospect of solution processing and easy control over surface functionality. Colloidal NCs consisting of two (or more) different semiconductors joined by heterointerfaces (*i.e.*, heteronanocrystals, HNCs) offer even more possibilities regarding property engineering.<sup>[1]</sup> The offsets between the energy levels of the materials that are combined at the heterointerfaces in HNCs can be tuned by controlling the composition, size and shape of each component, allowing the carrier localization regime to be controlled.<sup>[1]</sup> In Type-I HNCs the energy offsets are such that both carriers are confined in the same material (typically the core in core/shell HNCs). In contrast, the alignment between the energy levels of the different components in Type-II HNCs is staggered, leading to the formation of a spatially indirect exciton, in which the electron and hole wave functions are primarily localized in different segments of the HNC. In Type-I<sup>1/2</sup> HNCs one carrier is delocalized over the whole HNC while the other is localized in one of the components. Control over the energy offsets in HNCs thus allows the electron-hole spatial overlap to be tailored, yielding a remarkable degree of control over the properties of nanoscale excitons.<sup>[1-7]</sup>

These characteristics have turned semiconductor NCs and HNCs into promising materials for a variety of technologies, ranging from lighting and optoelectronics to biomedical imaging, photovoltaics and



thermoelectrics.<sup>[8,9]</sup> A comprehensive understanding of nanoscale excitons is a crucial prerequisite for all these potential applications. This has stimulated a vast research effort to unravel the fundamental properties of semiconductor nanostructures, leading to extensive investigations and great advances in the last few decades.<sup>[1,3,8-13]</sup> Phonons have a pervasive role in semiconductor materials, impacting on a wide variety of properties, such as charge carrier mobility, heat transport, exciton relaxation and lifetimes, and superconductivity.<sup>[14]</sup> The interaction between phonons and electrons (or excitons) in nanoscale semiconductors is expected to differ from that in bulk materials due to both quantum confinement effects on the excitonic energy levels and dimensional confinement of phonon modes.<sup>[14]</sup> The electron-phonon (el-ph) coupling is thus vital to our understanding of the properties of nanoscale systems. Coupling of the electron and/or hole to phonons provides an important energy relaxation pathway, being thus essential to a number of photophysical processes in semiconductor nanostructures (*viz.*, exciton and multiexciton relaxation dynamics, hot carrier cooling, carrier multiplication, interfacial charge separation, etc.)<sup>[2,3,10,12,13,15-18]</sup> El-ph coupling is also crucial for thermal transport processes,<sup>[19]</sup> and underpins the temperature dependence of both electron transport and non-radiative energy transfer processes in colloidal quantum dot (QD) superlattices.<sup>[20-22]</sup> Moreover, coupling to acoustic phonon modes determines the homogeneous linewidths of optical transitions and contributes to the resonant Stokes shift,<sup>[2,3]</sup> while coupling to longitudinal optical (LO) phonon modes has been observed to relax selection rules, yielding momentum-conserving optical transitions (*i.e.*, phonon-assisted transitions or phonon replicas) from the so-called “dark exciton states” in semiconductor QDs and quantum rods.<sup>[24-28]</sup> Interestingly, it has been recently proposed that coupling to low energy acoustic phonons transiently mix “dark” and “bright” exciton states,<sup>[29,30]</sup> thereby increasing the radiative decay rates of QDs, and leading to a pronounced temperature dependence of the exciton lifetimes below 20 K.<sup>[30]</sup>

The critical impact of the el-ph coupling on the properties of nanoscale excitons has spurred a large number of theoretical<sup>[31-37]</sup> and experimental<sup>[12,13,24,25,32,37-55]</sup> studies on the el-ph and the exciton-phonon (ex-ph) coupling strength in semiconductor NCs of a variety of materials, such as Si,<sup>[38]</sup> Ge,<sup>[39]</sup> CdS,<sup>[40]</sup> InP,<sup>[41]</sup> PbS,<sup>[42]</sup> ZnTe,<sup>[54]</sup> CdSe,<sup>[12,13,24,25,32,43-49]</sup> CdSe/ZnS,<sup>[28,44]</sup> CdSe/(Cd,Zn)S,<sup>[27,50,55]</sup> InAs/GaAs,<sup>[37,51,52]</sup> and (Ga,In)N/GaN.<sup>[53]</sup> To date, however, only single composition NCs and Type-I heterostructures have been addressed. A study of the ex-ph coupling in Type-II HNCs is still lacking,

despite the importance of these materials from both a fundamental and an applied viewpoints.<sup>[1-6]</sup> In this work, we address this need by investigating phonon-assisted transitions (LO-phonon replicas) in the low temperature (4.2 K) photoluminescence excitation (PLE) spectra of colloidal Type-I<sup>1/2</sup> and Type-II CdTe/CdSe HNCs. The relative intensities of the LO-phonon replicas are used to derive the Huang-Rhys parameter  $S$ , which reflects the strength of the ex-ph coupling. Colloidal CdTe/CdSe HNCs are chosen for this study for a number of reasons. First, highly luminescent colloidal CdTe/CdSe HNCs have become recently available,<sup>[56]</sup> and were thoroughly investigated by our group as a model system to unravel the formation of spatially indirect nanoscale excitons as a function of the size, shape, and composition of the HNC.<sup>[57]</sup> Second, CdTe and CdSe QDs are model systems themselves, being the most investigated and best understood colloidal QDs. In particular, the el-ph and ex-ph coupling strengths of CdSe NCs have been extensively investigated over the last two decades by a variety of experimental techniques,<sup>[12,13,24,25,32,43-49]</sup> including PLE and fluorescence line narrowing (FLN).<sup>[24-27]</sup> Colloidal CdSe QDs are therefore also investigated in this work as a reference for the ex-ph coupling strength. Our results clearly show that the ex-ph coupling strength increases with increasing spatial separation of the electron and hole wave functions.

## 6.2 – Experimental methods

**CdSe QDs:** In this work colloidal suspensions of organically capped CdSe QDs and CdTe/CdSe HNCs were investigated. Two different samples of CdSe QDs were used: 3 nm ( $\pm 10\%$ ) diameter spherical NCs capped with oleic acid (OA), and 4.3 nm ( $\pm 5\%$ ) diameter prolate (aspect ratio: 1.2) NCs capped with trioctylphosphineoxide (TOPO) and Hexadecylamine (HDA). TOPO-HDA capped CdSe QDs were synthesized as reported previously.<sup>[58]</sup> OA capped CdSe QDs were synthesized via an adaptation of the method reported by Qu and Peng.<sup>[59]</sup> Details of this adapted method are given below.

*TOPO-HDA capped CdSe QD synthesis:*

**Chemicals:** Anhydrous Cadmium acetate ( $\text{Cd}(\text{Ac})_2$ ) was synthesized from dimethylcadmium (99.99%, ARC Technologies) and acetic acid (99.99+%, Sial). Oleic acid (Tech., 90%), trioctylphosphine (TOP, 90%), trioctylphosphineoxide (TOPO, 90%), and 1-octadecene (ODE, 90%) were purchased from Aldrich. Selenium powder (Se, 99.999%), and octadecylamine (ODA, 90%) were purchased from Alfa Aesar and Fluka, respectively.

**Stock solutions:** A stock solution of cadmium oleate was made by heating a mixture of 0.32 g  $\text{Cd}(\text{Ac})_2$  and 1.86 g oleic acid in 16.4 mL (12.94 g) ODE

to 200°C under N<sub>2</sub> atmosphere. At this temperature Cd(Ac)<sub>2</sub> and oleic acid react to form cadmium oleate and acetic acid. The temperature was lowered to ~150°C when the reaction reached completion (colorless solution was obtained) and vacuum was applied during ~2 hours. The Se precursor stock solution was made by dissolving 0.11 g Se in 0.58 g TOP and 0.92 g ODE in a glove-box under nitrogen (< 5 ppm O<sub>2</sub> and H<sub>2</sub>O).

**Synthesis:** In a reaction flask, 2.62 g of Se stock solution, 0.54 g TOPO, and 1.64 g ODA, were heated to 300°C. At this temperature 2.6 g of Cd-oleate stock solution was injected into the reaction mixture under stirring. After 2 min the heating mantle was removed and the reaction mixture was allowed to cool down under stirring.

**CdTe/CdSe HNCs:** The colloidal CdTe/CdSe HNCs are capped by TOPO-HDA and were prepared by a multistage seeded growth approach described in detail previously.<sup>[56]</sup> Two different CdTe/CdSe HNC samples were used, both grown from the same batch of 2.6 nm diameter CdTe QD seeds: prolate Type-I<sup>1/2</sup> HNCs (4.4 nm long, 39% CdSe volume fraction, here on referred to as Type-I<sup>1/2</sup> CdTe/CdSe HNC), and bipod shaped Type-II HNCs (pod length: 8 nm; pod diameter: 2.9 nm; 88% CdSe volume fraction, here on referred to as Type-II CdTe/CdSe HNC) (Table 6.1, for further details). These two samples have been thoroughly investigated in previous works by our group.<sup>[56,57]</sup>

**Table 6.1.** Main characteristics of the colloidal CdTe/CdSe heteronanocrystal (HNC) samples used in this work. For TEM images and detailed optical spectroscopic properties the reader is referred to refs. [56,57].

Sample	PL peak (eV)	QY (%)	HNC dimensions <sup>b</sup> (nm)		V <sub>Nc</sub> (nm <sup>3</sup> )	V <sub>fr(CdSe)</sub> (%)	CdSe dimensions <sup>b</sup> (nm)	
			length	diameter			length direction	diameter direction
Type-I <sup>1/2</sup>	1.971	80	4.44±0.45	3.1±0.4	15.0	39	0.92	0.2
Type-II	1.610	75	8.0±1.6 <sup>c</sup>	2.9±0.3 <sup>c</sup>	80	88	6.7 <sup>d</sup>	2.9 <sup>d</sup>

*a:* photoluminescence peak (PL peak), PL quantum yield (QY), HNC dimensions, HNC volume (V<sub>Nc</sub>), volume fraction of CdSe in the HNC (V<sub>fr(CdSe)</sub>), and dimensions of the CdSe segment of the HNC along the length and diameter directions, assuming that the CdTe core occupies the center of the HNC. *b:* The CdTe core is the same in all cases (diameter: 2.6 ± 0.3 nm). *c:* Sample consists mostly of bipods. *d:* Arm length and diameter.

**Characterization:** Absorption spectra were measured on a double beam Perkin-Elmer Lambda 16 UV/Vis spectrometer. Photoluminescence (PL) and PL excitation (PLE) spectra were acquired using an Edinburgh Instruments FLS920 Spectrofluorimeter equipped with a 450 W Xenon lamp as the excitation source and double grating monochromators. The spectral resolution was 1 nm (2-4 meV, depending on the spectral region) for the excitation monochromator and 0.3-0.5 nm (0.6 – 2 meV, depending on the spectral region) for the emission monochromator. The excitation power was 100-200 mW/cm<sup>2</sup>. The spectra were corrected for the instrumental response and the spectral dependence of the excitation lamp intensity. Samples for optical measurements were prepared by directly dissolving the crude reaction mixture in anhydrous toluene in a glove box under nitrogen (< 1 ppm H<sub>2</sub>O, <5 ppm O<sub>2</sub>). In order to avoid energy transfer between the NCs and deviations from linearity in the PLE spectra, all optical measurements were carried out on samples with a low optical density ( $\leq 0.05$  at the lowest energy absorption maximum). For low temperature measurements the sample was contained in a sealed quartz cuvette (optical path: 2 mm) and mounted in a continuous He-flow cryostat allowing for measurements down to 4.2 K. Samples for TEM imaging were prepared by dipping a carbon coated polymer film copper grid (300 mesh) into a toluene solution of purified nanocrystals. The excess liquid was removed by blotting with filter paper. Transmission Electron Microscopy (TEM) measurements were performed on a Tecnaiz0F (FEI) microscope was operated at 200kV.

## 6.3 – Results and Discussion

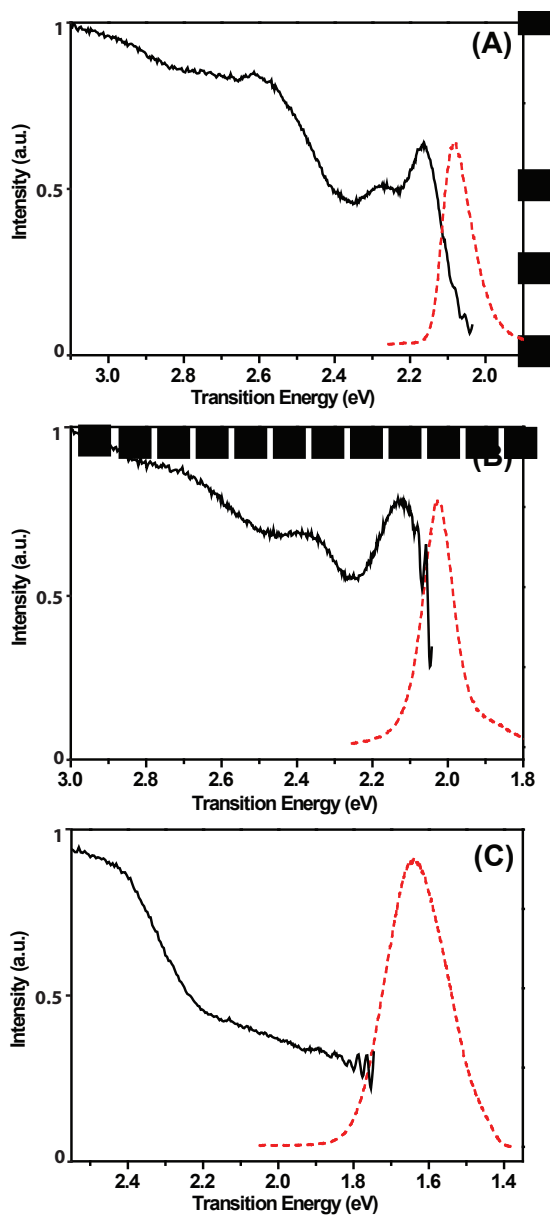
### 6.3.1 – LO-phonon replicas in the low temperature optical spectra of colloidal NCs

Figure 6.1 presents the low temperature (4.2 K) PL and PLE spectra of the CdSe QDs and CdTe/CdSe HNCs investigated in this work. The PL spectra consist of a single peak, while the PLE spectra comprise a number of different absorption transitions. An assignment for the transitions observed in the spectra will be presented later in this chapter (sections 6.3.2 and 6.3.3 below). It is interesting to note that fine-structure is clearly observed near the low energy edge of the PLE spectra (see figure 6.2 for a detailed view), in contrast to the featureless PL spectra. The lack of fine-structure in the PL spectra shown in figure 6.1 is due to the fact that the samples were excited far above the band gap (*viz.*, 440 nm). Therefore, the spectra reflect the full size and shape distribution of the NC (HNC) ensemble. It should be noted that the ensemble PL spectrum is however red-shifted from the statistically weighted maximum, since the density of states far above the band-edges is

proportional to the volume of the NC (or HNC),<sup>[60]</sup> and therefore larger NCs in the ensemble have relatively larger contributions to the full PL spectrum.

PLE spectroscopy is ideally suited to reveal the near band-edge fine-structure, since it effectively narrows the dispersion of the NCs (or HNCs) probed. This is done by monitoring a narrow spectral band of the full ensemble PL, while scanning the excitation energy with high resolution. In this way, sub-ensembles of NCs (HNCs) are spectrally selected, thereby minimizing the impact of size, shape and composition inhomogeneities on the transitions observed. The use of samples with low optical densities further minimizes the effects of polydispersity, since it prevents energy transfer from smaller to larger NCs in the ensemble. Another useful feature of the PLE technique is that only emitting NCs (HNCs) contribute to the spectra, ensuring that only information over the most efficient NCs (HNCs) in the ensemble is collected. Moreover, PL associated with radiative recombination in defects or surface states (*i.e.*, “trap PL”) occurs at lower energies than the band-edge PL and can thus be discarded by spectral selection. PLE spectroscopy can therefore effectively exclude defective NCs (HNCs) from the optical sampling process. However, only at low temperatures the benefits of PLE spectroscopy can be fully harvested. The bandwidth of exciton transitions in PL and PLE spectra is determined by homogeneous and inhomogeneous broadening. Inhomogeneous broadening is caused by size, shape, and composition inhomogeneities within the ensemble, whereas homogeneous broadening is due to intrinsic processes, such as exciton dephasing by coupling to acoustic phonons.<sup>[23]</sup> The homogeneous linewidths thus decrease with decreasing temperatures as a result of the lower phonon populations,<sup>[23]</sup> reaching values as narrow as 10-200  $\mu\text{eV}$  for single CdSe QDs at 2 K.<sup>[28,55]</sup> Therefore, at sufficiently low temperatures, the linewidths of ensembles of QDs are dominated by the inhomogeneous broadening contribution, allowing one to use PLE spectroscopy to select narrow sub-ensembles of emitting NCs (HNCs), effectively minimizing the impact of polydispersity and allowing the fine-structure of the spectral transitions to be observed.

As can be seen in figure 6.1, the PLE spectra consist of several partially overlapping broad bands and a number of weaker and narrow lines near the low energy edge. As the monitored PL is moved to lower energies the broad features broaden and become relatively weaker, while the narrow fine-structure features near the low energy edge of the PLE spectra become more pronounced (figure 6.3). This is due to a combination of effects (figure 6.3). First, when the PL is monitored on the blue edge of the full ensemble



**Figure 6.1** – Low temperature (4.2 K) PL (dashed lines,  $\lambda_{exc} = 440$  nm) and PLE (solid lines) spectra of (a) 4.3 nm diameter CdSe NCs ( $\lambda_{em} = 614$  nm), (b) CdTe/CdSe Type-I<sup>1/2</sup> HNCs ( $\lambda_{em} = 612$  nm), and (c) CdTe/CdSe Type-II HNCs ( $\lambda_{em} = 715$  nm).

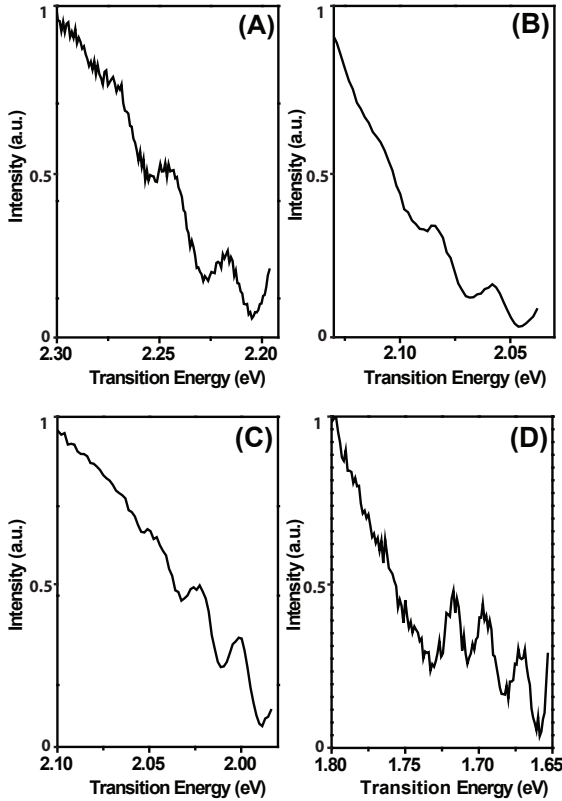


**Figure 6.2** – Low energy edge of the low temperature (4.2 K) PLE spectra of (a) 3 nm diameter CdSe NCs ( $\lambda_{em} = 568$  nm), (b) 4.3 nm diameter CdSe NCs ( $\lambda_{em} = 614$  nm), (c) CdTe/CdSe Type-I HNCs ( $\lambda_{em} = 630$  nm), and (d) CdTe/CdSe Type-II HNCs ( $\lambda_{em} = 756$  nm).

PL the smallest NCs in the ensemble are probed, while the largest NCs are probed when monitoring the red edge of the full ensemble PL (figure 6.3). Because larger NCs (smaller energy gaps) can reabsorb the emission of smaller NCs (larger energy gaps), the PLE spectra of the largest NCs in the ensemble will consist of a convolution of absorption transitions leading to direct excitation of the NCs (*i.e.*, the true PLE spectrum of the largest NCs) and absorption transitions of smaller NCs that indirectly excite the largest NCs via emission reabsorption. Therefore, the features in the PLE spectrum of the largest NCs become broader, particularly at higher energies, where the spectral overlap with the smaller NCs is more pronounced. For this reason, the highest spectral resolution in PLE for the strong and broad features is obtained while probing the smallest NCs in the ensemble (*i.e.*, the blue

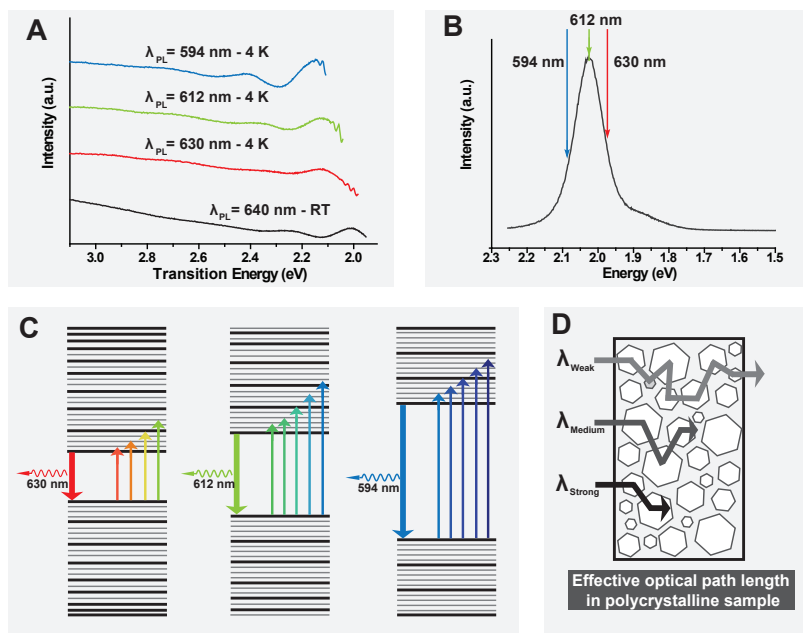


**Figure 6.3** – (a) Low temperature (4.2 K) and room temperature (RT) PLE spectra of CdTe/CdSe Type- $I^{1/2}$  HNCs obtained while monitoring different PL wavelengths. The wavelength chosen at RT corresponds to the low energy side of the RT PL spectrum. The PLE spectra at 4.2 K were measured while monitoring the high energy side ( $\lambda_{PL} = 594 \text{ nm}$ ), the peak ( $\lambda_{PL} = 612 \text{ nm}$ ), and the low energy side ( $\lambda_{PL} = 630 \text{ nm}$ ) of the 4.2 K PL spectrum (shown in b). (c) Schematic illustration of the energy levels of NCs of different sizes (size decreases from left to right). (d) Schematic illustration of the impact of saturation effects in the low temperature PLE spectra. Stronger transitions ( $\lambda_{Strong}$ ) will be shorter than that of weakly absorbed photons ( $\lambda_{Weak}$ ), since  $I_{Strong}$  will be more strongly attenuated than ( $\lambda_{Weak}$ ), and is eventually depleted.

edge of the full ensemble PL), since they are not affected by reabsorption effects. However, the near band-edge fine-structure is best observed while monitoring the largest NCs in the ensemble (*i.e.*, the red edge of the full ensemble PL), since they have the smallest band-gaps. Therefore, their near band-edge transitions are not affected by spectral overlap with transitions of smaller NCs (figure 6.3). In practice, the attainable spectral resolution is limited by a number of constraints, and therefore some spectral overlap still occurs.



Moreover, saturation effects in the PLE spectra also play a role. These effects originate from the fact that at sufficiently high optical densities the relationship between the absorption cross section and the concentration of the absorber becomes nonlinear, with larger deviations for stronger transitions.<sup>[61]</sup> Therefore, the relative intensities of different transitions in a PLE spectrum become distorted. This effect is important in the low temperature PLE spectra of colloidal suspensions of NCs, because the solution freezes out as a polycrystalline material. Light scattering at the inter-grain boundaries leads to effective optical path lengths significantly longer than the thickness of the cell containing the sample. The effective optical path length of photons capable of exciting stronger transitions will then be shorter than that of weakly absorbed photons (figure 6.3). As a result, the relative intensities in the PLE spectra are distorted, with weaker transitions appearing relatively stronger (see comparison between PLE spectra at low temperatures and at room temperature, where light scattering effects are absent, figure 6.3). This effect also favors the observation of the near band-edge fine-structure in the PLE spectrum of the largest NCs in the ensemble, since it enhances their relative intensity with respect to the broad background formed by the higher energy (and stronger) transitions, which, as explained above, contain contributions from all the emitting NCs in the ensemble that are smaller than the ones being monitored.

The low energy edge of the PLE spectra of the studied samples is shown in more detail in figure 6.2. Despite the pronounced differences between the overall features in the PLE spectra of CdSe QDs (figure 6.1a), Type-I<sup>1/2</sup> CdTe/CdSe HNCs (figure 1b), and Type-II CdTe/CdSe HNCs (figure 6.1c), the fine-structure near the lowest energy absorption edge is strikingly similar in all four cases (figure 6.2), consisting of a series of equally spaced narrow lines. The spacing between the lines (*viz.*,  $26 \pm 1$  meV for CdSe QDs, Fig. 2a,b;  $23 \pm 1$  meV for CdTe/CdSe Type-I<sup>1/2</sup> HNCs, Fig. 6.2c, and  $24 \pm 1$  meV for CdTe/CdSe Type-II HNCs, figure 6.2d) corresponds well to the frequency of longitudinal optical (LO) phonon modes in bulk CdSe (26 meV),<sup>[62]</sup> especially for CdSe QDs. The slightly smaller spacing observed in the spectra of the CdTe/CdSe HNCs is in fact very close to the volume average between the LO-phonon frequencies of bulk CdTe (21 meV)<sup>[63]</sup> and bulk CdSe, which corresponds to 23 meV for CdTe/CdSe Type-I<sup>1/2</sup> HNCs, (39% CdSe, 61% CdTe), and to 25 meV for CdTe/CdSe Type-II HNCs (88% CdSe, 22% CdTe).

We note that fine-structure can also be observed in the low temperature PL spectra upon selective excitation of narrow sub-ensembles of NCs. This is

typically achieved by using spectrally narrow lasers as the excitation source, yielding the so-called Fluorescence Line Narrowed (FLN) spectra,<sup>[24-27]</sup> but can also be (partially) observed by using narrow excitation and emission slits and near band-edge excitation (see, *e.g.*, figure 6.4). The spacing between the fine-structure features observed in the low temperature PL spectra (figure 6.4) is the same as that observed in the PLE spectra. The near band-edge fine-structure observed in both the PLE and PL spectra can thus be assigned to a LO-phonon progression. In the present work, we will focus on the PLE spectra because they are better suited to quantitatively investigate the near band-edge fine-structure, for reasons to be made clear below.

The main difference between the LO-phonon progressions observed for the different types of NCs is the relative intensities of the phonon replicas, which implies different exciton-phonon coupling strengths. Another difference is the relative contribution of the spectrally broad feature onto which the LO-phonon progression is superposed. To understand these differences, and to allow a proper quantitative analysis of the LO-phonon replicas, it is necessary to first clearly establish the nature of the emitting state probed by the PLE spectra and of the exciton absorption transitions that populate it. The near band-edge states of the fully relaxed exciton are of particular interest, since the PLE spectra probed the near band edge PL and the measurements were carried out at 4.2 K, under low power CW excitation, and using time integrated spectral acquisition. This analysis will be carried out in the next two sections (6.3.2. and 6.3.3). The intensity of the LO-phonon replicas will be addressed in section 6.3.4.

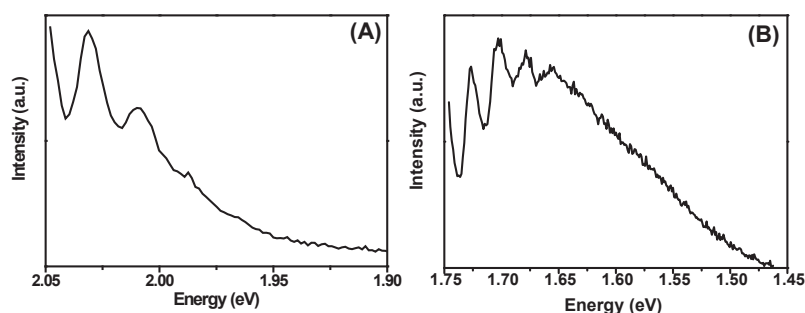


**Figure 6.4** – Low temperature (4.2 K) PL spectra of (a) CdTe/CdSe Type-I/2 HNCs ( $\lambda_{exc} = 605$  nm), and (b) CdTe/CdSe Type-II HNCs ( $\lambda_{em} = 710$  nm).

### 6.3.2 – Exciton transitions and exciton relaxation in colloidal CdSe QDs

We start by the CdSe QDs, since they have been thoroughly investigated over the last few decades, and are therefore well understood. The absorption transitions observed for the CdSe QDs (Fig. 1) can be assigned based on previous experimental and theoretical work:<sup>[64]</sup>  $1S_{3/2(h)} \rightarrow 1S_{(e)}$  (2.16 eV),  $2S_{3/2(h)} \rightarrow 1S_{(e)}$  (2.28 eV), and  $1P_{3/2(h);1/2(h)} \rightarrow 1P_{(e)}$  (2.6 eV). The emission transition is the  $1S_{(e)} \rightarrow 1S_{3/2(h)}$ . It can thus be concluded that the LO-phonon progression observed in figures 1 and 2 is associated with the  $1S_{3/2(h)} \rightarrow 1S_{(e)}$  transition. The lowest electron state ( $1S_{(e)}$ ) is doubly degenerate with respect to its spin projection, whereas the lowest hole state ( $1S_{3/2(h)}$ ) is fourfold degenerate with respect to the projection of its total angular momentum. The  $1S_{(e)}1S_{3/2(h)}$  exciton state of spherical CdSe (and CdTe) NCs with cubic structure (*i.e.*, zinc blende) is therefore eightfold degenerate.<sup>[64,65]</sup> In the framework of the effective mass approximation (EMA) this degeneracy is partially lifted in wurtzite CdSe QDs, due to the combined effects of crystal field asymmetry, shape anisotropy, and electron-hole exchange interaction, yielding five levels (*viz.*,  $E_0^U$ ,  $E_{\pm 1}^U$ ,  $E_0^L$ ,  $E_{\pm 1}^L$ , and  $E_{\pm 2}$ , in order of decreasing energy).<sup>[65]</sup> The levels are labeled according to their total angular momentum projection along the wurtzite hexagonal axis (figure 6.5).<sup>[65]</sup> Similar results have been obtained by many-body pseudopotential<sup>[66]</sup> and semi empirical tight-binding calculations.<sup>[67]</sup> The energy separation between the  $1S_{(e)}1S_{3/2(h)}$  exciton fine structure states is observed to be strongly size and shape dependent, regardless of the theoretical framework used for the calculations.<sup>[65-67]</sup>

The  $1S_{3/2(h)} \rightarrow 1S_{(e)}$  emission transition takes place from the lowest two fine-structure states ( $E_{\pm 1}^L$  and  $E_{\pm 2}$ ), typically referred to as the “bright” and “dark” excitons, since the  $E_{\pm 2}$  state is optically passive in the electric dipole approximation.<sup>[65]</sup> At low temperatures below 10 K the population of the “bright exciton” ( $E_{\pm 1}^L$  state) is negligible, and (emission will thus take place primarily from the “dark exciton” ( $E_{\pm 2}$  state), leading to long exciton lifetimes (*viz.*, ~0.2 to 1.4  $\mu$ s, depending on the QD size).<sup>[30,68,69]</sup> Within the EMA framework the  $E_{\pm 2}$  lifetime should be size independent and infinite.<sup>[65]</sup> However, semi-empirical tight-binding calculations have successfully reconciled experiment and theory by showing that triplet (“dark exciton”) radiative lifetimes in the microsecond range can be obtained for CdSe QDs by incorporating interactions with higher exciton states and explicitly taking into account spin-orbit interactions, which lead to mixing of singlet character into nominally triplet states (*i.e.*, the  $E_{\pm 2}$  state or “dark exciton”).<sup>[67]</sup>

It is interesting to note that the observation of long exciton lifetimes for CdSe QDs at low temperatures was initially ascribed to surface localization of the photogenerated hole.<sup>[24]</sup> However, subsequent work by the same group dismissed the surface-based interpretation for being inconsistent with data obtained by transient differential absorption and gated FLN spectra.<sup>[70]</sup> Since then a large body of experimental and theoretical work has established that the energetics and dynamics of the low temperature exciton PL of colloidal CdSe QDs can be understood in terms of the intrinsic band-edge exciton-fine structure. This model has successfully explained a wide variety of empirical data: the size size dependence of the fine-structure observed in excitation and emission,<sup>[25,26,65]</sup> the size-, temperature-, and magnetic field-dependence of the exciton lifetimes,<sup>[19,26-28,30,65,68-71]</sup> and the electron and hole spin relaxation dynamics.<sup>[72]</sup> Moreover, spectroscopic investigations led by a number of groups on colloidal CdSe QDs with a variety of different coatings (both organic ligands, such as TOPO, TOPO-HDA, 4-picoline, etc., and inorganic shells of ZnS or ZnSe) has shown that the low temperature (< 50 K) absorption, band-edge PL, FLN spectra, and exciton lifetimes, are remarkably insensitive to the properties of the QD surface.<sup>[69,73]</sup> These results strongly argue against the involvement of surface states, and provide compelling evidence that the exciton PL decay in colloidal CdSe QDs at low temperatures (<50 K) is due to an intrinsic mechanism (*i.e.*, radiative recombination from the  $E_{\pm 1}^L$  and  $E_{\pm 2}^L$  fine structure states).

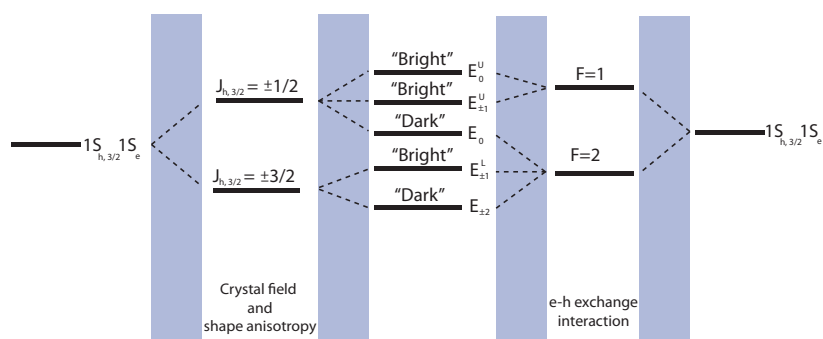


**Figure 6.5** – Energy levels of the exciton fine structure in Wurtzite CdSe QDs.<sup>86</sup> Due to the crystal field (and shape anisotropy) the  $1S_{h,3/2} 1S_e$  level splits in two levels ( $J_{h,3/2} = \pm 1/2$  and  $J_{h,3/2} = \pm 3/2$ ). Also the electron-hole exchange interactions splits the  $1S_{h,3/2} 1S_e$  level in 2 states ( $F=1$ , and  $F=2$ ). The effect of crystal field and electron-hole exchange interactions together leads to the splitting of the  $1S_{h,3/2} 1S_e$  into five levels ( $E_0^U, E_{\pm 1}^U, E_0^L, E_{\pm 1}^L, E_{\pm 2}^L$ ).

Nevertheless, the surface has an important impact on the PL properties of colloidal QDs, since carrier trapping by surface states, surface defects, and capping ligands gives rise to nonradiative relaxation pathways, leading to PL quenching.<sup>[1,69,70,73-78]</sup> Exciton trapping may also lead to defect assisted radiative recombination (the so-called trap PL).<sup>[1]</sup> Trap PL in CdSe and CdTe QDs is characterized by a broad band emission (~300 meV) that is strongly redshifted (300-600 meV) with respect to the lowest energy absorption transition.<sup>[12,58,79]</sup> In contrast, the band-edge PL (*i.e.*, the  $1S_{3/2(h)} \rightarrow 1S_{(e)}$  transition) is narrow (*viz.*, ~100 meV at 300 K for an ensemble with 10% polydispersity)<sup>[12,57,58,69]</sup> and presents a very small non-resonant Stokes shift (~20 meV).<sup>[57]</sup> Carrier trapping and PL quenching produce very clear signatures in PL decay curves, leading to deviations from a single exponential behavior.<sup>[69,74]</sup> We note that the CdSe QD samples investigated in this work have high room temperature PL QYs (>30%), and no trap related PL, even at 4.2 K. Moreover, the exciton lifetimes observed at 4.2 K are purely radiative (single exponential decays) and are consistent with values previously reported for similarly sized CdSe QDs.<sup>[68,69,80]</sup>

Considering the discussion above, it is clear that the emission monitored while scanning the PLE spectra of CdSe QDs at 4.2 K originates primarily from the  $E_{\pm 2}$  fine-structure state of the  $1S_{(e)}1S_{3/2(h)}$  exciton and that the involvement of surface states can be confidently excluded. The  $1S_{3/2(h)} \rightarrow 1S_{(e)}$  peak in the PLE spectra of CdSe QDs will thus consist of transitions involving the upper four fine-structure states (purely electronic and phonon assisted) and LO-phonon assisted  $E_{\pm 2}$  transitions. Most of the oscillator strength of the  $1S_{3/2(h)} \rightarrow 1S_{(e)}$  absorption transition is carried by the upper two fine-structure states.<sup>[64,65]</sup> The broad feature observed at ~2.16 eV in the PLE spectrum of the 4.3 nm diameter CdSe QDs (Fig. 1a) can thus be assigned to a combination of the  $E_0^U$  and  $E_{\pm 1}^U$  fine structure states. Possible reasons for the broad bandwidth of this spectral feature will be discussed below. The  $E_0^L$  fine structure level is not observed, as this state is optically passive.

The energy difference between the  $E_{\pm 1}^L$  level and the  $E_{\pm 2}$  fine-structure states (the so-called “dark-bright” splitting) is very small and strongly size-dependent.<sup>[64,65,69]</sup> The “dark-bright” splitting is equivalent to the resonant Stokes shift observed between the excitation and the zero-phonon line frequencies in FLN spectra, and has been reported to increase from 3 to 8 meV for CdSe QDs in the 4.5 to 3 nm diameter range.<sup>[73]</sup> Given that the PLE spectra reported here were collected only up to ~20 meV above the

monitored PL energy, we can conclude that the  $E_{\pm 1}^L$  zero-phonon line cannot be present in the PLE spectra shown in figs. 1 and 2. The narrow features near the lowest energy edge of the PLE spectra of the CdSe QD samples (Fig. 2a,b) can thus be unambiguously ascribed to a LO-phonon progression involving the  $E_{\pm 1}^L$  and  $E_{\pm 2}^L$  fine-structure states, with the lowest energy line corresponding to a one-phonon replica, rather than a zero-phonon line. Since the linewidths of the observed LO-phonon replicas (*viz.*, 15-20 meV) are larger than the “dark-bright” splitting, the differences between the LO-phonon progressions originating from the two states cannot be resolved.

The  $E_0^U$  and  $E_{\pm 1}^U$  fine-structure states are not resolved in the PLE spectra due to a combination of inhomogeneous and homogeneous broadening. The larger contribution of inhomogeneous broadening is due to the fact that the spectral size selection offered by PLE spectroscopy is less effective for higher energy transitions, since the higher energy transitions of larger CdSe QDs spectrally coincide with lower energy transitions of smaller CdSe QDs (figure 6.4). Moreover, the homogeneous linewidth of the  $E_0^U$  and  $E_{\pm 1}^U$  fine-structure states is inherently much larger than that of the  $E_{\pm 1}^L$  and  $E_{\pm 2}^L$  levels due to lifetime broadening, since the  $E_0^U$  and  $E_{\pm 1}^U$  levels experience a very rapid relaxation down to the lower fine-structure levels. The intra- and inter-band relaxation in CdSe QDs has been investigated in detail and is well-understood.<sup>[12,13,15,16,19,30,69,81]</sup> Relaxation from the higher exciton states to the lowest exciton state ( $1S_{(e)}1S_{3/2(h)}$ ) is very fast (*viz.*, 150-500 fs).<sup>[12,13,15,16,81]</sup> State specific pump-probe transient absorption measurements have determined that the  $1P_e \rightarrow 1S_e$  electron relaxation is size dependent (155 fs for 4 nm diameter and 250 fs for 6.4 nm diameter CdSe QDs), while the hole relaxation is size independent (250 fs for the  $2S_{3/2(h)} \rightarrow 1S_{3/2(h)}$ ).<sup>[81]</sup> The electron relaxation rates are determined by Auger energy transfer to holes (electron-hole Auger coupling time: 1 ps).<sup>[15,81]</sup> In contrast, hole relaxation has been proposed to take place primarily via coupling to phonons, either from the surface ligands or from the QD itself (both acoustic and LO-modes).<sup>[81]</sup> The final intra-band relaxation step occurs within the five exciton fine-structure sublevels of the  $1S_{(e)}1S_{3/2(h)}$ <sup>[16]</sup> and is essentially determined by the hole relaxation rate.<sup>[15,72]</sup> The  $E_0^U \rightarrow E_{\pm 1}^U$  relaxation is ultrafast (<100 fs) and is followed by the relaxation of the  $E_{\pm 1}^U$  sublevel, which takes ~700-1000 fs to reach the  $E_{\pm 1}^L$  sub-level when both electron and hole have been excited to higher states.<sup>[16]</sup> In such a case the hole is re-excited via Auger energy transfer from excited electrons, and therefore the relaxation takes longer than in the absence of hot electrons (*viz.*, 350 fs).<sup>[15]</sup> The relaxation from the  $E_{\pm 1}^L$  sublevel to the  $E_{\pm 2}^L$  sublevel requires a spin-flip and is therefore relatively slow (0.2-0.4

ps at 300 K,<sup>[16]</sup> and tens of ps below 10 K)<sup>[19]</sup> As mentioned above, relaxation of the  $E_{\pm 2}$  sublevel at low temperatures (<10 K) occurs only radiatively and takes ~0.2 to 1.4  $\mu$ s, depending on the QD size.<sup>[30,69]</sup>

### 6.3.3 – Exciton transitions and exciton relaxation in colloidal CdTe/CdSe HNCs

The evolution of the optical properties of CdTe/CdSe HNCs as a function of the CdSe volume fraction has been investigated in detail by our group.<sup>[57]</sup> The electron-hole spatial separation in CdTe-CdSe HNCs has been shown to be ultrafast (0.2-1 ps).<sup>[72]</sup> Hole relaxation in the CdTe part occurs in ~800 ps, while the electron relaxation in the CdSe part is much faster (8 ps).<sup>[82]</sup> The hole wave function localizes in the CdTe core already for very small CdSe volume fractions.<sup>[57]</sup> Therefore, the evolution of the optical transitions in the HNCs with the growth of the CdSe segment is determined by the localization regime of the electron wave function. For Type-I<sup>1/2</sup> CdTe/CdSe HNCs the lowest energy electron state is delocalized over the whole HNC (this state is labelled as  $1S_c$ (hetero)). The loss in electron confinement energy results in a shift of all exciton transitions to lower energies. Since the hole levels remain unperturbed and the  $1S_c$ (hetero) is a coherent state delocalized over the whole HNC, the absorption transitions remain direct, and therefore distinct and well-defined.<sup>[57]</sup> The peaks observed in the PLE spectrum of the Type-I<sup>1/2</sup> CdTe/CdSe HNCs shown in figure 6.1 can thus be ascribed to the following absorption transitions:<sup>[57]</sup>  $1S_{3/2(h)}(\text{CdTe}) \rightarrow 1S_{(e)}(\text{hetero})$  (2.13 eV);  $2S_{3/2(h)}(\text{CdTe}) \rightarrow 1S_{(e)}(\text{hetero})$  (2.39 eV);  $1P_{(h)}(\text{CdTe}) \rightarrow 1P_{(e)}(\text{hetero})$  (2.7 eV).

For Type-II CdTe/CdSe HNCs the lowest energy electron state is the  $1S_{(e)}(\text{CdTe})$  [or its equivalent in nanorods,  $1\Sigma_{(e)}(\text{CdSe})$ ].<sup>[57]</sup> The lowest energy absorption transition then becomes the spatially indirect transition  $1S_{3/2(h)}(\text{CdTe}) \rightarrow 1S_{(e)}(\text{hetero})$  [or  $1S_{3/2(h)}(\text{CdTe}) \rightarrow 1\Sigma_{(e)}(\text{CdSe})$  in branched HNCs]. This results in a further shift of all transitions to lower energies and gives rise to a featureless low-energy absorption tail characteristic of Type-II HNCs. The spatially indirect nature of the exciton in Type-II CdTe/CdSe HNCs also leads to an increase in the Stokes shift values and transition line widths, and longer exciton radiative lifetimes. Accordingly, the feature observed beyond 2.25 eV in the PLE spectrum of the Type-II CdTe/CdSe HNCs shown in figure 6.1 is assigned to the  $1S_{3/2(h)}(\text{CdTe}) \rightarrow 1\Sigma_{(e)}(\text{CdSe})$  absorption transition.<sup>[57]</sup>

The LO-phonon progression observed in the PLE spectra of the CdTe/CdSe HNCs (figures 6.1 and 6.2) can thus be ascribed to the (partially)

spatially indirect exciton transitions  $1S_{3/2(h)}(\text{CdTe}) \rightarrow 1S_{(e)}(\text{hetero})$  and  $1S_{3/2(h)}(\text{CdTe}) \rightarrow 1\Sigma_{(e)}(\text{CdSe})$ , for Type-I<sup>1/2</sup> and Type-II CdTe/CdSe HNCs, respectively. We note that the lowest energy exciton state in CdTe/CdSe HNCs [ $1S_{3/2(h)}(\text{CdTe})1S_{(e)}(\text{hetero})$  or  $1S_{3/2(h)}(\text{CdTe})1\Sigma_{(e)}(\text{CdSe})$ ] is eightfold degenerate, just like in the CdSe QD case. Exciton fine-structure states are therefore also expected, but studies aiming at their identification are still lacking. It may be expected that the decrease in the electron-hole exchange interaction due to the partial spatial separation of the electron and hole wave functions results in less pronounced splitting of the exciton fine-structure sublevels,<sup>[5,57]</sup> but this hypothesis remains to be verified. In any case, it is clear that the observed LO-phonon progression is associated with the lowest energy fine-structure states of the  $1S_{3/2(h)}(\text{CdTe})1S_{(e)}(\text{hetero})$  quasi-indirect exciton state of Type-I<sup>1/2</sup> CdTe/CdSe HNCs and the  $1S_{3/2(h)}(\text{CdTe})1\Sigma_{(e)}(\text{CdSe})$  spatially indirect exciton state of Type-II CdTe/CdSe HNCs. Similarly to the case of CdSe QDs, the lowest energy line is assigned to a one-LO-phonon replica, rather than to a zero-phonon line.

#### 6.3.4 – Exciton-phonon coupling strength of colloidal CdSe QDs and CdTe/CdSe HNCs

We now turn to the strength of the ex-ph coupling in the different types of NCs studied in the present work. The magnitude of the ex-ph coupling is typically expressed by using the Huang-Rhys parameter  $S$ . This parameter is defined under the assumption that the electron-phonon coupling is adiabatic, *i.e.*, the mixing of different electronic states by the phonon coupling is taken to be negligible.<sup>[83]</sup> The phonons are then described by an unperturbed Hamiltonian, and the electron-phonon interaction Hamiltonian is taken to be linear in the vibrational amplitude. This leads to a displaced harmonic oscillator model with the dimensionless displacement, as depicted in figure 6.6. This model predicts that at  $T=0$  the absorption band shape of an electric dipole transition can be expressed as a series of delta-functions at various energies differing by the phonon frequency  $\hbar\omega$ :<sup>[83]</sup>

$$I_{ab}(E) = \sum_n I_0 F_n(0) \delta(E_{0,0} + n\hbar\omega - E) \quad (6.1)$$

where  $E_{0,0} = E_{b,0} - E_{a,0}$  gives the energy of the transition between the zero vibrational levels of both initial (a) and final (b) states (*i.e.*, the energy of the zero-phonon line), and  $n$  gives the number of phonons generated in the transition (*i.e.*, the  $n^{\text{th}}$  phonon replica of the phonon progression). The term  $I_0$  corresponds to the intensity of the full band, which is determined by the total  $a \rightarrow b$  transition probability ( $|\langle \psi_b(\mathbf{r}_1 Q_0) | \mu | \psi_a(\mathbf{r}_1 Q_0) \rangle|^2$ , where  $\mu$  is



the electric dipole operator).  $F_n(0)$  is the zero-temperature Franck-Condon factor, which is determined by the square of the vibrational overlap integrals  $\langle \chi_b(n) | \chi_a(0) \rangle$  and can be expressed as<sup>[83]</sup>

$$F_n(0) = \frac{\exp(-S)S^n}{n!} \quad (6.2)$$

in which  $S$  is the Huang-Rhys parameter ( $S = \Delta^2/2$ ). Eqs. 6.1 and 6.2 show that the Huang-Rhys parameter  $S$  can be determined from experimental data, provided the intensity ratio between at least two members of the phonon progression is known. Typically, the ratio between the one-phonon line and the zero-phonon line ( $I_{0,1}/I_{0,0} = S$ ) is used for FLN data, while in Raman scattering experiments the ratio between the two-phonon and the one-phonon replicas is used to estimate the magnitude of  $S$  ( $I_{0,2}/I_{0,1} = S/2$ ). As

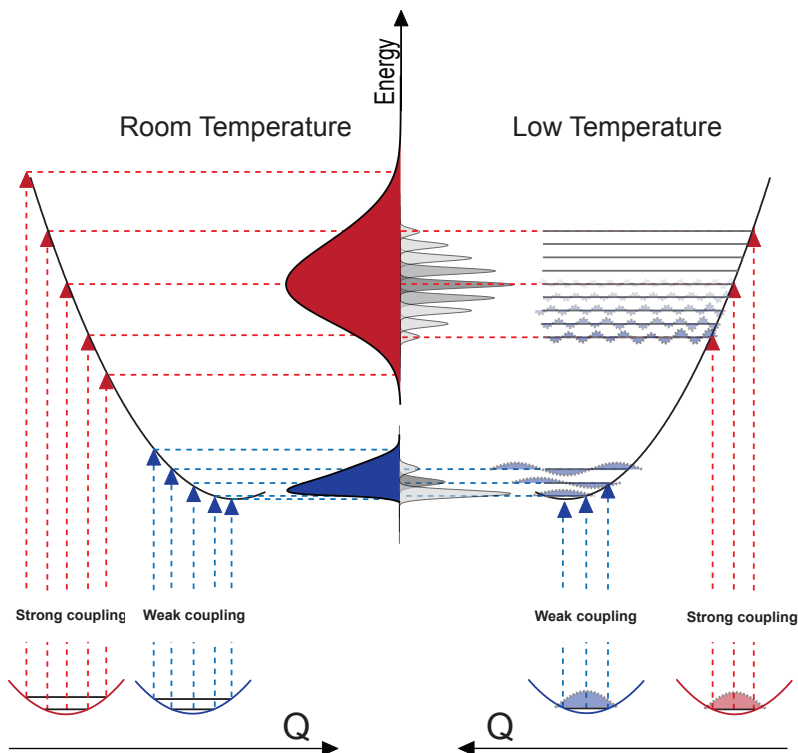


**Figure 6.6** – Schematic illustration of the effect of strong and weak exciton-phonon coupling strengths on optical spectra at room temperature and low temperature.

discussed above, the zero-phonon line is not observed in the PLE spectra reported here. Therefore, we will use the ratio between the integrated intensities of the two-LO-phonon (0-2) and the one-LO-phonon (0-1) replicas in the PLE spectra to estimate the Huang-Rhys parameter  $S$ . In order to determine the integrated intensities of the LO-phonon replicas, the contribution of the broad spectral feature was first subtracted from the PLE spectra, by modeling it as a polynomial baseline running from the onset of the PLE spectra (*i.e.*, the lowest excitation energy) to immediately after the highest order observable phonon replica. The intensity of the baseline at the lowest energy limit of the PLE spectra was constrained to the spectral background level (typically just a few counts/s) and increased to the peak intensity immediately after the highest energy observable LO-phonon replica. The uncertainties involved in this process will be discussed in more detail below. The LO-phonon progressions (figure 6.7) were subsequently fit to a sum of multiple Gaussian peaks. The  $S$  values determined for the 3 nm diameter CdSe QDs, 4.3 nm diameter CdSe QDs, Type-I<sup>1/2</sup> CdTe/CdSe HNCs, and Type-II CdTe/CdSe HNCs are, respectively, 1.0, 0.84, 1.56, and 2.88 (figure 6.7).

The expected ratios between the intensities of the  $n$ -phonon and the 1-phonon replicas ( $I_{0,n}/I_{0,1}$ ) calculated on the basis of the estimated  $S$  parameters are in good agreement with the experimental values determined from the PLE spectra (figure 6.7 gives both experimental and predicted values). Some of the predicted LO-phonon replicas were not observed: the 0-4 line for the 4.3 nm diameter CdSe QDs (predicted intensity: 0.02); the 0-5 line for the Type-I<sup>1/2</sup> CdTe/CdSe HNCs (predicted: 0.05); and the 0-6 line for the Type-II CdTe/CdSe HNCs (predicted: 0.28). The absence of the higher order LO-phonon replicas in the PLE spectra of the 4.3 nm diameter CdSe QDs and Type-I<sup>1/2</sup> CdTe/CdSe HNCs can be ascribed to their low intensities. The poor agreement between the predicted and observed intensities for the five-phonon-replica (0-5) in the PLE spectrum of the Type-II CdTe/CdSe HNCs can be attributed to the fact that at sufficiently high energies from the monitored PL energy the spectral selection of sub-ensembles is less effective. Therefore, higher order LO-phonon replicas of larger HNCs spectrally overlap with lower order LO-phonon replicas of smaller HNCs, giving rise to the featureless absorption tail characteristic of spatially indirect exciton transitions.

The good agreement between observed and expected intensity ratios shows that the method used to estimate the Huang-Rhys parameter is robust, and

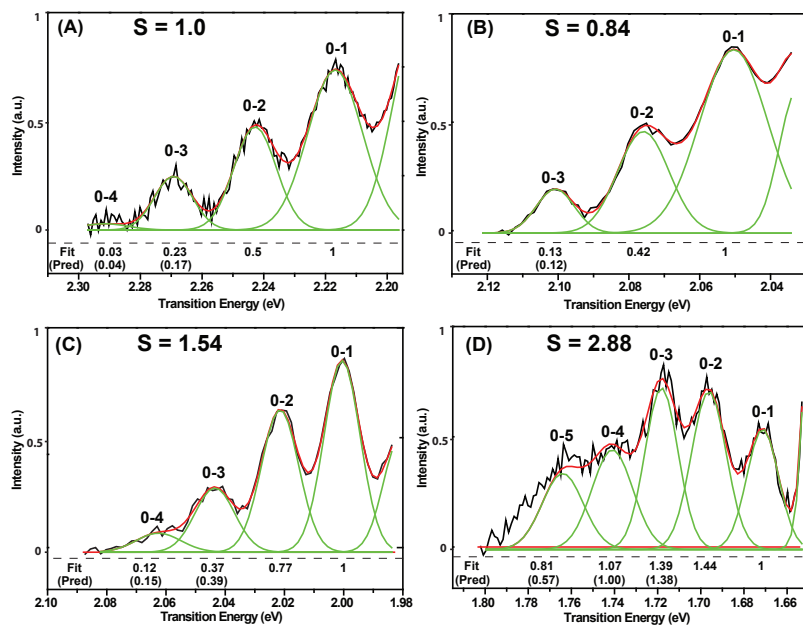


**Figure 6.7** – LO-phonon progressions (black lines) observed in the 4.2 K PLE spectra of (a) 3 nm diameter CdSe NCs ( $\lambda_{em} = 568$  nm), (b) 4.3 nm diameter CdSe NCs ( $\lambda_{em} = 614$  nm), (c) CdTe/CdSe Type-I<sup>1/2</sup> HNCs ( $\lambda_{em} = 630$  nm), and (d) CdTe/CdSe Type-II HNCs ( $\lambda_{em} = 756$  nm). The LO-phonon progressions were fit to a sum of multiple Gaussians. The LO-phonon replicas are labeled according to the phonon number of the initial and final states (0- $n$ ,  $n = 1, 2$ , etc.). The estimated Huang-Rhys parameter  $S$  is given above the spectra. The numbers under the dashed lines give the relative integrated intensity ratios between the 1-phonon and the  $n$ -phonon replicas obtained from the fit and predicted on the basis of the estimated  $S$  values (Pred).

leads to reliable  $S$  values. Nevertheless, as mentioned above, the background subtraction involves some uncertainty, which propagates to the intensity ratios of the LO-phonon replicas. To evaluate the impact of this uncertainty on the  $S$ -values estimated from the PLE spectra, the background was modeled by different baselines, varying from the limit of overestimated 0-1 intensity (*i.e.*, underestimated  $S$ ) to overestimated highest-order LO-phonon replica (*i.e.*, overestimated  $S$ ). This analysis is illustrated in the figure 6.8 using the PLE spectrum of the 3 nm diameter CdSe QDs as a representative example. It is clear that the extreme solutions are physically unrealistic and fail to describe the observed intensities of the LO-phonon progressions. For example, an  $S$ -value of 0.7 (figure 6.8d) should lead to  $I_{0,3}/I_{0,1}$  and  $I_{0,4}/I_{0,1}$  ratios of 0.08 and 0.01, respectively, which are inconsistent with the ratios observed in progression (figure 6.8d) (0.25 and 0.07, respectively). This implies that baseline A is incorrect since it leads to a LO-phonon progression with intensities that are not consistent with a single  $S$ -value. In fact, the mere observation of a LO-phonon progression with four replicas already suffices to demonstrate that the Huang-Rhys parameter  $S$  cannot be smaller than 0.7, since  $S < 0.7$  would lead to negligible intensities the 0-3 and 0-4 LO-phonon replicas. Taking into account the uncertainties involved in the baseline subtraction, the estimated  $S$ -values can be expressed as:  $(1.0 \pm 0.2)$ ,  $(0.85 \pm 0.15)$ ,  $(1.5 \pm 0.15)$ , and  $(2.9 \pm 0.3)$ , for the 3 nm diameter CdSe QDs, 4.3 nm diameter CdSe QDs, Type-I<sup>1/2</sup> CdTe/CdSe HNCs, and Type-II CdTe/CdSe HNCs, respectively. LO-phonon replicas are also observed in the PL spectra (figure 6.4). However, the contribution of the broad band features is more difficult to remove from the PL spectra, since in that case the peak maxima are not clearly observed. For this reason, the quantitative analysis reported here is limited to the LO-phonon progressions observed in the PLE spectra.

Before comparing the  $S$  values determined in the present work to those reported in the literature for CdSe QDs, and discussing the evolution observed in the Huang-Rhys parameter  $S$  from CdSe QDs to type-II CdTe/CdSe HNCs, it is useful to first consider the mechanisms behind the electron-phonon coupling in semiconductors and the theoretical predictions concerning the ex-ph coupling in semiconductor NCs. Coupling between electrons (or holes) and phonons can take place through several mechanisms.<sup>[14,34]</sup> The volume deformation potential interaction arises from local changes in the crystal's energy bands due to the lattice distortion (*i.e.*, changes in bond lengths and/or angles) created by a phonon. This interaction is more important for coupling to acoustic phonons (figure 6.9) and in non-polar materials such

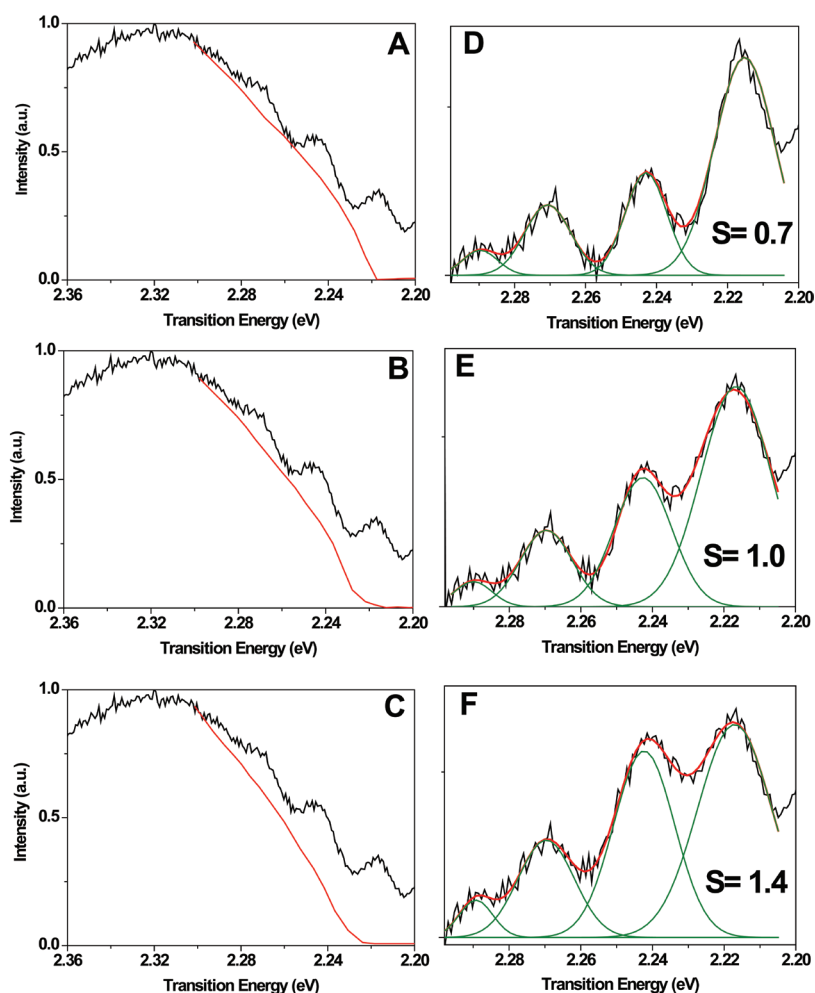


**Figure 6.8** – Low energy edge of the low temperature (4.2 K) PLE spectra of 3 nm diameter CdSe NCs ( $\lambda_{em} = 568$  nm) before (left column) and after (right column) subtraction of a polynomial baseline (red line in the left PLE spectra). The LO-phonon progressions were fit to a sum of multiple Gaussians. The estimated Huang-Rhys parameter  $S$  is given above the spectra. The intensity of the baseline at the lowest energy limit of the PLE spectra was constrained to the spectral background level and increased to the peak intensity immediately after the highest energy observable LO-phonon replica (0-4 in this case). To evaluate the impact of the uncertainty of the background subtraction, different baselines were used varying from the limit of (a) overestimated 0-1 intensity (i.e., underestimated  $S$ ) to (c) overestimated highest order LO-phonon replica (i.e., overestimated  $S$ ). Panels (d), (e) and (f) were obtained from (a), (b) and (c), respectively.

as Silicon. In polar semiconductors, such as CdSe and CdTe, the dominant coupling mechanism between charge carriers and phonons is the Fröhlich interaction.<sup>[14,34]</sup> This interaction arises from the lattice polarization field produced by the relative displacement of positive and negative ions within the unit cell. This induced polarization field is particularly strong for LO-phonons (figure 6.9). For example, the LO-phonon mode of CdSe has the Cd<sup>2+</sup> and Se<sup>2-</sup> atoms vibrating out of phase within each unit cell. Since the Cd-Se bond is relatively polar, this displacement creates a transient longitudinal dipole moment, which strongly couples to the electric field of the charge carriers. Since the contributions of the electron and hole have opposite signs, the strength of the exciton-LO-phonon coupling reflects the net dipole moment of the exciton, which is determined by the difference in the electron and hole charge distributions (*i.e.*, the spatial distribution of the electron and hole wave functions).<sup>[34,52]</sup>

To date, the large majority of the theoretical studies aiming at predicting the ex-ph coupling strength of nanoscale excitons in QDs has assumed that the charge distributions of the electron and hole in strongly confining semiconductor nanostructures are almost identical.<sup>[31-37]</sup> This assumption implies that the ex-ph coupling should vanish, in striking contrast with experimental studies, which have systematically reported significantly large  $S$  values (*viz.*, 0.1 – 1.0) for a variety of different materials (*e.g.*, CdS, PbS, InP, InAs, etc.).<sup>[24,25,32,38-53]</sup> To reconcile theory and experiment several processes have been invoked: partial separation of the electron and hole wave functions as a result of asymmetric shape,<sup>[51]</sup> presence of piezoelectric or strain fields,<sup>[37,53]</sup> and the breakdown of the adiabatic approximation.<sup>[32]</sup> Further, it has been argued that the coupling is highly sensitive to the exact form of the electron and hole wave functions.<sup>[52]</sup> Extrinsic effects such as the presence of charged point defects and surface trapping have also been invoked.<sup>[12,13,31,42,43,52]</sup>

In the specific case of CdSe QDs, the experimental values reported in the literature for the Huang-Rhys parameter  $S$  vary by two orders of magnitude (*viz.*, from 0.03 to 3).<sup>[24,25,32,43-50]</sup> This large disparity can be rationalized by considering that the  $S$  values have been deduced from different photophysical properties (*viz.*, homogeneous linewidths, exciton dephasing rates, intensity ratios, etc.), at different temperatures, and by using a wide variety of experimental techniques: spectral hole burning, 4-wave mixing, resonance Raman spectroscopy, FLN, PLE, single NC PL spectroscopy, etc. Different photophysical properties do not necessarily yield comparable

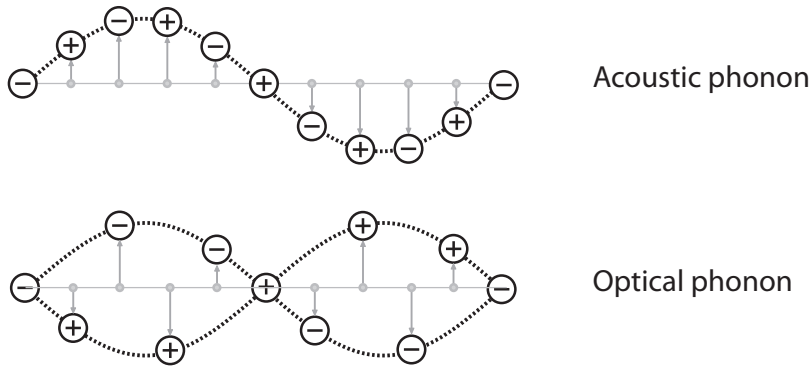


**Figure 6.9** – Schematic illustration of an acoustic phonon and optical phonon in a polar semiconductor.

S values, since coupling to acoustic phonons and to optical phonons is mediated by different mechanisms. Further, it has been demonstrated by state-resolved femtosecond pump-probe transient absorption spectroscopy that the exciton-phonon coupling strength is strongly state dependent for CdSe QDs, being maximum for the  $1S_{(e)}1S_{3/2(h)}$  exciton state ( $S=0.025$  for coupling to LO-phonons and 0.3 for coupling to acoustic phonons) and decreasing for higher-lying states (e.g., for the  $1S_{(e)}2S_{1/2(h)}$   $S=0.2$  for coupling to acoustic phonons and nearly zero for coupling to LO-phonons).<sup>43</sup> Moreover, the S values have also been reported to be strongly temperature dependent, especially for small CdSe QDs (e.g.,  $S=3.4$  at 1.75 K; 1.6 at 5 K; and 1.1 at 10 K for 2.3 nm diameter CdSe QDs).<sup>24</sup> Interestingly, PL spectroscopy on single CdSe QDs at 10 K has shown that the S values vary by a factor  $\sim 20$  (from 0.06 to 1.3) within the ensemble, and also fluctuate over time for a single QD.<sup>[49]</sup> The fluctuation in the S-values was clearly correlated to spectral diffusion, with larger S-values being associated with larger spectral jumps to lower energies. The rate and extent of spectral diffusion was shown to be highly power dependent, increasing with the excitation density. For example, PL peak jumps as large as 60 meV were observed at 2.5 KW/cm<sup>2</sup> excitation density, while at 25 W/cm<sup>2</sup> the spectral jumps were less frequent and much smaller (0.5 meV).<sup>[49]</sup> Subsequent work demonstrated that similar spectral shifts could be induced by applying external electric fields, and that the spectral shift was accompanied by enhanced S-values (e.g., from 0.3 to 0.8 for a 60 meV redshift induced by 350 KV/cm<sup>2</sup>).<sup>[84]</sup> The similarity between the spontaneous spectral diffusion in the absence and presence of an external

electric field was interpreted as evidence that spectral diffusion was caused by the transient accumulation of charges in the QDs.<sup>[84]</sup> The large S-values associated with large spectral redshifts were therefore thought of as being extrinsic in nature.<sup>[84]</sup> These results have been recently used to support the idea that CW frequency-domain spectroscopic techniques (*viz.*, resonance Raman, FLN, PLE, and single dot PL) probe primarily charged or surface trapped states, therefore yielding much larger (extrinsic) S-values than those observed by time-domain spectroscopic techniques.<sup>[12,13,43]</sup> This proposition is based on the assumption that the lowest energy exciton state in CdSe QDs is always a surface trapped state. We argue that this generalization is inconsistent with a large body of experimental and theoretical data, as discussed above (section 6.3.2) in relation to the  $1S_{(e)}1S_{3/2(h)}$  exciton fine-structure. Moreover, as mentioned above, surface trapped states lead to either PL quenching or strongly red shifted trap PL, and therefore cannot contribute to PL spectroscopic measurements that make use of spectral selection, such as FLN, PLE and single dot PL, particularly at the low temperatures ( $\leq 10$  K) typically used for these experiments. Additionally, QD charging is unlikely to take place under the low excitation densities used in typical PLE and FLN experiments, since single dot PL measurements have clearly established that the spectral diffusion is strongly power dependent and is negligible for low powers.<sup>[28,49,84]</sup> We therefore argue that, although the surface trapping hypothesis can adequately rationalize the large S-values observed for CdSe QDs by resonance Raman experiments at room temperature, it cannot explain the S-values extracted from FLN and PLE measurements at low temperatures. As it will be discussed below, the large S-values observed in the latter case are intrinsic in nature, and can be understood by considering the  $1S_{(e)}1S_{3/2(h)}$  exciton fine-structure.

From the discussion above it is evident that the S-values determined in the present work can only be meaningfully compared to literature values obtained using similar experimental techniques (*i.e.*, PLE and FLN), at low temperatures ( $\leq 10$  K), and at low excitation densities. The S values of TOPO capped CdSe QDs ranging from 3 to 10 nm in diameter have been determined by using both PLE and FLN at 10 K.<sup>[25]</sup> The S values extracted from FLN spectra were  $0.46 \pm 0.11$ , while PLE spectra yielded  $S = 0.14 \pm 0.05$ . No clear size dependence was observed.<sup>[25]</sup> The smaller S values obtained from the PLE spectra can be ascribed to the fact that the lowest energy line was assumed to be the zero-phonon line of the  $E_{+1}^L$  fine-structure sublevel.<sup>[25]</sup> However, as discussed above (section 6.3.2), this assumption is not justified. If the lowest energy line in the PLE spectra is taken to be the 0-1 LO-phonon



replica, the observed S values increase to  $\sim 0.3 \pm 0.1$ , which are comparable to those extracted from the FLN spectra. The Huang-Rhys parameter of TOPO capped CdSe QDs has also been estimated from FLN spectra in the 1.75 - 10 K range, and observed to be temperature- and size-dependent below 10 K, decreasing with increasing temperatures (*e.g.*,  $S = 3.4$  at 1.75 K; 1.6 at 5 K; and 1.1 at 10 K for 2.3 nm diameter CdSe QDs) and sizes (*viz.*,  $S$  at 5 K = 1.1, 1.3, and 1.6, for 8.3 nm, 3.3 nm, and 2.3 nm diameter, respectively).<sup>[24]</sup> The size dependence is absent at 10 K,<sup>[24]</sup> in agreement with subsequent work by Norris and coworkers.<sup>[25]</sup> These early observations have been recently corroborated by FLN spectroscopic investigations on CdSe/CdS core/shell QDs (core diameter: 3.6 nm; shell thickness: 1 nm) in the 1.2 - 4.2 K temperature range, under magnetic fields up to 30 Tesla.<sup>[27]</sup> The Huang-Rhys parameter is observed to decrease with increasing temperature (*viz.*,  $S = 1.2$  at 1.2 K and 0.8 at 4.2 K) and with increasing magnetic field (*viz.*,  $S = 1.2$  at 0 T; 0.4 at 30 T). The exciton lifetimes are also observed to decrease with increasing temperature and magnetic fields, in agreement with previous work by other groups.<sup>[26,30,65,68,69,71]</sup>

As discussed in section 6.3.2. above, the temperature- and magnetic field-dependence of the exciton lifetimes of CdSe QDs can be well understood by considering the  $1S_{(e)}1S_{3/2(h)}$  exciton fine-structure.<sup>[26,27,30,65,68,69,71]</sup> As the temperature decreases, the population of the lower lying  $E_{\pm 2}$  state (“dark exciton”) increases at the expenses of the higher lying  $E_{\pm 1}^L$  state (“bright exciton”), leading to progressively longer exciton lifetimes, which eventually become equal to the  $E_{\pm 2}$  radiative lifetime. Similarly, magnetic fields lead to mixing of the  $E_{\pm 2}$  and  $E_{\pm 1}^L$  states, and therefore the exciton radiative lifetime decreases with increasing magnetic fields. We note that the dependence of the Huang-Rhys parameter extracted from FLN measurements on both the temperature and the magnetic field strength can easily be explained by assuming that the  $E_{\pm 2}$  fine-structure state has the strongest ex-ph coupling amongst the  $1S_{(e)}1S_{3/2(h)}$  exciton fine-structure states of wurtzite CdSe QDs. This assumption has been recently verified by low temperature (2-20 K) spectroscopic measurements on single CdSe/ZnS core/shell QDs (core diameter = 8 nm), which allowed the direct observation of the lowest two  $1S_{(e)}1S_{3/2(h)}$  exciton zero-phonon lines and accompanying LO-phonon replicas.<sup>[28]</sup> These experiments clearly demonstrated that the ex-ph coupling of the  $E_{\pm 2}$  state is much stronger than that of the  $E_{\pm 1}^L$  state (*viz.*,  $S = 0.2$  and  $\sim 0$ , respectively).<sup>[28]</sup> The large ex-ph coupling strength for the  $E_{\pm 2}$  state can be understood by considering that phonon-assistance is very effective in relaxing selection rules by symmetry breaking/mixing,<sup>[65,83]</sup> and will be

active even at low temperatures for processes involving the creation of phonons (*viz.*, Stokes LO-phonon replicas, such as those observed in the low temperature FLN and PLE spectra of CdSe QDs). It is therefore clear that the large S-values extracted from low temperature ( $\leq 10$  K) FLN and PLE spectra of CdSe QDs reflect the intrinsic ex-ph coupling strength of the  $E_{\pm 2}$  exciton fine-structure state.

Based on the above discussion it can be concluded that the S values observed in the present work for CdSe QDs at 4.2 K (*viz.*,  $S = 1.0 \pm 0.2$  and  $0.85 \pm 0.15$ , for 3 nm and 4.3 nm diameter QDs, respectively) reflect the intrinsic ex-ph coupling, since they are in good agreement with the values reported in the literature for FLN measurements on similarly sized CdSe QDs at comparable temperatures (*viz.*,  $S = 1.3$  for 3.3 nm diameter TOPO capped CdSe QDs at 5 K,<sup>[24]</sup> and 0.8 for 3.6 nm diameter CdSe cores in CdSe/CdS core/shell QDs at 4.2 K<sup>[27]</sup>). The results presented above thus clearly demonstrate that the intrinsic exciton-LO-phonon coupling strength at 4.2 K increases from

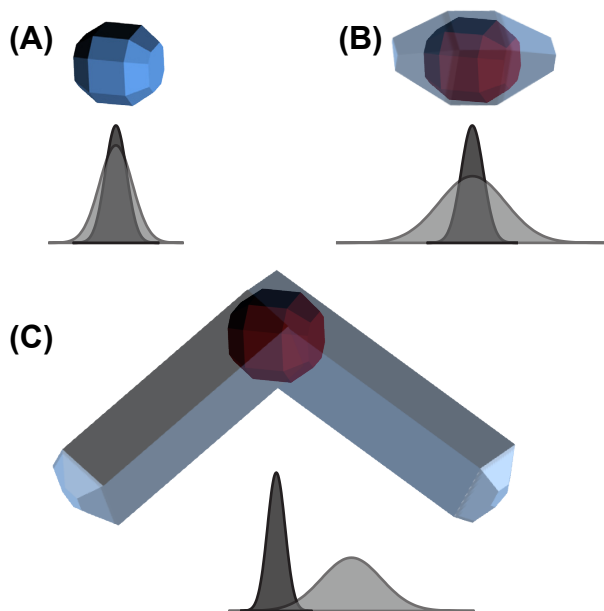


**Figure 6.10** – Schematic illustration of the spatial distribution of the electron and hole wave functions (light and dark gray respectively) in the NCs investigated in this work. (a) CdSe QDs, (b) CdTe/CdSe Type-I<sup>1/2</sup> HNCs, and (c) CdTe/CdSe Type-II HNCs.

CdSe QDs ( $S= 0.8-1.0$ ) to Type-I<sup>1/2</sup> CdTe/CdSe HNCs ( $S= 1.5$ ), and from these to Type-II CdTe/CdSe HNCs ( $S= 2.9$ ). The essential difference between these three types of colloidal NCs is that the overlap between the electron and hole wave functions progressively decreases from single composition CdSe QDs to Type-II CdTe/CdSe HNCs (figure 6.10).

The CdSe QDs investigated here have a radius of 1.5 and 2.15 nm, and are thus in the strong quantum confinement regime, since the exciton Bohr radius in bulk CdSe is 4.9 nm.<sup>[60]</sup> We note, however, that these sizes are not sufficiently small to induce significant confinement effects in the hole wave function (electron and hole Bohr radii in bulk CdSe are 3.8 and 1.1 nm, respectively).<sup>[60]</sup> This implies that the distribution of the hole and the electron wave functions in CdSe QDs may be considerably different for different exciton (fine-structure) states. The hole wave function in CdTe/CdSe HNCs is confined to the CdTe core, already for very small CdSe volume fractions.<sup>[57]</sup> Therefore, the evolution of the optical properties of CdTe/CdSe HNCs with increasing CdSe volume fraction is determined by the localization regime of the electron wave function.<sup>[57]</sup> In Type-I<sup>1/2</sup> CdTe/CdSe HNCs the electron wave function is delocalized over the whole HNC, while in Type-II CdTe/CdSe HNCs the electron wave function is centered in the CdSe segment of the HNC.<sup>[57]</sup> As a result of the change in the spatial distribution of the electron and hole wave functions, the electron-hole overlap in CdTe/CdSe HNCs progressively decreases with the growth of the CdSe segment. This leads to an increasingly larger exciton polarization, which in turn enhances the ex-ph coupling strength. The present results provide novel insights in the nature of spatially indirect exciton transitions, showing that the featureless absorption tail typically associated with the formation of spatially indirect excitons consists primarily of phonon-assisted exciton transitions, in agreement with the model proposed in ref. [57].

## 6.4 – Conclusion

In conclusion, LO-phonon progressions are clearly observed in the low temperature (4.2 K) PLE spectra of different types of colloidal NCs. The strength of the exciton-LO-phonon coupling, as reflected by the Huang-Rhys parameter  $S$ , is shown to increase from CdSe QDs ( $S= 0.8-1.0$ ) to Type-I<sup>1/2</sup> CdTe/CdSe HNCs ( $S= 1.5$ ), and from these to Type-II CdTe/CdSe HNCs ( $S= 2.9$ ). This trend can be explained by the decrease in the electron-hole wave function overlap that accompanies the gradual increase in the CdSe volume fraction in the HNCs, as the electron wavefunction gradually localizes in the CdSe segment. The decrease in the electron-hole overlap

leads to larger exciton polarizations, which in turn enhance the exciton-LO-phonon coupling via the Fröhlich interaction. The results provide novel insights in the nature of spatially indirect exciton transitions, showing that the featureless absorption tail typically associated with the formation of spatially indirect excitons consists primarily of phonon-assisted exciton transitions. Moreover, this work demonstrates that compositional control of semiconductor heteronanocrystals can be used as a very effective tool to tailor the exciton-phonon coupling strength of nanoscale excitons.

## REFERENCES

1. C. de Mello Donegá, *Chem. Soc. Rev.* 2011, 40, 1512-1546.
2. A. Pandey, P. Guyot-Sionnest, *Science* 2008, 322, 929-932.
3. S. S. Lo, T. Mirkovic, C. Chuang, C. Burda, G. D. Scholes, *Adv. Mater.* 2011, 23, 180-197.
4. D. Oron, M. Kazes, U. Banin, *Phys. Rev. B.* 2007, 75, 035330.
5. S. Brovelli, R. D. Schaller, S. A. Crooker, F. Garcia-Santamaria, Y. Chen, R. Viswanatha, J. A. Hollingsworth, H. Htoon, V. I. Klimov, *Nature Comm.* 2011, 2, 280.
6. E. Groeneveld, S. van Berkum, M. M. van Schooneveld, A. Gloter, J. D. Meeldijk, D. J. van den Heuvel, H. C. Gerritsen, C. de Mello Donegá, *Nano Lett.* 2012, 12, 749-757.
7. P. Tyagi, P. Kambhampati, *Phys. Chem. C* 2012, 116, 8154-8160.
8. P. Reiss, M. Protière, L. Li, *Small* 2009, 5, 154-168.
9. D. V. Talapin, J. Lee, M. V. Kovalenko, E. V. Shevchenko, *Chem. Rev.* 2010, 110, 389-458.
10. V. I. Klimov, *Annu. Rev. Phys. Chem.* 2007, 58, 635-673.
11. R. Costi, A. E. Saunders, U. Banin, *Angew. Chem., Int. Ed.* 2010, 49, 4878-4897.
12. P. Kambhampati, *J. Phys. Chem. C* 2011, 115, 22089-22109.
13. P. Kambhampati, *Acc. Chem. Res.* 2012, 44, 1-13.
14. M. A. Stroschio, M. Dutta, 'Phonons in Nanostructures', New York: Cambridge University Press, 2001.
15. E. Hendry, M. Koeberg, F. Wang, H. Zhang, C. de Mello Donegá, D. Vanmaekelbergh, M. Bonn, *Phys. Rev. Lett.* 2006, 96, 057408.
16. H. Wang, C. de Mello Donegá, A. Meijerink, M. Glasbeek, *J. Phys. Chem. B* 2006, 110, 733-737.
17. M. C. Beard, A. G. Midgett, M. C. Hanna, J. M. Luther, B. K. Hughes, A. J. Nozik, *Nano Lett.* 2010, 10, 3019-3027.
18. A. Boulesbaa, A. Issac, D. Stockwell, Z. Huang, J. Huang, J. Guo, T. Lian, *J. Am. Chem. Soc.* 2007, 129, 15132-15133.
19. D. Hannah, N. J. Dunn, S. Ithurria, D. V. Talapin, L. X. Chen, M. Pelton, G. Schatz, R. D. Schaller, *Phys. Rev. Lett.* 2011, 107, 177403.
20. A. J. Houtepen, D. Kockmann, D. Vanmaekelbergh, *Nano Lett.* 2008, 8, 3516-3520.
21. A. L. Rogach, T. A. Klar, J. M. Lupton, A. Meijerink, J. Feldmann, *J. Mater. Chem.* 2009, 19, 1208-1221.
22. S. F. Wuister, R. Koole, C. de Mello Donegá, A. Meijerink, *J. Phys. Chem. B* 2005, 109, 5504-5508.
23. T. J. Liptay, L. F. Marshall, P. S. Rao, R. J. Ram, M. G. Bawendi, *Phys. Rev. B* 2007, 76, 155314.

24. M. Nirmal, C. B. Murray, M. G. Bawendi, *Phys. Rev. B* 1994, 50, 2293-2300.
25. D. J. Norris, A. L. Efros, M. Rosen, M. G. Bawendi, *Phys. Rev. B* 1996, 53, 16347-16354.
26. M. Nirmal, D. J. Norris, M. Kuno, M. G. Bawendi, A. L. Efros, M. Rosen, *Phys. Rev. Lett.* 1995, 75, 3728-3731.
27. F. J. P. Wijnen, J. H. Blokland, C. T. K. Chin, P. C. M. Christianen, J. C. Maan, *Phys. Rev. B* 2008, 78, 235318.
28. L. Biadala, Y. Louyer, Ph. Tamarat, B. Lounis, *Phys. Rev. Lett.* 2009, 103, 037404.
29. V. M. Huxter, G. D. Scholes, *J. Chem. Phys.* 2010, 132, 104506.
30. D. Oron, A. Aharoni, C. de Mello Donegá, J. van Rijssel, A. Meijerink, U. Banin, *Phys. Rev. Lett.* 2009, 102, 177402.
31. S. Nomura, T. Kobayashi, *Phys. Rev. B* 1992, 45, 1305-1316.
32. V. M. Fomin, V. N. Gladilin, J. T. Devreese, E. P. Pokatilov, S. N. Balaban, S. N. Klimin, *Phys. Rev. B* 1998, 57, 2415-2425.
33. D. V. Melnikov, W. B. Fowler, *Phys. Rev. B* 2001, 64, 245320.
34. C. Delerue, M. Lannoo, 'Nanostructures: Theory and Modelling', Berlin: Springer-Verlag, 2004.
35. A. M. Kelley, *ACS Nano* 2011, 5, 5254-5262.
36. S. Schmitt-Rink, D. A. B. Miller, D. S. Chemla, *Phys. Rev. B* 1987, 35, 8113-8125.
37. R. Heitz, I. Mukhametzhanov, O. Stier, A. Madhukar, D. Bimberg, *Phys. Rev. Lett.* 1999, 83, 4654-4657.
38. J. Martin, F. Cichos, F. Huisken, C. von Borczyskowski, *Nano Lett.* 2008, 8, 656-660.
39. S. H. Kwok, P. Y. Yu, C. H. Tung, Y. H. Zhang, M. F. Li, C. S. Peng, J. M. Zhou, *Phys. Rev. B* 1999, 59, 4980-4984.
40. J. J. Shiang, S. H. Risbud, A. P. Alivisatos, *J. Chem. Phys.* 1993, 98, 8432-8442.
41. M. J. Seong, O. I. Micic, A. J. Nozik, A. Mascarenhas, H. M. Cheong, *Appl. Phys. Lett.* 2003, 82, 185-187.
42. T. D. Krauss, F. W. Wise, *Phys. Rev. B* 1997, 55, 9860-9865.
43. D. M. Sagar, R. R. Cooney, S. L. Sewall, E. A. Dias, M. M. Barsan, I. S. Butler, P. Kambhampati, *Phys. Rev. B* 2008, 77, 235321.
44. H. Lange, M. Mohr, M. Artemyev, U. Woggon, T. Niermann, C. Thomsen, *Phys. Status Sol. (b)* 2010, 247, 2488-2497.
45. M. R. Salvador, M. A. Hines, G. D. Scholes, *J. Chem. Phys.* 2003, 118, 9380-9388.
46. M. C. Klein, F. Hache, D. Ricard, C. Flytzanis, *Phys Rev B* 1990, 42, 11123-11132.
47. A. P. Alivisatos, T. D. Harris, P. J. Carroll, M. L. Steigerwald, L. E. Brus, *J. Chem. Phys.* 1989, 90, 3463-3468.
48. Z. Sun, I. Swart, C. Delerue, D. Vanmaekelbergh, P. Liljeroth, *Phys. Rev. Lett.* 2009, 102, 196401.

49. S. A. Empedocles, D. J. Norris, M. G. Bawendi, *Phys. Rev. Lett.* 1996, 77, 3873-3876.
50. M. J. Fernée, B. N. Littleton, S. Cooper, H. Rubinsztein-Dunlop, D. E. Gómez, P. Mulvaney, *J. Phys. Chem. C*. 2008, 112, 1878-1884.
51. A. Garcia-Cristobal, A. W. E. Minnaert, V. M. Fomin, J. T. Devreese, T.; A. Yu Silov, J. E. M. Haverkort, J. H. Wolter, *Phys. Stat. Sol. (b)* 1999, 215, 331-336.
52. A. Lemaitre, A. D. Ashmore, J. J. Finley, D. J. Mowbray, M. S. Skolnick, M. Hopkinson, T. F. Krauss, *Phys. Rev. B* 2001, 63, 161309(R).
53. S. Kalliakos, X. B. Zhang, T. Taliercio, P. Lefebvre, B. Gil, N. Grandjen, B. Damilano, J. Massies, *Appl. Phys. Lett.* 2002, 80, 428-430.
54. Q. Zhang, J. Zhang, M. I. B. Utama, B. Peng, M. De la Mata, J. Arbiol, Q. Xiong, *Phys. Rev. B* 2012, 85, 085418.
55. G. Chilla, T. Kipp, T. Menke, D. Heitmann, M. Nikolic, A. Fromsdorf, A. Kornowski, S. Förster, H. Weller, *Phys. Rev. Lett* 2008, 100, 057403.
56. P. T. K. Chin, C. de Mello Donegá, S. S. van Bavel, S. C. J. Meskers, N. A. J. M. Sommerdijk, R. A. J. Janssen, *J. Am. Chem. Soc.* 2007, 129, 14880-14886.
57. C. de Mello Donegá, *Phys. Rev. B.* 2010, 81, 165303.
58. C. de Mello Donegá, S. G. Hickey, S. F. Wuister, D. Vanmaekelbergh, A. Meijerink, *J. Phys. Chem. B* 2003, 107, 489-496.
59. L. Qu, X. Peng, *J. Am. Chem. Soc.* 2002, 124, 2049-2055.
60. C. de Mello Donegá, R. Koole, *J. Phys. Chem. C* 2009, 113, 6511-6520.
61. C. de Mello Donegá, A. Meijerink, G. Blasse, *J. Lumin.* 1994, 62, 189-201.
62. U. Rössler (editor), 'II-VI and I-VII Compounds; Semimagnetic compounds', 'Landolt-Börnstein – Group III Condensed Matter', Vol. 41, Berlin: Springer-Verlag, 1999.
63. P. Horodysky, P. Hlidek, *Phys. Stat. Sol. (b)* 2006, 243, 494-501.
64. D. J. Norris, M. G. Bawendi, *Phys. Rev. B* 1996, 53, 16338-16346.
65. A. L. Efros, M. Rosen, M. Kuno, M. Nirmal, D. J. Norris, M. G. Bawendi, *Phys. Rev. B* 1996, 54, 4843-4856.
66. A. Franceschetti, H. Fu, L. W. Wang, A. Zunger, A.; *Phys. Rev. B* 1999, 60, 1819-1829.
67. K. Leung, S. Pokrant, K. B. Whaley, *Phys. Rev. B* 1998, 57, 12291-12301.
68. O. Labeau, P. Tamarat, B. Lounis, *Phys. Rev. Lett.* 2003, 90, 257404.
69. C. de Mello Donegá, M. Bode, A. Meijerink, *Phys. Rev. B* 2006, 74, 085320.
70. D. J. Norris, M. G. Bawendi, *J. Chem. Phys.* 1995, 103, 5260-5268.
71. I. Moreels, G. Raino, R. Gomes, Z. Hens, T. Stoferle, R. F. Mahrt, *ACS Nano* 2011, 5, 8033-8039.
72. J. He, S. S. Lo, J. Kim, G. D. Scholes, *Nano Lett.* 2008, 8, 4007-4013.
73. M. Kuno, J. K. Lee, B. O. Dabbousi, F. V. Mikulec, M. G. Bawendi, *J. Chem. Phys.* 1997, 106, 9869-9882.

74. M. Jones, S. S. Lo, G. D. Scholes, *J. Phys. Chem. C* 2009, 113, 18632-18642.
75. D. Valerini, A. Creti, M. Lomascolo, L. Manna, R. Cingolani, M. Anni, *Phys. Rev. B* 2005, 71, 235409.
76. A. Pandey, P. Guyot-Sionnest, *Science* 2008, 322, 929-932.
77. R. Koole, P. Schapotschnikow, C. de Mello Donegá, T. J. H. Vlugt, A. Meijerink, *ACS Nano* 2008, 2, 1703-1714.
78. V. V. Matylitsky, L. Dworak, V. V. Breus, T. Basché, J. Wachtveitl, *J. Am. Chem. Soc.* 2009, 131, 2424-2424.
79. S. F. Wuister, I. Swart, F. van Driel, S. G. Hickey, C. de Mello Donegá, *Nano Lett.* 2003, 3, 503-507.
80. S. A. Crooker, T. Barrick, J. A. Hollingsworth, V. I. Klimov, *Appl. Phys. Lett.* 2003, 82, 2793-2795.
81. R. R. Cooney, S. L. Sewall, E. A. Dias, D. M. Sagar, K. E. H. Anderson, P. Kambhampati, *Phys. Rev. B* 2007, 75, 245311.
82. C. H. Chuang, T. L. Doane, S. S. Lo, G. D. Scholes, C. Burda, *ACS Nano* 2011, 5, 6016-6024.
83. B. Henderson, G. F. Imbusch, 'Optical Spectroscopy of Inorganic Solids', Oxford: Oxford University Press, 1989.
84. S. A. Empedocles, M. G. Bawendi, *Science* 1997, 278, 2114-2117.
86. J. H. Blokland, 'Optical properties of low-dimensional semiconductor nanostructures', (Ph.D. Thesis), Universiteit Nijmegen, Nijmegen, 2010.







## Chapter 7

# **Size dependence of the Exciton Transitions in Colloidal CdTe Quantum Dots**

—  
*Absorption, Analysis and  
Agreement: experimental versus  
calculations*

## Abstract

*In this chapter we present a detailed investigation of the size dependence of the optical transitions of colloidal CdTe QDs ranging in diameter from 2.9 to 14.8 nm. The energy integrated absorption cross section per CdTe unit is investigated in detail for the lowest two exciton transitions ( $1S_{3/2(h)}-1S_{(e)}$  and  $2S_{3/2(h)}-1S_{(e)}$ ) and shown to increase with decreasing size, although the size dependence of the  $2S_{3/2(h)}-1S_{(e)}$  is less pronounced. The experimental absorption spectra are compared to spectra calculated by using a tight-binding approach. The calculations were carried out with electron-hole configuration interaction (CI) and without (single-particle, SP). The agreement between the experimental values and spectra calculated by using the CI approach is excellent, demonstrating the importance of the configuration interaction between electron and hole states in CdTe QDs.*

## 7.1 – Introduction

Colloidal semiconductor nanocrystals (NCs) combine size- and shape-dependent properties with easy surface manipulation and solution processing.<sup>[1,2]</sup> These characteristics have turned them into promising materials for a variety of applications.<sup>[1,2]</sup> A comprehensive understanding of the size- and shape-dependence of quantum confinement effects is essential to realize the full potential of these nanomaterials. Over the last two decades, this has motivated research groups worldwide to investigate the synthesis and optoelectronic properties of a wide variety of semiconductor NC compositions.<sup>[1-7]</sup> CdSe and CdTe are the most investigated of these materials and have been frequently used as model systems to unravel the photophysical properties of nanoscale excitons<sup>[8-10]</sup> and to understand the complex chemistry involved in the nucleation and growth of colloidal NCs.<sup>[11-13]</sup> This latter aspect has led to a remarkable degree of control over the size and shape of CdTe and CdSe NCs.<sup>[1-3,14]</sup> The recent availability of high-quality colloidal CdTe and CdSe NCs has made it possible to investigate their optoelectronic properties in more detail, both from fundamental<sup>[8-10,15]</sup> and applied perspectives.<sup>[2,15-20]</sup> Colloidal CdTe and CdSe NCs have also attracted increasing interest in recent years as components of colloidal semiconductor heteronanocrystals.<sup>[1,2,7,21-24]</sup>

Despite this intense research activity the impact of quantum confinement effects on the electronic structure of CdTe NCs (or quantum dots, QDs) is not yet fully understood. The early work on the size-dependent electronic transitions of CdTe QDs was performed on ensembles of QDs embedded in glass,<sup>[25,26]</sup> and was thus hampered by the large size dispersion of the samples

and poor quality of the QD-glass interfaces. The availability of colloidal CdTe QDs with small size dispersion (<10%) and low defect concentrations (as attested by room temperature photoluminescence quantum efficiencies in the 30-80% range)<sup>[14,27]</sup> has led to a renewed interest in the fundamental properties of colloidal CdTe QDs. In recent years, many experimental studies have been published addressing a variety of topics related to the size-dependence of the electronic states and exciton fine-structure of CdTe QDs (*e.g.*, size-, temperature-, and magnetic-field dependence of the exciton lifetimes;<sup>[28-31]</sup> energy levels and exciton fine structure;<sup>[32]</sup> size-dependence of the absorption cross section and oscillator strength of the lowest energy exciton transition;<sup>[31,33]</sup> as well as sizing curves<sup>[31,33]</sup>). In contrast, theoretical studies have been scarce, and to date there are only a few calculations of the size-dependence of the exciton transitions in CdTe QDs in the envelope-function approximation.<sup>[26,34]</sup> In this work, we report a combined experimental and theoretical study of the size-dependence of the exciton transitions in high-quality colloidal CdTe QDs. The size-dependence of the absorption cross sections of the lowest two exciton transitions is also addressed. The theory is based on an atomistic tight-binding description of the electronic states. Because the size range investigated (*viz.*, 2.9 to 14.8 nm diameter) spans from the strong to the intermediate confinement regimes (exciton Bohr radius of CdTe is 7.3 nm<sup>[31]</sup>), excitonic effects are included in the calculations of the optical absorption spectra using a configuration-interaction (CI) approach. The agreement between the experimental and theoretical values is excellent. This chapter is organized as follows. First, the experimental and theoretical methods are described. Subsequently, the basic characteristics of the CdTe NCs (size and shape, absorption and emission spectra, crystal structure) are presented, followed by a quantitative analysis of the exciton transitions observed in the absorption spectra. Finally, the experimental and theoretical results are compared and discussed.

## 7.2 – Methods

**Chemicals:** Octadecylamine (ODA, >90%) was purchased from Fluka. Tributylphosphine (TBP, 99%) and Tetradecylphosphonic acid (TDPA, min 97%) were purchased from Bunschwig and STREM Chemicals, respectively. 1-Octadecene (ODE, tech. grade, 90%) and trioctylphosphine (TOP, tech. grade > 90%) were purchased from Aldrich. Cadmium acetate dihydrate (Cd(Ac)<sub>2</sub>·2H<sub>2</sub>O, 99.99+%) and tellurium powder (99.999%, ≤250 micron) were purchased from Heraeus. Oleic acid (tech. grade 90%), and anhydrous solvents (toluene, hexane, methanol, and acetone) were purchased from

Sigma-Aldrich. All reagents were used as purchased with the exception of ODE and ODA. Before use, ODE and ODA were dried and degassed under vacuum (3 h at 120°C).

Synthesis of colloidal CdTe NCs with diameter in the 2.9 nm to 7.3 nm range: CdTe QDs in 2.9 – 7.3 nm range were synthesized by using an adaptation of the method reported by Yu et al.<sup>[14]</sup> A stock solution of Cd-TDPA precursor (Cd-A) was made by heating 1.76 g (7.08 mmol) Cd(Ac)<sub>2</sub>·2H<sub>2</sub>O, 4.34 g TDPA and 10.61 mL (8.37 g) ODE to 300°C under N<sub>2</sub> atmosphere. After completion of the reaction the temperature was lowered to ~170°C and the solution was degassed under vacuum. Finally, 12.9 mL (10.18 g) ODE and 2 mL (1.66 g) TOP were added. The stock solution of the Te precursor (Te-A) was made by dissolving 0.31 g (2.41 mmol) Te in 5.70 g (7.04 mL) TBP in a glove-box under nitrogen (< 5 ppm O<sub>2</sub> and H<sub>2</sub>O). The synthesis was performed in a glove-box under N<sub>2</sub> (< 5 ppm O<sub>2</sub> and H<sub>2</sub>O). 0.4 g of Cd-A stock solution and 3.6 g ODE were loaded in a reaction flask and heated to 300°C. At this temperature a mixture of 0.5 g Te-A stock and 1.5 g (1.9 mL) ODE was swiftly injected under stirring. The temperature was allowed to cool to ~270°C and kept constant. A 1 mL aliquot was taken 10 min after the Te injection. The synthesis was continued 12 min after the injection of Te by alternate dropwise additions of Cd and Te stock solutions, which are referred to as addition cycles. Every addition cycle took about 3 min, and was started by 10 drops of Cd-A stock solution, followed by alternate additions of Cd-A and Te-A stock (10 drops at a time) until the total intended volume had been added. The precursors were allowed to react for 12 min after each addition cycle. In the first four addition cycles 0.26 g Te-A stock, and a mixture of 0.31 g Cd-A stock and 0.35 g ODE were added. From addition cycle five to eight 0.5 g Te-A stock, and a mixture of 0.43 g Cd-A stock and 0.17 g ODE were added. In the final addition cycle 1 g Te-A stock and 0.36 g Cd-A stock were added. The mixture of Cd-A stock solution and ODE was pre-heated to 250°C and added as a hot solution, whereas the Te-A stock was kept at ambient temperature. Aliquots of ~1mL were taken from the reaction mixture 3 min before the start of every addition cycle. The temperature was lowered to 250°C after the second addition cycle. The synthesis was stopped by removing the heating mantle 18 min after completion of the final addition cycle.

Purification of colloidal CdTe NCs with diameter in the 2.9 nm to 7.3 nm range: The CdTe NCs were purified by mixing a solution of the crude reaction mixture in anhydrous hexane, and anhydrous methanol (1:1:1 volume ratio). The colored top layer containing the NCs was removed and the NCs were

precipitated by adding anhydrous acetone (1:1 volume ratio). The sediment was isolated by centrifugation (3000 rpm, 15 min), and redissolved in anhydrous toluene (or in ODE if they were to be used as seeds).

**Synthesis of colloidal CdTe NCs larger than 8 nm:** CdTe NCs with diameter larger than 8 nm were grown from 7.3 nm diameter CdTe NC seeds by slow and alternate addition of Cd and Te precursors. Stock solution of 0.093 M Cd-Oleate in ODE (Cd-B) was made by heating 0.926 g  $\text{Cd}(\text{Ac})_2 \cdot 2\text{H}_2\text{O}$  and 2.92 mL oleic acid in 37.05 mL ODE to 100°C under  $\text{N}_2$  for 1h. Subsequently this Cd-stock solution was dried and degassed under vacuum (2 h at 100°C). A stock solution of 0.1M Te in TOP and ODE (stock Te-B, TOP:ODE, 1:9 volume ratio) was prepared by dissolving 0.514 g Te powder in 4 mL TOP and 36 mL ODE under  $\text{N}_2$ . The synthesis was performed in a glove-box under nitrogen (< 5 ppm  $\text{O}_2$  and  $\text{H}_2\text{O}$ ). ODA (0.81 g), ODE (1.5 mL), and 1.3 mL of CdTe NC (7.3 nm diameter) stock solution in ODE ( $37.5 \times 10^{-9}$  mol CdTe NCs) were loaded in a reaction flask and heated to 230°C. The amount of Cd and Te needed for additional layers was calculated based on a Cd-Te monolayer thickness of 0.375 nm. The synthesis was started by the addition of Cd-B stock solution of the first monolayer, and continued with alternate additions of Te-B and Cd-B stock solutions (each during ~2 min). Before every Cd-B stock solution addition, 0.5 mL aliquots were taken from the reaction mixture. Each monolayer was allowed to grow for 30 minutes. After the third monolayer the waiting time was increased to 45 min. The synthesis was finished after the addition of fourteen monolayers.

**Purification of colloidal CdTe NCs larger than 8 nm:** The CdTe NCs were purified by precipitation from a solution of the crude reaction mixture in toluene (1:1 volume ratio) by adding anhydrous methanol. The sediment was isolated by centrifugation (3000 rpm, 15 min) and redissolved in anhydrous toluene. By using post-preparative size selective precipitation, ensembles of monodisperse (5 - 7% standard deviation) spherical CdTe NCs of 14.8 nm were isolated from the reaction mixture.

**Characterization:** Absorption spectra were measured on a double beam Perkin-Elmer Lambda 16 UV/Vis spectrometer (scan rate: 1 nm/s). Photoluminescence (PL) and PL excitation (PLE) spectra were recorded by an Edinburgh Instruments FLS920 Spectrofluorimeter equipped with a 450W Xenon lamp as excitation source and double grating monochromators. Samples for optical measurements were prepared by directly dissolving the crude reaction mixture in anhydrous toluene under nitrogen and

stored in sealed cuvettes. All measurements were performed at room temperature. In order to avoid deviations from linearity in the absorption spectra, all measurements were carried out on samples with a low optical density ( $\leq 0.18$  at lowest energy optical transition). Transmission electron microscopy (TEM) was performed using a Tecnai microscope (FEI TECNAI G2 T20F) operating at 200 kV. The TEM measurements were carried out on CdTe NC samples which had been purified in order to remove the excess of organic molecules and unreacted precursors. Samples for TEM imaging were prepared by dipping a carbon-coated copper (400-mesh) TEM grid into a toluene solution of CdTe NCs. The excess liquid was removed by blotting using filter paper. X-Ray Diffraction (XRD) diagrams were obtained by using a PW 1729 Philips diffractometer, equipped with a Cu K $_{\alpha}$  X-ray source ( $\lambda=1.5418 \text{ \AA}$ ). Samples for XRD analysis were prepared by depositing a concentrated solution of purified CdTe NCs on a Si wafer substrate under inert atmosphere.

**Analysis of the absorption spectra:** At energies well above the absorption edge, the absorption spectrum of NCs becomes featureless because quantum confinement effects become no longer relevant (spectral density of states is approaching that of bulk).<sup>[31]</sup> Normalizing the absorption spectra at sufficiently high energies ( $E \geq 3.1 \text{ eV}$ ) is equivalent to adjusting the volume fraction of semiconductor material in solution to be the same for all samples.<sup>[31]</sup> This normalization allows the energy integrated absorption cross section per CdTe ion pair unit for each transition to be extracted from the spectra. To avoid interference of solvent and surfactant absorption transitions at higher energies normalization at 3.1 eV is used. The absorption cross sections and energy positions of the optical transitions can be extracted from the normalized absorption spectra (in transmittance scale) by fitting the spectra to a sum of multiple Gaussian bands (average  $\chi^2 = 0.999$  stdv = 0.0009) (an illustrative example is given in figure 7.1). The maximum of each Gaussian band was noted as the energy position of each exciton transition and the integrated area of each Gaussian band was taken as the integrated absorption cross section per CdTe ion pair unit of the corresponding transition.

**Tight-binding calculations:** Calculations were performed by C. Delerue, G. Allan from the IEMN institute (department ISEN) in Lille (France) and Y.-M. Niquet from 'Laboratoire de simulation atomistique (L Sim)' in Grenoble (France). The electronic structure of zinc blende (ZB) CdTe NCs was calculated in tight-binding following the method described in ref. [35].



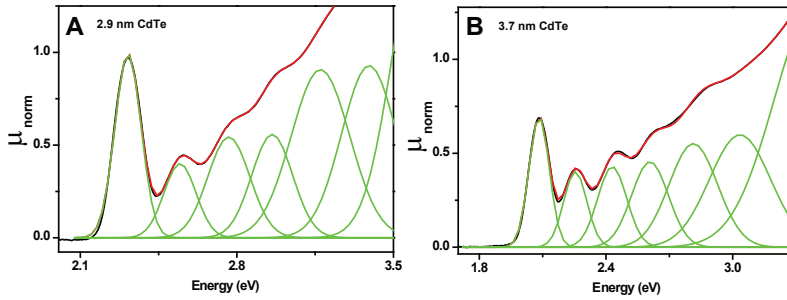


**Figure 7.1** – Absorption spectra (black lines) of colloidal CdTe NCs with 2.9 nm (a) and 3.7 nm (b) diameter fit to a sum of Gaussians (green lines). The spectra have been normalized at 3.1 eV.

The NCs are modeled as spheres. The Hamiltonian matrix is written in a  $sp_3d_5s^*$  basis, the overlaps are neglected, and the hopping integrals are restricted to first nearest neighbor interactions. Because Cd and Te are heavy elements, the spin-orbit coupling is included, which requires doubling the basis set. The tight-binding parameters are obtained by fitting a reference band structure at the main points of the Brillouin zone and in a large energy range (figure 7.2). This reference band structure was calculated using the ab-initio pseudopotential code ABINIT (ref. [36]) in the local density approximation. A scissor operator was applied to adjust the bandgap to its experimental value at 0K.

The tight-binding calculation provides the single-particle (SP) states from which the optical absorption spectra can be calculated in the independent-particle approximation. SP states also serve as input for calculations of the excitonic states in a configuration- interaction (CI) technique.<sup>[37]</sup> The excitonic states are defined as linear combinations of electron-hole states as follows:

$$|\psi_{exc}^i\rangle = \sum_{vc} a_{cv}^i |\psi_{vc}\rangle \quad (7.1)$$

where  $|\psi_{vc}\rangle$  is a Slater determinant which describes the excitation of a single electron from the valence state  $|v\rangle$  of energy  $\varepsilon_v$  to a conduction state  $|c\rangle$  of energy  $\varepsilon_c$ , the ground state  $|0\rangle$  corresponding to all valence states filled and all conduction states empty. The matrix elements of the excitonic Hamiltonian in this basis are given by<sup>[38]</sup>:

$$\begin{aligned}
\langle \psi_{vc} | H | \psi_{v'c'} \rangle &= ([\varepsilon_c + \Sigma_c] - [\varepsilon_v + \Sigma_v]) \delta_{cc'} \delta_{vv'} \\
&- \int c^*(\mathbf{x}_1) v^*(\mathbf{x}_2) V_{coul}(\mathbf{r}_1, \mathbf{r}_2) c'(\mathbf{x}_1) v'(\mathbf{x}_2) d\mathbf{x}_1 d\mathbf{x}_2 \\
&+ \int c^*(\mathbf{x}_1) v^*(\mathbf{x}_2) V_{coul}(\mathbf{r}_1, \mathbf{r}_2) v'(\mathbf{x}_1) c'(\mathbf{x}_2) d\mathbf{x}_1 d\mathbf{x}_2
\end{aligned} \tag{7.2}$$

where  $\mathbf{x}_1$  stands for  $(\mathbf{r}_1, \xi_1)$  in which  $\mathbf{r}_1$  is the position and  $\xi_1$  the spin variable of the particle 1. The second term in Eq. (7.2) describes the direct Coulomb interaction between the electron and the hole, the third one comes from the exchange interaction.  $V_{coul}(\mathbf{r}_1, \mathbf{r}_2)$  represents the energy potential of a charge  $+e$  at  $\mathbf{r}_1$  induced by a charge  $+e$  at  $\mathbf{r}_2$ :

$$V_{coul}(\mathbf{r}_1, \mathbf{r}_2) = \int \varepsilon^{-1}(\mathbf{r}_1, \mathbf{r}) \frac{e^2}{|\mathbf{r}_2 - \mathbf{r}|} d\mathbf{r} \tag{7.3}$$

in which  $\varepsilon^{-1}(\mathbf{r}_1, \mathbf{r}_2)$  is the generalized dielectric constant taken here in the static limit. In the case of spherical NCs that we consider here,  $V_{coul}(\mathbf{r}_1, \mathbf{r}_2)$  is easily obtained using classical electrostatics assuming a dielectric sphere of dielectric constant  $\varepsilon_{in}$  (*viz.*, 7.4, the value for bulk CdTe) in a medium of dielectric constant  $\varepsilon_{out}$  (*viz.*, 2.2, since toluene was used as solvent in the experiments).

The term  $\Sigma_c$  ( $\Sigma_v$ ) in Eq. (7.1) represents the self-energy of the electron (hole) coming from its interaction with the polarization charges induced at the surface by its own presence (see ref.[38] for justification of this methodology):

$$\Sigma_c = \frac{1}{2} \int |c(\mathbf{r}_1)|^2 \lim_{\mathbf{r}_2 \rightarrow \mathbf{r}_1} \left( V_{coul}(\mathbf{r}_1, \mathbf{r}_2) - \frac{e^2}{\varepsilon_{in} |\mathbf{r}_2 - \mathbf{r}_1|} \right) d\mathbf{r}_1 \tag{7.4}$$

The absorption coefficient at the photon energy  $h\nu$  is written as

$$\alpha(h\nu) \propto \sum_i \left| \left\langle 0 \left| \sum_n \mathbf{e} \cdot \mathbf{r}_n \right| \psi_{exc}^i \right\rangle \right|^2 \delta(h\nu - E_i) \tag{7.5}$$

where  $\mathbf{e}$  is the polarization vector of the light and  $\mathbf{r}_n$  is the position of the electron  $n$ . The optical matrix element  $\langle 0 | \sum_n \mathbf{e} \cdot \mathbf{r}_n | \psi_{exc}^i \rangle$  is equal to  $\Sigma_{vc} a_{vc} \langle v | \mathbf{e} \cdot \mathbf{r} | c \rangle$  which is easily calculated in tight-binding.<sup>[38]</sup>

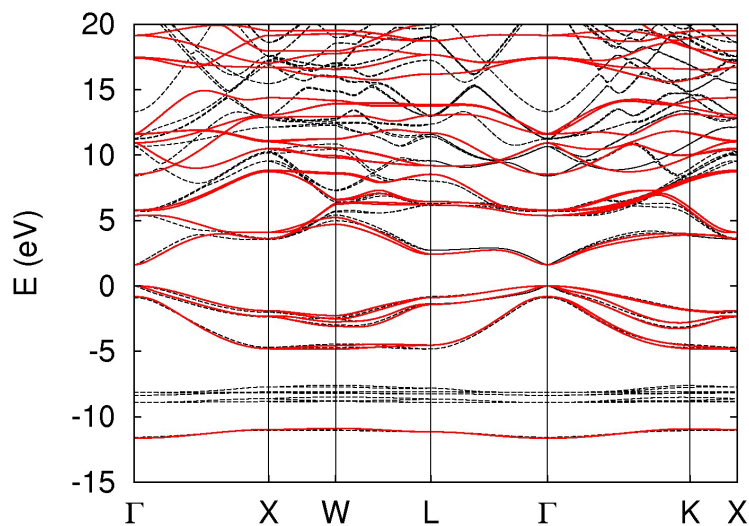


**Figure 7.2** – Reference band structure of CdTe obtained by *ab-initio* pseudopotential DFT calculations and adjusted to the experimental bandgap at 0 K (black dashed lines). The solid red lines are obtained by a tight-binding fitting to the reference *ab-initio* values.

## 7.3 – Results and Discussion

### 7.3.1 – General Characterization

Selected TEM images of the as-synthesized CdTe NC samples are given in figure 7.3. The TEM images demonstrate that the smaller NCs ( $d \leq 5$  nm) are nearly spherical and faceted (size dispersion: 5-7%). As the growth proceeds the NCs become prolate (see, *e.g.*, figure 7.3d, standard deviation: 10%) and at later stages ( $d > 6$  nm) assume a trigonal pyramidal shape (figure 7.3e, size dispersion: ~10%). The largest NCs (14.8 nm diameter, figure 7.3f) are grown by seeded growth from 7.3 nm diameter NCs (figure 7.3e) and recover during the growth a nearly spherical and faceted shape. The XRD diffractograms (figure 7.4) indicate that the NCs crystallize in the wurtzite structure, although the peak broadening induced by finite size effects renders the XRD diffraction patterns of NCs smaller than 4 nm (see, *e.g.*, 3.7 nm diameter in figure 7.4) ambiguous. Moreover, the relative intensity of the (103) diffraction peak is lower than expected for a standard wurtzite structure. This suggests that the NCs contain at least one stacking fault perpendicular to the wurtzite *c*-axis.<sup>[14]</sup> The possibility that zinc blende and wurtzite NCs co-exist can also not be excluded.<sup>[26,39]</sup> The similarity between

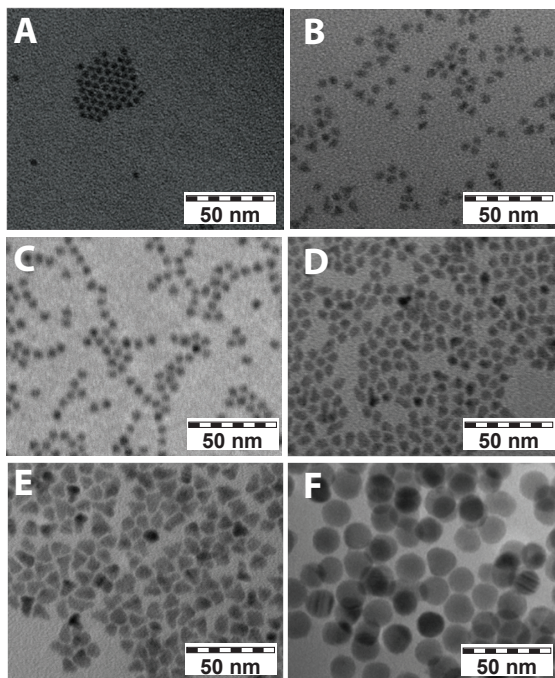


**Figure 7.3** – Overview TEM images of colloidal CdTe nanocrystals of different sizes: (a) 3.7 nm, (b) 4.6 nm, (c) 5.0 nm, (d) 5.6 nm, (e) 7.3 nm, (f) 14.8 nm.

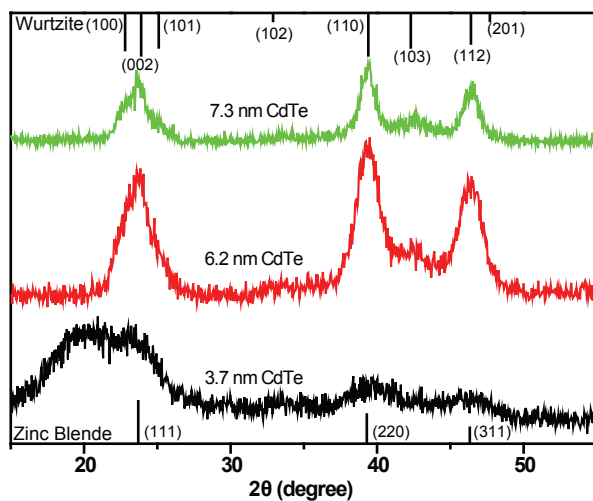


**Figure 7.4** – XRD patterns of 7.3, 6.2, and 3.7 nm diameter CdTe NCs. Solid lines at the top and bottom indicate lattice positions and relative intensities for zinc blende and wurtzite bulk CdTe<sup>[14]</sup>

wurtzite and zinc blende structures and the small activation energy for inter-conversion makes both scenarios very plausible. The potential impact of these structural variations on the optical transitions of CdTe QDs will be addressed later in this chapter.

### 7.3.2 – Size dependence of the optical transitions

The absorption and PL spectra of a size series of CdTe NCs are given in figure 7.5. The efficient PL observed for all samples, and the absence of defect related emission,<sup>[27]</sup> shows that the CdTe NCs investigated in the present work possess well passivated surfaces and low defect concentration. The diameters indicated in figure 7.5 are determined by using an empirical sizing curve correlating the position of the lowest energy absorption transition in CdTe QDs with the QD size.<sup>[31]</sup> Sizing curves provide a very fast and accurate method to determine the average size of an ensemble of QDs, because they are constructed from a large body of experimental data, which (partially) averages out the uncertainties and errors associated with size determination by TEM. Moreover, the average transition energy (*i.e.*, the peak position) of an ensemble of colloidal QDs can be determined with a much larger accuracy than the average size determined from TEM images.

The absorption spectra (figure 7.5a) clearly show multiple sharp peaks

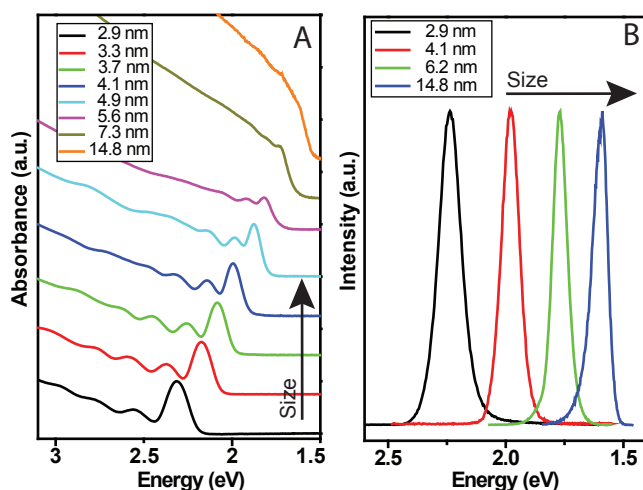


**Figure 7.5** – Absorption (a) and photoluminescence (b) spectra of colloidal CdTe nanocrystals ranging from 2.9 nm to 14.8 nm in diameter.

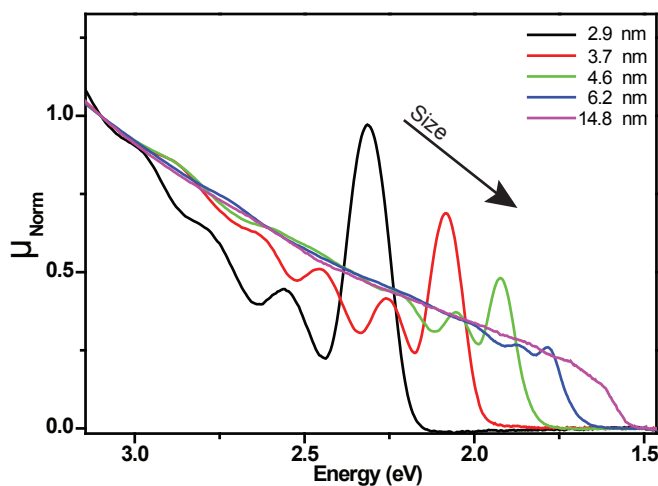


**Figure 7.6** – Absorption spectra of colloidal CdTe nanocrystals in the 2.9 to 14.8 nm diameter range. The spectra have been normalized at 3.1 eV.  $\mu_{norm}$  gives the normalized absorption cross section per CdTe unit.

corresponding to electronic transitions in the CdTe NCs. As a result of quantum confinement effects, these transitions shift towards lower energies as the NC size increases. This shift is also clearly observed in the PL spectra. The lowest energy absorption transition shifts from 2.31 eV to 1.6 eV from 2.9 nm to 14.8 nm diameter CdTe QDs, while the PL maximum shifts from 2.24 eV to 1.59 eV in the same size range. The full-width-at-half-maximum (FWHM) of the PL peak decreases from 114 to 75 meV in the 2.9 to 14.8 nm diameter range. Along with the shift of the peak positions, the energy difference between the optical transitions decreases with increasing QD size. As the transition peaks become increasingly closer they start to overlap, which leads to an increase in broadening of the absorption spectrum with increasing NC size and decrease of the spectral resolution, especially for the higher energy transitions. Up to five exciton transitions can be clearly distinguished in the absorption spectra (figure 7.5a). Following previous theoretical work,<sup>[34]</sup> these transitions are assigned to (1)  $1S_{3/2(h)}-1S_{(e)}$ , (2)  $2S_{3/2(h)}-1S_{(e)}$ , (3)  $1P_{3/2(h)}-1P_{(e)}$ , (4)  $1S_{1/2(h)}-1S_{(e)}$ , and (5)  $1P_{1/2(h)}-1P_{(e)}$ , starting from the lowest energy optical transition.

### 7.3.3 – Integrated absorption cross sections per CdTe unit

Figure 7.6 displays the absorption spectra of selected CdTe QD samples. These spectra are normalized at 3.1 eV to allow for a quantitative comparison of the energy integrated absorption cross section per CdTe unit of the exciton

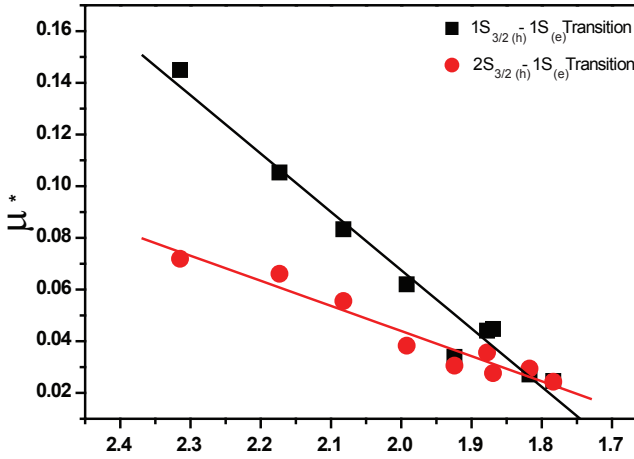


**Figure 7.7** – Size dependence of the relative energy integrated absorption cross section per CdTe unit ( $\mu^*$ ) of the lowest two exciton transitions in CdTe nanocrystals ranging from 2.9 to 14.8 nm diameter. The position of the lowest energy transition is used as a surrogate variable for the QD size. Straight lines are linear fittings to the experimental data.

transitions. Figure 7.6 clearly shows that the relative oscillator strengths of the exciton transitions are redistributed as the QD size increases. The oscillator strength per CdTe unit for the  $1S_{3/2(h)}-1S_{(e)}$  transition increases as the NC size decreases. This is in agreement with previous work from our group, where the size dependence of the energy integrated absorption cross section per CdTe unit was investigated in detail.<sup>[31]</sup> The higher spectral resolution achieved for the presently investigated size series allowed us to study here also the energy integrated absorption cross section of the second lowest energy absorption transition ( $2S_{3/2(h)}-1S_{(e)}$ ), which is presented in figure 7.7 as a function of the energy of the lowest exciton transition ( $1S_{3/2(h)}-1S_{(e)}$ ). The trend for both transitions can be well described by linear fits:

$$\mu^* (1S_{3/2(h)}-1S_{(e)}) = -0.384 (\pm 0.031) + 0.226 (\pm 0.016) * P(\text{eV}) \quad (7.6)$$

$$\mu^* (2S_{3/2(h)}-1S_{(e)}) = -0.150 (\pm 0.018) + 0.097 (\pm 0.009) * P(\text{eV}) \quad (7.7)$$

in which  $P(\text{eV})$  is the position of the lowest energy exciton transition. Figure 7.7 clearly shows that the  $2S_{3/2(h)}-1S_{(e)}$  transition has smaller absorption cross sections per CdTe unit and is less sensitive to quantum confinement effects (smaller slope) than the  $1S_{3/2(h)}-1S_{(e)}$  transition.

### 7.3.4 – Size dependence of the exciton transitions: comparison theory-experiment

Although the experimental results discussed above were obtained for wurtzite CdTe NCs, the calculations presented in this paper were performed for zinc blende CdTe NCs (bulk CdTe crystallizes in the zinc blende structure). To evaluate whether the difference in crystal structures leads to any significant difference in the exciton transitions we compared wurtzite and zinc blende CdTe QDs of similar sizes (3.5 – 4.1 nm). The zinc blende CdTe QD sample is capped by TDPA and has been prepared as described above. The wurtzite CdTe QD sample is capped by dodecylamine and TOP and has been prepared as described in the literature.<sup>[27]</sup> The PLE spectra and XRD diagrams of both samples are presented in figure 7.8. PLE spectra were used instead of absorption spectra because they minimize the effects of inhomogeneous broadening, since PLE spectra are obtained by probing a narrow spectral band of the full ensemble PL, while scanning the excitation energy with high resolution. A small sub-ensemble of NCs is thus spectrally selected and thereby the impact of size inhomogeneities on the exciton transitions is minimized. Analysis of the PLE spectra shown in figure 7.8 leads to the conclusion that there are no significant differences between the optical spectra of wurtzite and zinc blende CdTe QDs. These observations are in agreement with previous reports,<sup>[14]</sup> and imply that the comparison between experimental and theoretical values is justified, despite the differences in the crystal structures. We note that these results also show that the position of the exciton transitions is largely insensitive to the nature of the capping ligands, in line with the behavior previously reported for colloidal CdSe QDs.<sup>[40]</sup>

The electronic structure of II-VI semiconductors has been described by k.p theory, which predicts S-type conduction band levels and P-type upper valence band levels, split into the topmost  $J=3/2$  band and the split-off  $J=1/2$  band.<sup>[26]</sup> CdTe has the largest spin-orbit splitting (0.927 eV) and the smallest band gap (1.606 eV) among the cadmium chalcogenide semiconductors. Therefore, the split-off band ( $J=1/2$ ) is expected to weakly mix with the topmost valence band.<sup>[34]</sup> The size dependence of electron and hole levels in spherical CdTe QDs has been previously theoretically investigated by Efros and Rosen using an eight-band k.p model.<sup>[34]</sup> These calculations yielded the optical transition energies deduced from the position of the SP levels but excitonic effects have not been considered.<sup>34</sup> The CI tight-binding approach used in the present work provides the oscillator strengths of the excitonic transitions, making it possible to compare calculated and experimental absorption spectra from the strong to the intermediate confinement regimes.



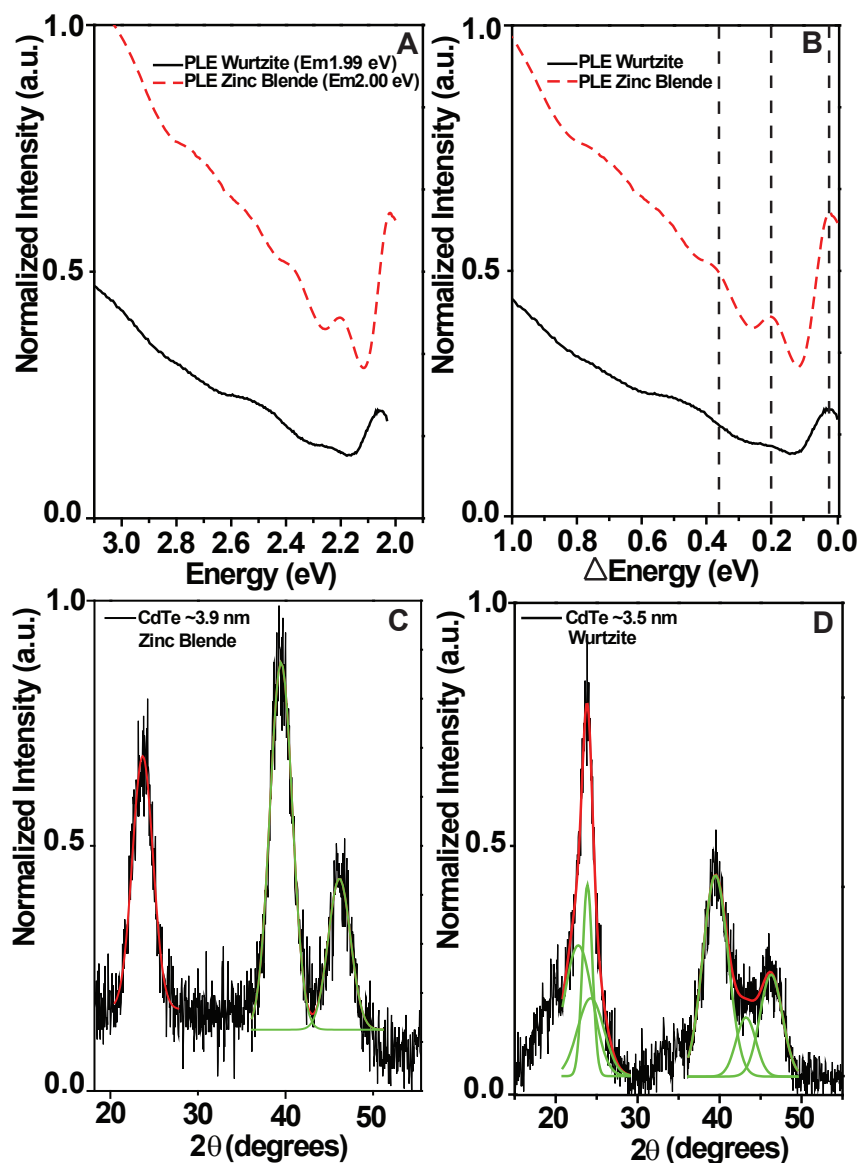


**Figure 7.8** – PLE spectra (a,b) and XRD pattern (c,d) of 2 different CdTe NC samples of comparable sizes, but different crystal structures (wurtzite and zinc blende). The PLE spectra shown in (b) have been normalized with respect to the energy of the lowest exciton transition, which has been set to zero to allow comparison of the relative energy positions of the exciton transitions in the wurtzite and zinc blende CdTe NCs.

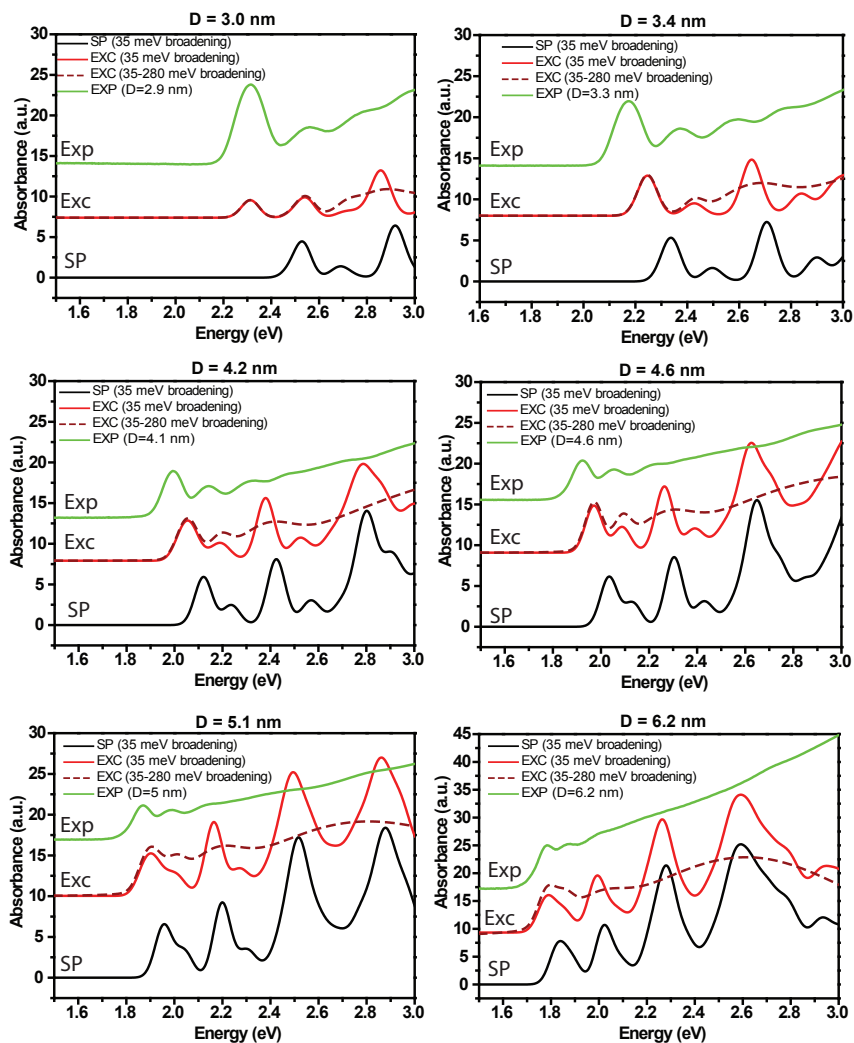


**Figure 7.9** – Comparison between experimental (Exp) and calculated absorption spectra of CdTe QDs with diameters ranging from 3.0 to 6.2 nm. Tight-binding single-particle calculations are indicated as SP, while calculations involving electron-hole configuration interaction are indicated by EXC. The bandwidth of the calculated peaks was set to 35 meV for the theoretical spectra given by solid lines, and allowed to increase with increasing transition energy (from 35 to 280 meV) for the EXC spectra given by dashed lines.

Figure 7.9 presents a selection of experimental and calculated spectra of CdTe QDs ranging from 3 nm to 6.2 nm in diameter. To allow comparison between the experimental spectra (obtained at room temperature) and the calculated spectra (obtained from parameters adjusted to the bandgap at 0 K), the calculated values were corrected for the temperature dependence of the bulk CdTe bandgap by subtracting 116 meV. Moreover, the bandwidth of the calculated peaks was set to 35 meV. We have considered up to 28000 excitonic states to calculate the spectra shown in figure 7.9. The spectra calculated taking into account the electron-hole configuration interaction (CI) show a much better agreement with the experimental ones than those based on single-particle calculations. The main effect of the electron-hole interaction is to shift all exciton transitions to lower energies. The general trend for the oscillator strengths (*i.e.*, higher energy transitions possess higher oscillator strengths) is well reproduced by the calculations. The oscillator strengths obtained by CI or SP are comparable and deviate from the experimental ones if the spectral broadening is taken to be the same for all exciton transitions (figure 7.9), particularly for smaller sizes. However, the agreement between the calculated and experimental peak intensities is greatly improved by allowing the peak broadening to increase with the transition energy (dashed lines in figure 7.9). This variable broadening can be understood by considering that the density of states increases with the exciton transition energy. Moreover, higher energy transitions depend not only on the volume of the QD but also on its shape, and are thus more affected by the shape distribution of the CdTe nanocrystals investigated here, which are highly faceted and in some cases have shapes that strongly deviate from spherical (see figure 7.3 above). In this way, QDs with similar volumes may have rather different shapes and faceting, therefore presenting similar lowest exciton transition energies, but differing for higher exciton transitions.

The peak positions calculated using the tight-binding CI approach are in excellent agreement with the experiment. This is clearly observed in figure 7.10, where the calculated position of the first allowed optical transition (*i.e.*, the  $1S_{3/2(h)} - 1S_{(e)}$ ) is plotted as a function of the CdTe QD diameter, and compared to the empirically determined size dependence of the bandgap of colloidal CdTe QDs, which has been shown to be well described by the following expression:<sup>[31]</sup>

$$E_g(d)(CdTe) = 1.596 + \frac{1}{0.137d^2 + 0.0000d + 0.206} \quad (7.8)$$

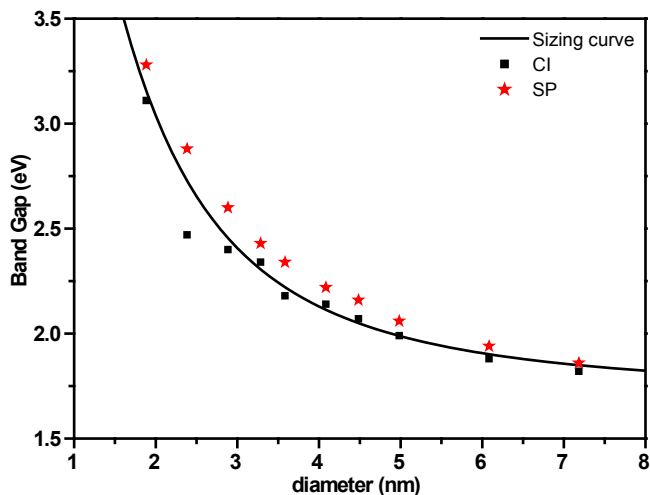


**Figure 7.10** – Size dependence of the position of the first allowed optical transition ( $1S_{3/2(h)}-1S_{(e)}$ ) of CdTe QDs obtained by tight-binding calculations with electron-hole configuration interaction (CI, squares) and without (single-particle, SP, stars). The solid line gives the empirically determined size dependence of the bandgap of colloidal CdTe QDs<sup>[31]</sup>

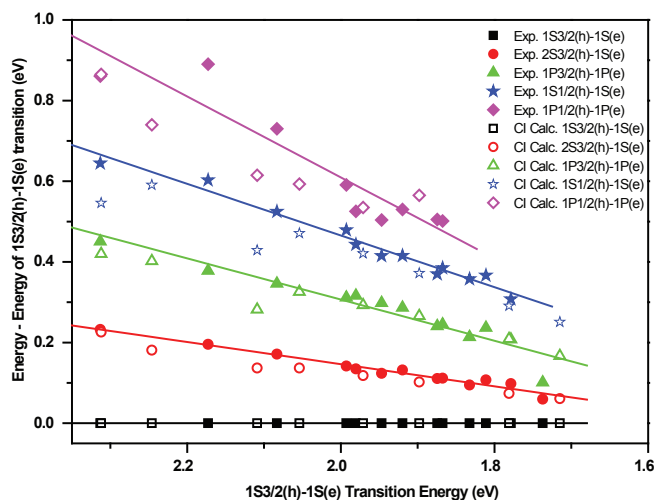


**Figure 7.11** – Energy separation between the five lowest exciton transitions of CdTe QDs and the lowest exciton transition ( $1S_{3/2(h)}-1S_{(e)}$ ) as a function of the  $1S_{3/2(h)}-1S_{(e)}$  transition energy. The solid symbols represent the experimental data, while the values obtained by tight-binding CI calculations are given by empty symbols. The solid lines are linear fits to the experimental data.

where  $E_g$  is the bandgap (*i.e.*, the  $1S_{3/2(h)}-1S_{(e)}$  transition energy) of a colloidal CdTe QD of diameter  $d$ . It is clear that the single-particle (SP) calculations overestimate the bandgap, while the tight-binding calculations taking into account the electron-hole configuration interaction (CI) are in excellent agreement with the empirical size dependent trend. The tight-binding CI calculations are also in excellent agreement with the experimental positions of the higher energy exciton transitions, especially up to the fourth absorption peak. This is illustrated in figure 7.11, where the energy separation between higher energy transitions and the  $1S_{3/2(h)}-1S_{(e)}$  transition is plotted as a function of the energy of the  $1S_{3/2(h)}-1S_{(e)}$  transition. It should be noted that the experimental values for the fifth peak (the  $1P_{1/2(h)}-1P_{(e)}$  transition) have a larger uncertainty due to the larger degree of spectral broadening at higher energies, which makes the multi-Gaussian fit solutions at higher energies less well defined. This is reflected in the larger scattering of the experimental values for the fifth peak, which may explain the larger deviation between calculated and experimental values for this transition. Figure 7.11 also shows that the slope of the linear fits to the experimental data are different for the different transitions, increasing with the energy of the transition. This can be ascribed to the increase of the quantum numbers of the orbitals involved in the transition, in agreement with previous observations reported for PbSe QDs.<sup>[5]</sup> We note that the good agreement observed between the calculated transition energies and the experimental ones further supports the observation made above that the differences between the optical spectra of zinc blende and wurtzite CdTe QDs are not significant.

#### 7.4 – Conclusions

We presented a detailed investigation of the size dependence of the optical transitions of colloidal CdTe QDs ranging in diameter from 2.9 to 14.8 nm. The energy integrated absorption cross section per CdTe unit is investigated in detail for the lowest two exciton transitions ( $1S_{3/2(h)}-1S_{(e)}$  and  $2S_{3/2(h)}-1S_{(e)}$ ) and shown to increase with decreasing size, although the size dependence of the  $2S_{3/2(h)}-1S_{(e)}$  is less pronounced. Further, the experimental absorption spectra are compared to spectra calculated by using a tight-binding approach. The calculations were carried out with electron-hole configuration interaction (CI) and without (single-particle, SP). The optical absorption spectra calculated by using the CI approach are in excellent agreement with the experiment, as well as the evolution of the optical gap and the optical transitions with NC size.

## REFERENCES

1. C. de Mello Donegá, *Chem. Soc. Rev.* 2011, 40, 1512-1546.
2. D. V. Talapin, J.-S. Lee, M. V. Kovalenko, E. V. Shevchenko, *Chem. Rev.* 2010, 110, 389-458.
3. P. D. Cozzoli, T. Pellegrino, L. Manna, *Chem. Soc. Rev.* 2006, 35, 1195.
4. J. Park, J. Joo, S. G. Kwon, Y. Jang, T. Hyeon, *Angew. Chem. Int. Ed.* 2007, 46, 4630.
5. R. Koole, G. Allan, C. Delerue, A. Meijerink, D. Vanmaekelbergh, A. J. Houtepen, *Small* 2008, 4, 127-133.
6. Q. Dai, Y. Wang, X. Li, Y. Zhang, D. J. Pellegrino, M. Zhao, B. Zou, J. Seo, Y. Wang, W. W. Yu, *ACS Nano* 2009, 3, 1518-1524.
7. P. Reiss, M. Protière, L. Li, *Small* 2009, 5, 154.
8. C. de Mello Donegá, M. Bode, A. Meijerink, *Phys. Rev. B* 2006, 74, 085320.
9. G. D. Scholes, *Adv. Funct. Mater.* 2008, 18, 1157.
10. V. I. Klimov, *Annu. Rev. Phys. Chem.* 2007, 58, 635-673.
11. C. de Mello Donegá, P. Liljeroth, D. Vanmaekelbergh, *Small*, 2005, 1, 1152.
12. A. L. Rogach, D. V. Talapin, E. V. Shevchenko, A. Kornowski, M. Haase, H. Weller, *Adv. Funct. Mater.* 2002, 12, 653-664.
13. C. Bullen, P. Mulvaney, *Nano Lett.* 2004, 4, 2303.
14. W. W. Yu, Y. A. Wang, X. G. Peng, *Chem. Mater.* 2003, 15, 4300-4308.
15. A. L. Rogach, T. A. Klar, J. M. Lupton, A. Meijerink, J. Feldmann, *J. Mater. Chem.* 2009, 19, 1208-1221.
16. R. C. Somers, M. G. Bawendi, D. G. Nocera, *Chem. Soc. Rev.* 2007, 36, 579-591.
17. P. V. Kamat, *J. Phys. Chem. C* 2008, 112, 18737-18753.
18. E. Tekin, P. J. Smith, S. Hoepfner, A. M. J. van den Berg, A. S. Sussha, A. L. Rogach, J. Feldmann, U. S. Schubert, *Adv. Funct. Mater.* 2007, 17, 23-28.
19. E. Jang, S. Jun, H. Jang, J. Lim, B. Kim, Y. Kim, *Adv. Mater.* 2010, 22, 3076-3080.
20. T. Skajaa, Y. Zhao, D. J. van den Heuvel, H.C. Gerritsen, D. P. Cormode, R. Koole, M. M. van Schooneveld, J. A. Post, E. A. Fisher, Z. A. Fayad, C. de Mello Donegá, A. Meijerink, W. J. Mulder, *Nano. Lett.* 2010, 10, 5131-5138.
21. P. T. K. Chin, C. de Mello Donegá, S. S. van Bavel, S. C. J. Meskers, N. A. J. M. Sommerdijk, R. A. J. Janssen, *J. Am. Chem. Soc.* 2007, 129, 14880-14886.
22. D. Oron, M. Kazes, U. Banin, *Phys. Rev. B* 2007, 75, 035330.
23. S. S. Lo, T. Mirkovic, C. Chuang, C. Burda, G. D. Scholes, *Adv. Mater.* 2011, 23, 180-197.
24. C. de Mello Donegá, *Phys. Rev. B.* 2010, 81, 165303.
25. C. R. M. De Oliveira, A. M. de Paula, F. O. P. Filho, J. A. M. Neto, L. C. Barbosa, O. L. Alves, E. A. Menezes, J. M. M. Rios, H. L. Fragnito, C. H. B. Cruz, C. L. Cesar, *Appl. Phys. Lett.* 1995, 66, 439-441.

26. Y. Masumoto, K. Sonobe, *Phys. Rev. B.* 1997, 56, 9734-9737.
27. S. F. Wuister, I. Swart, F. van Driel, S. G. Hickey, C. de Mello Donegá, *Nano Lett.* 2003, 3, 503.
28. J. H. Blokland, V. I. Claessen, F. J. P. Wijnen, E. Groeneveld, C. de Mello Donegá, D. Vanmaekelbergh, A. Meijerink, J. C. Maan, P. C. M. Christianen, *Phys. Rev. B* 2011, 83, 035304.
29. D. Oron, A. Aharoni, C. de Mello Donegá, J. van Rijssel, A. Meijerink, U. Banin, *Phys. Rev. Lett.* 2009, 102, 177402.
30. A. F. Van Driel, G. Allan, C. Delerue, P. Lodahl, W. L. Vos, D. Vanmaekelbergh, *Phys. Rev. Lett.* 2005, 95, 236804.
31. C. de Mello Donegá, R. Koole, *J. Phys. Chem. C* 2009, 113, 6511-6520.
32. H. Zhong, M. Nagy, M. Jones, G. D. Scholes, *J. Phys. Chem. C* 2009, 113, 10465-10470.
33. J. S. Kamal, A. Omari, K. Van Hoecke, Q. Zhao, A. Vantomme, F. Vanhaecke, R. K. Capek, Z. Hens, *J. Phys. Chem. C* 2012, 116, 5049-5054.
34. Al. L. Efros, M. Rosen, *Phys. Rev. B* 1998, 58, 7120-7135.
35. G. Allan, Y.M. Niquet, C. Delerue, *Appl. Phys. Lett.* 2000, 77, 639.
36. X. Gonze, J.-M. Beuken, R. Caracas, F. Detraux, M. Fuchs, G.-M. Rignanese, L. Sindic, M. Verstraete, G. Zerah, F. Jollet, M. Torrent, A. Roy, M. Mikami, Ph. Ghosez, J.-Y. Raty, D. C. Allan, *Comput. Mater. Sci.* 2002, 25, 478-492.
37. E. Martin, C. Delerue, G. Allan, M. Lannoo, *Phys. Rev. B* 1994, 50, 18258.
38. C. Delerue, M. Lannoo, 'Nanostructures: Theory and Modelling', Berlin: Springer-Verlag, 2004.
39. B. Mahler, N. Lequeux, B. Dubertret, *J. Am. Chem. Soc.* 2010, 132, 953-959.
40. M. Kuno, J. K. Lee, B. O. Dabbousi, F. V. Mikulec, M. G. Bawendi, *J. Chem. Phys.* 1997, 106, 9869-988





## Chapter 8

# Formation of ZnSe/CdSe heteronanocrystals and alloy nanocrystals via cation-exchange

---

*Living on the edge: cation exchange*

## Abstract

*In this chapter cation exchange of Zn atoms by Cd atoms in ZnSe NCs was investigated. Cation exchange reaction on 5.6 nm ZnSe NCs at 150°C led to the formation of Type- I<sup>1/2</sup> ZnSe/CdSe concentric core/shell (5.0 nm/ 0.3 nm) HNCs. Increasing the reaction temperature to 220°C led to further cation exchange and formation of a thicker shell accompanied by the shrinking of the NC core (4.2 nm/0.7 nm ZnSe/CdSe core/shell). The optical properties indicate that the 4.2 nm/0.7 nm ZnSe/CdSe core/shell HNCs are in the Type-I<sup>1/2</sup> carrier localization regime. Increasing the reaction temperature led to a higher degree of cation exchange and at 220°C the formation of gradient alloyed HNCs was observed.*

## 8.1 – Introduction

Colloidal semiconductor nanocrystals (NCs) form a new class of materials of which the properties can be tailored by their dimensions. An even higher degree of property control is achieved in Heteronanocrystals (HNCs), which are composed of two (or more) different semiconductors joined by heterointerface(s). In HNCs the charge carrier localization after photoexcitation can be controlled by tuning the offsets between the energy levels of the semiconductors that are combined at the heterointerface.<sup>[1]</sup> As discussed in chapter 3, three different regimes of charge carrier localization can be identified, namely Type-I, Type-II and Type I<sup>1/2</sup> (also referred to as quasi type-II). In Type-I HNCs the energy offsets are such that both carriers are confined in the same material, whereas in Type-II HNCs the staggered alignment between the energy levels leads to the formation of a spatially indirect exciton. The electron and hole wave functions in type-II HNCs are thus primarily localized in different segments of the HNC. Type-I<sup>1/2</sup> forms an intermediate regime between Type-I and Type-II and is characterized by the localization of one charge in one of the components, while the other charge carrier is delocalized over the whole HNC. These tunable properties make HNCs interesting materials for a number of applications (e.g., low-threshold lasers, photovoltaic devices, solar energy conversion, LED's, biomedical imaging, etc.).<sup>[1]</sup>

Concentric core/shell HNCs of specific material combinations (e.g., ZnSe/CdS<sup>[2]</sup>, ZnTe/CdSe<sup>[3]</sup>, CdTe/CdSe<sup>[4]</sup>) allow tailoring the charge carrier localization regime from Type-I to Type-II by varying the shell thickness and core diameter. CdSe/ZnSe and ZnSe/CdSe concentric core/shell HNCs have been synthesized by a number of groups over the last decade.<sup>[5,6,8,9]</sup> ZnSe-CdSe is a material combination with a type-I band alignment in the

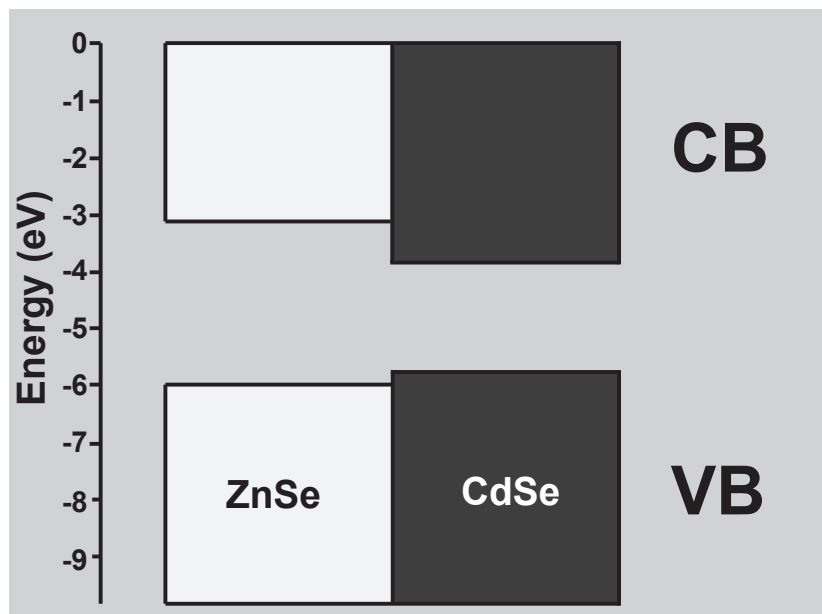


**Figure 8.1** – The energy positions of the electronic band edges of bulk ZnSe and CdSe relative to vacuum (VB: valence band, CB: conduction band). The space between the solid bars gives the band gap.<sup>[10]</sup>

bulk limit (figure 8.1). However, for concentric ZnSe/CdSe core/shell NCs the charge carrier localization can be Type-I,<sup>[5,6]</sup> Type-I<sup>1/2</sup>,<sup>[7]</sup> or Type-II<sup>[8]</sup> depending on the core diameter and shell thickness. In CdSe/ZnSe/ZnS core/multishell HNCs, the ZnSe coating over CdSe cores acts as an intermediate lattice strain reducing layer, yielding HNCs with a higher quantum yield and higher stability than CdSe/ZnS and CdSe/ZnSe.<sup>[6]</sup> ZnSe/CdSe core/shell HNCs were made to study the continuous transition from the Type-I to the Type-I<sup>1/2</sup> localization regime.<sup>[7,8]</sup> Thin CdSe shells yield type-I HNCs, while increasing the shell thickness leads to the evolution of the HNCs towards the Type-I<sup>1/2</sup> regime.

The intense research activity in the field of NC synthesis has resulted in a significant degree of size and shape control over NCs and HNCs<sup>[11-13]</sup>, and has yielded various HNC morphologies, such as concentric core/(multi) shell HNCs<sup>[14]</sup>, heterodumbbells<sup>[15]</sup>, and heteronanorods.<sup>[16]</sup> Traditionally, colloidal HNC structures have been synthesized via heteroepitaxial growth over a pre-existing NC seed. However, heteroepitaxial growth is for some

material combinations prevented by large lattice-mismatches,<sup>[17]</sup> or thermal instability of the NC seed.<sup>[18]</sup> Recently, cation exchange<sup>[19]</sup> has emerged as a versatile alternative strategy to synthesize NCs and HNCs which would not be achievable by heteroepitaxial growth.<sup>[20-24]</sup> This approach has led to the successful preparation of complex HNCs such as PbSe/CdSe core/shell HNCs,<sup>[18,25]</sup> PbSe/CdSe dot core/rod shell heteronanorod,<sup>[26]</sup> CdS/CuS heterorods,<sup>[27]</sup> and CdSe/CdS hetero-octapods.<sup>[22]</sup>

In this work, the formation of ZnSe/CdSe HNCs from ZnSe QDs via cation exchange is addressed. The influence of the reaction temperature on the degree of Zn<sup>2+</sup> by Cd<sup>2+</sup> exchange and the compositional distribution profile of the resulting nanocrystals is investigated. This chapter is organized as follows. First, the experimental details are described, followed by the characteristics of the parent ZnSe NCs. Finally, the results of the cation exchange experiments are presented and analysed. Our observations show that the reaction temperature can be used to control the elemental distribution profile after the Zn for Cd exchange, yielding either concentric ZnSe/CdSe core/shell NCs, or gradient (Zn,Cd)Se alloy NCs.

## 8.2 – Experimental methods

**Chemicals:** Cadmium acetate dihydrate (Cd(Ac)<sub>2</sub>xH<sub>2</sub>O, 99.99+%), Octadecene (ODE, 90%), oleic acid (OA, 90%), trioctylphosphine (TOP) were purchased from Sigma-Aldrich. Octadecylamine (ODA, >90%), diethylzinc (Zn(Et)<sub>2</sub>, 98%), and selenium (Se, 99.999%) were purchased from Fluka, STREM Chemicals, and Alfa Aesar, respectively. Anhydrous toluene, anhydrous hexane, anhydrous methanol, and anhydrous acetone were all purchased from Sigma-Aldrich. All reagents were used as purchased with the exception of ODE, and ODA. Before use, ODE, and ODA were dried and degassed under vacuum (3 h at 120°C).

**Stock solutions:** A 0.4 M Zn(Et)<sub>2</sub> stock solution was prepared by dissolving 0.494 g (4 mmol) Zn(Et)<sub>2</sub> in 10 mL ODE. The stock solution of 0.4 M Zn-Oleate was made by dropwise addition of 5.05 mL OA to a solution containing 0.494 g (4 mmol) Zn(Et)<sub>2</sub> and 4.95 mL ODE. This mixture was allowed to react for 5 minutes at 300°C, and subsequently for 3 hours at 120°C. Cd-oleate stock solution (0.04 M) was prepared by heating a mixture of 0.128 g (0.479 mmol) Cd(Ac)<sub>2</sub>xH<sub>2</sub>O, 1.2 mL OA, and 10.8 mL ODE to 280°C. Subsequently this Cd-stock solution was dried and degassed for 3 hours at 150°C. The 1M Se stock solution in TOP was prepared by dissolving 0.79 g (10 mmol) Se powder in 10 mL TOP. All stock solutions were prepared under N<sub>2</sub> atmosphere

**ZnSe NC Synthesis:** 2.5 mL ODE and 0.55 g ODA were loaded in a reaction flask and heated to 290°C in a glove-box under nitrogen (< 5 ppm O<sub>2</sub> and H<sub>2</sub>O). At this temperature a mixture of 0.5 mL Zn(Et)<sub>2</sub>-stock and 1 mL Se-Stock was swiftly injected under stirring. The temperature was allowed to cool to 270°C and a dropwise addition of 1.5 mL Zn-oleate stock solution in 3 mL ODE was started 5 minutes after the initial injection. Another two 1.5 mL Zn-oleate stock solution in 3 mL ODE additions were started 15 minutes after the initial injection with 10 minute interval. The synthesis was stopped by removing the heating mantle 10 minutes after the 3<sup>th</sup> Zn-oleate addition.

**ZnSe-CdSe NC synthesis:** Cation exchange was performed by injection of Cd-precursor to a hot solution containing purified ZnSe parent NCs at a preset temperature in a glove-box under nitrogen (< 5 ppm O<sub>2</sub> and H<sub>2</sub>O). In a typical synthesis ODA (1.477 g), ODE (6.3 mL) were loaded in a reaction flask and heated to a preset reaction temperature (see main text for employed temperature). When the preset temperature was reached a ZnSe NC seed stock solution containing 10<sup>-4</sup> mmol NCs was injected and subsequently after 15 seconds a 0.1 mL aliquot was taken from the reaction mixture. After the injection of the ZnSe parent NCs every 20 minutes 0.5 mL Cd-oleate stock solution was injected and before every Cd-oleate injection a 0.1 mL aliquot was taken from the reaction mixture. 80 Minutes after the seed injection (after third Cd-precursor injection), half of the reaction mixture was removed and allowed to cool down to RT and remaining reaction mixture was heated at the initial temperature or further heated to a higher temperature in 23 minutes. The synthesis was stopped by removal of the heating mantle 108 minutes after the injection of the ZnSe parent NCs.

**Purification of the ZnSe and ZnSe-CdSe NCs:** Purification of the crude reaction mixture consisted of a hexane/methanol extraction in order to remove unreacted Zn and Se precursors. Extraction was performed by mixing a solution of the crude reaction mixture in anhydrous hexane, and anhydrous methanol (1:4:2 volume ratio). The colored top layer containing the nanocrystals was removed. Subsequently an equal volume of methanol was added to the NC hexane solution layer for a second hexane/methanol extraction step. In total, this hexane/methanol extraction purification step was repeated 5 times and after the fifth extraction cycle, the nanocrystals were precipitated by adding anhydrous acetone (1:6 volume ratio). The sediment was isolated by centrifugation (3000 rpm, 15 min), and redissolved in anhydrous toluene, yielding a concentrated stock solution of 3.5\*10<sup>-4</sup> M. The molarity of this stock solution was determined from the absorbance

maximum of the lowest energy transition peak and taking  $1.8 \times 10^5 \text{ Lmol}^{-1} \text{ cm}^{-1}$  as the extinction coefficient. This extinction coefficient was taken from ref. [28] where it was determined for ZnSe NCs with a lowest absorption transition at 390 nm. For purification of the ZnSe-CdSe NCs an identical procedure as the ZnSe NCs was followed, with exception that now only 1 methanol/hexane extraction cycle was performed instead of 5 cycles.

**Characterization:** Absorption spectra were measured on a double beam Perkin-Elmer Lambda 16 UV/Vis spectrometer (scan rate: 1 nm/s). Photoluminescence (PL) spectra were recorded by an Edinburgh Instruments FLS920 Spectrofluorimeter equipped with a 450 W Xenon lamp as excitation source and double grating monochromators. Samples for optical measurements were prepared by directly dissolving the crude reaction mixture in anhydrous toluene under nitrogen and stored in sealed cuvettes. All measurements were performed at room temperature. Transmission electron microscopy (TEM) and Energy Dispersive X-Ray Spectroscopy (EDS) were performed using a Tecnai microscope (FEI TECNAI G2 T20F) a Field emission Gun, a Gatan 694 CCD camera and an EDAX spectrometer and operating at 200 kV. Acquisition time for EDS measurements was ~30 s – ~1 min. The TEM measurements were carried out on NC samples which had been purified in order to remove the excess of organic molecules and unreacted precursors. Samples for TEM imaging were prepared by dipping a carbon-coated copper (400-mesh) TEM grid into a toluene solution of NCs. The excess liquid was removed by blotting using filter paper. X-Ray Diffraction (XRD) diagrams were obtained by using a PW 1729 Philips diffractometer, equipped with a Cu K $\alpha$  X-ray source ( $\lambda = 1.5418 \text{ \AA}$ ). Samples for XRD analysis were prepared by depositing a concentrated solution of purified CdTe NCs on a Si wafer substrate under inert atmosphere. High Angle Annular Dark Field (HAADF)- Scanning Transmission Electron Microscopy (STEM) and STEM-Electron Energy Loss Spectrum (EELS) experiments were carried out by K. Xiaoxing and S. Balls at the EMAT institute in Antwerp. Measurements were performed on a FEI Titan 50-80 cubed microscope fitted with an aberration-corrector for the imaging lens and another for the probe forming lens as well as a monochromator, operated at 120 kV to acquire the data. Spectroscopy experiments were performed on a GIF-QUANTUM spectrometer. Monochromator was not excited in order to increase the signal-to-noise ratio due the small contribution from the ultra-small QDs. The STEM convergence semi-angle used was ~21.4 mrad, providing a probe size of ~15  $\text{\AA}$  at 120 kV.

## 8.3 – Results and discussion

### 8.3.1 – Characterization of the ZnSe NCs

The as-prepared ZnSe NCs were characterized by transmission electron microscopy (TEM) analysis, absorption and photoluminescence spectroscopy, and X-ray diffraction (XRD). A TEM image of the ZnSe NCs is given in figure 8.1b and shows that the ZnSe NCs are faceted and isotropic (nearly spherical) with an average diameter of 5.6 nm and a small size dispersion ( $\pm 0.7$  nm). The X-ray diffractogram, given in figure 8.2c, indicates that the NCs have the zinc blende crystal structure. The absorption spectrum (figure 8.2a) consists of multiple sharp features, which can be assigned to the electronic transitions of the ZnSe QDs. As a result of the small size distribution 4 different electronic transitions can be distinguished, the lowest energy one being at 423 nm. Following previous theoretical work on CdSe,<sup>[29]</sup> these transitions can be assigned to (from lowest to highest energies): (1)  $1S_{3/2(h)}-1S_{(e)}$ , (2)  $2S_{3/2(h)}-1S_{(e)}$ , (3)  $1S_{1/2(h)}-1S_{(e)}$ , and (4)  $1P_{3/2(h)}-1P_{(e)}$ . Photoluminescence (PL) peak of ZnSe NCs (figure 8.2a) is red shifted compared to the first absorption peak by a non-resonant Stokes shift ( $\Delta_{ST}$ ) of 11 nm (81 meV) and has a full-width at half-maximum (FWHM) of 108 meV. The FWHM, which is a result of homogeneous and inhomogeneous line broadening, confirms the small size dispersion of the ZnSe NCs and is to our knowledge the narrowest FWHM reported for ZnSe NCs (best PL FWHM reported in the literature for similarly sized ZnSe Ncs is ~120 meV<sup>[30]</sup>).

### 8.3.2 – ZnSe/CdSe concentric core/shell HNC via cation exchange

The above described ZnSe QDs were used as parent NCs in a cation exchange reaction in which  $Zn^{2+}$  was replaced by  $Cd^{2+}$ . The synthesis involved two sequential heating steps. The reaction was started by a Cd-precursor injection at 150°C. After the third Cd-precursor injection the temperature was raised to 220°C. When the temperature reached 220°C the synthesis was stopped by removal of the heating mantle. The absorption and PL spectra of the ZnSe parent NCs, and the samples taken at the end of the 150°C stage (S150), and at the end of the reaction (S150-220) are given in figure 8.3. The absorption spectra clearly show that the optical transitions shift to lower energies and broaden upon the addition of Cd precursors at 150°C. The raise in temperature to 220°C results in a further shift of the optical transitions to lower energies. The PL peak shifts by 83 meV and 289 meV, for the S150 and S150-220 samples, respectively. Along with this shift a broad band at lower energies appears in the PL spectra, which may be ascribed

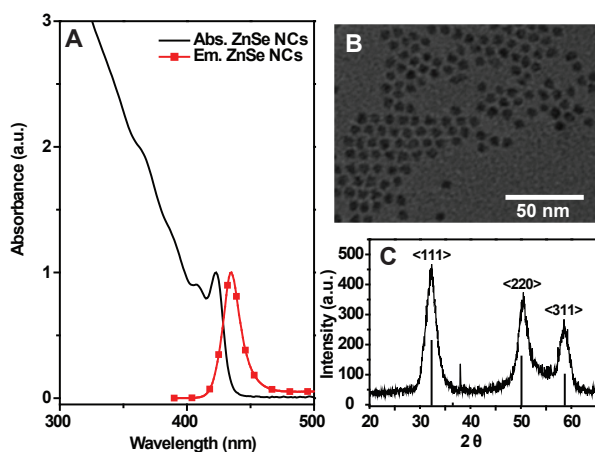


**Figure 8.2** – Characteristics of the as-prepared ZnSe NCs. (a) Absorption and emission spectrum (excitation light of 380 nm). (b) TEM image (c) XRD diagram (bars indicate position and relative intensity of diffraction peaks for bulk zinc blende ZnSe).

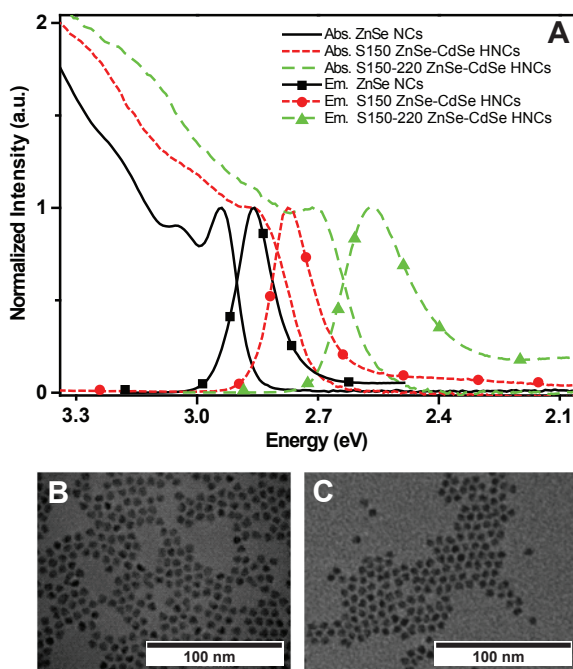


**Figure 8.3** – (a) Absorption and emission spectra of ZnSe parent NCs, S150 ZnSe-CdSe HNCs, and S150-220 ZnSe-CdSe HNCs. TEM images of S150 ZnSe-CdSe HNCs (b), and S150-220 ZnSe-CdSe HNCs (c).



to radiative recombination in trap states. The FWHM of the PL peak is 119 meV and 201 meV for the S150 and S150-220 sample, respectively. The  $\Delta_{ST}$  is 83 meV for the S150 sample, which is similar to the  $\Delta_{ST}$  of the ZnSe parent NC, whereas it increases to 134 meV for the S150-220 NCs. To understand the changes in the optical properties, knowledge of the composition of the NCs is needed. The average composition of the NCs was determined by TEM energy dispersive X-ray spectroscopy (EDS) measurements on wider areas containing ~100 to ~1000 HNCs. The elemental concentrations (atomic %) of the NCs in the S150 sample are  $(13.71 \pm 3.50)\%$  Cd,  $(39.74 \pm 3.34)\%$  Zn, and  $(46.55 \pm 6.83)\%$  Se, whereas the S150-220 sample consists of  $(28.92 \pm 1.43)\%$  Cd,  $(21.02 \pm 2.05)\%$  Zn, and  $(50.07 \pm 3.03)\%$  Se. These measurements clearly show that the Zn atoms in the ZnSe parent NCs are exchanged by Cd atoms (27% and 58% of the Zn atoms in the S150 and S150-220 samples, respectively). The increase of the reaction temperature to 220°C leads to a larger degree of cation exchange, but not to a complete exchange of Zn for Cd. TEM images show that the size of the NCs are  $5.7 \pm 0.4$  nm and  $5.6 \pm 0.5$  nm for the NCs in the S150 and S150-220 sample, respectively. These sizes are similar to that of the parent ZnSe NCs. This is expected since in cation exchange reactions the native cation sublattice is (partly) replaced by different ions, while the anionic sublattice of the parent NC is preserved.<sup>[1,22,23]</sup> Therefore, the size and the shape of the parent NC are maintained in the cation-exchanged NC. HR-TEM-images of the S150-220 sample are given in figure 8.4a and 8.4b and demonstrate that the NCs are highly faceted. The elemental distribution profile of the NCs was determined by scanning transmission electron microscopy electron energy loss spectroscopy (STEM-EELS) measurements, through which element-specific chemical maps were constructed for Cd and Zn (figure 8.5). These elemental maps demonstrate that Zn is concentrated in the NC core while Cd is located in a shell surrounding the ZnSe core. Clearly, a core/shell ZnSe/CdSe HNC has been formed. From these results we can conclude that the sample obtained at the end of the 150°C heating stage (S150) was already a ZnSe/CdSe core/shell QD, albeit with a thinner shell, since the optical properties had already clearly changed with respect to the parent ZnSe NCs. An estimate of the shell thickness and core diameter of both HNC samples can be made from the average atomic compositions determined by EDS and the average HNC size (5.6 nm). The ZnSe/CdSe HNCs in the S150 and the S150-220 sample are estimated to have a 5.0 nm/0.3 nm, and 4.2 nm/0.7 nm core/shell structure, respectively.

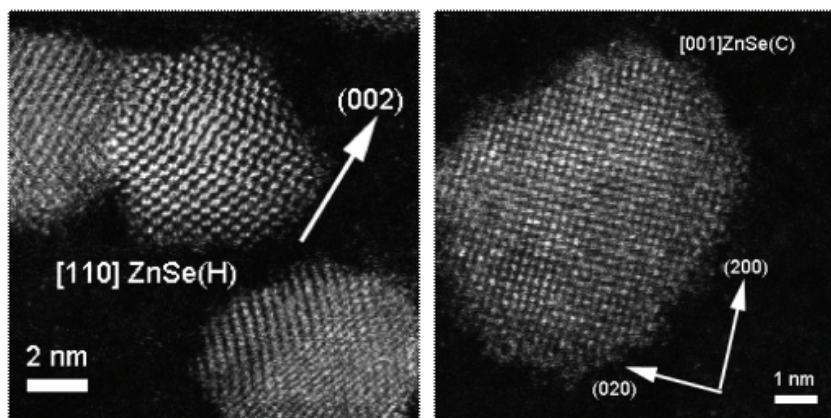


**Figure 8.4** – HR-TEM images of HNCs obtained from ZnSe NCs via cation exchange at consecutive temperature stages (150°C, and 220°C, respectively).

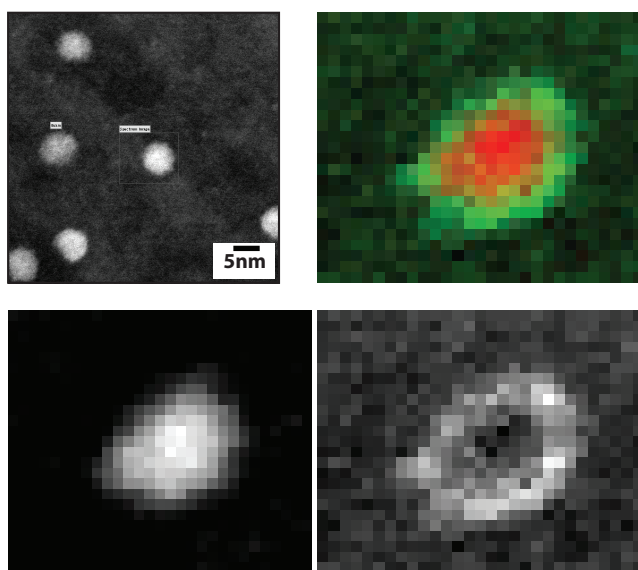


**Figure 8.5** – (a) STEM-HAADF image of HNCs obtained from ZnSe NCs via cation exchange at consecutive temperature stages (150°C, and 220°C, respectively). The square indicates the region selected for EELS analysis. The chemical distribution profile of Zn and Cd in the HNC shown in (b) was constructed from the chemical maps for Zn (c), and Cd (d).

The optical properties of the S150 and S150-220 HNCs can be explained by considering their elemental distribution profiles. As mentioned above, ZnSe-CdSe is a material combination with a Type-I band alignment in the bulk limit (figure 8.1). However, ZnSe/CdSe core/shell QDs with large ZnSe cores ( $d = 5\text{ nm}$ ) and thin CdSe shells (1.0-1.5 nm) have been shown to be in the Type-I<sup>1/2</sup> (or quasi Type-II) regime.<sup>[7]</sup> The hole localizes in the ZnSe core, while the electron wavefunction remains initially centered in the ZnSe core but extends into the CdSe shell.<sup>[7,9]</sup> Therefore, the evolution of the optical properties of ZnSe/CdSe core/shell QDs is mostly determined by the degree of delocalization of the electron wavefunction. The present results are consistent with a Type-I<sup>1/2</sup> localization regime. In a Type-I ZnSe/CdSe core/shell QD the emission would result from the recombination of a direct exciton in the ZnSe core, and would thus reflect the HOMO-LUMO gap of the core QD. Since the cation exchange reaction leads to progressive in-growth of a CdSe shell at the expense of the ZnSe core, the PL of a Type-I ZnSe/CdSe core/shell QD would shift to higher energies with the progress of the exchange reaction, which is in striking contrast with our observations (figure 8.3). The Type-II localization regime can also be excluded, based on the fact that the absorption transitions remain relatively narrow, and the featureless absorption tail characteristic of spatially indirect excitons<sup>[29]</sup> is absent. The increase in the non-resonant Stokes shift observed from sample S150 to S150-220 (*i.e.*, from 83 meV to 134 meV) may reflect a larger degree of electron delocalization, but may also be due to a larger degree of compositional inhomogeneity. It is interesting to note that the PL shifts progressively to lower energies with the progress of the exchange reaction, although the total NC volume is preserved. This observation suggests that the redshift cannot be ascribed to the loss in electron confinement energy, but rather to a change in the nature of the electron wavefunction, which acquires increasingly more Cd 5s character with increasing thickness of the CdSe shell. Nevertheless, to corroborate this hypothesis theoretical work is needed, which is beyond the scope of this work.

### 8.3.3 – Temperature dependence of the Zn<sup>2+</sup> by Cd<sup>2+</sup> exchange reaction

The results discussed above (section 8.3.2) suggest that the amount of Zn atoms exchanged by Cd atoms in the cation exchange reaction is largely influenced by the reaction temperature. To investigate the influence of reaction temperature, cation exchange syntheses at 200°C, 220°C, and 250°C were performed following the same method used for the two temperature stages (150 - 220°C) synthesis. The reaction temperature was

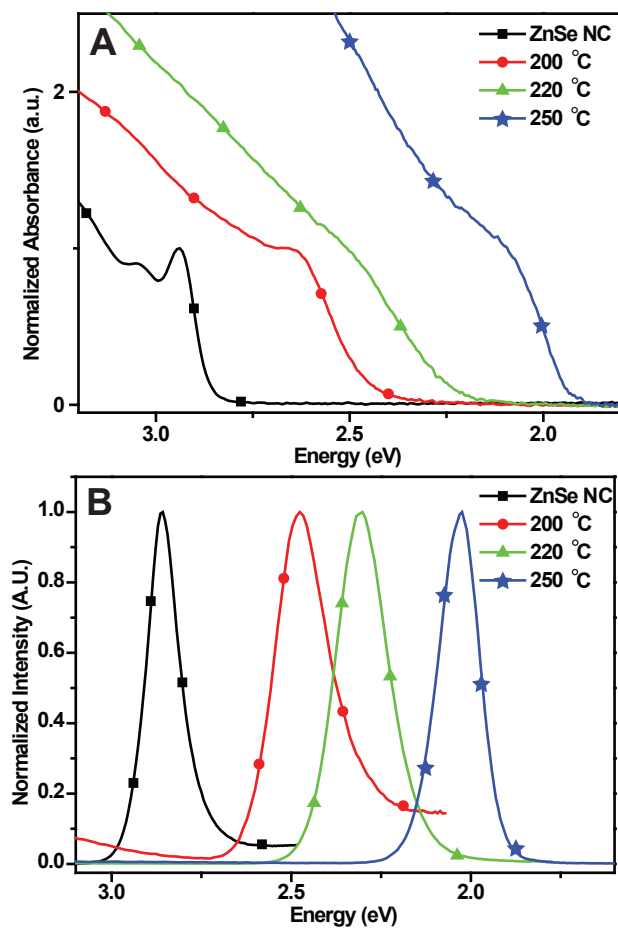


**Figure 8.6** – Evolution of absorption (a) and emission (b) spectra of ZnSe-CdSe NCs obtained via  $\text{Zn}^{2+}$  by  $\text{Cd}^{2+}$  exchange reaction at 200 °C, 220 °C, and 250 °C. The spectra of the ZnSe parent NCs are also shown for comparison.

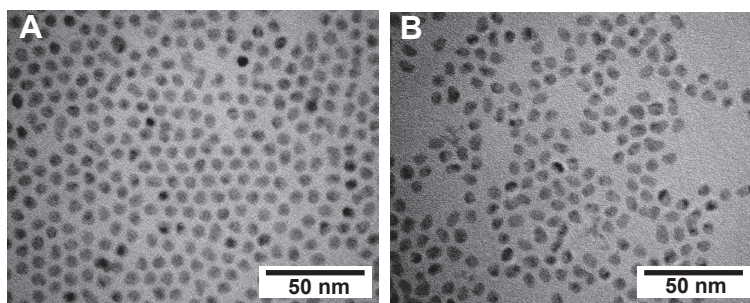


**Figure 8.7** – TEM images of ZnSe-CdSe NCs prepared at (a) 220 °C and (b) 250 °C

kept stable throughout the whole experiment. Absorption and emission spectra of the final samples of the three syntheses are given in figure 8.6. These spectra show that a higher synthesis temperature results in a larger shift of the optical transitions to lower energies. The average elemental compositions (atomic %, determined by TEM-EDS) of the NCs obtained at 220°C were  $(28.43 \pm 0.83) \% \text{ Cd}$ ,  $(22.36 \pm 0.90) \% \text{ Zn}$ , and  $(49.21 \pm 0.07) \% \text{ Se}$ , while the NCs obtained at 250°C consist of  $(33.83 \pm 2.88) \% \text{ Cd}$ ,  $(18.82 \pm 1.66) \% \text{ Zn}$ , and  $(47.36 \pm 4.54) \% \text{ Se}$ . Clearly, with increasing temperatures the Cd/Zn ratio increases, while the (Cd+Zn)/Se ratio remains constant, indicating that more  $\text{Zn}^{2+}$  is exchanged for  $\text{Cd}^{2+}$  at higher temperatures (57% at 220°C and 68% at 250°C). According to TEM measurements (figure 8.7), the shape and size ( $5.7 \pm 0.4 \text{ nm}$ ) of the parent ZnSe NCs is preserved upon Zn for Cd exchange for reactions at temperatures up to 220°C. At 250°C the HNCs become anisotropic and the size dispersion increases. This may be ascribed to inter- and intra-particle ripening.

### 8.3.4 – Influence of sequential thermal stages in the $\text{Zn}^{2+}$ by $\text{Cd}^{2+}$ exchange reaction

It is remarkable that the size and average elemental compositions of the NCs prepared at 220°C (S220, shown in figure 8.7) and S150-220 HNCs (figure 8.3b) are similar, while their optical properties, displayed in figures 8.6 and 8.3a, respectively, are not. The absorption and emission spectra of the NCs prepared at 220°C are shifted to lower energies compared to the spectra of the S150-220 HNCs (figure 8.8). The PL maximum for the NCs prepared at 220°C is at 2.31 eV, which is 260 meV lower energy than the PL maximum of the S150-220 HNCs. This is intriguing, considering that the Cd/Zn ratio is similar for both samples (*viz.*, 1.38 and 1.27 for S150-220 and S220, respectively). STEM-EELS measurements showed that the cation exchange reaction with sequential temperature stages at 150°C and 220°C leads to the formation of ZnSe/CdSe core/shell HNCs. The difference in optical properties between the ZnSe/CdSe core/shell HNCs described in section 8.3.2 above and ZnSe-CdSe NCs prepared by heating the reaction mixture directly to 220°C implies that the latter must have a different elemental distribution profile. ZnSe-CdSe NCs containing a fixed amount of Zn, Cd, and Se can have various elemental distribution profiles, of which two extremes can be distinguished: (a) ZnSe/CdSe core/shell QDs with a well-defined heterointerface, and (b) homogeneous (Zn,Cd)Se alloy QDs, where Zn and Cd are fully and homogeneously mixed. The formation of (Zn,Cd)Se alloy QDs from ZnSe QDs via cation exchange of  $\text{Zn}^{2+}$  by  $\text{Cd}^{2+}$  has been observed before.<sup>[32]</sup> The bulk bandgap of a  $\text{Cd}_x\text{Zn}_{1-x}\text{Se}$  alloy is known

to decrease nonlinearly from 2.63 eV ( $E_g$  bulk ZnSe) to 1.74 eV ( $E_g$  bulk CdSe), when the composition changes from fully ZnSe ( $x=0$ ) to fully CdSe ( $x=1$ ). The band gap of the (Zn,Cd)Se alloy can be described by an empirical curve,<sup>[33]</sup> which can be used to calculate the expected  $E_g$  of a 5.7 nm  $Cd_xZn_{1-x}Se$  homogeneously alloyed NC by using the band gap of 5.7 nm CdSe NCs<sup>[34]</sup> and 5.7 nm ZnSe NCs (from absorption spectrum in figure 8.2a) as follows:

$$E_{g,(Cd_xZn_{1-x}Se)NC} = 2.93 - 1.99x + 0.75x^2 \quad (8.1)$$

For the S220 NCs 57% of the Zn atoms are exchanged by Cd atoms, which should result in a bandgap (according to equation 8.1) of 2.04 eV, if the NCs were homogeneous  $Cd_{0.57}Zn_{0.43}Se$  alloys. The bandgap of the NCs can be estimated from the lowest absorption transition peak, which in the case of the NCs prepared at 220°C is at ~2.5 eV. This value is higher than expected for homogeneously alloyed  $Cd_{0.57}Zn_{0.43}Se$  NCs. The NCs prepared at 220°C are thus not homogeneous alloy NCs, but instead gradient alloy NCs with a concentration gradient towards the NC interior (figure 8.9b). This is an intermediate elemental distribution profile between a true core/shell HNC and an homogeneously alloyed NC. Cation exchange reactions involve the diffusion of cations from and to the NC surface, and the exchange of cations at the NC surface. The exchange of Zn atoms by Cd atoms in ZnSe NCs is driven by the higher stability of the CdSe crystal structure<sup>[35,36]</sup> and

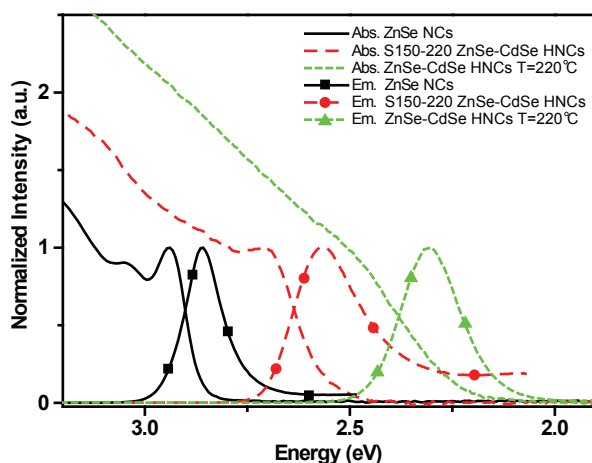


**Figure 8.8** – Absorption and emission spectra of the parent ZnSe NCs, ZnSe/CdSe core/shell S150-220 HNCs, and ZnSe-CdSe NCs prepared at 220°C.

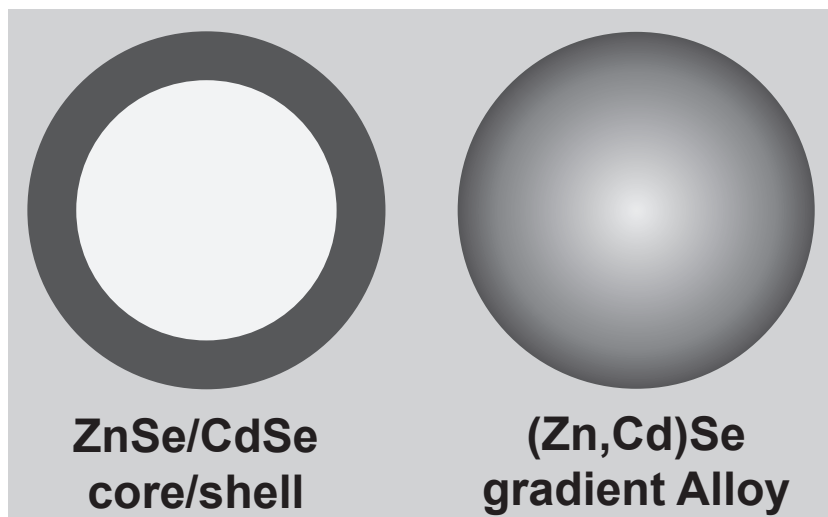


**Figure 8.9** – Schematic illustration of a concentric core/shell HNC and a gradient alloy NC.

the higher solubility of the outgoing Zn atoms in solution. This is similar to the observations reported in chapter 5, where the higher stability of the  $\text{Zn}^{2+}$  complexes with the ligands led to the exchange of Zn by Cd in ZnTe magic size clusters. Cation exchange can take place by various mechanisms such as vacancy-assisted migration and interstitial cation diffusion.<sup>[23]</sup> In the present case, it is likely that a combination of both mechanisms occur. Zn vacancies are created both at the surface of the NC, by binding of Zn atoms to surfactant molecules, and in the interior of the NC, by displacement of Zn atoms to interstitial positions. Zn vacancies at the surface are filled by Cd atoms, which start migrating inwards by the sequential occupation of vacancies left by Zn atoms that moved to interstitial positions. This process is favored by the larger Cd-Se bond strength with respect to that of Zn-Se ( $310 \text{ kJ mol}^{-1}$  and  $126 \text{ kJ mol}^{-1}$ , respectively).<sup>[35,36]</sup> The filling of the vacancies by diffusing Cd atoms, prevents the return of interstitial Zn atoms to their normal positions and create an outwards diffusion flow of interstitial Zn atoms towards the surface. Once at the surface the interstitial Zn atoms can be either sequestered by surfactant molecules or exchanged by Cd in a one-step process in which a Cd precursor complex leaves the Cd atom at the surface, while binding to the available Zn atom. This process is driven both by the higher stability of the Zn-ligand complex in solution and by the higher binding energy of the Cd atom in the NC. The concentration of Zn

vacancies and interstitial Zn atoms increases with increasing temperature.<sup>[23]</sup> The diffusion rate of cations is determined by the concentration of vacancies, the kinetic energy of cations, and by the presence of an external driving force (solubility of the cations in solution and stability in the NC lattice). Our results clearly show that temperature plays a crucial role in cation exchange because it determines both the cation diffusion rates and the distribution of cation kinetic energies. At 220°C the concentration of vacancies and interstitials was higher than at 150°C, leading to faster exchange and diffusion rates. In combination with the larger distribution of cation kinetic energies this leads to the formation of a gradient alloy NC. In contrast, the exchange at 150°C was slower and the distribution of cation kinetic energies was narrower than at 220°C, leading to core/shell HNCs with a sharp interface. The thin (0.3 nm) CdSe shell of the ZnSe/CdSe core/shell appears to act as a protective layer at higher temperatures (up to 220°C), allowing the preservation of the core/shell structure despite the further cation exchange. The protective effect of the CdSe layer can be explained by the difference in bond strengths of Zn-Se and Cd-Se,<sup>[35,36]</sup> which decreases the concentration of vacancies and interstitials in the CdSe shell and at the surface of the NC. This decreases the impact of the distribution of kinetic energies of the diffusing cations at 220°C, making the migrating front less diffuse. The effect of temperature on the formation of ZnSe-CdSe NCs with different elemental distribution profiles, but with the same chemical composition, implies that there is an energy barrier for the formation of a (Cd,Zn)Se alloy from a ZnSe/CdSe core/shell HNCs. Indeed, the presence of an activation energy for conversion of core/shell QDs to alloy QDs has been observed before for CdSe/ZnSe core/shell QDs prepared by heteroepitaxial growth of ZnSe over CdSe NCs.<sup>[35]</sup>

#### 8.4 – Conclusions

In this chapter cation exchange of Zn atoms by Cd atoms in ZnSe NCs was investigated. Our results establish that the formation of Type- I<sup>1/2</sup> ZnSe/CdSe concentric core/shell HNCs (5.0 nm/ 0.3 nm) via Zn<sup>2+</sup> by Cd<sup>2+</sup> cation exchange on 5.6 nm ZnSe NCs occurs at 150°C. Increasing the temperature to 220°C leads to further cation exchange and formation of a thicker shell over the expense of the NC core (4.2 nm/0.7 nm ZnSe/CdSe core/shell). The optical properties of the 4.2 nm/0.7 nm ZnSe/CdSe core/shell red shift compared to the 5.0 nm/ 0.3 nm ZnSe/CdSe core/shell HNCs. This change in optical properties is not due to the formation of a Type-II HNC, which can be excluded based on the fact that the absorption transitions remain relatively narrow and the featureless absorption tail is



absent. The HNCs are thus still in the Type- I<sup>1/2</sup> regime and the differences in optical properties can be attributed to differences in the nature of electron wavefunction with increasing CdSe volume fraction. Increasing the reaction temperatures results in a higher degree of cation exchange and at 220°C the formation of gradient alloy NCs is observed. The 0.3 nm CdSe shell in the 5.0/0.3 nm core/shell HNCs prepared at 150°C seems to act as a protective shell that prevents the formation of a gradient alloy structure when the reaction temperature is increased to 220°C .

## REFERENCES

1. C. de Mello- Donegá, *Chem. Soc. Rev.* 2011, 40, 1512-1546.
2. A. Nemchinov, M. Kirsanova, N. N. Hewa-Kasakarage, M. Zamkov, *J. Phys. Chem. C* 2008, 112, 9301-9307.
3. R. Xie, X. Zhong, T. Basché, *Adv. Mater.* 2005, 17, 2741-2745.
4. S. Kim, B. Fisher, H.-J. Eisler, M. Bawendi, *J. Am. Chem. Soc.* 2003, 125, 11466-11467.
5. P. Reiss, J. I. Bleuse, A. Pron, *Nano Lett.* 2002, 2, 781-784.
6. J. Bleuse, S. Carayon, P. Reiss, *Physica E* 2004, 21, 331-335.
7. S. A. Ivanov, A. Piryatinski, J. Nanda, S. Tretiak, K. R. Zavadil, W. O. Wallace, D. Werder, V. I. Klimov, *J. Am. Chem. Soc.* 2007, 129, 11708-11719.
8. A. Pandey, P. Guyot-Sionnest, *J. Chem. Phys.* 2007, 127, 104710.
9. L. P. Balet, S. A. Ivanov, A. Piryatinski, M. Achermann, V. I. Klimov, *Nano Lett.* 2004, 4, 1485-1488.
10. D. J. Norris, A. L. Efros, S. C. Erwin, *Science* 2008, 319, 1776.
11. Y.-W. Jun, J.-S. Choi, J. Cheon, *Angew. Chem. Int. Ed.* 2006, 45, 3414 – 3439.
12. P. D. Cozzoli, T. Pellegrino, L. Manna, *Chem. Soc. Rev.* 2006, 35, 1195-1208.
13. J. Park, J. Joo, S. G. Kwon, Y. Jang, T. Hyeon, *Angew. Chem. Int. Ed.* 2007, 46, 4630 – 4660.
14. X. Wang, X. Ren, K. Kahen, M. A. Hahn, M. Rajeswaran, S. Maccagnano-Zacher, J. Silcox, G. E. Cragg, A. L. Efros, T. D. Krauss, *Nature* 2009, 459, 686-689.
15. L. Carbone, S. Kudera, C. Giannini, G. Ciccarella, R. Cingolani, P. D. Cozzoli, L. Manna, *J. of Mat. Chem.* 2006, 16, 3952-3956.
16. B. Koo, B. A. Korgel, *Nano Lett.* 2008, 8, 2490-2496.
17. J. Zhang, Y. Tang, K. Lee, M. Ouyang, *Science* 2010, 327, 1634-1637.
18. J. M. Pietryga, D. J. Werder, D. J. Williams, J. L. Casson, R. D. Schaller, V. I. Klimov, J. A. Hollingsworth, *J. Am. Chem. Soc.* 2008, 130, 4879-4885.
19. D. H. Son, S. M. Hughes, Y. Yin, A. P. Alivisatos, *Science* 2004, 306, 1009-1012.
20. J. Zhang, Y. Tang, K. Lee, M. Ouyang, *Science* 2010, 327, 1634-1638.
21. H. Li, M. Zanella, A. Genovese, M. Povia, A. Falqui, C. Giannini, L. Manna, *Nano Lett.* 2011, 11, 4964-4970.
22. K. Miszta, D. Dorfs, A. Genovese, M. R. Kim, L. Manna, *ASC Nano* 2011, 5, 7176-7183.
23. J. M. Luther, H. Zheng, B. Sadtler, A. P. Alivisatos, *J. Am. Chem. Soc.* 2009, 131, 16851-16857.
24. M. Casavola, M. A. Van Huis, S. Bals, K. Lambert, Z. Hens, D. Vanmaekelbergh, *Chem. Mater.* 2012, 24, 294-302.
25. D. Grodzinska, F. Pietra, M. A. van Huis, D. Vanmaekelbergh, C. de Mello- Donegá, *J. Mater. Chem.* 2011, 21, 11556-11565.

26. P. K. Jain, L. Amirav, S. Aloni, A. P. Alivisatos, *J. Am. Chem. Soc.* 2010, 132, 9997-9999.
27. B. Sadtler, D. O. Demchenko, H. Zheng, S. M. Hughes, M. G. Merkle, U. Dahmen, L.-W. Wang, A. P. Alivisatos, *J. Am. Chem. Soc.* 2009, 131, 5285-5293.
28. D. Dorfs, A. Salant, I. Popov, U. Banin, *Small* 2008, 9, 1319-1323.
29. D. J. Norris, M. G. Bawendi, *Phys. Rev. B* 1996, 53, 16338-16346.
30. L. S. Li, N. Pradhan, Y. Wang, X. Peng, *Nano Lett.* 2004, 4, 2261-2264.
31. C. de Mello Donegá, *Phys. Rev. B.* 2010, 81, 165303.
32. X. Zhong, Y. Feng, Y. Zhang, Z. Gu, L. Zou, *Nanotechnology* 2007, 18, 385606.
33. B. T. Kolomiets, C. M. Ling, *Sov. Phys-Solid State* 1960, 2, 154.
34. C. de Mello Donegá, R. Koole, *J. Phys. Chem. C* 2009, 113, 6511-6520.
35. X. Zhong, M. Han, Z. Dong, T. J. White, W. Knoll, *J. Am. Chem. Soc.* 2003, 125, 8589-8594.
36. J. A. Dean, 'Lange's Handbook of Chemistry', 15th ed., New York: McGraw-Hill, 1999.
37. Y.-M. Sung, Y.-J. Lee, K.-S. Park, *J. Am. Chem. Soc.* 2006, 128, 9002-9003.



## Chapter 9

# Ligand Mediated Surface Reconstruction and Relaxation of Colloidal CdTe QDs

---

*Shining Light on Photobrightening*

## Abstract

*This chapter describes a study of the photoluminescence (PL) enhancement of suspensions of colloidal CdTe QDs as a function of the equilibration time after dilution. Two different alkylamines (viz., dodecylamine, DDA, and octadecylamine, ODA) were used as capping ligands. The temporal evolution of the PL quantum yields (QYs) was followed both under periodic illumination and in the dark, for up to 25 h. To exclude the influence of oxygen and water the samples were prepared, stored, manipulated and measured in a glove box under nitrogen atmosphere. The PL of ODA capped CdTe QDs undergoes enhancement only under illumination, whereas the PL QY of dispersions of DDA capped CdTe QDs increases also under dark conditions. Based on our results, a ligand mediated surface reconstruction and surface relaxation model is proposed to explain the PL enhancements.*

## 9.1 – Introduction

Colloidal semiconductor nanocrystals (NCs) have tuneable optoelectronic properties which in combination with their colloidal stability makes them interesting materials for various applications.<sup>[1,2]</sup> The colloidal stability of the NCs is given by a layer of organic surfactant molecules (also referred to as ligands) that coat the NC surface. The inorganic-organic nature of colloidal NCs offers many possibilities regarding property control, since the inorganic core and the organic surfactant layer can be independently manipulated to tune the properties of the NCs (*e.g.* shape<sup>[3]</sup>, photoluminescence quantum yield, solubility, *etc.* <sup>[1,4]</sup>). Colloidal NCs are easily dispersible in various solvents, which is advantageous for applications since NCs can be used directly in solution or easily processed from solution.<sup>[1]</sup> The solubility of the NC can be changed via ligand exchange,<sup>[5]</sup> which demonstrates the dynamic character of the organic layer. The dynamics of several ligands at various NCs surfaces have been studied via NMR.<sup>[6-11]</sup> These studies indicated that the binding strength of the ligand has a large influence on their dynamic, since weakly binding ligands were found to be more dynamic at the NC surface (*e.g.* amines, *viz.* ligand residence times  $\geq 0.05$  ms<sup>-1</sup>) than strongly binding ligands (*e.g.* oleic acid, *viz.* ligand residence time s<sup>-1</sup> range).<sup>[1,8]</sup>

The photoluminescence quantum yield (PL-QY) of a semiconductor NC (or quantum dot, QD) strongly depends on the nature of the capping ligand and on the degree of ligand surface coverage.<sup>[1,12]</sup> Dangling orbitals at the NC surface give rise to energy states that lie within the HOMO-LUMO gap of the QD.<sup>[13]</sup> These mid-gap states efficiently trap the photoexcited carriers, thereby creating additional non-radiative relaxation pathways that reduce

the PL QY. Non-radiative relaxation of the exciton is prevented (or in other words PL-QY is enhanced) when the bond between the capping ligand and the dangling orbitals at the NC surface shift the energy of the surface states away from the HOMO-LUMO gap. Surface and trap states can also be shifted away from the HOMO-LUMO gap by self-passivation, which is a reorganization of the surface atoms in such a way that the dangling orbitals at the NC surface partially overlap.<sup>[14]</sup> This reorganisation redistributes the electronic density at the surface and can be achieved by surface relaxation and/or surface reconstruction.<sup>[1,14,15]</sup> Capping ligands are expected to strongly influence surface relaxation and surface reconstruction processes, since they modify the free energies of the NC surface and thereby may hinder or facilitate the reorganization of surface atoms.<sup>[1]</sup> Furthermore, the degree of order in the capping ligand shell can largely influence the PL-QY of QDs, as observed in the temperature anti-quenching effect.<sup>[16,17]</sup>

The PL QYs of QDs has also been observed to be enhanced or reduced by illumination, which is referred to as photobrightening (photoenhancement), and photodarkening, respectively. PL photobrightening has been reported for colloidal QDs of a number of different materials (*e.g.*, CdTe<sup>[18,19]</sup>, CdSe<sup>[18-22]</sup>, CdSe/CdS<sup>[20]</sup>, PbS<sup>[23]</sup>, InAs<sup>[19]</sup>, ZnS/Mn-doped<sup>[24]</sup>) and under a variety of conditions. Although several different models have been proposed for photobrightening (*e.g.*, photoannealing, photooxidation, ligand assisted photobrightening, and adsorption of water and methanol molecules on the NC surface), the effect is yet not fully understood.<sup>[18]</sup>

In this chapter the PL enhancement of colloidal CdTe QDs upon light irradiation and in the dark is investigated. The chapter is organized as follows. First, the characteristics of the investigated colloidal CdTe QDs are described. Then a description of the observed PL enhancement effect in the CdTe QD dispersions is given. Furthermore the influence of the capping ligand is investigated by monitoring the temporal evolution of the PL intensity of octadecylamine and dodecylamine capped CdTe QDs upon illumination over long periods (13-25 hours). ODA capped QDs only showed PL-enhancement after illumination whereas the PL-intensity of DDA capped CdTe QDs increased also in the dark. Finally, we propose a model for the PL enhancement observed in both colloidal CdTe QD systems.

## 9.2 – Experimental methods

**Chemicals:** Dimethylcadmium (99.9%) was purchased from ARC Technologies. Tellurium (99.999%, < 250 mm) was purchased from Heraeus.

Dodecylamine (DDA, 98%), Tri-octylphosphine (TOP, 90%), methanol and chloroform were purchased from Aldrich. Octadecylamine (ODA, >90%) was purchased from Fluka. Before use, ODA, and DDA were degassed and dried under vacuum (3 h at 120°C).

**Synthesis of DDA capped CdTe QDs:**<sup>[17]</sup> Three different sized CdTe QDs were prepared following a procedure given in ref [17] In a three necked flask 10 g of dry DDA and 7 mL of TOP were heated to 50 °C. To this solution 0.22 g (1.54 mmol) Cd(Me)<sub>2</sub> in 7 mL of TOP and 0.16 g (1.25 mmol) Te powder were added. The reaction mixture was heated to 145°C under vigorous stirring and kept at this temperature for 2h and 10min. Subsequently the reaction mixture was further heated to 165°C and kept stable for 3h and 40 min. Fractions of different sized QDs were obtained by taking samples at different stages in the synthesis. The 2.7, and 2.9 nm CdTe QDs fractions originate from the same synthesis, whereas the 2.8 nm CdTe were formed in another, but similar, synthesis.

**Purification of CdTe NC:** Purification of the QDs involves 2 steps. In a first step the undissolved Tellurium powder was removed from the reaction mixture by centrifugation (3000 rpm 15 min). The colored top layer, which is the crude reaction mixture without the unreacted Te powder, was removed (purification step 1). Further purification (purification step 2) of the CdTe NC crude reaction mixture without unreacted Te powder was done for some experiments. In the second step, QDs were precipitated from the coloured top solution layer (formed in purification step 1) in anhydrous toluene (1:1 volume ratio) by adding anhydrous methanol. The sediment was isolated by centrifugation (3000 rpm, 15 min), and redissolved in anhydrous toluene or in dodecane.

**Ligand exchange of the CdTe QDs:** The CdTe QDs used in the experiments given in figure 9.4. were prior measuring subjected to ligand exchange. Ligands exchange QDs was performed on purified CdTe QDs (purification step 2). For DDA capped CdTe QDs, 197 µL of a 4.8 µM purified (step 2) 2.9 nm CdTe NC stock solution was mixed with 204.6 µL DDA and stirred for 14 hours at 55°C. For ODA capped CdTe QDs, 180.7 µL of a 4.8 µM purified (step 2) 2.9 nm CdTe NC stock solution was mixed with 299.3 µL (0.257 gram) ODA (at 50°C) and stirred for 14 hours at 55°C. Both ligand exchange solutions had a ligand concentration of 2M.



**Characterization:** Absorption spectra were measured on a double beam Perkin-Elmer Lambda 16 UV/Vis spectrometer (scan rate: 1 nm/s). Photoluminescence (PL) spectra were recorded by using a Princeton Instrument Liquid N<sub>2</sub>-cooled CCD-detector and a 0.3 m Acton Research monochromator (150 lines/mm grating blazed at 500 nm). As excitation source a 400 nm 10W LED was used. PL quantum yields were determined using a rhodamine B solution in absolute ethanol, following the method reported in reference [25].

**Protocol for measuring photoluminescence spectra series:** All PL spectra time series were performed in a glove-box under nitrogen (< 5 ppm O<sub>2</sub> and H<sub>2</sub>O) with the use of a fixed measurement set up (figure 9.1). An optical fiber was used to direct the excitation light (400 nm LED, outside glovebox) onto a quartz cuvet containing the NC solution and to direct the emitted PL light to the CCD detector. The fixed measurement set up was covered by a cap to prevent any influence of external light. PL spectra were taken with 10 minutes interval. Switching-on of the excitation source (400 nm LED) and recording of the spectra was automatically regulated by an ST133 controller configured via WinSpec32 software. NC dilutions were prepared by diluting a CdTe NC stock solution by a factor of 100.

**Protocol for integrated intensity analysis of PL spectra time series:** Analysis of PL spectra time series were performed following two different methods. First analysis method was used for the measurements with the 2.7 nm and 2.8 nm CdTe NC samples and involved the numerical area integration between two fixed points on the wavelength axis. The PL peak maximum position was determined as the position of the highest intensity in the FFT filter smoothed spectra. The second analysis method was used for the sample in which the defect PL was clearly observed in the PL spectra (2.9 nm CdTe). A Mathematica script was used to fit each PL spectrum, which was corrected for background noise, to 2 Gaussian functions. The integrated area of the Gaussian function for the excitonic PL peak was taken as the integrated PL intensity and maximum of this Gaussian function was taken as the position of the excitonic PL peak maximum.

**Dynamic light scattering (DLS) experiments:** DLS measurements were performed on a Malvern ZetaSizer Nano, using ZetaSizer software 6.20. A purified (purification step 1) 2.9 nm CdTe NC dispersion in toluene was diluted 100 times in toluene in a nitrogen-filled glovebox. Subsequently, the diluted NC dispersion was filtered twice by a hydrophobic filter (pore

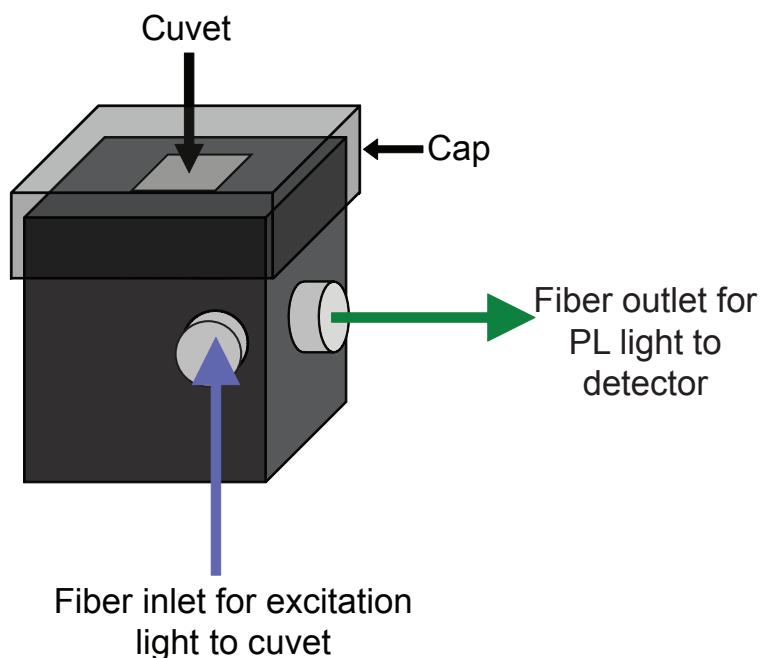


**Figure 9.1** – Schematic illustration of the fixed measurement set-up used for PL spectra time series.

size 0.2  $\mu\text{M}$ ) to remove dust particles. Samples were measured in a sealed quartz cuvet at 25°C. Backscatter signal was measured at 173°, and forward scattering was measured at 12.8°.

**Fourier Transform Infrared (FTIR) spectroscopy experiments:** FTIR measurements were performed on a Perkin Elmer Frontier infrared spectrometer and with a nitrogen flushed measurement chamber. 0.213 g DDA was added to a stock solution (16  $\mu\text{M}$ ) of purified (purification step 2) 2.8 nm CdTe QDs in dodecane. A FTIR measurement cell with KBr windows was used to measure a liquid NC solution. The cell was filled with a 100 times diluted stock dispersion (containing QDs, DDA and dodecane) in a nitrogen filled glovebox.

## 9.3 – Results and discussion

### 9.3.1 – Characteristics of the colloidal CdTe QDs investigated

CdTe QDs were synthesized in a heating-up synthesis method with the use of dodecylamine (DDA) and trioctylphosphine (TOP) as coordinating ligands.<sup>[17]</sup> Different sized CdTe QDs were isolated from the reaction mixture after different reaction times. The absorption spectra of three different CdTe QDs, used in the experiments described below, are given in figure 9.2a. The size of the QDs was estimated to be 2.7, 2.8, and 2.9 nm by using an empirical sizing curve correlating the position of the lowest energy absorption transition in CdTe QDs with the QD size.<sup>[26]</sup> The 2.7 and 2.8 nm CdTe NCs were used in the PL-enhancement experiments by diluting from their crude reaction mixture (purification step 1), whereas the 2.9 nm CdTe NC dispersion was used either after purification (purification step 2) or after ligand exchange by dodecylamine (DDA, C<sub>12</sub>H<sub>25</sub>NH<sub>2</sub>) and octadecylamine (ODA, C<sub>18</sub>H<sub>37</sub>NH<sub>2</sub>). The photoluminescence (PL) spectra of the samples are given in figure 9.2b and in all PL spectra a sharp excitonic peak and a broad trap related band at lower energies can be observed. The relatively higher intensity of the trap related broad band in for the 2.9 nm CdTe QDs compared to the 2.7 and 2.8 nm CdTe QDs can be ascribed to the decreased surface passivation caused by the ligand exchange after purification (purification step 2).<sup>[11,27]</sup> The full width half maximum (FWHM) of the excitonic peak is 110, 153, and 134 eV for the 2.7, 2.8, and 2.9 nm CdTe QDs, respectively.

### 9.3.2 – Temporal evolution of the PL enhancement of DDA capped CdTe QDs

The PL intensity of diluted CdTe QDs dispersion has been followed as a function of the time after dilution by measuring PL spectra with a 5 (or 10) minute time interval over a certain time period ( $t_0$  = directly after diluting the stock solution of CdTe NC crude reaction mixture by a factor of 100). In this chapter such a series of measurements will be referred to as 'PL spectra time series'. Figure 9.3a shows a few PL spectra from a time series of a dispersion of DDA capped CdTe QDs diluted from the crude reaction mixture (2.7 nm CdTe NCs, purification step 1). The temporal evolution of the total PL intensity can be followed by plotting the (normalized) integrated PL intensity of the complete PL spectra time series against the equilibration time. In this chapter such a PL evolution plot, given in figure 9.3b, will be referred to as integrated PL spectra time series. The integrated PL spectra times series given in figure 9.3 shows that the PL-intensity increases rapidly during the first ~3 hours of the measurement and more slowly after ~3 hours.

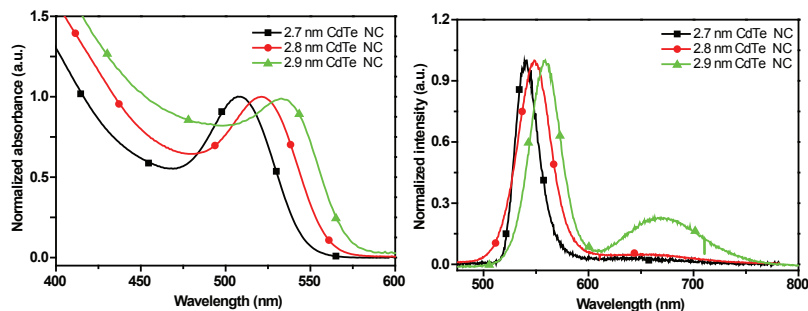


**Figure 9.2** – Absorption (**left panel**) and emission (**right panel**) spectra of the as prepared 2.7, 2.8 nm CdTe QDs and the purified 2.9 nm CdTe QDs.

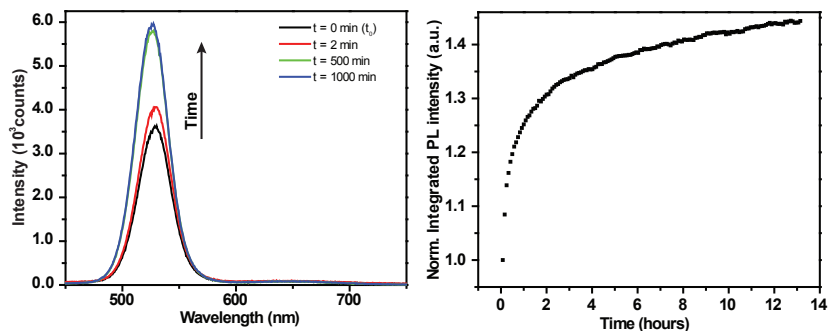


**Figure 9.3** – (**left panel**) PL spectra, taken from a PL spectra time series, of a 2.7 nm (1.8  $\mu\text{M}$ ) CdTe NC dispersion in toluene ( $t_0$  = directly after diluting the stock solution of CdTe QDs by a factor of 100) (**right panel**) normalized integrated PL intensity of the all PL spectra during a PL spectra time series (referred to as integrated PL spectra time series). The NC dispersion was illuminated for spectral acquisition for 1 second with time intervals of 5 minutes between the sequential spectral acquisition over a period of  $\sim 13$  hours.

### 9.3.3 – Influence of ligands on the PL enhancement

Ligands are an important aspect of colloidal QDs since they are not only responsible for the colloidal stability of the QDs, but also influence their optical properties. For CdTe and CdSe QDs it has been demonstrated that the nature of the ligands has a large influence on the PL-QY.<sup>[11,28-30]</sup> To examine the influence of the ligands on the PL enhancement during a PL spectra time series, PL spectra time series of DDA as well as ODA capped CdTe QDs were measured (figure 9.4). The absorption spectra of the ODA and DDA recapped CdTe QDs dispersions (referred to as ODA-Sample and DDA-Sample) are identical and the PL-QY of both solutions immediately after preparation are comparable (19.4%, and 20.6% for ODA-Sample, and DDA-Sample, respectively). During the PL spectra time series samples were illuminated for spectral acquisition for 1 second with time intervals of 10 minutes between the sequential spectral acquisitions. Besides the samples that would be illuminated during the PL spectra time series, two ODA and DDA capped CdTe NC dispersions (identical to the illuminated NC dispersions) were prepared. These samples were allowed to equilibrate in the dark for ~25 hours before measuring their PL spectrum and they are referred to as dark-ODA-Sample and dark-DDA-Sample. The integrated PL intensity values were converted into PL-QYs by comparing to a standard dye solution of which the PL-QY is known.<sup>[25]</sup> Figure 9.4. shows the evolution of the PL-QY as a function of the equilibration time of illuminated ODA-Sample and DDA-Sample, and the dark-ODA-Sample and dark-DDA-Sample. The PL-QY of the ODA-Sample increases from 19.4% to 23.3% after 24 h and 38 minutes, which corresponds to a relative increase of 20%. The PL-QY of the dark-ODA-Sample is 17.2%, which is lower than all PL-QY measured in the PL spectra time series. These results clearly establish that the PL-QY of the ODA capped CdTe NC dispersion only enhances after periodic illumination, which can thus be ascribed to photobrightening. The PL-QY of the DDA-Sample increases from 20.6% to 29.9% after 24 h and 38 minutes, which is a relative increase of 45%. Remarkably, the PL-QY of the DDA-sample kept in the dark increased as well, reaching 27.7%, which is just slightly lower than the final PL-QY of the DDA-Sample that was subjected to periodic illumination. These results indicate that PL-QY enhancement occurs for 2.9 nm DDA capped CdTe QDs even without the illumination, albeit to a somewhat lower extent.

### 9.3.4 – Influence of equilibration time on PL enhancement

The results above clearly show that for the DDA capped 2.9 nm CdTe QDs the PL enhancement occurs even without illumination. To investigate

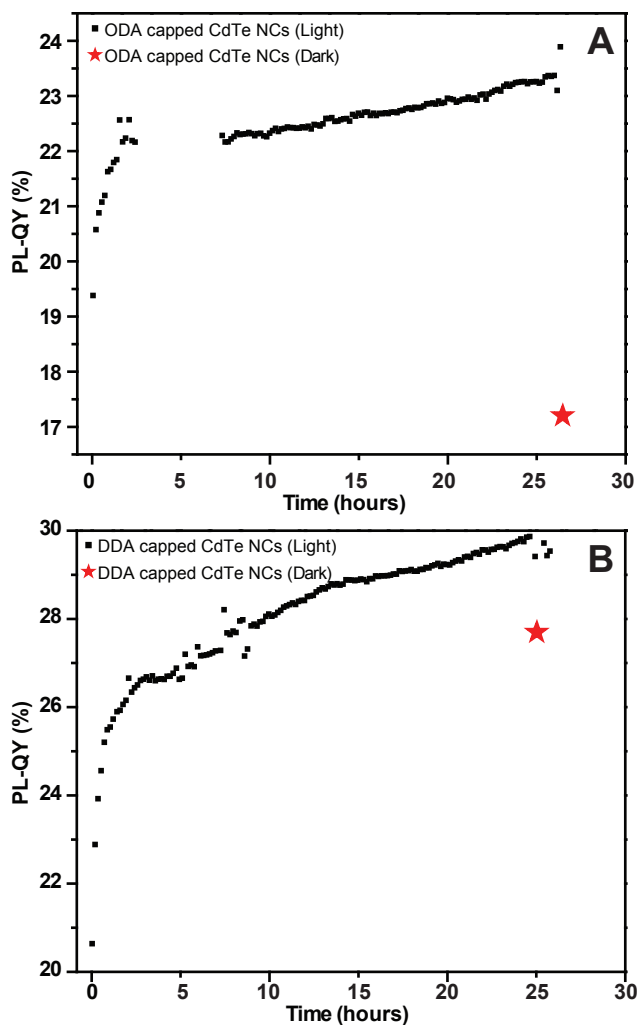


**Figure 9.4** – Temporal evolution of the PL-QY of 2.9 nm CdTe NC dispersions in toluene ( $t_0$  = directly after diluting the stock solution of CdTe QDs by a factor of 100) (a) ODA recapped (0.14 mM) CdTe NC dispersion in toluene. (b) DDA recapped (0.18 mM) CdTe NC dispersion in toluene. The NC dispersions were illuminated for spectral acquisition for 1 second with time intervals of 10 minutes between the sequential spectral acquisition over a period of ~26,5 hours. Stars indicate the PL-QY of NC dispersion, which were identical to the dispersions measured in (a) and (b), after ~26,5 hours equilibration time in the dark.

the influence of the equilibration time on the PL enhancement, a 2.7 nm CdTe NC dispersion (identical to the solution measured in figure 9.3) was allowed to equilibrate 24 h in the dark prior to measuring the PL spectra time series. The integrated PL spectra time series of the two identical 2.7 nm CdTe NC dispersions of which one was measured after 24 h being stored in the dark (Equilibrated-sample) and the other was measured directly after dilution (Fresh-sample) are given in figure 9.5. The integrated PL intensity (counts) of the Fresh-sample is at  $t_0$  127612 counts and it increases to 184231 counts after ~13 h, which corresponds to an increase of 44.4%. The Equilibrated-sample has at  $t_0$  an integrated PL intensity of 191608 counts and this increases to 204017 after ~13 h, which corresponds to an increase of 6.5%. The integrated PL intensity of the Equilibrated-sample starts thus at much higher values than the Fresh-sample, which implies that the PL intensity of the Equilibrated-sample has already increased during the 24 h of equilibration in the dark. The PL enhancement in the Fresh-sample PL spectra time series shows an initial fast nonlinear increase which slows down after ~3 h. At longer equilibration times, such as in the Equilibrated-sample an almost linear increase is observed.

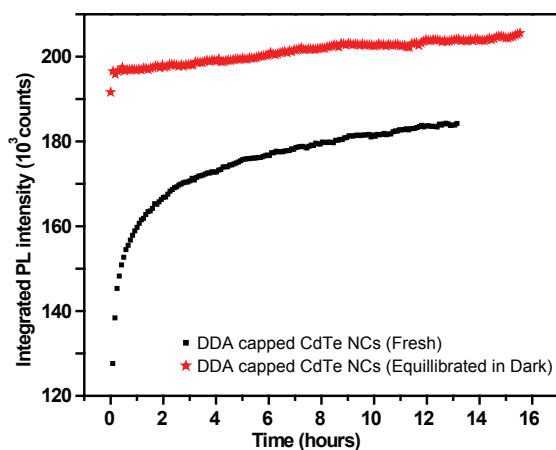


**Figure 9.5** – Temporal evolution of the integrated PL intensity from PL spectra of a 2.7 nm (1.8  $\mu\text{M}$ ) CdTe NC dispersion in toluene ( $t_0$  = directly after diluting the stock solution of CdTe QDs by a factor of 100). NC dispersions were illuminated for spectral acquisition for 1 second with time intervals of 5 minutes between the sequential spectral acquisition over a period of ~13 hours. (squares) PL spectra time series started directly after preparation of the sample (stars) PL spectra time series was started after the dilution equilibrated for ~24 hours in the dark.

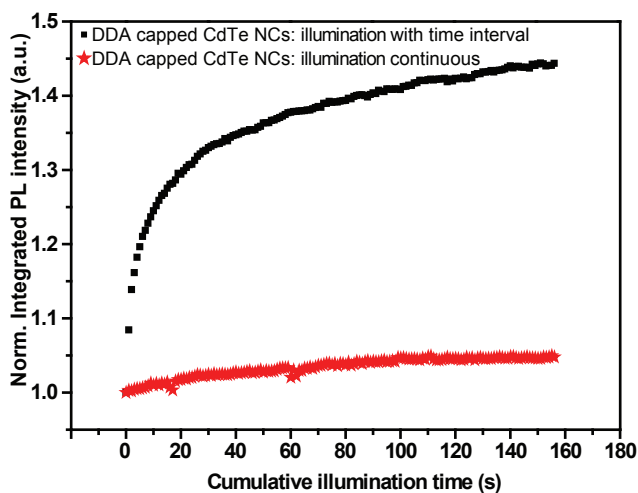


**Figure 9.6** – Temporal evolution of the integrated PL intensity from PL spectra of a 2.7 nm (1.8  $\mu\text{M}$ ) CdTe NC dispersion in toluene ( $t_0$ = directly after diluting the stock solution of CdTe QDs by a factor of 100). (**squares**) NC dispersion was illuminated for spectral acquisition for 1 second with time intervals of 5 minutes between the sequential spectral acquisition over a period of ~13 hours. (**stars**) NC dispersion was continuously illuminated and PL spectra were acquired with a time interval of 8 second over a period of 156 seconds

So far, all PL spectra time series given above were measured by illuminating the NC dispersions for 1 second with a 5 or 10 minute interval between consecutive spectral acquisitions. The measurements shown in figure 9.5 and discussed above suggest that the influence of light on the PL enhancement of DDA capped CdTe QDs is minor. To further investigate the influence of the equilibration time and the illumination time, an identical 2.7 nm CdTe NC dispersion as given in figure 9.3b was measured in a PL spectra time series in which the dispersion was continuously illuminated (continuous illuminated NC dispersion) instead of illuminated for 1 second with an interval of 5 minutes (figure 9.3b, periodically illuminated NC dispersion). Illuminating a NC sample 1 s every 5 min during 13 h corresponds to a total illumination time of 156 s. Therefore, the continuously illuminated NC dispersion was exposed to 156 consecutive light pulses of 1 s duration. The integrated PL spectra time series of the continuously illuminated NC dispersion and of the dispersion illuminated with time intervals between acquisitions are plotted against the cumulative illumination time (figure 9.6). Each data point corresponds to one second of illumination, which



allows direct comparison of the two series. Although both samples were exposed to same amount of light (*i.e.*, 156 s), the PL intensity enhancement in the continuously illuminated sample is much smaller (4.8%) than that observed for the periodically illuminated NC dispersion (44.4%). These observations, along with the results given in figure 9.5, clearly indicate that the equilibration time is a more important factor for the PL enhancement than illumination.

### 9.3.5 – Ligand mediated surface reconstruction/relaxation model

The increase of PL intensity of QDs upon illumination (photobrightening) has been reported for various materials (*e.g.*, CdTe<sup>[18,19]</sup>, CdSe<sup>[18-22]</sup>, CdSe/CdS<sup>[20]</sup>, CdSe/ZnSe<sup>[22]</sup>, PbS<sup>[23]</sup>, InAs<sup>[19]</sup>, ZnS:Mn<sup>[24]</sup>). Due to the various experimental conditions under which photobrightening has been observed, many different explanations have been proposed for this phenomenon, such as photoinduced passivation of the NC surface by water or methanol<sup>[22]</sup>, oxygen passivation of the NC surface<sup>[21]</sup>, elimination of topological surface defects via photocorrosion<sup>[20]</sup>, and surface reconstruction and relaxation<sup>[18,19]</sup>. The experiments described above were carried out in a glove-box under nitrogen (< 5 ppm O<sub>2</sub> and H<sub>2</sub>O), which excludes the possibility that the PL enhancement observed here was caused by oxygen or water passivation of the NC surface. It should be noted that deliberate exposure of the samples to air led to PL quenching upon illumination, rather than PL enhancement. The possibility that the enhancement is caused by methanol molecules adsorbed to the surface of the CdTe NCs during the purification step can also be excluded, since the same behavior is observed for samples that had never been exposed to methanol.

Our results indicate that the ligands strongly affect the observed PL QY enhancement of the CdTe QDs. The PL QY of ODA capped CdTe QDs was enhanced only after illumination, whereas that of DDA capped CdTe QDs increases also after equilibration in the dark. The effect of capping ligands on the PL-QYs of colloidal QDs has been the subject of several studies.<sup>[11,16,17,27,29,30]</sup> The PL-QY is found to depend on the degree of ligand surface coverage<sup>[11]</sup>, the nature of the ligand<sup>[27-29]</sup>, and the organization of the ligands on the NC surface.<sup>[16,17]</sup> For example, the energy position of thiols on a CdTe NC surface is such that it removes trap states from the HOMO-LUMO gap. In contrast, thiol molecules are very efficient hole acceptors for CdSe QDs.<sup>[28]</sup> Thiols are thus known to quench the PL of CdSe QDs, while enhancing the PL of CdTe QDs.<sup>[28]</sup> Furthermore, the (des)organization of the

ligand layer on the NC surface has been found to have a large influence on the PL-QY. Cooling down of CdTe and CdSe NC dispersions below a specific temperature has been observed to induce PL quenching, presumably due to surface defects created by the ordering of the alkylamine capping layer on the NC surface. This effect is fully reversible, and the PL of the NCs was observed to recover to its original intensity upon increase of the temperature above a characteristic temperature related to a phase transition in the alkylamine capping monolayer at the surface of the QD (temperature anti-quenching effect).<sup>[16,17]</sup> To study the ligand layer on the CdTe NC surface, Fourier transform infrared (FT-IR) spectra of a dispersion of DDA capped CdTe QDs were measured as a function of the equilibration time after dilution from the crude reaction mixture. No changes were observed in the FT-IR spectra during equilibration, except for the intensity of the peak at  $721\text{ cm}^{-1}$ . This peak corresponds to the rocking vibration of the alkyl chain.<sup>[31]</sup> The absorbance at this frequency decreases rapidly over the first 2.5 h after dilution (figure 9.7) Ligands taking part of an ordered monolayer have less freedom to move and, depending on the level of ordering, are not able to perform the rocking vibration. Therefore, the decrease of the intensity of the peak due to the rocking vibration can be taken as indication

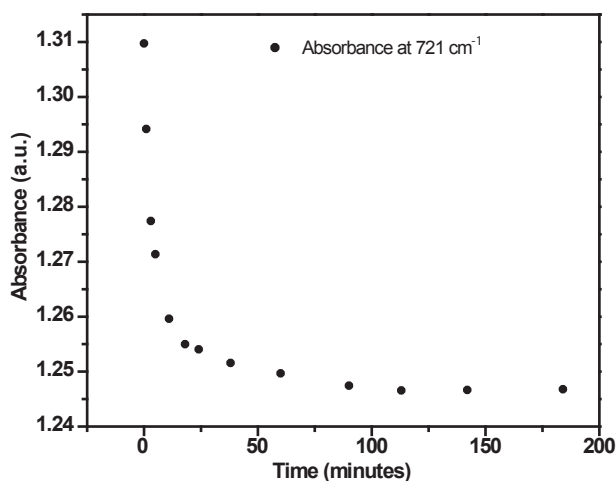


**Figure 9.7** – Temporal evolution of the absorbance of the  $721\text{ cm}^{-1}$  peak in IR spectra, corresponding to the rocking vibration of the C-chain<sup>[31]</sup>, of a purified (purification step 2)  $2.8\text{ nm}$  ( $1.6\text{ }\mu\text{M}$ ) CdTe NC dispersion in dodecane monitored over a period of 180 minutes.  $t_0$  = Directly after diluting the stock solution of CdTe QDs by a factor of 100.

that the DDA molecules have become more organized on the NC surface. It is remarkable that this 2.5 h time window coincides with the fast initial increase in the integrated PL spectra time series. This suggests that the initial fast increase of PL intensity is related to the reorganization of the ligands on the NC surface.

From the results presented in figure 9.5 it is clear that the PL enhancement in DDA capped CdTe NC dispersions starts directly after the preparation of the diluted suspension. In literature, a hypothesis was proposed that stated that the dilution of a NC dispersion can lead to disaggregation of pre-existing NC clusters.<sup>[32]</sup> In clusters of QDs the inter-NC distance is sufficiently small to allow strong electric dipole interactions which can result in non-radiative energy transfer. Energy transfer can occur from luminescent 'bright' QDs to other luminescent 'bright' QDs or to non-luminescent 'dark' QDs. In the latter case, the excitation energy will be lost non-radiatively. Therefore, inter-NC energy transfer increases the probability of non-radiative recombination, thereby lowering the PL-QY. The disaggregation of pre-existing NC clusters upon dilution could thus lead to PL enhancement. To investigate whether clusters of NCs were being formed or dismantled during the equilibration of the colloidal CdTe QDs after dilution, the hydrodynamic size of the particles present in solution was followed over time by using dynamic light scattering (DLS). Figure 9.8 displays the hydrodynamic diameter of particles in a dispersion of 2.9 nm DDA capped CdTe QDs as a function of the equilibration time after dilution of the crude reaction mixture in toluene. The hydrodynamic radius is ca. 16 nm and remains constant throughout the whole experiment (~18 h). The hydrodynamic radius is defined by the size of the NC (including the capping ligand shell), and the solvent molecules that are dragged along by the NC and which reside in a so called solution sphere.<sup>[33]</sup> The inorganic core of the colloidal NC has a radius of 1.45 nm and is capped by DDA ligands that have an estimated length of ~1.8 nm<sup>[34,35]</sup> and the thickness of the solvent layer is then estimated as 4.75 nm. The fact that only particles of this size are observed throughout the whole measurement excludes the possibility that the presently observed PL enhancement is a result of the disaggregation of pre-existing NC clusters. It also shows that the colloidal suspensions of DDA capped CdTe QDs investigated here are very stable, since no NC clusters are formed during the equilibration period.

To explain the photobrightening of the ODA capped CdTe QDs and the brightening of the DDA capped CdTe QDs we propose a model in which the

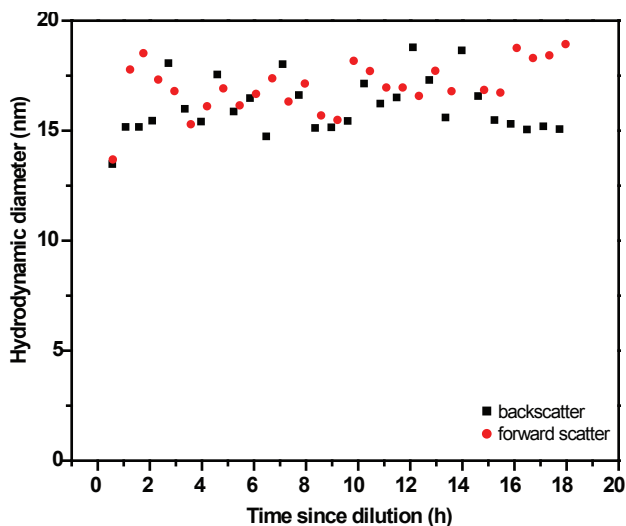


**Figure 9.8** – Temporal evolution of the hydrodynamic radius, observed via dynamic light scattering, in a 2.9 nm (2.1  $\mu\text{M}$ ) CdTe NC dispersion in toluene monitored over a period of ~18 hours.  $t_0$  = Directly after diluting the stock solution of CdTe QDs by a factor of 100.

ligand mediates the surface reconstruction and the surface relaxation of CdTe NCs. Extensive investigation of bulk semiconductors has shown that surface reconstruction and relaxation occur in II-VI semiconductors.<sup>[1,12]</sup> Surface relaxation involves shortening of the bonds between the surface atoms and the atoms underneath.<sup>[1]</sup> Surface reconstruction involves a more extensive reorganisation of the surface atoms which changes both the bond lengths and the coordination geometry.<sup>[1]</sup> Surface relaxation and reconstruction lead to a NC configuration that has a lower total free energy. Surface defects and unsatisfied surface bonds (*i.e.*, dangling orbitals) are ‘high energy’ sites that increase the total free energy of the ligand capped NC. As mentioned in the introduction, high energy sites give rise to surface and trap states that can promote non-radiative exciton recombination. Removal of high energy sites thus leads to a lower total free energy and simultaneously to a higher PL-QY. Ligands can mediate the removal of high energy sites because they coordinate to surface atoms and can form a dynamic ligand layer at the NC surface. Capping ligands are thus capable of transporting atoms from high energy surface sites to low energy surface sites. Furthermore, ligands can change the free energy of crystal NC facets, thereby lowering the activation energy for reconstruction of facets.

The integrated PL spectra time series, given in figure 9.4 can be roughly divided into two regimes: (1) an initial fast increase of the PL-QY observed at a shorter equilibration time scales, (2) a relatively slow PL-QY enhancement at longer equilibration time scales. In our model we propose that the increase in PL-QY in the different regimes can be ascribed to surface reconstruction and surface relaxation. The FT-IR results, given in figure 9.7, suggest that the initial fast increase of the PL-QY is related to the organisation of the capping ligands at the NC surface (figure 9.9), leading to surface reconstruction or surface relaxation. The PL enhancement of ODA capped CdTe NC dispersions needs illumination to occur, whereas that of DDA capped CdTe NCs occurs also in the dark. This implies that there is an energy barrier for the relaxation and/or reconstruction of the surface of alkylamine capped CdTe QDs and that this activation energy is higher for ODA capped CdTe QDs. The energy barrier for the PL enhancement of DDA capped CdTe QDs is in the order of  $kT_{RT}$  ( $T_{RT}$  = room temperature), since the enhancement occurs at room temperature and in the dark. The melting temperature of ODA and DDA are different (52.9°C, and 28.3°C, respectively<sup>[36]</sup>), which implies that the interaction between the longer alkylchains of ODA is larger than that between the shorter alkylchains of DDA. The stronger interchain interactions in ODA results in a more rigid ligand layer at the NC surface that impose a higher energetic barrier for surface reorganization. Although both ODA and DDA ligands are known to be dynamic at the NC surface (residence times  $\geq 0.05$  ms<sup>-1</sup>), the ODA molecules will have a lower mobility due to the interchain interactions and are therefore less effective in transporting atoms from high energy to low energy surface sites (figure 9.9).

At longer equilibration times an increase in PL-QY via surface reconstruction is proposed. The ligands bound at the NC surface influence the surface reconstruction by increasing or decreasing the free energy of the NC surface. Important to realize is that the equilibrium configuration of ligand capped NCs is the one that has the lowest total free energy. When the system is perturbed (such as by diluting a NC dispersion) the NCs will adjust their configuration to a (new) configuration that minimizes the total free energy in the new situation. Our model includes the balance between the free energies of the capping monolayer and the NC surface. The surface of DDA capped CdTe NCs is able to relax/reconstruct at room temperature because the weaker interchain interactions make the DDA capping layer more dynamic, thereby lowering the activation energies involved in the surface relaxation and reconstruction process. It is likely that the process is further boosted by a positive feedback between the NC surface and the capping layer, since the ordered surface may work as a template, guiding the organization of

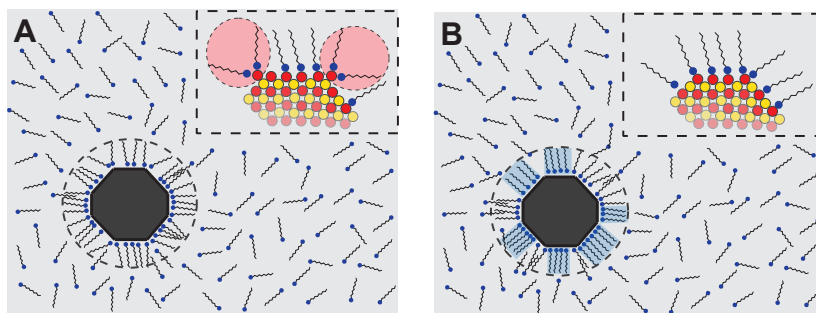


**Figure 9.9** – Schematic illustration of the ordering of the ligand layer and removal of high energy points (see inset) on a colloidal NC from situation (a) to situation (b).

the capping ligand shell, thereby maximizing the interchain interactions and further lowering the total free energy of the system. This feedback is more important for the DDA capped QDs, since DDA monolayers would be disordered at room temperature in the absence of a templating effect. For ODA capped CdTe NCs the interactions between the alkylchains are much higher, imposing energy barriers higher than  $kT_{RT}$  for the surface relaxation and reconstruction process. Therefore, light absorption is required. Further, the potential energy gain of the templating effect of the NC surface is less important for ODA monolayers, which are probably already well ordered at RT.

#### 9.4 – Conclusions

In this chapter, the PL-enhancement of CdTe QDs was investigated. A PL enhancement of ODA capped CdTe NC dispersion was observed only when the NC dispersion was irradiated by light (photobrightening). For DDA capped CdTe QDs a PL-enhancement was observed with and without the illumination of the NC dispersion. The PL enhancement of the illuminated ODA and DDA capped CdTe NC dispersions showed an initial fast non linear increase and after 3 h a relatively slow linear PL intensity increase was observed. The PL enhancement of DDA capped CdTe NCs seem to start immediately after the preparation of the NC solution (dilution from a concentrated stock) and the degree of PL-enhancement is determined mostly by the equilibration time. Light appears to have a small influence of the PL-enhancement in DDA capped NC dispersions. Based on our results we propose a ligand mediated surface reconstruction and surface relaxation model. This model emphasizes the importance of the ligand-ligand and ligand-NC surface interactions which determine the evolution of the PL-enhancement of the CdTe QDs.

## REFERENCES

1. C. de Mello Donegá, *Chem. Soc. Rev.* 2011, 40, 3, 1512-1546.
2. D. V. Talapin, J.-S. Lee, M. V. Kovalenko, E. V. Shevchenko, *Chem. Rev.* 2010, 110, 389-458.
3. C. Fang, M. A. Van Huis, D. Vanmaekelbergh, H. W. Zandbergen, *ACS Nano* 2010, 4, 211.
4. R. Koole, 'Fundamentals and applications of semiconductor nanocrystals', (Ph.D. Thesis), Utrecht University, Utrecht, 2008.
5. D. V. Talapin, J.-S. Lee, M. V. Kovalenko, E. V. Shevchenko, *Chem. Rev.* 2010, 110, 389-458.
6. R. L. Donkers, Y. Song, R. W. Murray, *Langmuir* 2004, 20, 4703
7. J. R. Sachleben, E. W. Wooten, L. Emsley, A. Pines, V. L. Colvin, A. P. Alivisatos, *Chem. Phys. Lett.* 1992, 198, 431-436.
8. A. Hassinen, I. Moreels, C. de Mello Donegá, J. C. Martins, Z. Hens, *J. Phys. Chem. Lett.* 2010, 1, 2577-2581.
9. J. R. Sachleben, V. Colvin, L. Emsley, E. Wrenn Wooten, A. P. Alivisatos, *J. Phys. Chem. B* 1998, 102, 10117-10128.
10. B. Fritzing, I. Moreels, P. Lommens, R. Koole, Z. Hens, J. C. Martins, *J. Am. Chem. Soc.* 2009, 131, 3024.
11. X. Ji, D. Copenhaver, C. Sigmund, X. Peng, *J. Am. Chem. Soc.* 2008, 130, 5726-5735.
12. R. Koole, P. Schapotschnikow, C. de Mello Donegá, T. J. H. Vlucht, A. Meijerink, *ACS Nano* 2008, 2, 1703.
13. A. P. Alivisatos, *J. Phys. Chem.* 1996, 100, 13226.
14. A. Kahn, *Surf. Sci.* 1994, 299-300, 469.
15. D. D. Lovingood, R. Achey, A. K. Paravastu, G. F. Strouse, *J. Am. Chem. Soc.* 2010, 132, 3344.
16. S. F. Wuister, A. van Houselt, C. de Mello Donegá, D. Vanmaekelbergh, A. Meijerink, *Angew. Chem. Int. Ed.* 2004, 43, 3029.
17. S. F. Wuister, C. de Mello Donegá, A. Meijerink, *J. Am. Chem. Soc.* 2004, 126, 10397.
18. C. Carrillo-Carrión, S. Cárdenas, B. M. Simonet, M. Valcárcel, *Chem. Commun.* 2009, 35, 5214-5226.
19. D. V. Talapin, A. L. Rogach, E. V. Shevchenko, A. Kornowski, M. Haase, H. Weller, *J. Am. Chem. Soc.* 2002, 124, 5782-5790.
20. Y. Wang, Z. Tang, M. A. Correa-Duarte, I. Pastoriza-Santos, M. Giersig, N. A. Kotov, L. M. Liz-Marzán, *J. Phys. Chem. B* 2004, 108, 15461-15469.
21. Z. Zhelev, R. Jose, T. Nagase, H. Ohba, R. Bakalova, M. Ishikawa, Y. Baba, *J. of Photochemistry and Photobiology B: Biology* 2004, 75, 99-105.

22. M. Jones, J. Nedeljkovic, R. J. Ellingson, A. J. Nozik, *J. Phys. Chem. B* 2003, 107, 11346-11352.
23. J. J. Peterson, T. D. Krauss, *Phys. Chem. Chem. Phys.* 2006, 8, 3851-3856.
24. A. A. Bol, A. Meijerink, *J. Phys. Chem. B* 2001, 105, 10203.
25. C. de Mello Donegá, S. G. Hickey, S. F. Wuister, D. Vanmaekelbergh, A. Meijerink, *J. Phys. Chem. B*, 2003, 107, 489-496.
26. C. de Mello Donegá, R. Koole, *J. Phys. Chem. C* 2009, 113, 16, 6511-6520
27. G. Kalyuzhny, R. W. Murray, *J. Phys. Chem. B* 2005, 109, 7012-7021.
28. S. F. Wuister, C. de Mello Donegá, A. Meijerink, *J. Phys. Chem. B*. 2004, 108, 17393-17397.
29. C. Bullen, P. Mulvaney, *Langmuir* 2006, 22, 3007.
30. A. M. Munro, I. J.-L. Plante, M. S. Ng, D. S. Ginger, *J. Phys. Chem. C* 2007, 111, 6220.
31. J. K. Cooper, A. M. Franco, S. Gul, C. Corrado, J. Z. Zhang, *Langmuir* 2011, 27, 8486-8493.
32. A. J. Morris-Cohen, V. Vasilenko, V. A. Amin, M. G. Reuter, E. A. Weiss, *ACS Nano* 2012, 6, 557-565.
33. P. W. Atkins, 'Physical Chemistry', Fifth edition, Oxford: Oxford University Press, 1995.
34. Y.-X. Kong, Y.-Y. Di, Y.-Q. Zhang, W.-W. Yang, Z.-C. Tan, *Thermochimica Acta* 2009, 495, 33-37.
35. M. Rutland, A. Walthermo, P. Claesson, *Langmuir* 1992, 8, 176-183.
36. 'CRC Handbook of Chemistry and Physics', 92nd edition 2011-2012, W. M. Haynes (Ed.), Boca Raton (USA): CRC Press, 2012







# Chapter 10

## **Samenvatting in het Nederlands**

—

*“Voetballen is heel simpel, maar het moeilijkste wat er is, is simpel voetballen.” - Johan Crujff*

## 10.1 – Introductie

In de afgelopen vier jaar heb ik mij beziggehouden met het maken van nanokristallen en het bestuderen van de eigenschappen ervan. Dit heeft geresulteerd in dit proefschrift over de synthese en opto-elektronische eigenschappen van colloïdale halfgeleider nanokristallen. Fysisch scheikundigen begrijpen de zin hiervoor, maar de meeste mensen komt alleen het woorddeel nano bekend voor. Nano is in de afgelopen 5 tot 10 jaar een algemeen bekend begrip geworden. Veel mensen hebben wel eens van nanotechnologie gehoord of anders kennen ze de iPod nano wel. In nanotechnologische toepassingen worden materialen (nanodeeltjes) gebruikt die door hun geringe afmetingen speciale eigenschappen hebben. Een nanometer is  $0,000000001$  ( $10^{-9}$ ) meter, wat onvoorstelbaar klein is omdat we dit niet met het blote oog kunnen waarnemen. Maar gelukkig is alles relatief. Om toch een gevoel te krijgen van hoe groot  $0,000000001$  meter is kun je daarom de verhouding nanometer tot een meter vergelijken met de grootte van een basketbal tot de grootte van de aardbol (Figuur 10.1).

Wat veel mensen niet weten is dat het gebruik van nanomaterialen niet eens zo nieuw is. In het Romeinse Rijk en in de middeleeuwen gebruikten vakmensen deze materialen al in hun producten. Zo wordt bijvoorbeeld de kleur van glas in lood bepaald door de grootte van bijvoorbeeld gouden of zilveren nanodeeltjes. Deze deeltjes worden in het glas gevormd tijdens het afkoelen van verhit glas met metaaloxide. Destijds hadden de vakmensen verschillende recepturen om verschillende kleuren glas te

---



**Figuur 10.1** – De verhouding van een basketbal tot de aardbol is gelijk aan de verhouding van een nanometer tot een meter.

maken, zonder dat men precies wist waarom het glas een bepaalde kleur kreeg. Tegenwoordig zijn we in staat zijn om nanodeeltjes bewust toe te passen. Dit wordt nanotechnologie genoemd en wordt bijvoorbeeld gebruikt in computerprocessoren of metalen constructies versterkt met koolstofnanobuisjes. De verwachting is dat nanotoepassingen een nog belangrijkere rol gaan innemen in onze toekomst. Hoewel het zangduo Saskia en Serge al in 1970 over 'de kleine dingen die het doen' zongen, waren wij Nederlanders niet de eersten die met nanodeeltjes aan de slag gingen. Het was de Amerikaanse natuurkunde professor Richard Feynmann die in zijn lezing 'There is plenty of room at the bottom' al in 1959 voorstelde om atomen als bouwstenen te gebruiken. Op deze manier zou je kleine structuren en materialen van enkele atomen groot kunnen maken die nieuwe interessante eigenschappen zouden bezitten.

Nanotechnologie is volgens velen belangrijk voor de toekomst. Maar wat is er nou zo speciaal aan materialen van enkele nanometers groot en hoe kunnen we ze gebruiken? De eigenschappen van materialen die we in ons dagelijks leven gebruiken lijken altijd hetzelfde te zijn. Zo verandert de kleur van papier niet wanneer je het in kleine stukjes knipt en smelt zowel de extra grote (XL) hagelslag als de normale hagelslag in je mond. Echter, wanneer de afmetingen van de materialen enkele nanometers groot worden, kunnen eigenschappen als de kleur of het smeltpunt van materialen wel degelijk veranderen. Zo wordt bijvoorbeeld de kleur van goud bepaald door de grootte van het kristal. Relatief grote gouden nanokristallen (150 nm) zijn blauw terwijl relatief kleine gouden nanokristallen (5 nm) rood zijn.

In deze samenvatting wil ik graag laten zien waarom nanokristallen zo interessant zijn. Het is namelijk niet voor niets dat vele onderzoekers deze materialen al tientallen jaren bestuderen. Dit proefschrift gaat over colloïdale halfgeleider nanokristallen. Dit zijn hele kleine halfgeleider kristallen waarvan de eigenschappen bepaald worden door de grootte. Zo kunnen ze bijvoorbeeld afhankelijk van hun grootte bepaalde soorten licht opnemen en ook weer uitzenden. Grotere halfgeleider cadmium-telluride nanokristallen zenden bijvoorbeeld rood licht uit terwijl kleinere nanokristallen van hetzelfde materiaal blauw licht uitzenden. De theorie achter deze nanokristallen laat zien waarom deze deeltjes zo bijzonder zijn, vandaar dat ik deze graag aan jullie wil uitleggen. Aan het einde van deze samenvatting ga ik wat dieper in op mijn onderzoek (10.8).

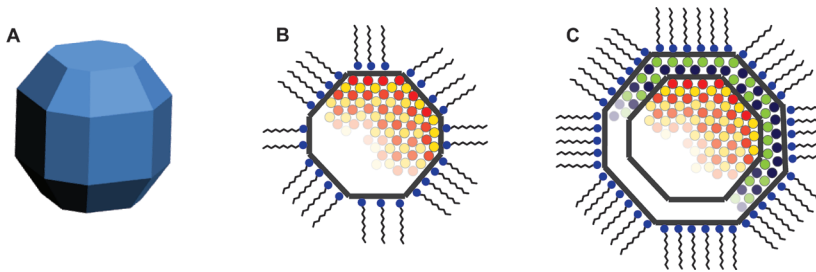
## 10.2 – Hoe ziet een halfgeleider nanokristal eruit?

Je beseft het misschien niet direct, maar iedere dag maken we tijdens het koken gebruik van kristallen. Zoutkorrels zijn namelijk kristallen die bestaan uit de atomen natrium (Na) en chloor (Cl). Een kristal bevat atomen die periodiek gerangschikt zijn en een herhalend patroon vormen. Dit herhalende patroon wordt een eenheidscel genoemd. In zout zitten natrium en chloride in een kubusvormige eenheidscel (figuur 10.2a). Deze vorm is de meest simpele en meest voorkomende eenheidscel. Deze eenheidscel is belangrijk omdat deze bepalend is voor de vorm van een kristal. Zo hebben hele grote, langzaam gegroeide/gekristalliseerde, zoutkristallen (bestaande uit triljarden,  $10^{21}$ ) atomen, net als de eenheidscel, de vorm van een kubus (figuur 10.2b). De vlakken die te vinden zijn op de zijanten van een kristal worden kristalvlakken genoemd. Een kubusvormig kristal heeft daarom in totaal, net als een dobbelsteen, 6 kristalvlakken. Nanokristallen bestaan niet uit triljarden atomen maar uit 50 tot 10000 atomen en zijn hierdoor vele malen kleiner dan een groot kristal. Nanokristallen zijn enkele tot tientallen nanometers groot en hebben net als hun grote broertjes verschillende kristalvlakken (figuur 10.3a).

De nanokristallen die beschreven worden in dit proefschrift zijn zogeheten colloïdale halfgeleider nanokristallen bestaande uit de atomen cadmium (Cd) of zink (Zn) in combinatie met de atomen tellurium (Te) of selenium (Se). Deze halfgeleider nanokristallen (CdTe, CdSe, ZnTe, en ZnSe) zijn colloïdale kristallen. Dit betekent dat ze stabiel zijn in een oplosmiddel als bijvoorbeeld water of olie, waardoor de nanokristallen in staat zijn om daarin individueel rond te zweven. De kristallen zakken niet naar de bodem, zoals zandkorrels in water. Ook drijven ze niet in klonten naar het oppervlak, zoals peperkorrels in water. De colloïdale nanokristallen zijn stabiel in oplossing doordat er moleculen aan het oppervlak zitten die speciale eigenschappen hebben (figuur 10.3b). Deze moleculen worden liganden genoemd en zien er uit als kikkervisjes. De staart van de liganden lost goed op in het oplosmiddel en de kop hecht aan het oppervlak van het nanokristal. Wanneer een nanokristal bedekt is met deze liganden wordt het kristal door de staarten van de liganden oplosbaar in een oplosmiddel. Een gedeelte van dit proefschrift gaat over heteronanokristallen. Een heteronanokristal is een kristal dat bestaat uit twee verschillende halfgeleidermaterialen. Dit nanokristal kun je vergelijken met een chocoladepinda (figuur 10.3c) en wordt ook wel een kern/schil-heteronanokristal genoemd. De kern van dit heteronanokristal is gemaakt van een bepaald halfgeleidermateriaal terwijl de schil uit een ander halfgeleidermateriaal bestaat. Later zal nog



**Figuur 10.2** – (a) met behulp van knikkers kun je een kubusvormig kristal bestaande uit 2 verschillende atomen (zoals NaCl) gemakkelijk nabouwen (wit = atoom nr. 1, gekleurd grijs = atoom nr. 2). (b) Wanneer een zoutkristal heel langzaam groeit (bijvoorbeeld in een zoutmijn) kunnen hele grote kubusvormige NaCl kristallen ontstaan.



**Figuur 10.3** – (a) een uitvergroete driedimensionale weergave van een nanokristal. (b) een colloïdale nanokristal is bedekt met moleculen (liganden) die ervoor zorgen dat het nanokristal oplosbaar is in een oplosmiddel. (c) een voorbeeld van een heteronanokristal waarin de kern van het kristal uit een ander materiaal bestaat dan de schil van het kristal.

worden uitgelegd waarom twee materialen in een nanokristal verschillende eigenschappen kunnen hebben.

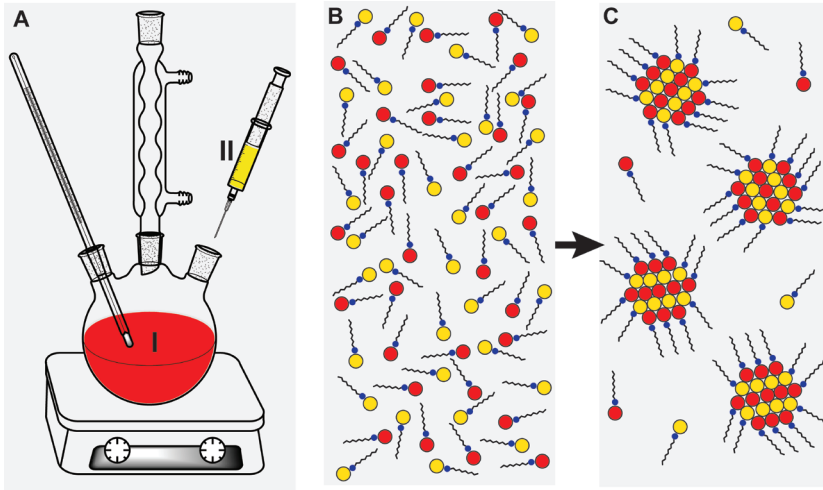
### 10.3 – Hoe maak je een halfgeleider nanokristal?

Zoals eerder gezegd bestaan de in dit proefschrift beschreven halfgeleider nanokristallen uit 2 verschillende atomen (CdTe, CdSe, ZnTe, en ZnSe). Om ervoor te zorgen dat deze atomen samen kristallen vormen (kristalliseren) die bedekt zijn met liganden worden deze nanokristallen in een oplosmiddel gemaakt. Het maken van moleculen en materialen wordt synthese genoemd. Het synthetiseren van nanokristallen heeft veel weg van koken (figuur 10.4a). Je warmt een oplossing die één soort atomen (het eerste ingrediënt, figuur 10.4a - I) en liganden bevat op tot een bepaalde temperatuur. Deze temperatuur hangt af van meerdere zaken: bijvoorbeeld het type atomen dat je gebruikt, de gewenste nanokristal-vorm en de gewenste hoeveelheid nanokristallen. Vervolgens voeg je een oplossing van een ander soort atomen toe (het volgende ingrediënt, figuur 10.4a - II). De oplossing bevat na de toevoeging van de tweede soort atomen heel veel atomen (figuur 10.4b). Net als met een oplossing van suiker in water komt er een moment dat er niet meer atomen kunnen worden opgelost. De oplossing is dan verzadigd. Wanneer er meer atomen aan de oplossing worden toegevoegd dan er eigenlijk kunnen worden opgelost, kan een reactiemengsel worden verkregen dat oververzadigd is. De atomen in een oververzadigde oplossing vormen liever kristallen met elkaar dan dat ze los in oplossing zitten. Dit is namelijk gunstiger om te doen, doordat het systeem hierdoor zo laag mogelijk in energie komt te zitten (energetisch gunstiger). Het proces van de vorming van kristallen noemen we nucleatie. Na de nucleatie kunnen de kristallen groter worden doordat er één voor één atomen aan het kristal worden toegevoegd. De groei van de nanokristallen kan worden gestopt door de temperatuur te verlagen en kan net als bij koken gedaan worden door de kookplaat uit te zetten.

### 10.4 – Wat zijn de bijzondere eigenschappen van halfgeleider nanokristallen?

Om te begrijpen wat halfgeleider nanokristallen zo bijzonder maakt, zullen we meer in de natuurkundige theorie moeten duiken. Het is namelijk belangrijk om te snappen hoe de elektronische structuur van deze deeltjes in elkaar zit, iets wat voor veel mensen waarschijnlijk nog onbekend terrein is. In de onderstaande paragrafen zal stap voor stap worden uitgelegd wat een elektronische structuur is en hoe deze er in nanokristallen uitziet. Allereerst zal aan de hand van het atoom het begrip elektronische structuur





**Figuur 10.4** – (a) Nanokristallen worden gemaakt door een oplossing met één bepaald soort atomen en liganden in een bolvormig glas (rondbodemkolf) te verwarmen door middel van een verwarmingsplaatje. Bij een bepaalde temperatuur wordt een oplossing met de 2e soort atomen toegevoegd waardoor de kristallen worden gevormd. (b) de verschillende atomen in de oververzadigde oplossing zullen kristalliseren en vele nanokristallen vormen waarvan enkele zijn weergegeven in (c).

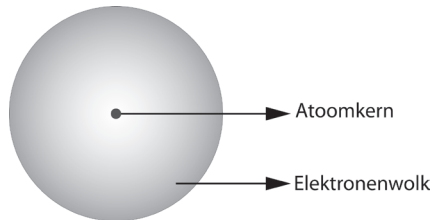
worden uitgelegd. Vervolgens zal worden gekeken naar de elektronische structuur van een molecuul, een kristal en een halfgeleider kristal. Wanneer we de elektronische structuur van een halfgeleider kristal snappen kunnen we kijken wat er met de eigenschappen gebeurt als we het halfgeleider kristal enkele nanometers groot maken.

#### 10.4.1 – Elektronische structuur van een atoom

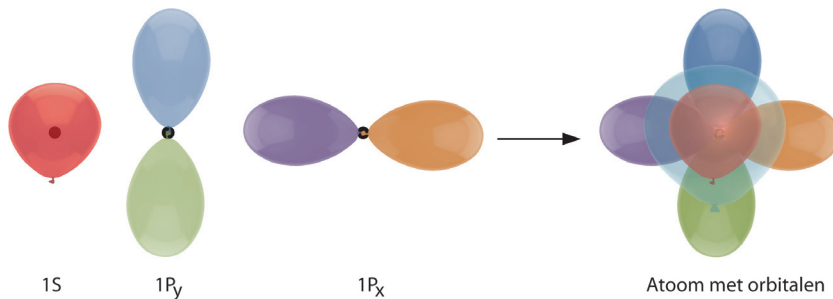
Atomen vormen de bouwstenen van onze wereld. Ze zijn opgebouwd uit zogenoemde elementaire deeltjes, waaronder protonen, neutronen en elektronen. We kennen in totaal 117 verschillende soorten atomen (ook wel elementen genoemd) die van elkaar verschillen door de hoeveelheid elementaire deeltjes. Protonen en neutronen vormen de hele kleine (positief geladen) kern van het atoom terwijl de elektronen (negatief geladen) zich rondom de atoomkern in een zogenoemde elektronenwolk bevinden (Figuur 10.5). Hoe meer elektronen het atoom bevat hoe groter deze elektronenwolk is en des te groter het atoom. Deze elektronenwolk

wordt gevormd doordat de elektronen zich in bepaalde banen om de kern bewegen. Deze elektronenbanen worden orbitalen genoemd en je kunt ze het beste vergelijken met ballonnen (Figuur 10.6). Er zijn verschillende orbitalen die ieder 2 elektronen kunnen bevatten en ieder een verschillende naam hebben ( $1s$ ,  $2s$ ,  $2p_x$ ,  $2p_y$ ,  $2p_z$ ,  $3s$  etc.). Kort samengevat bevat een atoom verschillende met elektronen gevulde banen die samen de elektronenwolk vormen.

De elektronen in de verschillende orbitalen hebben verschillende energieën. Deze energie is de energie die het kost om een elektron te verwijderen uit het atoom. Omdat over een zogenaemde ‘verwijderingsenergie’ wordt gesproken wordt deze energie aangegeven als negatieve energie. Hoe



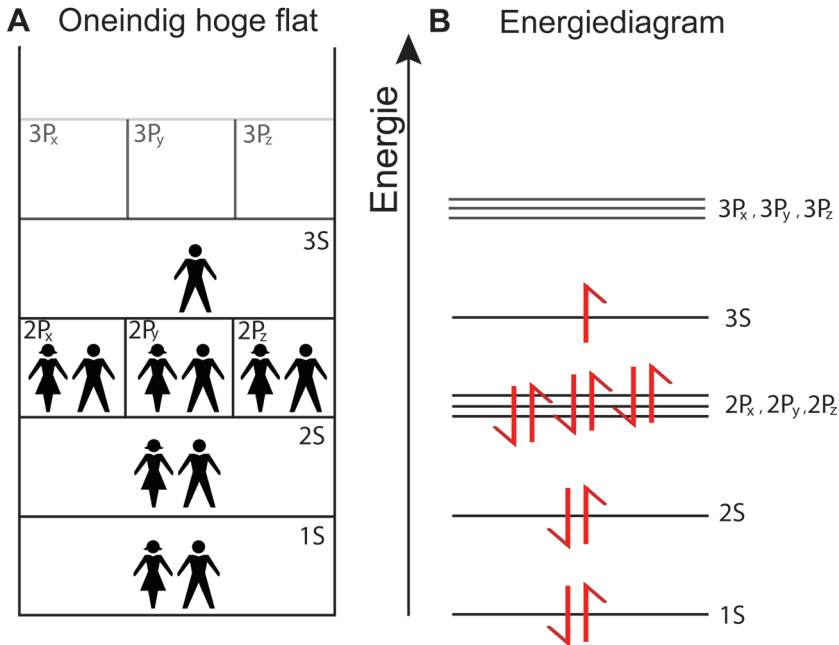
**Figuur 10.5** – Het atoom; bestaat uit een atoomkern met daaromheen een wolk van elektronen. De atoomkern bestaat onder andere uit protonen en neutronen.



**Figuur 10.6** – De elektronen in de elektronenwolk bevinden zich in een bepaalde baan (orbitaal) rondom de atoomkern (zwarte stip). De vorm van deze banen zijn te vergelijken met verschillend gevormde ballonnen (links van de pijl). In een atoom met meerdere elektronen, bevinden de elektronen zich in verschillende orbitalen rondom de atoomkern die samen de elektronenwolk vormen (rechts van de pijl).

dichter bij de kern hoe meer energie het kost om een elektron te verwijderen en des te negatiever is de corresponderende energie van het elektron. In atomen met meerdere elektronen zullen de elektronen zich niet willekeurig gaan verspreiden over de verschillende elektronenbanen (orbitalen). Een atoom zal altijd zo opgebouwd zijn dat het zo laag mogelijk in energie zal zitten, elektronen zullen dus in opeenvolgende orbitalen zo dicht mogelijk rondom de kern gaan zitten. Zo zullen bijvoorbeeld de elektronen van een atoom met 2 elektronen zich in de 1s orbitaal bevinden.

Het atoom kun je eigenlijk vergelijken met een oneindig hoge flat van tweepersoons appartementen (de orbitalen) die van onder naar boven (van de atoomkern naar de buitenkant van de elektronenwolk) wordt



**Figuur 10.7** – Een energiediagram van een atoom beschrijft hoe de elektronen verdeeld zijn over de verschillende orbitalen/energieniveaus in het atoom. De elektronen worden in het energiediagram weergegeven als een halve pijl. Je kunt dit energiediagram van een atoom het beste vergelijken met een oneindig hoge flat waarin tweepersoonsappartementen zitten. Hoe hoger het appartement (orbitaal) hoe hoger in energie het is. Er zijn bewoonde appartementen (bewoners zijn elektronen) en onbewoonde appartementen.

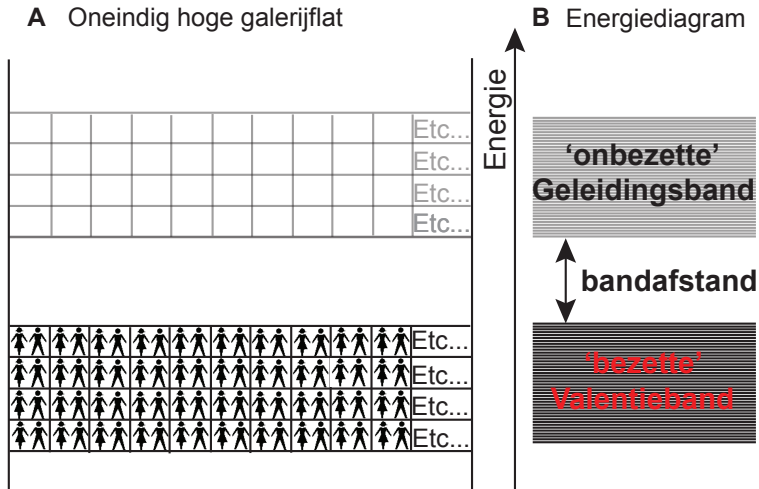
gevuld met bewoners (elektronen). De bezetting van de orbitalen kunnen worden weergegeven in een zogenoemd energiediagram (figuur 10.7) waarin de energieniveaus en de elektronen zijn weergegeven. Ieder element (waterstof, zuurstof, koolstof etc.) bevat een specifiek aantal elektronen en heeft daarom een specifiek energiediagram. De verdeling van de elektronen over de orbitalen (weergegeven in een energiediagram) wordt de elektronenstructuur van een atoom genoemd. Belangrijk om te onthouden is dat deze energieniveaus gevuld (kunnen) zijn met elektronen (bezette orbitalen/bezette appartementen). Energieniveaus zonder elektronen (onbezette orbitalen/onbewoonde appartementen) zijn ook aanwezig en elektronen kunnen altijd verplaatst worden van bezette orbitalen naar onbezette orbitalen. Het verplaatsen van elektronen kost (net als het verhuizen van iemand naar een hoger gelegen appartement) echter wel energie.

#### 10.4.2 – Elektronische structuur van een molecuul

Een molecuul bestaat uit meerdere atomen die met elkaar verbonden zijn. Atomen kunnen zich met elkaar verbinden door elektronen te delen. De elektronen zijn dan niet alleen meer van het atoom maar ze zijn onderdeel van het molecuul geworden. De elektronenbanen waarin ze zich bevinden worden dan niet beschreven door atomaire orbitalen maar door zogenoemde moleculaire orbitalen. Omdat de elektronen in een molecuul gedeeld worden bevat een molecuul met 2 atomen net zo veel energieniveaus als de 2 afzonderlijke atomen samen. De energieniveaus van het molecuul worden bezet door de elektronen van de atomen waaruit het molecuul bestaat. Een molecuul is als mensen die getrouwd zijn in gemeenschap van goederen: ze delen de elektronen samen.

#### 10.4.3 – Elektronische structuur van een kristal

In een kristal vormen de atomen, net als in moleculen, verbindingen door het delen van elektronen. De energieën van de elektronen in het kristal kunnen net als voor atomen en moleculen door een energiediagram worden beschreven (figuur 10.8). Omdat een kristal niet uit een paar, maar uit triljarden atomen bestaat, bevat het energiediagram van een kristal ontzettend veel energieniveaus die gevuld worden door ontzettend veel elektronen. In een kristal zitten veel atomen die energieniveaus bevatten van bijna dezelfde energie. De vele energieniveaus van bijna gelijke energie vormen energiebanden. De verschillende energiebanden bevinden zich op bepaalde afstanden van elkaar.



**Figuur 10.8** – Energiediagram van een kristal. De vele energieniveaus die ongeveer dezelfde energie hebben vormen een zogenaamde energieband. De energiebanden zijn van elkaar gescheiden door een zogenoemde verboden zone (bandafstand). In een halfgeleider kristal is de hoogst bezette energieband (valentieband) compleet gevuld met elektronen (alle niveaus zijn bezet) terwijl de opeenvolgende energieband (geleidingsband) volledig leeg is.

Je kunt het energiediagram van een halfgeleider vergelijken met een oneindig brede galerijflat waarbij een appartementenlaag volledig is gevuld. De opeenvolgende appartementenlaag erboven is leeg en bovendien verwijderd van de bovenste bezette appartementenlaag door een verboden ruimte ofwel de bandafstand.

Wanneer een energieband gedeeltelijk gevuld is kunnen de elektronen zich bewegen van en naar de verschillende energieniveaus binnen deze energiebanden. Het bewegen van elektronen is wat we de geleiding van stroom noemen. Deze stroomgeleiding kan gemakkelijk plaatsvinden in kristallen die we aanduiden als een metaal. Echter wanneer de energieband volledig gevuld is met elektronen kunnen de elektronen zich niet verplaatsen en kan het kristal niet gemakkelijk of geen stroom geleiden (halfgeleider of isolator). Een energiediagram van een kristal kun je het beste vergelijken met een ontzettend brede en oneindig hoge galerijflat bestaande uit appartementenlagen (energiebanden) op verschillende hoogtes. De appartementen binnen een laag zitten dicht op elkaar gepakt en bevinden zich ongeveer op dezelfde hoogte in de flat. Wanneer een

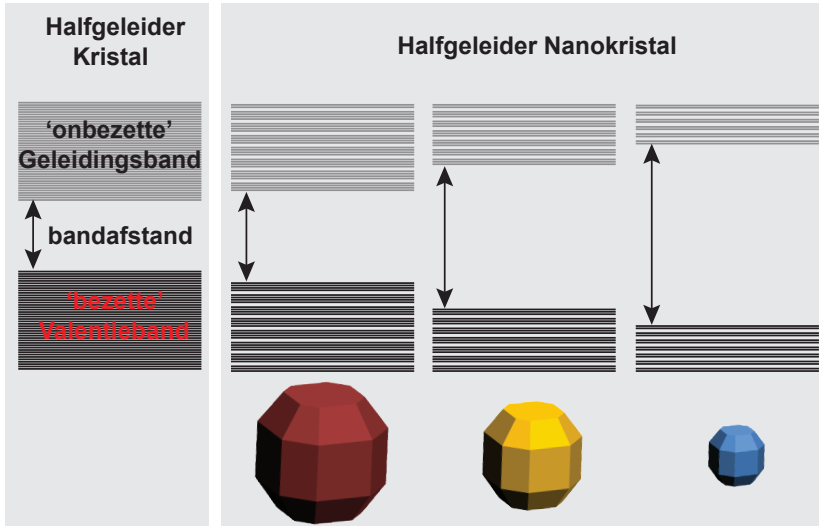
appartementenlaag niet volledig bewoond is (zoals bijvoorbeeld bij een metaal), kunnen de bewoners (elektronen) zich gemakkelijk naar de lege appartementen verplaatsen (geleiding van stroom). Wanneer de appartementenlaag wel volledig gevuld is (bij een isolator of halfgeleider) kan niemand van de bewoners zich verplaatsen. Er is dan dus geen geleiding van stroom. Het belangrijkste om te onthouden is dat de elektronische structuur van een kristal verschillende energiebanden bevat die op hun beurt weer uit veel energieniveaus bestaan en veel elektronen bevatten.

#### **10.4.4 – Elektronische structuur van een halfgeleider kristal**

Een halfgeleider kristal is een kristal dat een energieband bevat die compleet gevuld is met elektronen en waarbij de volgende lege energieband dusdanig ver weg in energie is dat elektronen alleen door energie van buitenaf (bijvoorbeeld warmte of licht) naar de lege energieband kunnen worden gebracht. De met elektronen bezette energieband wordt de valentieband genoemd en de onbezette energieband wordt de geleidingsband genoemd. Het verschil tussen de valentie en geleidingsband wordt de bandafstand van het betreffende materiaal genoemd. Het energiediagram van een halfgeleider kristal ziet eruit als weergegeven in figuur 10.8. Er bestaan verschillende soorten halfgeleiders die ieder een bandafstand van een bepaalde energie hebben. Zo is de bandafstand van bijvoorbeeld de halfgeleider cadmium-telluride (CdTe) groter dan die van de halfgeleider loodselenide (PbSe).

#### **10.4.5 – Elektronische structuur van een halfgeleider nanokristal**

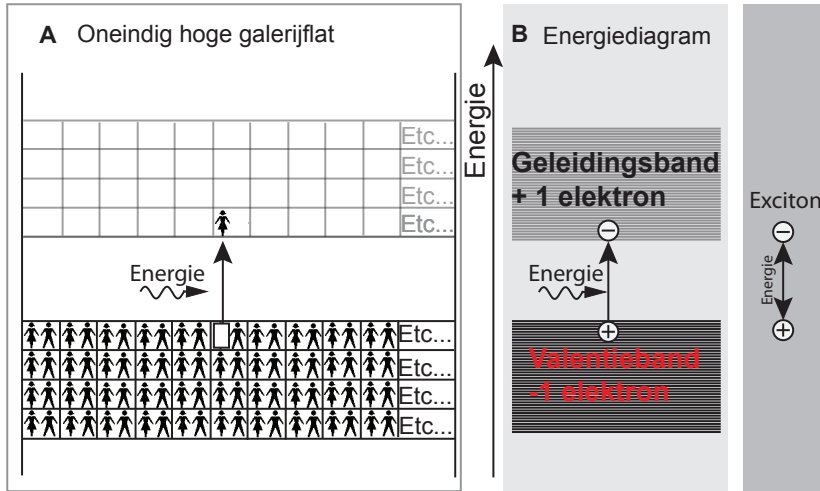
Een nanokristal bestaat, zoals eerder gezegd, uit 50-10000 atomen. Hoe minder atomen een nanokristal bevat, hoe minder elektronen het ook bevat. Er bestaan in nanokristallen daarom minder energieniveaus ten opzichte van een groot kristal. De lagere hoeveelheid energieniveaus in nanokristallen is vooral duidelijk te zien aan de randen van de energieband. Hoe kleiner de halfgeleider nanokristallen hoe minder energieniveaus aan de rand van de energieband te zien zijn en des te groter de bandafstand zal zijn. Als de afmetingen van een halfgeleider nanokristal beneden een bepaalde grootte komen, hangt de grootte van het energiegat af van de grootte van het kristal (figuur 10.9).



*Figuur 10.9 – De energiediagrammen van halfgeleider nanokristallen van verschillende grootte. Beneden een bepaalde kristalgrootte verandert de bandafstand van het materiaal als functie van de grootte van het kristal. Hoe kleiner de nanokristal hoe groter de bandafstand.*

### 10.5 – De elektronische structuur van nanokristallen in actie!

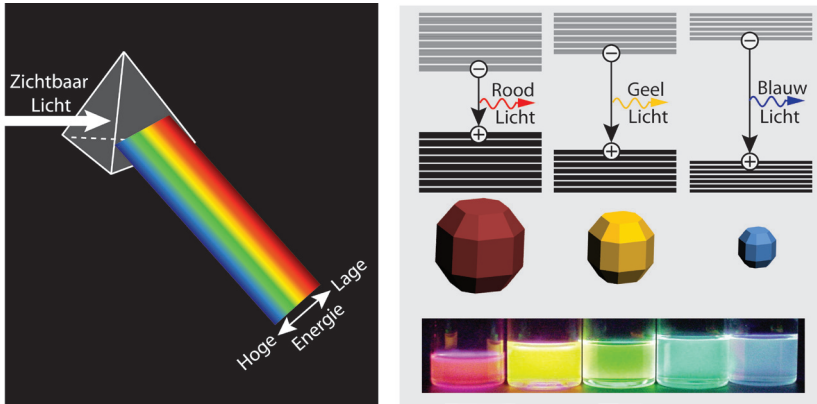
Hierboven is een algemene omschrijving van een colloïdaal halfgeleider nanokristal gegeven. We hebben nu antwoord op de vragen: hoe zien ze eruit en hoe is hun energiediagram opgebouwd. Het bijzondere aan deze nanokristallen is dat de bandafstand afhankelijk is van de grootte van het kristal. Een energiediagram kun je niet direct waarnemen. De grootte van de bandafstand vaststellen, kan dus alleen op een indirecte manier. Zoals eerder gezegd bestaat de halfgeleider uit een compleet gevulde energieband (valentieband) en een compleet onbezette energieband (geleidingsband). De bandafstand tussen deze beide banden is zo groot dat een elektron alleen van de valentieband naar de geleidingsband kan worden gebracht wanneer er energie in het kristal wordt gestopt. Dit wordt de absorptie van energie genoemd. Afhankelijk van de bandafstand van het halfgeleiderkristal is er een bepaalde minimale energie nodig om deze verplaatsing voor elkaar te krijgen. Doordat een elektron naar de geleidingsband gaat, ontstaat er een gat in de valentieband (figuur 10.10a). Een elektron is een negatief geladen deeltje, het gat is derhalve een positief geladen deeltje. Het elektron en zijn positief geladen tegenhanger worden samen het 'exciton' genoemd. Het



**Figuur 10.10** – Schematische weergave van de vorming van een exciton in een halfgeleider kristal. Doordat de verschillende banden op afstand van elkaar staan, kunnen elektronen enkel van de bezette energieband naar de onbezette energieband worden gebracht door energie aan het kristal toe te voegen. Wanneer een elektron van de valentieband naar de geleidingsband gaat, krijg je een situatie waarin de geleidingsband 1 elektron bevat, terwijl de valentieband 1 elektron mist. Daar ontstaat dus een gat. Dit gat is eigenlijk het tegenovergestelde van het elektron, wat een negatief geladen deeltje is. Daardoor wordt het gat beschreven als een positief geladen deeltje. Samen vormen de door energie gescheiden elektron en het 'gat' een paar dat het exciton wordt genoemd.

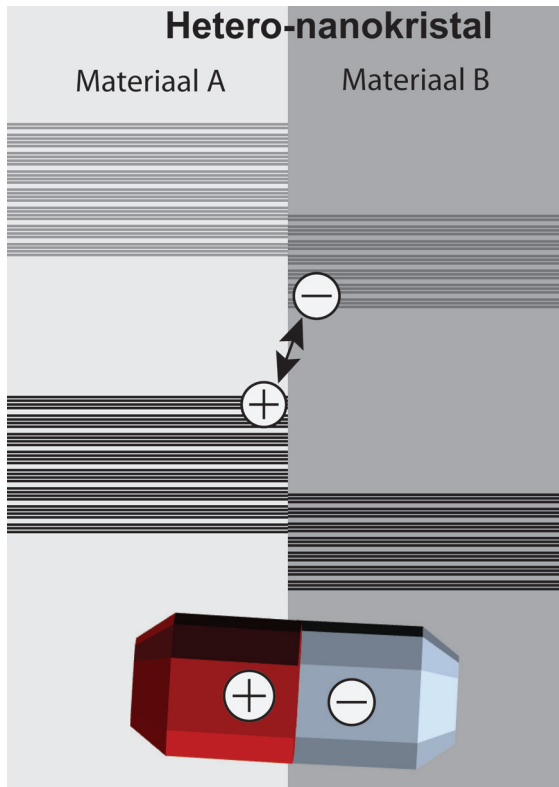
kristal wil uiteindelijk (net als beschreven voor de elektronen in individuele atomen in 10.4) naar een toestand die zo laag mogelijk is in energie. Dit betekent dat het elektron na een bepaalde tijd weer naar de valentieband terug zal gaan. Deze terugverplaatsing van het elektron wordt het verval van het exciton genoemd. Een halfgeleider kristal kan daarom energie opnemen en deze vervolgens weer afstaan aan zijn omgeving. Deze energie kan in de vorm van hitte of licht zijn. Wanneer er licht wordt uitgezonden wordt dit luminescentie genoemd. Het materiaal heet halfgeleider omdat het soms wel en soms geen stroom kan geleiden. In normale toestand kan de halfgeleider geen stroom geleiden, doordat de energieband volledig is gevuld. Als er echter een elektron naar een lege energieband wordt gebracht, kan deze zich vrij bewegen en is deze in staat om wel stroom te geleiden.





**Figuur 10.11** – (links) Zichtbaar wit licht bestaat uit verschillende kleuren licht. Deze kleuren licht verschillen van elkaar doordat ze een verschillende energie hebben. (rechts) Nanokristallen van hetzelfde materiaal maar van verschillende grootte hebben een verschillende bandafstand. Het verval van het elektron van de geleidingsband naar de valentieband kan met het blote oog worden waargenomen door de verschillende kleuren licht die de nanokristallen uitzenden. In de foto zie je dat grotere CdTe-nanokristallen (5 nm) rood licht uitzenden, terwijl kleinere CdTe-nanokristallen (1.5 nm) blauw licht uitzenden.

Licht bestaat uit energiestralen die zich met een geweldig hoge snelheid verplaatsen. Wij kunnen met onze ogen zichtbaar licht waarnemen. Zo zien wij onze wereld in verschillende kleuren; blauwe hemellucht, groen gras, gele bananen, rode tomatensaus. Al deze verschillende kleuren zijn energiestralen die een verschillende energie hebben (figuur 10.11a). Zo is blauw licht hoger in energie dan rood licht. Wanneer de bandafstand van een halfgeleider nanokristallen (bijvoorbeeld voor CdTe, CdSe, ZnSe, ZnTe) vergelijkbaar is met de energie van zichtbaar licht, kun je met je eigen ogen het verval van het elektron van de geleidingsband naar de valentieband zien. Het elektron geeft dan zijn energie aan de omgeving af door het uitzenden van licht van een bepaalde kleur. Zo zenden kleine CdTe-nanokristallen een grotere bandafstand en daarom licht van hogere energie uit (bijvoorbeeld blauw) dan grotere CdTe-nanokristallen (figuur 10.11b) die op hun beurt licht van een lagere energie uitzenden (bijvoorbeeld rood licht). We kunnen aan de hand van de grootte (en vorm) de (licht)eigenschappen van het nanokristal bepalen. Omdat we tijdens de synthese controle over de vorm en grootte hebben, hebben we ook controle over de uiteindelijke eigenschappen van het nanokristal.



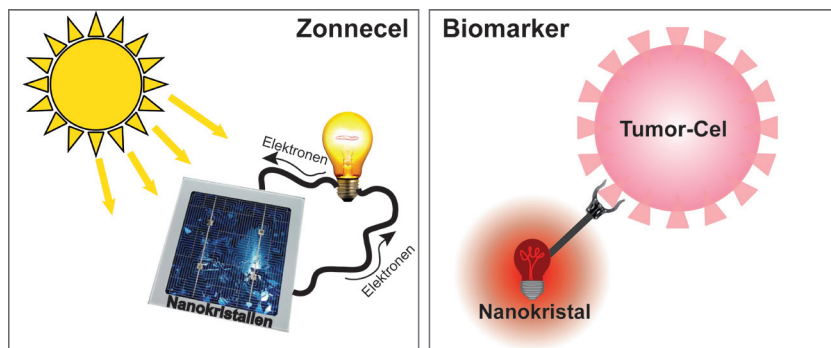
**Figuur 10.12** – Energiediagram van een heteronanokristal dat uit 2 verschillende materialen bestaat (materiaal A en materiaal B). Doordat beide materialen aan elkaar gekoppeld zijn kunnen elektronen worden uitgewisseld. De geleidingsband van materiaal B is lager in energie dan dat van materiaal A en het elektron van het gevormde exciton zal daarom naar materiaal B gaan terwijl het gat naar materiaal A zal gaan. Hierdoor wordt een zogenoemd ruimtelijk gescheiden exciton gevormd.

Een gedeelte van dit proefschrift gaat over halfgeleider heteronanokristallen. Zoals hierboven uitgelegd is zo'n heteronanokristal een nanokristal dat bestaat uit twee verschillende halfgeleidermaterialen. De halfgeleidermaterialen omvatten ieder een ander gedeelte van het heteronanokristal (bijvoorbeeld kern of schil). Ieder gedeelte heeft een eigen bandafstand, die afhangt van de afmetingen en de vorm van het gedeelte. Doordat deze twee gedeeltes met elkaar in contact staan, zijn hun energiediagrammen wel met elkaar verbonden (figuur 10.12). Als een heteronanokristal energie opneemt, wordt net als in gewone nanokristallen

een exciton gevormd. Het exciton zal zo laag mogelijk in energie gaan zitten. Het elektron zal daarom naar het materiaal gaan waarbij de geleidingsband het laagst is. Doordat alle overgebleven elektronen in de valentieband ook zo laag mogelijk in energie gaan zitten, zal het gat zo hoog mogelijk in de valentieband gaan zitten. Het gat zal daarom naar het materiaal gaan waarvan de valentieband de hoogste energie voor elektronen heeft. In figuur 10.12 is een voorbeeld gegeven van een bepaald type heteronanokristal (een zogenoemde type-II heteronanokristal). In dit type heteronanokristal gaan door de verschillen in de positie van de energiebanden het elektron en het gat in een verschillend materiaal zitten. Hierdoor vormen ze een zogenoemd ruimtelijk gescheiden exciton. Bij een ruimtelijk gescheiden exciton duurt het langer voor het elektron teruggaat naar de valentieband dan bij een exciton dat zich in hetzelfde materiaal bevindt. Het elektron vult namelijk bij het teruggaan naar de valentieband altijd de plek van het gat op. Wanneer zowel het gat als het elektron in verschillende materialen zit, duurt het langer voordat het elektron het gat in de valentieband gevonden heeft. Verder zie je ook dat in dit type heteronanokristal het energieverschil tussen het elektron en gat veel kleiner kan worden dan in de afzonderlijke materialen (figuur 10.12). Een heteronanokristal is in staat om licht van een lagere energie uit te zenden dan mogelijk in de verschillende materialen waaruit het heteronanokristal bestaat. Deze twee eigenschappen (langere levensduur exciton, lagere energie van luminescentie) zijn gunstig voor de toepassingen van nanokristallen die in de volgende paragraaf worden beschreven.

### 10.6 – Toepassingen; waar kun je nanokristallen voor gebruiken

Maar waar kunnen we bovenstaande kennis nu voor gebruiken? Het is een vraag die ik in de afgelopen vier jaar vaak te horen kreeg als ik over mijn onderzoek vertelde. Halfgeleider nanokristallen kunnen mogelijk in de toekomst voor verschillende doeleinden gebruikt worden, bijvoorbeeld in zonnecellen, biomarkers, LEDs en lasers. In een zonnecel wordt zonlicht opgenomen die wordt omgezet in een elektrische stroom. Hierbij worden dus elektronen verplaatst. Een nanokristal kan licht opnemen van verschillende soorten energie, waarna zich een exciton vormt. Het elektron in de geleidingsband kan terugkeren naar de valentieband door het uitzenden van licht. Wanneer je in staat bent om dit elektron niet te laten vervallen door het uitzenden van licht maar door het via een elektrisch circuit te laten lopen (elektrische stroom) komt de energie van het exciton vrij in het elektrisch circuit als elektrische stroom. Het nanokristal werkt dan als een zonnecel. Doordat je de bandafstand van een nanokristal kunt



**Figuur 10.13** – Nanokristallen kunnen mogelijk gebruikt worden in zonnecellen en als biomarkers (bio-indicatoren).

variëren kun je een zonnecel aanpassen op de verschillende kleuren licht die de zon uitzendt (zonnenspectrum). Op deze manier zou de zonnecel het licht van de zon efficiënter kunnen omzetten in stroom. Een andere toepassing van nanokristallen is te vinden in de biomedische hoek. Het nanokristal kan worden gebruikt als een zogenoemde biomarker (bio-indicator). Een bio-indicator is een stof die biologische processen in het lichaam zichtbaar kan maken. Je kunt op een halfgeleider nanokristal moleculen vastzetten die specifiek binden aan tumorcellen. Omdat het nanokristal licht van een bepaalde kleur kan uitzenden kun je deze als een soort indicatorlamp gebruiken. De positie van deze lamp kan dan aangeven of en waar de tumorcellen zich begeven.

### 10.7 – Wat doet een Phd onderzoeker precies?

De afgelopen 4 jaar heb ik me in het lab intensief beziggehouden met het maken en meten van de hierboven beschreven halfgeleider nanokristallen. Deze maakte ik in een zogenoemde handschoenenkast, een doos met aan één kant een glazen doorkijkscherm waar lange handschoenen in bevestigd zijn. Deze kast is gevuld met stikstofgas en bevat hierdoor geen water en zuurstof, welke schadelijk kunnen zijn voor je nanokristallen. Door de handschoenen kon ik experimenten in de doos uitvoeren zonder dat de spullen aan de buitenlucht worden blootgesteld. Als er nanokristallen waren gevormd, moest ik deze nog wassen en in een schoon oplosmiddel brengen voor ik de eigenschappen kon gaan bestuderen. Ik gebruikte bijvoorbeeld een elektronenmicroscop om de vorm en grootte van de kristallen te bepalen. In onze groep (gecondenseerde materie en oppervlakken) zijn we gespecialiseerd in het bestuderen van de optische eigenschappen,

de eigenschappen die met licht te maken hebben. Zo onderzoeken we bijvoorbeeld welk soort licht (energie) de nanokristallen kunnen absorberen. Dit doen we door nanokristallen in een potje met een oplossing te doen en deze met licht te bestralen. De nanokristallen nemen deze energie in de vorm van licht op en vormen dan een exciton. Ook kan worden gekeken naar het licht wat de nanokristallen uitzenden wanneer het elektron van het gevormde exciton vervalst. Het verval kunnen we dan met eigen ogen zien doordat de oplossing licht van een bepaalde kleur uitzendt. Aan de hand van de eigenschappen van dit uitgezonden licht zijn we meer te weten gekomen over de elektronische structuur van de nanokristallen. Hierbij letten we bijvoorbeeld op de energie van het licht (kleur) en de tijd die het elektron er gemiddeld over doet om te vervallen, dus hoelang de nanokristallen nog licht uitzenden wanneer we stoppen met belichten. Ook kijken we naar wat er gebeurt wanneer we licht van verschillende energieën (andere kleuren licht) op de nanokristallen afsturen. Het onderzoeken van nanokristallen is een veelzijdig klusje omdat je zowel je chemische als je natuurkundige kennis moet gebruiken.

### **10.8 – Samenvatting van dit proefschrift**

Hieronder volgt er een beschrijving van hoofdstukken van dit proefschrift. Vanaf nu zullen we meer de diepte ingaan. In hoofdstuk 1 wordt een inleiding gegeven en in hoofdstuk 2 en 3 wordt de benodigde theorie van (hetero) nanokristallen besproken, die we hiervoor ook deels besproken hebben.

Hoofdstuk 4 gaat over zogenoemde magische clusters van zink-telluride (ZnTe). Magische clusters zijn hele kleine nanokristallen (10-100 atomen) en enkel clusters van een bepaalde grootte (ook wel configuratie genoemd) zijn stabiel. Dit betekent dat nanokristallen die net iets groter of net iets kleiner zijn dan de magische cluster minder stabiel zijn en daarom niet worden gevormd. De magische clusters groeien anders dan de 'normale' nanokristallen. Ze groeien namelijk niet atoom voor atoom, maar ze groeien van de ene magische cluster grootte direct naar de volgende magische cluster grootte. Deze magische clusters worden onder bepaalde synthese-omstandigheden gemaakt. Vorming van magische ZnTe-clusters was mogelijk voor bepaalde liganden (alkylamines), bepaalde Zn en Te-concentratie en vanaf een bepaalde synthesesettemperatuur die bovendien weer afhangt van de concentratie. Hoe hoger de concentratie van Zn en Te hoe sneller de groei van de magische clusters. Ook was bij een hogere precursorconcentratie (uitgangsstofconcentratie: Zn en Te-concentratie respectievelijk) een lagere temperatuur nodig om magische clusters te

vormen. Een hogere synthesesettemperatuur leidde tot snellere groei van de clusters en boven een bepaalde temperatuur werd er geen magische cluster groei meer waargenomen. De nanokristallen werden boven die temperatuur continu groter door de aangroei van atoom per atoom. De liganden spelen een belangrijke rol in de stabiliteit en groei van magische clusters. Voor de synthese van nanokristallen kunnen verschillende soorten liganden gebruikt worden die ieder op een andere manier binden. De ene ligande bindt sterker aan de Zn en/of Te-atoom dan de andere ligande. Het was duidelijk dat het gebruik van zogenoemde alkylamine-liganden cruciaal is voor het vormen van de magische ZnTe-clusters.

De magische clusters zijn ook een belangrijk onderdeel van hoofdstuk 5. In dit hoofdstuk wordt beschreven hoe vanuit deze magische ZnTe-clusters heteronanokristallen worden gemaakt. De magische clusters worden gebruikt als groeikiemen waarop een nieuw materiaal kan worden gegroeid door het toevoegen van nieuwe precursors. Door het toevoegen van Cd en Se-precursors aan de magische ZnTe-clusters werden heteronanodraden gevormd. Deze draden zijn 2 nm in diameter en zijn verschillend in lengte (25-100 nm). De draden worden op een bijzondere manier gevormd, namelijk via een zogenoemde kationuitwisseling gevolgd door georiënteerde aanhechting van de nanokristallen. Als de Cd-precursor aan het synthesesmengsel met magische ZnTe-clusters wordt toegevoegd, wordt een groot gedeelte (90 %) van de Zn-atomen uitgewisseld voor Cd-atomen. Dit mechanisme wordt kationuitwisseling genoemd en als gevolg hiervan zitten er na uitwisseling, in plaats van magische ZnTe-clusters, (Zn,Cd)Te-clusters in het synthesesmengsel. Vervolgens vormen deze (Zn,Cd)Te-clusters nanodraden via georiënteerde aanhechting. De clusters klikken als het ware in elkaar en vormen een streng van kralen. Vervolgens vult de Se-precursor samen met de Cd-atomen de beschikbare plaatsen in de kralenketting op. Op deze manier ontstaat een heteronanodraad die vele segmenten van (Zn,Cd)Te/CdSe bevat. Het licht dat de heteronanodraden uitzenden vertelt ons iets over de elektronische structuur. Zo nam de golflengte (maatstaf voor de energie) van het licht toe naarmate de fractie CdSe hoger werd. Hieruit kan worden geconcludeerd dat het elektron en het gat meer en meer ruimtelijk van elkaar gescheiden worden wanneer de hoeveelheid CdSe in de heteronanodraad toeneemt. Ook is de levensduur van het exciton (de tijd die het exciton er gemiddeld over doet om te vervallen) langer naarmate de fractie CdSe in de heteronanodraad toeneemt. Beide waarnemingen (lagere energie van het licht en langere levensduur van het exciton) duiden op de vorming van een heteronanokristal waarin het elektron en het gat ruimtelijk van elkaar worden gescheiden.

In hoofdstuk 6 wordt dieper ingegaan op de koppeling van kristaltrillingen (fononen) en het exciton in zogenoemde type-II heteronanokristallen. Fononen zijn kristaltrillingen van specifieke energieën en kunnen grofweg in twee categorieën worden ingedeeld; akoestische en optische fononen. Bij akoestische fononen volgen alle atomen (bijvoorbeeld in CdSe; Cd en Se) een gezamenlijke golfbeweging terwijl in optische fononen enkel dezelfde atomen een gezamenlijke golfbeweging maken. In een optische fonon in CdSe zullen de positief geladen Cd-atomen een golfbeweging maken die gemiddeld genomen de positieve atomen op een ander punt centreert dan de negatief geladen Se-atomen. Deze verplaatsing van de ladingen betekent dat er binnen het kristal een elektrisch veld ontstaat (dipoolmoment). Dit elektrisch veld kan met het exciton koppelen wat zorgt dat het verval van het exciton beïnvloed wordt. Door de luminescentie van heteronanokristallen te bestuderen kan informatie over het exciton en zijn verval worden verkregen. In excitatiespectra wordt gekeken naar welke absorptie verantwoordelijk is voor de luminescentie afkomstig van het exciton. De koppeling van fononen en het exciton zijn zichtbaar in de excitatiespectra als scherpe kleine pieken (fonon-pieken) die van elkaar gescheiden zijn door een vaste energie (~25 meV voor fononen in CdSe). De sterkte van de koppeling is af te lezen door het aantal pieken en de verhouding van het oppervlak onder de fonon-pieken. In de excitatiespectra van de type-II CdSe/CdTe-heteronanokristallen zijn deze fonon-pieken te zien. Hieruit kunnen we concluderen dat het ruimtelijk gescheiden exciton en de optische fononen gekoppeld zijn. De sterkte van de koppeling was groter dan waargenomen voor CdSe-nanokristallen en type I<sup>1/2</sup> CdSe/CdTe-heteronanokristallen. In een type-I<sup>1/2</sup> heteronanokristal bevindt zich als gevolg van de elektronische structuur één van de ladingsdragers (elektron of gat) in één materiaal terwijl de andere ladingsdrager zich in beide materialen bevinden. De ladingsdragers zijn in deze heteronanokristallen gemiddeld genomen meer ruimtelijk gescheiden dan in CdSe-nanokristallen, maar nog niet zoveel als in type-II heteronanokristallen. Het feit dat de exciton-fonon koppeling sterker is in de type-II heteronanokristallen ten opzichte van de andere onderzochte nanokristallen is een gevolg van het ruimtelijk gescheiden elektron en gat. Deze ruimtelijke scheiding van het exciton zorgt voor een elektrisch veld binnen het heteronanokristal, welke de exciton-fonon koppeling sterker maakt via een zogenoemde Fröhlich-interactie. De controle over het maken van heteronanokristallen die een ruimtelijk gescheiden exciton (indirect exciton) kunnen bevatten geeft de mogelijkheid om de mate van ruimtelijke scheiding van het exciton te bepalen.

In hoofdstuk 7 is de afhankelijkheid van de elektronische structuur van CdTe-nanokristallen van de grootte is onderzocht aan de hand van absorptiespectra. Absorptiespectra van oplossingen die colloïdale CdTe-nanokristallen van verschillende grootte bevatten zijn geanalyseerd en vergeleken met elkaar. Absorptiespectra geven aan hoeveel licht van een bepaalde golflengte wordt geabsorbeerd. Deze geabsorbeerde hoeveelheid licht correspondeert met een bepaalde energieovergang in het energiediagram van een nanokristal. Uit de absorptiespectra kun je de relatieve positie van de energieniveaus van de elektronische structuur van een nanokristal aflezen. De experimentele absorptiespectra van CdTe-nanokristallen van verschillende groottes (2.9 - 14 nm) zijn vergeleken met berekende spectra verkregen door tight-binding-berekeningen. In deze berekeningen werden de interacties tussen het elektron en het gat wel en niet meegenomen. De resultaten laten zien dat de elektron-gat interacties belangrijk zijn voor het berekenen van het absorptiespectrum.

In hoofdstuk 8 wordt de synthese en karakterisering van ZnSe/CdSe-kern/schil-heteronanokristallen beschreven. Heteronanokristallen kunnen op een traditionele manier gemaakt worden. Deze traditionele groei houdt in dat je een tweede materiaal op een voorgevormde kristal laat groeien. Een alternatieve manier om een heteronanokristal te produceren is via de eerdergenoemde kationuitwisseling. Via deze methode worden de kationen uitgewisseld terwijl de oorspronkelijke vorm van het kristal behouden blijft. Wanneer dit onder milde omstandigheden plaatsvindt worden van buiten naar binnen de kationen uitgewisseld. Doordat het een uitwisseling is en de grootte van het kristal behouden blijft, zal in de tijd een steeds dikker wordende schil worden gevormd die in dikte toeneemt ten koste van de kerngrootte. De in dit hoofdstuk beschreven heteronanokristallen zijn gemaakt door middel van uitwisseling van Zn-kationen voor Cd-kationen. De optische eigenschappen van ZnSe/CdSe-kern/schil-heteronanokristallen geven aan dat dit type-I<sup>1/2</sup>-heterokristallen zijn. Hoe hoger de reactietemperatuur die gebruikt werd hoe meer Zn-atomen worden uitgewisseld voor Cd. Wanneer een reactietemperatuur boven de 220°C werd gebruikt, werd er niet meer een nette schil gevormd maar vermengden de kernkationen zich gedeeltelijk met de schilkationen. Hierdoor ontstaat een gradiënt aan Cd-atomen richting de kern. Dit soort nanokristallen wordt een gradiënt-kern/schil-heteronanokristal genoemd.

De halfgeleider nanokristallen beschreven in dit proefschrift zijn colloïdale nanokristallen. Dit betekent dat het oppervlak van de nanokristallen



bedekt is met moleculen die voor de stabiliteit en de oplosbaarheid van de kristallen zorgt. Deze moleculen (liganden) hebben invloed op de eigenschappen van nanokristallen. Atomen op het kristaloppervlak zijn maar deels omringd met de atomen uit het kristal en dit is ongunstig voor een aantal energieniveaus in dat atoom. Enkele van de energieniveaus van dit oppervlakatoom kunnen hoger in energie zijn en daardoor kunnen ze zich in de verboden zone (bandafstand) bevinden (inter-bandafstand energieniveaus). Wanneer een gevormd exciton verval kan het zijn energie afgeven door het uitzenden van licht (stralend verval). Het nanokristal ontvangt energie (lichtabsorptie) en geeft dit af aan zijn omgeving door licht (luminescentie) en doet dit met een bepaalde efficiëntie (quantum-efficiëntie). De aanwezigheid van energieniveaus in de bandafstand geeft het exciton nieuwe manieren om te vervallen. Verval via deze inter-gat energieniveaus kan plaats vinden door de uitzending van licht van een lagere energie of het kan plaatsvinden zonder dat licht wordt uitgezonden. Dit laatste wordt verval genoemd en zorgt voor een lagere niet stralende quantum-efficiëntie. Liganden binden aan de oppervlakte atomen en zijn in staat om de energieniveaus in de bandafstand weg te nemen. Liganden kunnen ook zorgen voor een beter of gunstiger oppervlak door atomen over het oppervlak te transporteren. Door deze reorganisatie van de atomen kunnen de energieniveaus in de bandafstand worden verminderd. Het exciton heeft hierdoor minder de mogelijkheid om niet-stralend te vervallen en de quantum-efficiëntie gaat omhoog. In hoofdstuk 9 wordt gekeken naar de invloed van de liganden op de intensiteit van de luminescentie van CdTe-nanokristallen. De luminescentie van CdTe-nanokristallen met octadecylamine (ODA) en dodecylamine (DDA) aan het oppervlak zijn met elkaar vergeleken. Twee geconcentreerde oplossingen van CdTe-nanokristallen (bedekt met ODA en DDA) werden bereid. Vanuit deze geconcentreerde oplossingen werden verdunningen gemaakt waarvan de luminescentie intensiteit werd gevolgd als functie van de tijd na verdunning. De luminescentie werd gevolgd door het opnemen van emissiespectra. Een emissiespectrum geeft de hoeveelheid licht per energie (kleur/golflengte) aan. De quantum-efficiëntie van met ODA bedekte CdTe-nanokristallen ging omhoog wanneer de nanokristallen werden beschonen met violet licht (golflengte: 400 nm). Wanneer dezelfde nanokristallen volledig in het donker werden bewaard was er geen verbetering van de quantum-efficiëntie waar te nemen. Het effect dat de quantum-efficiëntie van de nanokristallen toeneemt als gevolg van de blootstelling aan licht is bekend als het Engelse woord photo-brightening. Het resultaat verkregen bij de met DDA bedekte CdTe-nanokristallen was tegenovergesteld aan dat

van met ODA bedekte nanokristallen. De quantum-efficiëntie ging omhoog bij zowel de oplossingen bewaard in het donker als blootgesteld aan violet licht gedurende een bepaalde periode. Dit geeft aan dat DDA bedekte CdTe-nanokristallen al efficiënter worden zonder dat ze worden blootgesteld aan violet licht. Het oppervlak van deze CdTe-nanokristallen reorganiseert zonder violet licht. De efficiëntietoename kan worden verklaard door aan te nemen dat de DDA-liganden relatief mobiel zijn bij kamertemperatuur op het CdTe-oppervlak, in tegenstelling tot de ODA liganden. Bij kamertemperatuur kunnen hierdoor DDA-liganden al voor de reorganisatie van het kristaloppervlak zorgen. Voor ODA liganden kan deze reorganisatie echter enkel worden bereikt wanneer er energie in de nanokristaloplossing wordt gepompt door het beschijnen met violet licht. Deze resultaten laten duidelijk zien dat deze colloïdale nanokristallen en hun liganden een zeer complex en dynamisch systeem vormen.



# List of publications

## THIS THESIS IS BASED ON THE FOLLOWING PUBLICATIONS:

1. E. Groeneveld, S. van Berkum, A. Meijerink, C. de Mello Donegá, Growth and stability of ZnTe Magic Size Nanocrystals, *Small* 7 (2011) 1247 - 1256. (Chapter 4)
2. E. Groeneveld, S. van Berkum, M. M. van Schooneveld, A. Gloter, J. D. Meeldijk, D. J. van den Heuvel, H. C. Gerritsen, C. de Mello Donegá, Highly luminescent (Zn,Cd)Te-CdSe colloidal heteronanowires with tunable electron-hole overlap, *Nano Letters* 12 (2012) 749-757. (Chapter 5)
3. E. Groeneveld, C. de Mello Donega, Enhanced Exciton-Phonon coupling in colloidal Type-II CdTe-CdSe heteronanocrystals, *Journal of Physical Chemistry C* 116 (2012) 16240-16250. (Chapter 6)
4. E. Groeneveld, C. Delerue, G. Allan, Y. Niquet, C. de Mello Donega, Size dependence of the exciton transitions in colloidal CdTe quantum dots, submitted to *Journal of Physical Chemistry C*, August, 2012. (Chapter 7)
5. E. Groeneveld, L. Witteman, X. Ke, S. Bals, C. de Mello Donegá, Formation of concentric ZnSe/CdSe core/shell Heteronanocrystals via cation-exchange, in preparation. (Chapter 8)
6. E. Groeneveld, A. Onnink, J. Van Rijssel, B. Erne, A. Meijerink, C. de Mello Donegá, Ligand Mediated Surface Reconstruction and Relaxation of Colloidal CdTe nanocrystals, in preparation. (Chapter 9)
7. E. Groeneveld and C. de Mello Donegá, The challenge of colloidal nanoparticle synthesis, in: "Nanoparticles: Workhorses of Nanoscience. Fundamentals, Preparation and Applications.", Ed. C. de Mello Donegá, Ch. 4 (Springer-Verlag, Berlin, 2013). (Chapter 2)
8. R. Koole, E. Groeneveld, D. Vanmaekelbergh, A. Meijerink, and C. de Mello Donegá, Size effects on Semiconductor Nanoparticles, in: "Nanoparticles: Workhorses of Nanoscience. Fundamentals, Preparation and Applications.", Ed. C. de Mello Donegá, Ch. 2 (Springer-Verlag, Berlin, 2013). (Chapter 3)

## OTHER PUBLICATIONS BY THE AUTHOR:

1. M.C.D. Mourad, E. Groeneveld, P.J. de Lange, C. Vonk, D. van der Beek, and H.N.W. Lekkerkerker, 'Columnar liquid crystals of gibbsite platelets as templates for the generation of ordered silica structures', *Journal of Materials Chemistry* 18, (2008), 3004.
2. V.W.A. de Villeneuve, R.P.A. Dullens, D.G.A.L. Aarts, E. Groeneveld,

- J.H. Scherff, W.K. Kegel, and H.N.W. Lekkerkerker, 'Colloidal hard-sphere crystal growth frustrated by large spherical impurities', *Science* 309, (2005), 1231-1233.
3. J. H. Blokland, V. I. Claessen, F. J. P. Wijnen, E. Groeneveld, C. de Mello Donegá, D. Vanmaekelbergh, A. Meijerink, J. C. Maan, and P. C. M. Christianen, Exciton Lifetimes of CdTe Nanocrystal Quantum Dots in High Magnetic Fields, *Physical Review B* 83 (2011) 035304-1 / 035304-5.
  4. J. J. Eilers, E. Groeneveld, C. de Mello Donega, A. Meijerink, Optical properties of Mn-doped ZnTe Magic Size Nanocrystals, *Journal of Physical Chemistry Letters* 3 (2012) 1663-1667.
  5. R. Ulbricht, J.J.H. Pijpers, E. Groeneveld, R. Koole, C. de Mello Donega, D. Vanmaekelbergh, C. Delerue, G. Allan, M. Bonn, Loosening quantum confinement: Observation of real conductivity in semiconductor nanoparticles smaller than the Bohr radius, *Nano Letters* 12 (2012), DOI: 10.1021/nl302517z.
  6. Z. Krumer, S. J. Pera, R. J. A. van Dijk-Moes, Y. Zhao, S. de Brouwer, E. Groeneveld, W. G. J. H. M. van Sark, R. E. I. Schropp, C. de Mello Donegá, Tackling self-absorption in Luminescent Solar Concentrators with type-II colloidal quantum dots, submitted to *Solar Energy Materials and Solar Cells*, July, 2012.

#### CONTRIBUTIONS TO SCIENTIFIC CONFERENCES AS PRESENTING AUTHOR:

1. 4th International Conference on Colloidal Semiconductor and Metal Nanocrystals – NaNaX4, April 2010, Munich, Germany. Poster: Groeneveld\*, E.; Van Berkum, S.; and de Mello Donegá, C.; From magic size ZnTe clusters to highly luminescence ZnTe/CdSe colloidal nanowires
2. 2011 Materials Research Society - Spring Meeting, April 2011, San Francisco, USA. Symposium E: Energy Harvesting – From Fundamentals to devices. Talk: Groeneveld,\* E.; Van Berkum, S.; de Mello Donegá, C.; Synthesis and Optical Spectroscopy of Highly Luminescent Type-II ZnTe/CdSe Colloidal Heteronanowires
3. NWO Meeting: Chemistry related to Physics and Materials Science, March 2011, Veldhoven, Netherlands. Talk: Groeneveld,\* E.; van Berkum, S.; Meijerink, A.; de Mello Donegá, C.; The start of something small: ZnTe magic size clusters. (Best Lecture Award)
4. NWO Meeting: Chemistry related to Physics and Materials Science, March 2011, Veldhoven, Netherlands. Poster: Groeneveld,\* E.; van Berkum, S.; de Mello Donegá, C.; Semiconductor Nanospaghetti: Highly Luminescent ZnTe-CdTe-CdSe colloidal heteronanowires.

5. HERODOT Summer School “Nanomaterials based on Inorganic Heterostructures”, April 2011, Corsica, France. Poster: Groeneveld,\* E.; van Berkum, S.; de Mello Donegá, C.; Semiconductor Nanospaghetti: Highly Luminescent ZnTe-CdTe-CdSe colloidal heteronanowires.
6. 2011 European Materials Research Society - Spring Meeting, May 2011, Nice, France. Symposium 11 C: Size-dependent properties of nanomaterials. Poster: Groeneveld,\* E.; van Berkum, S.; Meijerink, A.; de Mello Donegá, C.; Growth and Stability of ZnTe Magic Size Nanocrystals. (Young Scientist Award)
7. Second European Energy Conference- E2C 2012, April 2012, Maastricht, Netherlands. Symposium 2 “Sciences for Energy – Solar”. Talk: Groeneveld\*, E.; Van Berkum, S.; De Mello Donegá, C.; Highly luminescent colloidal heteronanowires for solar energy harvesting and conversion.
8. 5th International Conference on Colloidal Semiconductor and Metal Nanocrystals – NaNaX5, May 2012, Fuengirola, Spain. Poster: Groeneveld\*, E.; van Berkum, S.; van Schooneveld, M. M.; Gloter, A.; Meeldijk, J. D.; van den Heuvel, D. J.; Gerritsen, H. C.; de Mello Donegá, C.; Highly Luminescent (Zn,Cd)Te-CdSe Colloidal Heteronanowires with Tunable Electron-Hole Overlap.



# Dankwoord

1461 dagen, 4 sinterklaasvieringen, 7 buitenlandse werktripjes, ontzettend veel uren in de glovebox, verscheidene (lange) nanokristal-discussies, 4 keigave basketbalseizoenen, minstens 40 kilo pure chocoladehagelslag, honderden bittergarnituren en ontelbaar veel leuke en bijzondere momenten verder: wat gaat 4 jaar promoveren toch snel! Promoveren is niet 4 jaar lang alleen maar onderzoek doen. Het is meer dan dat. Het is een leerzaam langtermijnproject waarbij je veel van en door andere mensen leert en wat eindigt met het schrijven van je proefschrift. Ondanks dat vele mensen zullen geloven dat ik best in staat ben om een boek van meer dan tweehonderd pagina's te schrijven, durf ik te stellen dat dit boekwerk zonder een aantal mensen een heel stuk dunner zou zijn geweest. Een promovendus is als een wielrenner in de Tour de France als promoveren de Tour de France winnen is. Je rijdt het hele stuk zelf, maar om ritzeges te pakken moet je een goed team achter en om je heen hebben. In de gele trui het Academieggebouw bereiken is niet alleen een verdienste van jezelf maar ook zeker een verdienste van de mensen om je heen. Dit gedeelte van het proefschrift wil ik daarom gebruiken om alle mensen om me heen te bedanken voor alles wat ze direct of indirect hebben bijgedragen aan dit proefschrift.

Celso, allereerst bedankt voor het feit dat je me de mogelijkheid hebt gegeven om te promoveren. Ik ben erg blij met alle resultaten die we samen hebben behaald. We begonnen altijd met het voornemen om een onderzoek kort en bondig op te schrijven. De realiteit was echter altijd dat we toch altijd uitkwamen op een artikel dat (iets) langer maar ook zeker interessanter was dan we in eerste instantie verwachtten. Dankzij je enthousiasme en kennis over nanokristallen, je oog voor detail en je kritische blik heb ik veel van je geleerd. Ik wil je daarvoor hartelijk bedanken.

Andries, jij ook bedankt voor het geven van de mogelijkheid om bij jullie te promoveren. Jouw liefde voor het onderzoek is inspirerend. Het is dan ook mooi om te zien hoe jij als professor met veel plezier eerste- tot en met laatstejaars studenten (ook op het lab) begeleidt. Iets wat ik van jou heb geleerd, en wat ik ook zeker in mijn verdere werkzaamheden mee zal nemen, is dat (wetenschappelijke) kennis en humor prima met elkaar gecombineerd kunnen worden.



Dan zijn er nog een aantal mensen die ook belangrijk zijn geweest voor het onderzoek. Allereerst is daar natuurlijk Hans (Ligthart), de man die alles voor het lab kan maken wat je bedenkt. Niet alleen je technische kunde maar ook zeker je gezelligheid en de manier waarop je het woord 'Faantàstisch' uitspreekt, zijn gewoonweg geweldig. Stephan, mijn held op computergebied. De dag dat mijn computer 'plof' zei zal ik niet snel meer vergeten. Wanneer ik vragen had over mijn computer stond jij altijd binnen een minuut klaar om mij te helpen: super! Van de elektronenmicroscopiegroep wil ik graag Hans (Meeldijk) en Chris bedanken. Jullie stonden altijd klaar om vragen te beantwoorden of om de microscoop juist in te stellen voor mooie TEM-plaatjes. De hoge resolutie en cryo-TEM metingen van Hans hebben dan ook geleid tot mooie publicabele resultaten! I would also like to thank the people that helped with my publications and research: Suzanne, Matti, Hans (Meeldijk), Dave, Hans (Gerritsen), Christophe, Jos, Ben, Ke, Sara, Alexander, Guy and Yann-Michel. I wouldn't have succeeded without your knowledge and skills: Thank you! Een samenvatting voor leken schrijven is gemakkelijker gezegd dan gedaan. Voor dit hoofdstuk wil ik graag pap, ome Cees en Mim bedanken voor hun belangrijke bijdrage!

Bij deze wil ik ook graag de leden van mijn leescommissie, John Kelly, Daniël Vanmaekelbergh, Hans Gerritsen en Henk Lekkerkerker bedanken. Het was fijn dat jullie midden in de zomer tijd vrij konden maken om mijn manuscript te lezen. Veel dank hiervoor!

Ik heb de afgelopen jaren verschillende studenten begeleid. Ik vond dit erg leuk en zeker ook leerzaam om te doen. Rianne, je hebt naast veel nanokristallen syntheses ook veel optische metingen gedaan. Ik vind het echt heel knap dat je ondanks de grote hoeveelheid en verschillende soorten data er een overkoepelend verhaal van hebt kunnen maken. Aldo, onze eerste kennismaking zal ik niet vergeten. Ik ontmoette een lange jongen met een flinke bos krullen die wel van een praatje hield. Dat wetenschap voor veel mensen toegankelijk kan zijn, heb jij me laten zien toen jij en Mark bezig waren met het opzetten van de website [scheikundejongens.nl](http://scheikundejongens.nl). Misschien zien we je nog wel een keer bij De wereld draait door. Sander, een gezellige Brabo die heel wat uurtjes nanokristallen-makend achter de glovebox heeft doorgebracht. Dat je doorzettingsvermogen hebt werd me ook duidelijk. In een paar maanden heb jij je rechtshandige glovebox-skills eigen gemaakt terwijl je eigenlijk linkshandig bent: respect daarvoor! Verder vermoed ik dat jij na jouw project geen plaatje van een 'uitgevallen dennenbos' meer kon zien. Merel, de University College studente die van (echt) dansen houdt

en die zich ook maar even naast haar studie in de dames 8 van Orca heeft geroeid. Is er eigenlijk iets dat je niet kunt? Je pikte alles supersnel op en jouw onderzoek is het startpunt van mijn hoofdstuk 8 geworden. Arnoud, op het moment van schrijven ben je net in Australië aangekomen voor je stage. Je hoopt in Australië ook wat te kunnen genieten van allerlei zaken naast de studie. Dit heb je zeker verdiend! Je hebt namelijk hier al hard gewerkt en veel mooie resultaten behaald. Jouw onderzoek, wat soms meer weg had van een Russische matroesjka, is terug te zien in hoofdstuk 9. Léon, jij bent mijn laatste student. Ik kan je zeggen dat ik jaloers ben op de manier waarop jij je labjournaal bijhoudt. Een deel van jouw resultaten is beschreven in hoofdstuk 8 en terwijl ik de groep zal verlaten, zul jij nog even verdergaan met het binnenharken van ongetwijfeld nog meer mooie onderzoeksresultaten.

Doing a Phd may sound lonely but it doesn't mean you are locked-up alone in a dark cave, doing long experiments, sitting in an uncomfortable position behind your computer, and talking to yourself. Luckily I have had a lot of colleagues to talk to and to have fun with. First of all I would like to thank Wiel, Rosa, Timon and Dennis for being my roommates. It was always helpful to bounce off ideas, nice to do sports, and nice to talk about my favorite subject: food. Furthermore I would like to thank all my colleagues (Dominika, Francesca, Marianna, Dariusz, Joren, Relinde, Mark, Zachar, Ingmar, Joost, Freddy, Yiming, Bert, Alek, Linda, Zhixiang, Peter, Harold, Onno + all the students + other staff) for all the good times: conversations, lunch and coffee breaks, cakes, abroad trips, sports (basketbal, dancing, workout, etc.), FOM days (FOM party!), and Sinterklaas.

Basketbal is naast slapen en eten één van mijn belangrijkste hobby's. Basketballen doe je net als promoveren niet alleen: hier heb je de allerleukste teamgenoten van de wereld voor nodig. De afgelopen 4 jaar heb ik bij verschillende teams gespeeld. Het eerste jaar van mijn promotie speelde ik nog bij de Barons in Breda. Het was elke training en wedstrijd een eindje reizen maar dat was het dubbel en dwars waard. Nadat ik voltijd in Utrecht kwam wonen, leek het me praktischer om ook in Utrecht te gaan basketballen. Hier kwam ik terecht bij de Utrecht Bull's dames 1. Ik denk dat ik me geen betere overstap had kunnen wensen. We zijn nu 3 seizoenen, 3 MIT toernooien, ontelbaar veel bittergarnituurtjes en veel lol verder en ik hoop dat we nog veel plezier op en buiten het veld gaan beleven. Bedankt lieve teamies jullie zijn toppers!

Er zijn nog meer mensen die de afgelopen jaren voor de nodige afleiding hebben gezorgd. Allereerst zijn daar de vriendinnen uit Brabant (Ilse, Juud, Marichèlle, Martine en Rianne). Ook al hebben we een halfjaarplanning nodig om een datum te prikken: als we eenmaal bij elkaar zijn, is het altijd gezellig! Dan zijn er 'de mannen van scheikunde'. Dit boekje is het publiceren niet waard als ik jullie niet zou noemen. Vanaf dag 1 van onze opleiding tot aan nu hebben we naast samen colleges volgen ook de meest fantastische/grappige/bizarre momenten en blessures met elkaar meegemaakt. Goss, Parcival, David, Nik, Stefan: Neutronen bedankt! Ook wil ik graag Thomas bedanken. Zelf had ik nooit zo'n mooi super-vet-strak-keigaaf ontwerp en opmaak van mijn thesis kunnen maken. Natuurlijk horen er nog meer andere mensen in dit bedankrijtje thuis. Daarom, voor iedereen met wie ik de afgelopen jaren veel plezier heb beleefd en wie ik onverhoopt vergeten ben geldt: super bedankt!

Dan is er nog mijn lieve familie. Verjaardagen, feestjes, kerst, wintersport, maar ook gewoon gezelligheid omdat het kan. Ook jullie hebben indirect bijgedragen aan dit boekje, door jullie belangstelling, afleiding, maar ook gewoon door er voor mij te zijn! Bedankt: Arno, Riet, Zeger, Annemarie, Patrick, Carolien, Henkjan, ooms, tantes, neven en nichten.

Lieve pap en mam, ook jullie ben ik natuurlijk ontzettend dankbaar. Jullie zijn me heel erg dierbaar en ik ben blij met jullie liefde, steun en vertrouwen. Ik hoop dat jullie net zo trots zijn op mij als ik op jullie!

Lieve Hans, dit is ook een beetje jouw boekje. Je bent er altijd voor mij geweest. Het was fijn dat je (bijna) altijd met veel interesse naar mijn (ik geef toe: soms ietwat lange) verhalen luisterde. De laatste weken toen ik het 'aardig' druk had heb jij ervoor gezorgd dat iedere dag, zoals altijd (!), een feestje was. Dankjewel!

# Curriculum vitae

Esther Groeneveld was born on February 2, 1985 in Breda, the Netherlands. After she obtained her pre-university diploma in 2003 at the Altena College in Sleeuwijk, she started studying Chemistry at Utrecht University (the Netherlands). She received her Bachelor diploma (honours; 'met genoegen') in 2006 after finishing her bachelor's research project in the Van 't Hoff laboratorium for Physical and Colloidal Chemistry under supervision of dr. Maurice Mourad and Prof. dr. Henk Lekkerkerker. In September 2006 she started her Master's research project in the Condensed Matter and Interfaces group under supervision of dr. Celso de Mello Donegá and Prof. dr. Andries Meijerink. Her research project involved studying the synthesis and optical properties of ZnTe and ZnTe/CdSe nanocrystals. As part of her master she conducted a 5,5 month internship at the Soft Condensed Matter group of Fribourg University in Switzerland under supervision of dr. Kitty van Gruijthuijsen and Prof. dr. Peter Schurtenberger. This project involved the study of depletion interactions in non-charged polymer-colloid mixtures. After finishing her internship she received her Master diploma (honours; Cum Laude) in September 2008.

From October 2008 she was employed as Phd researcher in the Condensed Matter and Interfaces group in the chemistry department of Utrecht University. The subject of her research project was 'the synthesis and optical study of colloidal semiconductor (hetero)nanocrystals' and this research was performed under supervision of Prof. dr. Andries Meijerink and dr. Celso de Mello Donegá. Main results of this project are described in this thesis, published in scientific journals, and presented at international conferences. For her conference contributions she has received a best lecture award (NWO studiegroepen meeting, Veldhoven, The Netherlands, 2011) and a young scientist award (E-MRS meeting, Nice, France, 2011).

During her Phd project Esther supervised 4 master students and 2 bachelor students during their final research projects. Furthermore, she has taught first and second year students during their practical analytical chemistry course. From April 2011 to April 2012 she was a member (Secretary) of the Debye Phd committee. This committee represents all Phd students in the Debye Institute for Nanomaterials science at Utrecht University.

Besides spending time with her family and friends, Esther enjoys playing basketball. She has been an active member of various basketball associations since 1999. Besides playing she has been a coach of several teams, and official referee of the Dutch Basketball union. Currently she is a board member (Competition secretary) of the Utrecht Bull's basketball association.





